Dynamics of Particle Clouds Related to Open-Water Sediment Disposal

by

Gordon J. Ruggaber

Submitted to the Department of Civil and Environmental Engineering
in partial fulfillment of the requirements for the degree of

Doctor of Philosophy in Environmental Engineering

at the

MASSACHUSETTS INSTITUTE OF TECHNOLOGY

June 2000

Author .....
Department of Civil and Environmental Engineering
May 1, 2000

Certified by .....
E. Eric Adams
Senior Research Engineer
Thesis Supervisor

Accepted by .....
Daniele Veneziano
Chairman, Departmental Committee on Graduate Studies

Dynamics of Particle Clouds Related to Open-Water Sediment Disposal

by

Gordon J. Ruggaber

Submitted to the Department of Civil and Environmental Engineering
on May 1, 2000, in partial fulfillment of the
requirements for the degree of
Doctor of Philosophy in Environmental Engineering

Abstract

Open-water disposal and capping is a promising solution for disposing of the 14 to 28 million m^3 of contaminated sediment dredged annually in the United States (National Research Council, 1997). Such practice raises concerns about the feasibility of accurately placing the material in a targeted area and the loss of material to the environment during disposal. To better predict the fate of these materials, the objective of this research was to gain new insight into the physical processes governing the mechanics of their convective descent.

Instantaneously released sediments form axisymmetric "clouds" resembling self-similar thermals. Current particle cloud models employ thermal theory and an integral approach using constant entrainment (α), drag (C_D), and added mass (k) coefficients. The aim of this study was to investigate how real sediment characteristics (particle size, water content, and initial momentum) affect cloud behavior (i.e., velocity, growth rate, and loss of particles) and time variations in α, C_D, and k.

Flow visualization experiments were conducted using a glass-walled tank, special sediment release and capture (i.e., "trap") mechanisms, and various cohesive and non-cohesive particles. Particle sizes were scaled to real-world dimensions through the cloud number (N_c), defined as the ratio of the particle settling velocity to the characteristic cloud velocity. An "inverse" integral model was developed in which the conservation equations were solved for α and k using measured velocity and radius data. Based on the "inverse" model results, particle cloud experiments were simulated with an integral model using constant and time-varying α and k.

The non-cohesive sediments evolved rapidly into "thermals" with asymptotic deceleration and large growth rates ($\alpha = 0.2 - 0.3$). The particles eventually organized into "circulating thermals," with linear growth rates obeying buoyant vortex ring theory. In this phase, large particles ($N_c > 10^{-4}$) produced laminar-like vortex rings with small α (0.1 - 0.2). Compared to the cohesive sediments, which exhibited a wide range of growth rates, changes in water content and initial momentum of the non-cohesive particles produced 10 - 20 % variations in α.

Material not incorporated into the cloud upon release formed a narrow "stem"

behind the cloud, which contained as much as 30 % of the original mass depending on the release conditions. Much of the "stem" material either re-entrained into the cloud later in descent or reached the bottom shortly after it. Material not incorporated into the "stem," which may be advected by ambient currents, was found to be only a small fraction (< 1 %) of the original mass.

Inverse integral model results suggest that C_D and k are close to zero within the "thermal" phase. In the "circulating thermal" phase, the reduction in α caused by large particles ($N_c > 10^{-4}$) increased k to a value similar to that of a solid sphere. Integral model results confirm the suitability of using constant coefficients for modeling particle clouds with N_c less than 10^{-4}. When N_c is greater than 10^{-4}, time-varying α and k are required to properly simulate cloud behavior in the "circulating thermal" phase.

Thesis Supervisor: E. Eric Adams
Title: Senior Research Engineer

Acknowledgments

I would like to acknowledge the MIT Sea Grant College Program and the New England Division of the U.S. Army Corps of Engineers for sponsoring this research.

I would like to thank my thesis advisor, Dr. E. Eric Adams, for his helpful advice and direction provided over the course of this work. I wish to also show my sincere appreciation to my thesis committee members, Professor Ole S. Madsen, Professor Kelin Whipple, and Dr. Thomas Fredette, for their time, effort, and thoughtful input.

I would like to recognize Scott Socolofsky for his help in constructing the experimental facilities, programming the data acquisition software, and assisting with experiments. Special credit must be given to Elizabeth Bruce and Christopher Resto for their contributions to this work. Their many hours of assistance with experiments and data analysis are greatly appreciated. I wish to also thank Paul Fricker for his friendship and help with experiments as well as Ling Tang and Sanjay Pahuja for their friendship and moral support.

Special thanks go to Sheila Frankel for her many efforts in making Parsons Lab a more enjoyable place work.

I wish express my gratitude to my parents, Rudolf and Joan, and parents-in-law, Ben and Connie Sheffy, for all of their love and support during this endeavor.

Most of all, I am forever grateful to my wife, Alese, and children, Ben and Chelsea, for their constant love, encouragement, and patience over the past four years. Without their many sacrifices, my Ph.D. would not have been possible.

Contents

List of Figures

List of Tables

Chapter 1

Introduction

In this chapter, the real-world problems motivating this work are described. The scope of this investigation, as related to the ultimate fate of sediments discharged to open waters is discussed next, followed by an outline of objectives for this work.

1.1 Motivation

An estimated 14 to 28 million m^3 of contaminated sedimentary material is dredged annually in the United States, which represents approximately 5 to 10 % of all sediments dredged in the U.S. (National Research Council, 1997). A lack of low-cost upland disposal alternatives has made open-water disposal followed by placement of capping materials (e.g., sand) an attractive solution. Such practice raises not only water quality concerns associated with the potential loss of contaminated material to the water column during disposal, but also engineering challenges related to the ability of barges or scows to accurately place dredged and capping materials within a targeted area.

The Boston Harbor Navigation Improvement Project (BHNIP) provides a timely example of the technological problems posed by a dredging disposal/capping project. The project, which involves dredging portions of Boston Harbor to accommodate newer and larger ocean vessels, is expected to ultimately generate about 1.0 million m^3 of contaminated silt, 2.7 million m^3 of underlying parent material (mainly clay),

and 0.1 million m^3 of rock (Massport and USACE, 1995). The contaminated silt is being disposed of in excavated in-channel disposal cells (15-20 m deep) and covered with a 1 m layer of clean sand, while the parent material is being disposed of at the Massachusetts Bay Disposal Site (approximately 90 m deep). Implementation of a test cell in the summer of 1997 resulted in unanswered questions concerning the amount of lateral spreading (surging) that occurred following disposal of the silt material, as well as the amount of mixing that took place during placement of the coarser sand cap on top of the softer sediments (SAIC, 1997).

Clearly, successful implementation of sediment disposal and capping technologies, whether in shallow depths, such as Boston Harbor, or in deeper and more ecologically sensitive areas, requires an understanding of, and the ability to predict, the short-term mechanics of these materials in the environment (i.e., velocity, growth rate, and loss of particles to the environment). As discussed in Chapter 2, a limited number of studies have been performed to investigate the behavior of particle clouds as related to the disposal of dredged material. Thescopes of these studies were rather limited in that only gross comparisons were made between the motion of the particle clouds and that of classical "thermals." No detailed studies have been performed to investigate the influence of real sediment characteristics and release conditions (e.g., in-vessel settling, water content, initial momentum) on the behavior of released sediments. Field measurements suggest that the amount of material lost to the ambient environment during disposal to be in the range of 1 to 5 % of the original mass. However, to date, no studies have been conducted to investigate the physical mechanisms responsible for this loss and how such mechanisms are affected by initial sediment conditions. Hence, the aim of this research is to gain new insight intohow initial sediment characteristics and release conditions affect the physical processes governing the short-term fate of dredged and capping materials discharged into open waters.

The short-term behavior of materials discharged into open waters has been conceptualized into the following three phases (Clark et al., 1971; Koh and Chang, 1973) as shown in Figure 1.1:

- Convective Descent: Released sediments form a particle cloud that is trans-

ported downward by its negative buoyancy (submerged weight).

- Dynamic Collapse: When the cloud impacts the bottom or reaches a level of neutral buoyancy, the cloud collapses and spreads horizontally.

- Passive diffusion: When dynamic spreading has ceased, cloud particles advect and diffuse through action of the ambient current.

The research discussed herein focuses on the first phase of particle clouds, convective descent.

1.2 Qualitative Description of Convective Descent

It is most convenient to view the motion of suspended particles from a macroscopic point of view in which the particle cloud is assumed to act as a distributed source of negative buoyancy released suddenly (i.e., instantaneously) to its surroundings. In this respect, the cloud of particles is viewed as a continuous, single-phase density field, no different than a source of heavy fluid with the same average density. In the meteorological and fluid mechanics literature, such a sudden release of buoyancy (either positive or negative with respect to the ambient fluid) has been given the name "thermal" (Scorer, 1958; Woodward, 1959) based on early studies of free convection in the atmosphere due to temperature differences (e.g., cumulus cloud formation). Herein, the term "thermal" will be used in the context of a heavy thermal, falling through a fluid of lower density.

The typical velocity profile of a particle cloud has been categorized into the following three regimes (Rahimipour and Wilkinson, 1992; Noh and Fernando, 1993) as shown in Figure 1.2:

- Initial Acceleration Phase

- Self-Preserving or Thermal Phase

- Dispersive or Particle-Settling Phase

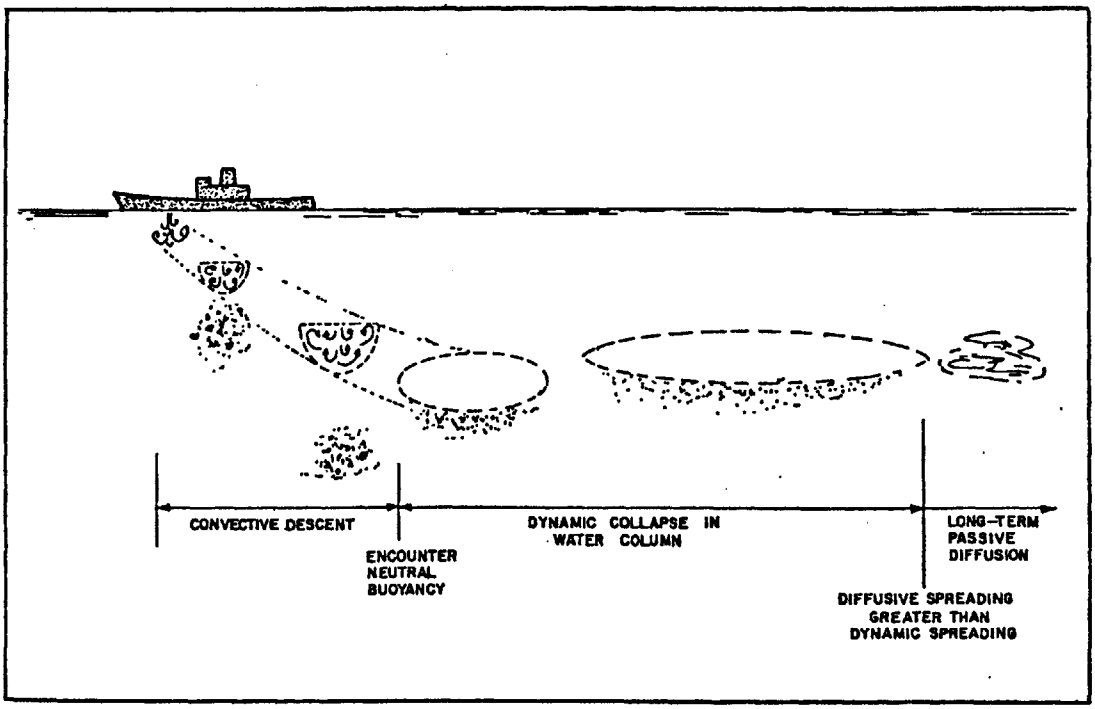

Figure 1-1: Idealized particle cloud phases (after Brandsma and Divoky, 1976).

Initial Acceleration Phase:

Upon release, the sediment/fluid mixture accelerates and expands rapidly, entraining ambient fluid over all of its surface through the action of small, turbulent eddies produced by the hydrostatic instability associated with density differences and velocity shear at the cloud boundary. It has been shown theoretically and experimentally (Escudier and Maxworthy, 1973; Baines and Hopfinger, 1984) that the duration of the initial acceleration phase is a function of the initial buoyancy, and that a thermal will typically reach the self-preserving phase after it has traveled a depth equivalent to 1 - 3 initial cloud diameters. Similar durations have also been observed for particle clouds (Nakatsuji et al., 1990; Li, 1997).

Self-Preserving Phase:

In this phase, thermals and particle clouds undergo an asymptotic deceleration caused by the rapid entrainment of less dense ambient fluid into the cloud. Since there is no representative length scale in this region, it is typically assumed that the thermal has reached a state of self-similarity in which all lengths are in proportion, and the mean velocity and buoyancy profiles across a horizontal section of the cloud are similar at all depths (Batchelor, 1954; Morton, Taylor, and Turner, 1956). Initially, the distribution of buoyancy must resemble either a tophat or gaussian-type profile, with a maximum value in the center of the cloud. As the cloud grows, larger eddies are produced which induce flow of ambient fluid into the rear of the cloud. These large eddies are responsible for organizing the cloud into an axisymmetic, vortical structure similar to a vortex ring, or more accurately, a spherical vortex as described by Hill (1894). The buoyancy distribution in a vortex ring is bimodal, with the buoyancy concentrated in the rotating core. The spherical vortex is characterized by a downflow of fluid (and particles) through the center and upflow of fluid along the edges. As this structure matures, the induced internal circulation cause the cloud to flatten and evolve into the characteristic mushroom-shaped (upside-down) thermal.

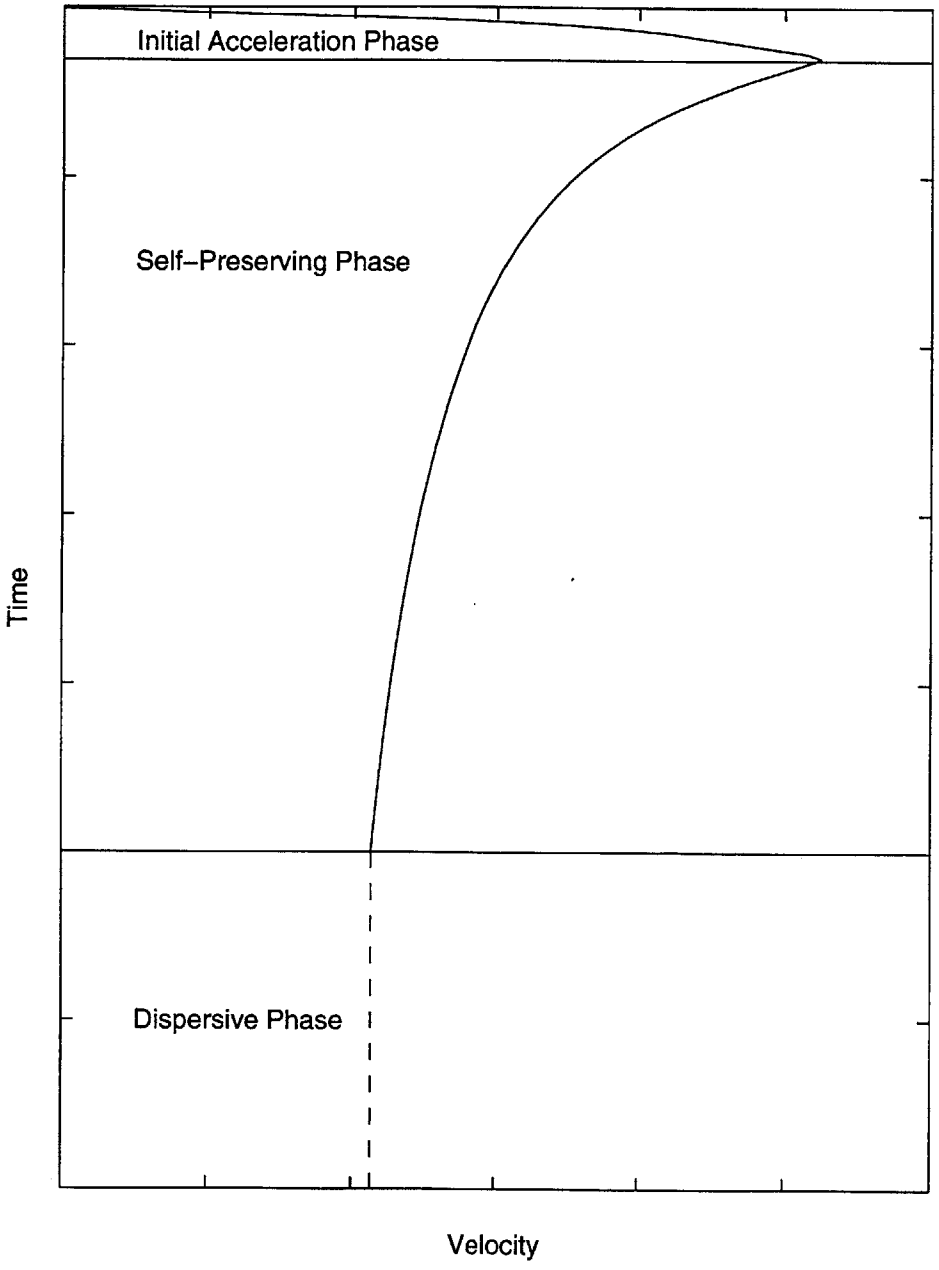

Figure 1-2: Idealized particle cloud convective descent phases.

Dispersive Phase:

As the descending particle cloud decelerates and its velocity approaches the settling velocity of the individual particles, the circulation is insufficient to keep the particles in suspension. At this point, the particles settle out of the cloud leaving behind a neutrally buoyant fluid volume descending only with the inertia it possesses at that time. The settling particles descend as a particle "swarm" (Nakatsuji et al., 1990; Papantoniou et al., 1990; Bühler and Papantoniou, 1991) that continues to expand (at a much slower rate) via weak inter-particle dispersive pressures (Rahimipour and Wilkinson, 1992).

1.3 Objectives

The goal of this research is to improve our understanding of the factors influencing the convective descent phase of particle clouds. The specific objectives of this work are to answer the following questions:

- Under the expected range of sediment disposal scenarios, do real sediments organize into self-similar clouds that behave as dense "thermals" during convective descent?

- What roles do the initial conditions, namely particle size, water content, and initial momentum, play in determining cloud behavior within the initial acceleration and self-preserving phases?

- What mechanisms are responsible for the loss of cloud particles and fluid to the environment during initial formation and convective descent?

- How accurately can the behavior of particle clouds be predicted using an integral-type model with constant entrainment, drag, and added mass coefficients?

- How do the entrainment, drag, and added mass coefficients vary in time and space during convective descent, and how are they affected by the initial conditions?

Chapter 2

Background

As noted in Chapter 1, during convective descent, particle clouds behave similarly to classical thermals and buoyant vortex rings, both of which have been the subject of several key studies, some dating back to the late 1950's and early 1960's. Thus, an understanding of the characteristics of these convective elements provides a basis on which to investigate the dynamics of particle clouds. To this end, the results of early studies of thermals and vortex rings are discussed in the first two sections, followed by a synopsis of more recent particle cloud investigations.

2.1 Thermals

In this section, the theoretical analysis of thermals will be discussed first followed by a review of some key laboratory studies. In this section, the terms "thermal" and "cloud" are used interchangeably.

2.1.1 Theoretical Analysis of Thermal

In the analysis of thermals, it is convenient to use an integral approach in which the thermal is treated as a moving, expanding control volume (e.g., sphere or hemisphere) for which the following conservation equations apply in a uniform density environment (Koh and Chang, 1973):

Conservation of Mass:

$$\frac{d}{dt}\left(\rho r^3\right) = 3\alpha\rho_a r^2 w \tag{2.1}$$

Conservation of Momentum:

$$\frac{d}{dt}\left(V(\rho + k\rho_a)w\right) = B - 0.5\rho_a C_D \pi r^2 w^2 \tag{2.2}$$

Conservation of Buoyancy:

$$\frac{d}{dt}B = \frac{d}{dt}\left(V(\rho - \rho_a)g\right) = 0 \tag{2.3}$$

where: r is the thermal radius; V is the cloud volume; ρ and ρ_a are the densities of the cloud and ambient fluid, respectively; k and C_D are the added mass and drag coefficients, respectively; and g is the gravitational constant. Equation 2.3 is based on the assumption that no buoyancy is lost to the wake of the thermal. Equation 2.1 is based on the classic entrainment assumption that the mean entrainment velocity is proportional to the mean center of mass velocity (w) through the entrainment coefficient (α). Hence, the mean flow rate of ambient fluid into the cloud is equal to the entrainment velocity multiplied by the surface area of the cloud. By assuming $\rho \approx \rho_a$, setting $w = \frac{dz}{dt}$, and using the chain rule of differentiation, it can be shown that:

$$r = \alpha z \tag{2.4}$$

where z is the center of mass position.

Thus, use of the continuity equation and entrainment assumption results in a linear relationship between r and z, in which case α can be regarded as both a spreading angle (i.e., $\frac{r}{z} = tan\alpha$) and an entrainment coefficient. The assumption that $\rho \approx \rho_a$ represents a type of Boussinesq approximation, where it is assumed that density changes are so small that they may be neglected in the inertia terms and are

retained only in the buoyancy term.

Baines and Hopfinger (1984) used dimensional arguments to show that when the Boussinesq approximation is not made, Equation 2.4 should be modified as follows:

$$r = \alpha \left(\frac{\rho_a}{\rho} \right)^{\frac{1}{3}} z \tag{2.5}$$

The authors noted that the functional dependency of r on the ratio $\frac{\rho_a}{\rho}$ made physical sense since the static instability at the cloud surface producing the entraining eddies is known to depend on the density difference between the thermal and the ambient fluid. Baines and Hopfinger also demonstrated both theoretically and experimentally that the entrainment rate for thermals is so large that the Boussinesq approximation is reached after the thermal descends about two initial diameters.

The three conservation equations contain three unknown variables (r, w, and ρ) and three unknown coefficients (α, k, and C_D), which are largely empirical in nature and need to be determined by experiment. The equations do not permit an analytical solution without the use of simplifying assumptions, since elimination of two of the variables results in a second-order nonlinear differential equation in terms of the remaining variable.

If constant pressure and inviscid conditions are assumed (i.e., rate of work done by pressure and viscous shear forces is negligible), dimensional analysis can be used to derive the following similarity solutions for the motion of an axisymmetric thermal in a uniform density environment originating from a point source (Turner, 1973):

$$\begin{aligned} r &= \alpha z \\ w &= \left(\frac{B}{\rho_a} \right)^{\frac{1}{2}} z^{-1} f_1 \left(\frac{\mathbf{r}}{r} \right) \\ g' &= \left(\frac{B}{\rho_a} \right) z^{-3} f_2 \left(\frac{\mathbf{r}}{r} \right) \end{aligned} \tag{2.6}$$

where: $\mathbf{r}$ is a position vector relative to the axis of symmetry; g' is the modified gravitational acceleration, $(\frac{\rho - \rho_a}{\rho_a})$g; and f_1 and f_2 are profile functions for w and g',

respectively. Using an integral approach and neglecting the velocity and buoyancy distributions within the interior of the cloud, the following time dependencies for r and w can be deduced using $w = \frac{dz}{dt}$ (Turner, 1973):

$$\begin{aligned} r &\sim \alpha \left(\frac{B}{\rho_a}\right)^{\frac{1}{4}} t^{\frac{1}{2}} \\ w &\sim \left(\frac{B}{\rho_a}\right)^{\frac{1}{4}} t^{-\frac{1}{2}} \end{aligned} \tag{2.7}$$

Using some simplifying assumptions, Wang (1971) and Escudier and Maxworthy (1973) derived asymptotic solutions to the three conservation equations that are applicable to very short (i.e., early in the initial acceleration phase) and long times (i.e., well into deceleration phase). The authors nondimensionalized the equations by introducing the characteristic (i.e., initial) length scale, r_o, and buoyancy, $F_o = \frac{(\rho_o - \rho_a)}{\rho_a}$, and defining the following dimensionless variables:

$$\tilde{r} = \frac{r}{r_o}\,; \qquad \tilde{t} = \left(\frac{\alpha g F_o}{r_o}\right)^{\frac{1}{2}} t\,; \qquad \tilde{w} = \left(\frac{\alpha}{r_o F_o g}\right)^{\frac{1}{2}} w \tag{2.8}$$

Assuming that the drag forces are small and can be neglected, and that there is no loss of fluid (buoyancy) to the thermal's wake, Escudier and Maxworthy (1973) derived the following asymptotic solutions for a spherical thermal:

Short times, $(\tilde{r} - 1) \ll 1$:

$$\tilde{r} - 1 \approx \frac{\tilde{t}^2}{2(1+k) - F_o}\,; \quad \tilde{w} \approx \frac{\tilde{t}}{1 + k - F_o} \tag{2.9}$$

Long times, $\tilde{r} \gg 1$:

$$\tilde{r} \approx \frac{\tilde{t}^{\frac{1}{2}}}{2(1+k)^{\frac{1}{4}}}\,; \quad \tilde{w} \approx \frac{\tilde{t}^{-\frac{1}{2}}}{2^{\frac{3}{4}}(1+k)^{\frac{1}{4}}} \tag{2.10}$$

In dimensional form, Equation 2.10 yields the following:

$$r = \left(\frac{3\alpha B}{4\pi\rho_a}\right)^{\frac{1}{4}} \frac{t^{\frac{1}{2}}}{(2(1+k))^{\frac{1}{4}}}; \quad w = \left(\frac{3B}{4\pi\rho_a}\right)^{\frac{1}{4}} \frac{t^{-\frac{1}{2}}}{(2\alpha)^{\frac{3}{4}}(1+k)^{\frac{1}{4}}} \tag{2.11}$$

Equation 2.11 is similar in form to Equation 2.7 except for the constant coefficients, functionality in α, and inclusion of the added mass coefficient (k). These differences are the result of the inclusion of k in the momentum equation by Escudier and Maxworthy (1973) as well as their choice of nondimensional parameters and their inclusion of α.

Morton et al. (1956) provided the first theoretical development of the behavior of thermals in a stably stratified environment in which they used, in addition to the mass and momentum conservation equations, the following conservation of buoyancy principle:

$$\frac{d}{dt}\int(\rho - \rho_a(0))dV = 4\pi r^2 \alpha w(\rho_a - \rho_a(0)) \tag{2.12}$$

where $\rho_a(0)$ is the reference density of the ambient fluid taken at $z = 0$. In words, Equation 2.12 states that the time rate of change in buoyancy, integrated over the entire volume of the thermal, is equal to the inflow of buoyancy integrated over the surface area of the cloud. By substituting the mass and momentum conservation equations into Equation 2.12, neglecting the added mass and drag force, and using the Boussinesq approximation, Morton et al. (1956) expressed the conservation of buoyancy in terms of the Brunt-Väisälä frequency (N) as follows:

$$\frac{d}{dt}\left(r^3 g\frac{(\rho - \rho_a)}{\rho_a(0)}\right) = -r^3 N^2 w \tag{2.13}$$

where $N^2 = \frac{g}{\rho_a(o)}\frac{d\rho_a}{dz}$. Morton et al. (1956) nondimensionalized the conservation equations and normalized the time scale by N (i.e., $t_1 = Nt$; $0 \leq t_1 \leq 2\pi$), which resulted in the following solutions for w and maximum, or "trap," depth (z_{max}):

$$
\begin{aligned}
w &\simeq \alpha^{-\frac{3}{4}} \left(\frac{B_o}{\rho_a}\right)^{\frac{1}{4}} N^{\frac{1}{2}} W \\
z_{max} &\simeq \alpha^{-\frac{3}{4}} \left(\frac{B_o}{\rho_a}\right)^{\frac{1}{4}} N^{-\frac{1}{2}} Z
\end{aligned} \tag{2.14}
$$

where

$$
W = \frac{sint_1}{(1 - cost_1)^{\frac{3}{4}}} \; ; \quad Z = 4(1 - \cos t_1)^{\frac{1}{4}} \; , \quad for \quad t_1 \leq \pi
$$

$$
W = \frac{sint_1}{(3 + cost_1)^{\frac{3}{4}}} \; ; \quad Z = 8 \cdot 2^{\frac{1}{4}} - 4(3 + \cos t_1)^{\frac{1}{4}} \; , \quad for \quad t_1 \geq \pi
$$

Thus, for a negatively buoyant thermal, z_{max} is proportional to ${B_o}^{\frac{1}{4}}$ and inversely proportional to $N^{\frac{1}{2}}$, since the falling cloud entrains positively buoyant fluid from the upper layers thereby increasing its buoyancy. The cloud eventually reaches a point where its velocity reverses sign and begins to oscillate around the level of neutral buoyancy at the frequency, N. The oscillation results from the fact that the cloud still possesses some momentum when it first reaches the point of neutral buoyancy, causing it to overshoot this level. At this point, its buoyancy becomes positive with respect to its surroundings causing it to rise and the oscillations to begin. Although not included in Equation 2.14, drag forces eventually dampen the oscillations, and the density stratification causes the cloud to collapse (i.e., enter dynamic collapse phase) and spread horizontally as the interior fluid seeks a hydrostatic equilibrium with the ambient fluid. By replacing the sine and cosine functions in W by their Taylor series expansions and neglecting higher order terms (i.e., $\sin t_1 \simeq t_1; \cos t_1 \simeq 1 - \frac{1}{2}{t_1}^2$), w in Equation 2.14 reduces to a form similar to that of Equation 2.11 when t_1 approaches zero.

2.1.2 Laboratory Studies of Thermals

Early experiments with thermals in the 1950's and 1960's were motivated by meteorological phenomena (e.g.. cumulus clouds), whereas dredged material disposal concerns

provided the impetus for later experiments conducted during the past decade. Laboratory procedures in the early experiments involved releasing a dense fluid, usually a salt solution, into an illuminated, quiescent tank by manually inverting a hemispherical cup at the water surface. The descent of the thermal was then recorded on video tape from which velocity and entrainment estimates were made. In conjunction with these experiments, Equation 2.4 was used to determine α, and dimensional analysis was used to derive the following similarity solutions:

$$w = C(gF_o r)^{\frac{1}{2}} \quad (Scorer, 1957) \tag{2.15}$$

$$z^2 = c_1 \alpha^{-\frac{3}{2}} \left(\frac{B}{\rho_a}\right) t \quad (Richards, 1961) \tag{2.16}$$

where C and c_1 are constants.

Scorer (1957) reported values of α ranging from 0.20 to 0.34 with a mean of 0.25. Woodward reported an average value of 0.27 for α, whereas Richards (1961) reported α values between 0.13 and 0.53. These authors noted that the entrainment rate was quite sensitive to the initial release condition (i.e., the manner in which the cup was inverted), which was difficult to reproduce consistently, but that α remained roughly constant in a given experiment. Scorer (1957) calculated a mean value of 1.2 for C, which, not surprisingly, exhibited variability similar to that of α, since Turner (1964) showed that the two coefficients are related as follows: $C^2\alpha(1-\alpha) = \frac{1}{3}$. In contrast, Richards found that $c_1 = 0.73$ for nearly all of the thermals in his experiments. Turner (1964) showed that c_1 is mainly a function of the shape of the thermal and the associated added mass coefficient, with only a small dependence on α.

2.2 Buoyant Vortex Rings

2.2.1 Theoretical Analysis of Buoyant Vortex Rings

It is instructive to compare the motion of a thermal, which moves from rest under its own buoyancy, to that of a buoyant vortex ring, which, in addition to buoyancy,

is generated with initial momentum, or impulse (I), as well as circulation (K). The hydrodynamic impulse, defined as the total mechanical impulse of body forces required to instantaneously generate a circulating volume (V) of fluid from rest, can be expressed as follows (Lamb, 1932):

$$I = \frac{1}{2}\rho \int_V \mathbf{x} \times \omega dV \tag{2.17}$$

where $\mathbf{x}$ is a position vector, and ω is the vorticity vector. For an axisymmetric vortex ring, which is a toroidal-shaped element with mean radius (r), and cross-sectional radius (a), Equation 2.17 becomes (in cylindrical coordinates):

$$I = \rho\pi \int_A r^2 \omega_\phi dz dr \tag{2.18}$$

where I is in the direction of motion (i.e., along z axis); A is the cross-sectional area of the ring (πa^2); and ω_ϕ is the azimuthal vorticity component. The circulation is related to ω_ϕ through the surface integral:

$$K = \int_A \omega_\phi dz dr \tag{2.19}$$

Using Equations 2.18 and 2.19, Lamb (1932) defined the characteristic length scale, $r_o^2 = \frac{I}{\pi\rho_a K}$, resulting in $I \simeq \pi\rho_a K r^2$. The conservation of momentum (impulse) equation can now be expressed as follows:

$$\frac{dI}{dt} \simeq \pi\rho_a K \frac{dr^2}{dt} = B_o \tag{2.20}$$

Recognizing that $K = \oint \mathbf{u} \cdot \mathbf{ds}$, where $\mathbf{u}$ is the tangential velocity vector and $\mathbf{ds}$ is an element of a contour enclosing A, leads to the following expression for the vertical velocity of the ring (w):

$$w = c\frac{K}{r} \tag{2.21}$$

where c is a constant which is dependent on the shape of the vortex ring.

Turner (1957) integrated Equation 2.20 and used Equation 2.21 along with $w = \frac{dz}{dt}$ to obtain:

$$r = \frac{B_o}{c2\pi\rho_a K^2} z \tag{2.22}$$

The author related this equation to Equation 2.4 for a thermal by defining a new entrainment coefficient as follows:

$$\alpha_o = \frac{B_o}{c2\pi\rho_a K^2} \tag{2.23}$$

In deriving Equation 2.23, Turner assumed that the vorticity does not extend to the axis of the ring. This assumption allowed him to invoke Kelvin's circulation theorem along a circuit passing through the center of the ring and around the outside so that $\frac{dK}{dt} = 0$, and thus K is constant. The assumption of constant circulation was based on the heuristic argument that as the ring progresses, its diameter increases faster than the rate at which entrained fluid can spread from turbulent diffusion (Turner, 1957). Through Equation 2.23, Turner argued that the buoyant vortex ring represents a broader category of convective elements in which the buoyant thermal is a special case.

The following expression for w can be obtained by integrating Equation 2.20 and using Equation 2.21:

$$w \sim \left(\frac{B_o}{\rho_a}\right)^{-\frac{1}{2}} K_o{}^{\frac{3}{2}} t^{-\frac{1}{2}} \tag{2.24}$$

Thus, for a given initial K_o, an increase in buoyancy produces a decrease in velocity, which, at first, seems counter-intuitive since this conflicts with Equation 2.7. The physics can be explained by the fact that buoyancy serves to increase the expansion of the ring, which decreases the velocity since $w \sim \frac{K}{R}$. However, as Turner pointed out, B_o and K are not independent in a thermal since circulation is produced by the buoyancy force. Hence, if B_o is increased, the circulation should also increase. Since

$K \sim \sqrt{B_o}$ and B_o is constant in a uniform environment, the circulation in a thermal must be constant in a uniform environment. Obviously, this condition does not hold for a thermal during the initial acceleration phase but only after it has reached the self-preserving phase. As Scorer (1957) noted, at this stage, the buoyancy profile within the thermal must change to a distribution that does not continue to produce circulation, at which point an equilibrium is reached in which the drag forces balance the portion of the buoyancy force producing the circulation.

The similarity solutions for the motion of a buoyant vortex ring in a stably stratified environment are very similar to the preceding analysis of buoyant vortex rings under isothermal conditions with the exception that the buoyancy is no longer constant but varies with the ambient density profile as follows:

$$\frac{dB}{dt} = -cN^2 r^3 w \tag{2.25}$$

Not surprisingly, the above equation is identical in form to Equation 2.13 for a thermal. Hence, in addition to B_o and K_o, N must now be introduced into the similarity solution. Dimensional analysis based on these variables gives the following relation for the maximum height (z_{max}):

$$z_{max} = c_1 \left(\frac{B_o}{\rho_a}\right)^{-\frac{1}{2}} K_o{}^{\frac{3}{2}} N^{-\frac{1}{2}} \tag{2.26}$$

where c_1 is a constant. Expressions for w, r, and B may be obtained through normalization and substitution into the governing equations in a manner similar to the approach used by Morton et al. (1956) in their analysis of thermals. Based on his analysis of I and K for a vortex ring, Turner (1960) showed that density stratification serves to decrease the circulation as follows:

$$\frac{dK}{dt} = -\frac{1}{2} s N^2 r^2 \tag{2.27}$$

where s is an empirical constant.

2.2.2 Laboratory Studies of Buoyant Vortex Rings

Though a wealth of literature exists concerning research of vortex rings, few experimental studies have been performed on buoyant vortex rings. Turner (1957, 1960) conducted experiments in uniform density and stratified environments using light buoyant vortex rings with density differences ranging from 4 % to 18 %. Results from these experiments yielded values for c in Equation 2.21 ranging from 0.13 to 0.27, a mean value of 0.18 for α, and a value of 3 for s in Equation 2.27.

Maxworthy (1974) conducted flow visualization experiments with vortex rings (i.e., neutral buoyancy) produced by forcing a mass of fluid through a sharp-edged orifice by the motion of a piston. This apparatus produced turbulent vortex rings with a mean α value of 0.011. By taking the slope of nondimensionalized velocity versus depth data, Maxworthy (1974) also estimated the value of the drag coefficient (C_D) to be in the range of 0.084 - 0.108 for an equivalent spherical volume.

In later experiments using more sophisticated flow visualization and laser-Doppler techniques, Maxworthy (1977) observed that compact, "well-organized" vortex rings grew at a much slower rate (mean $\alpha = 0.001$) than those with "disorganized" cores with much larger entrainment coefficients (mean $\alpha = 0.015$). The author hypothesized that the differences in entrainment rates were associated with the amount of turbulence within the ring and surrounding fluid.

2.3 Particle Clouds

In this section, a theoretical analysis of particle clouds is presented first, followed by a summary of laboratory and field studies conducted to date. The theoretical analysis includes a discussion of scaling arguments using the cloud number (N_c) and a brief summary of some theoretical and empirical relationships for particle cloud behavior in the dispersive (particle settling) phase.

2.3.1 Scaling Analysis of Particle Clouds

For a particle cloud, the initial buoyancy (B_o) can be computed simply from the submerged weight of the particles as follows:

$$B_o = m(1 - \frac{\rho_a}{\rho_s})g \tag{2.28}$$

where m is the total mass of particles in the cloud, and ρ_s is the density of an individual particle.

For fully turbulent particle clouds for which viscous effects can be ignored, dimensional analysis can be used to derive the following characteristic cloud velocity scale:

$$w_o = \left(\frac{B_o}{\rho_a r_o^2}\right)^{\frac{1}{2}} \tag{2.29}$$

Equation 2.29 can also be derived by equating the drag and buoyancy forces.

Rahimipour and Wilkinson (1992) defined the cloud number (N_c) as the ratio of particle settling velocity (w_s) to the characteristic cloud velocity (w_o), which, using Equation 2.29, simplifies to the following expression for non-cohesive particles:

$$N_c = w_s r\left(\frac{\rho_a}{B}\right)^{\frac{1}{2}} \tag{2.30}$$

Since N_c is proportional to the cloud radius, its magnitude continually increases as the cloud descends and grows. Since w_s is related to particle diameter (d_s) and w_o is related to the total mass or volume of particles, the cloud number can be viewed as a type of size ratio, relating the mean grain size of the individual particles to the overall size of the cloud. Thus, N_c can be used to scale a small volume of small-diameter particles in the laboratory to a larger volume of large-diameter particles released from a full-scale barge. This type of scaling analysis was performed to determine how a 40 g sample of particles ($B_o = 23,520\ g\ cm\ s^{-2}, V_o = 27\ cm^3$), used for most of the experiments in this study, scales to much larger volumes in the real world. The analysis was performed by calculating the fall velocity of particles contained in

Laboratory Diameter (mm)	Real-World Diameter (mm)			
	10 m^3	*100 m^3*	*1,000 m^3*	*5,000 m^3*
0.01	0.027	0.033	0.040	0.045
0.05	0.172	0.221	0.290	0.353
0.10	0.418	0.572	0.807	1.05
0.50	5.97	13.0	33.3	64.8
1.00	33.0	83.3	165	258

Table 2.1: N_c scaling of particle cloud grain sizes between 27 cm^3 laboratory volume and barge volumes of 10, 100, 1,000, and 5,000 m^3.

different full-scale volumes (i.e., 10 m^3, 100 m^3, 1,000 m^3, and 5,000 m^3) by matching the cloud numbers corresponding to the 40 g laboratory sample containing particles ranging from 0.01 - 1.0 mm in diameter. Settling velocities were calculated from particle diameters and vice versa using the following empirical relationship developed by Dietrich (1982) for spherical particles:

$$w^* = -3.76715 + 1.92944\, log(D^*) - 0.09815\, log(D^*)^2 - 0.00557\, log(D^*)^3 + 0.00056\, log(D^*)^4 \tag{2.31}$$

where

$$w^* = \frac{{w_s}^3}{(s-1)g\nu} \quad ; \quad D^* = \frac{(s-1)g{d_s}^3}{\nu^2}$$

and s is the specific gravity of a sediment grain (e.g., $s = \frac{\rho_s}{\rho_a} = 2.5$ for glass beads).

The results of the cloud number scaling analysis are plotted in Figure 2.1 and tabulated in Table 2.1. Since Dietrich developed Equation 2.31 using velocity data for particles sizes ranging from 0.01 mm to about 100 mm in diameter, the accuracy of the scaling analysis for particles above this size is uncertain.

As shown in Table 2.1, results of the N_c scaling analysis show that laboratory-sized sand and silt particles scale to real-world dimensions by factors of $\frac{1}{10}$ and $\frac{1}{5}$, respectively. Thus, use of large particle sizes in the lab (i.e., 0.5 - 1.0 mm) scales

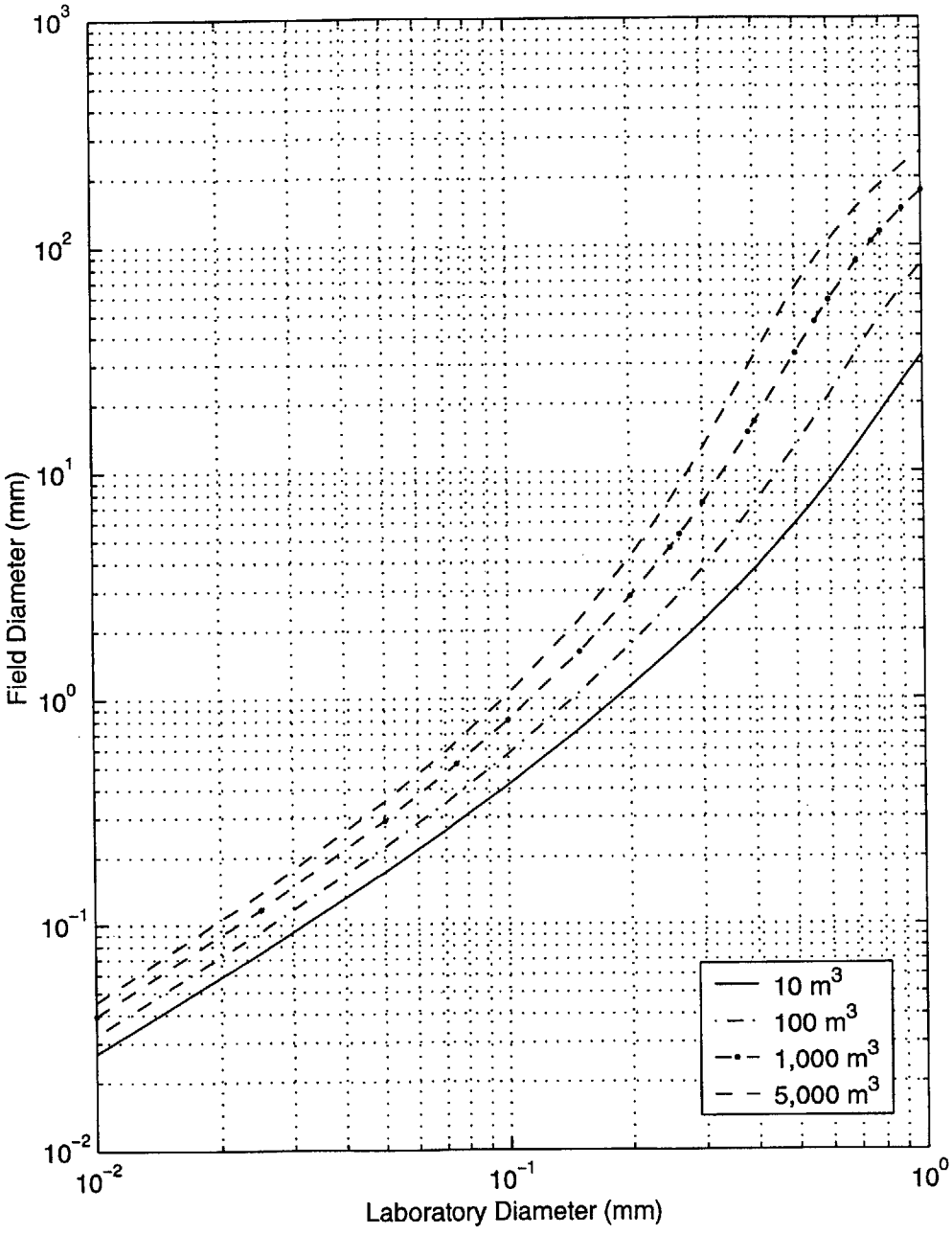

Figure 2-1: Particle size correlation between 40 g laboratory sample and real-world barge sizes based on cloud number scaling.

to extremely large particles in the field (i.e., gravels and cobbles). Particles of this size must therefore be used with caution in the laboratory when attempting to reproduce the real-world dynamics of particles of similar size using N_c scaling. Strict N_c compliance, however, may not be required to reproduce the dynamics of clouds with very small N_c (i.e., cloud dynamics may be insensitive to N_c). The influence of N_c on cloud behavior is discussed in Chapter 4.

As one might expect, flow visualization studies using different sizes of sand and glass beads show that three-dimensional, axisymmetric clouds enter the dispersive (particle settling) phase when the cloud velocity approaches the settling velocity of the particles (i.e., $N_c \rightarrow 1$) (Rahimipour and Wilkinson, 1998; Bühler and Papantoniou, 1991; Boothroyd, 1971).

Based on experiments with two-dimensional particle clouds (i.e., originating from a line source), Noh and Fernando (1993) observed that the depth (z_d) associated with the cloud's transition to the dispersive phase obeyed the following relationship:

$$\frac{z_d w_s}{\nu} \sim \left(\frac{Q}{\rho_a \nu w_s} \right)^{\alpha} \tag{2.32}$$

where Q is the buoyancy of the released particles per unit length.

The authors hypothesized that, in addition to N_c, the transition depth depended on particle inertia, turbulent intensity, and inter-particle spacing. They noted that the transition occurred when N_c was less than 1, possibly due to the increase in particle settling velocity resulting from particle interactions and the downward background fluid velocity of the cloud.

Bühler and Papantoniou (1991) studied the growth rate of the particle "swarm" that emerges when the cloud transitions from the "thermal" to dispersive phase. Upon integrating the momentum equation and solving for the velocity by invoking the similarity assumption (i.e., $\frac{dr}{dt} \sim w$), the authors derived the following expression for radial growth of the particle "swarm:"

$$r \sim \left(\frac{Bz}{\rho_a {w_s}^2} \right)^{\frac{1}{3}} \tag{2.33}$$

Bühler and Papantoniou (1999) explained that the growth of the particle swarm is caused by shear induced entrainment and lateral displacement flow resulting from the wake behind each particle.

2.3.2 Laboratory and Numerical Modeling Studies of Particle Clouds

Bowers and Goldenblatt (1978) released samples of silty clay sediments containing various amounts of water to determine the effect of moisture content on entrainment. As will be discussed in Chapter 7, their results indicate that for cohesive materials, the entrainment coefficient is quite sensitive to water concentration. The authors note that samples with low water content tended to drop as clumps with virtually no entrainment, whereas more dilute slurries behaved very much like negatively buoyant thermals.

Nakatsuji et al. (1990) performed flow visualization experiments using 75-300 cm^3 volumes of 0.8 mm, 1.3 mm, and 5.0 mm diameter glass beads. The authors derived a nondimensional expression for cloud velocity using conservation of mass and momentum equations similar in form to Equations 2.1 and 2.2. Using α and k values selected by the authors, their theoretical thermal velocity failed to accurately match measured velocities in the acceleration phase, as well as the cloud's peak velocity, which exceeds the predicted value by 20 %. The distance traveled during the initial acceleration period was equal to approximately 2.5 initial cloud diameters. Under the assumptions of constant α (0.4), constant k (1.0), no drag, and Boussinesq conditions, the authors showed that the smaller beads ($\leq$ 1.3 mm) behaved according to thermal theory in the deceleration phase, whereas clouds formed from the larger 5 mm beads descended at a relatively constant speed, close to the settling velocity of the beads ($N_c \approx 0.5$). Cloud growth data and associated entrainment coefficients were not provided by the authors.

Tamai and Muraoka (1991) analyzed two-dimensional (i.e., line) particle clouds in the laboratory using fine (0.15 mm) and coarse (3.4 mm) sand. Their results showed linear growth rates (no α values given) and a velocity versus time profile that loosely follows thermal theory (i.e., $w \sim t^{-\frac{1}{3}}$) for a line thermal. No information was provided by the authors as to how the theoretical curve was fit to the experimental data.

Rahimipour and Wilkinson (1992) conducted flow visualization experiments on particle clouds using graded sand ($d_s = 0.15 - 0.35mm$). They compared velocity and growth rate data to analytical curves generated for a miscible thermal with the same buoyancy. Similar to the study by Nakatsuji et al. (1990), the authors show that thermal theory somewhat captures the decaying trend of cloud velocity in the asymptotic (deceleration) region, after the cloud has traveled about two diameters, but does not predict velocities very accurately in the initial acceleration phase. By varying initial volumes and particle sizes, Rahimipour and Wilkinson (1992), developed the following relationship between the entrainment coefficient and cloud number:

$$\alpha = 0.31(1 - 0.44{N_c}^{1.25}) \quad for \ N_c < 1.5 \tag{2.34}$$

The above equation shows that, for small cloud numbers (i.e., $N_c < 0.3$), the entrainment rate remains approximately constant ($\alpha = 0.31$), but decreases rapidly once N_c exceeds unity. The authors did not explicitly comment on when they consider the clouds to be in the dispersive phase (based on N_c) but note that the clouds are in the dispersive phase when $N_c = 1.5$. Rahimipour and Wilkinson (1992) derived the following empirical expression for the radial growth rate in the dispersive phase:

$$r = 1.5\left(\frac{B}{\rho_a}\right)^{\frac{1}{2}} \frac{1}{w_s} \quad for \ N_c > 1.5 \tag{2.35}$$

Luketina and Wilkinson (1994) released particle clouds with various initial N_c values into a linearly stratified environment and compared maximum and final penetration depths to those predicted by an integral model based on the three conservation equations. Their model predicted maximum and final penetration depths that were consistently lower than measured experimentally. Their results confirmed the propor-

tionality given by Equation 2.13 and also showed that the oscillations were damped more rapidly than simulated by the model. The authors hypothesized that increased drag on the particle cloud resulting from internal wave production was responsible for these discrepancies. They also noted that the model's performance was relatively insensitive to the drag coefficient.

Johnson and Fong (1995) conducted disposal tests at the USACE Waterways Experiment Station using 1:50 scale replicas of a split-hull barge and multiple bin disposal vessel. A series of tests was performed in water depths of 0.61 - 1.83 m using crushed coal, clay, silt and sand. The study focused mainly on the mechanics of the dynamic collapse and the associated the bottom surge rather than the initial acceleration and deceleration convective descent phases. Cloud growth and velocity data during convective descent were not provided. The authors compared depth-averaged and bottom surge velocities from test measurements to predictions generated by the Short-Term Fate (i.e, STFATE) model, originally developed by Koh and Chang (1973) and currently used by the U.S. Army Corps of Engineers (USACE) to predict the fate of dredged materials released from barges or scows. Little information was provided by the authors concerning the details of the model calibration and verification effort. Johnson and Fong (1995) noted that large values of α produced the best results, and that they used a value of 0.6 for α, which was estimated from on Mobile, Alabama field data (Kraus, 1991) and held C_D at 1.0, which was used in earlier USACE modeling studies. Modeling results show differences between measured and simulated depth-averaged velocities ranging from 9 - 47 %.

Wen and Nacamuli (1996) conducted flow visualization experiments by releasing 3 - 500 g quantities of different sand grain sizes (0.11 - 1.25 mm) and natural San Francisco Bay mud (d = 0.005 mm) into a 1.2 m deep glass tank. The authors observed that grain sizes larger than 0.11 mm produce "thermal-like" clouds with a $t^{-\frac{1}{2}}$ velocity deceleration and α values ranging from 0.25 - 0.30. They referred to these clouds as "vortex rings" because of their toroidal structure and associated circulation. Wen and Nacamuli (1996) found that the smaller particles formed a fast-moving "comet-shaped" element with a dense core and large wake of particles trailing

behind it. They refer to these clouds as "wakes." They also observed a $t^{-\frac{1}{2}}$ velocity dependency for these elements but lower entrainment rates ($\alpha = 0.1$). The authors defined a Raleigh number for the cloud as $Ra = \frac{B}{(\rho_a {w_s}^2 {r_o}^2)}$, which is essentially the inverse of the square of the initial N_c, and proposed that the clouds changed from a "vortex ring" to a "wake" when Ra exceeded a critical value of 1000.

Li (1997) used a three-dimensional finite-difference model, based on the conservation of mass, buoyancy, and momentum (i.e., Navier-Stokes) equations, to simulate the motion of particle clouds. He invoked the Boussinesq approximation and used the Prandtl mixing length model to specify the spatial and temporal distribution of eddy viscosity. In this model, the mixing length was scaled according to cloud width through a proportionality, or mixing length, coefficient. Turbulent mass flux was assumed to be related to the gradient of the time average density excess through the turbulent Schmidt number. Li (1997) calibrated the model using Scorer's (1957) experimental results for dense thermals and verified it using the particle cloud results from Nakatsuki et al. (1990) and Bühler and Papantoniou (1991). For smaller particle sizes (0.15 - 0.30 mm), the numerical model reproduced the bimodal transverse velocity and buoyancy distributions associated with the vortex ring structure. The model did not simulate the double-peak distributions for the larger particles (0.6 - 1.18 mm), which the author claimed did not form well-organized vortex rings because of their high settling velocities. A plausible explanation for this result is the rather small initial volume used in the simulations (i.e., 1.52 cm^3).

While finite-difference models provide insight into the cloud's interior characteristics, they often suffer problems associated with mass and momentum conservation, boundary condition specification, turbulence closure, and definition of a coordinate system appropriate for a rapidly expanding volume. Integral models avoid these problems by characterizing the gross motion of the cloud through the three conservation equations and associated initial conditions. For particle clouds, integral models also provide a convenient framework for simulating the settling of particles from the cloud when the cloud's velocity approaches the particle fall velocity (i.e., transition from "thermal" to dispersive phase). Several researchers (Koh and Chang, 1973; Abdel-

rhman and Dettmann, 1993; Luketina and Wilkinson, 1994; and Swanson et al., 1994) have used numerical integral models to evaluate the fate of particle clouds.

To date, few researchers have attempted to incorporate mechanisms into a model for simulating the loss of particles to the environment (i.e., stripping) during convective descent. The loss of particles from the cloud is handled by the current STFATE model (Johnson and Fong, 1995) in a generic manner by means of a user-specified stripping coefficient, which gives the percentage of parent material that is "stripped" away from the cloud as it descends. The flux of material leaving the cloud is calculated by simply multiplying this coefficient by the cloud's velocity and surface area. In STFATE, the material that is periodically stripped from the cloud is formed into separate smaller Gaussian clouds composed of the same particle size distribution as the parent cloud. These separate clouds are transported by passive diffusion with a vertical velocity equal to the mean settling velocity of the particles. The time increment associated with the frequency of stripping is completely arbitrary. Hence, at this time, the stripping process in STFATE has no physical basis and is simply an empirical means of allowing a pre-determined fraction of particles (e.g., based on field observations) to strip away from the cloud as it descends.

Abdelrhman and Dettmann (1993) incorporated a mechanistic stripping process into the STFATE model by simulating detachment of outer layers of the cloud (i.e., Δr) associated with the entrained volume for each time step. For each particle size category, the authors assumed a different three-dimensional Gaussian distribution for particle concentration. For each time step, the model compares the concentration of particles in the outermost "Δr" layer to the value 0.01 $\frac{g}{cm^3}$, a commonly cited concentration associated with hindered settling (Teeter, 1984), and allows the outer layer to detrain from the cloud when the concentration falls below this value. The authors justified the hindered settling criterion because it characterizes the limit for particle interaction in sediment suspensions. Thus, their major assumption was that the entrainment and detrainment mechanisms are related to particle concentration, which has not been supported by theoretical arguments or from experimental studies. The authors applied the revised STFATE model to a hypothetical sediment material

containing particle sizes ranging from silt to large clay clumps. The simulations showed the finer fractions leaving the cloud first with only the coarse sand and clay clumps remaining at deeper depths.

2.3.3 Field Studies of Particle Clouds

Over the past few decades, a limited number of field studies have been performed in the U.S. to investigate the short-term fate of dredged material discharged into open waters. The results of these studies are summarized below.

- Long Island Sound

Gordon (1974) was among the first researchers to quantify residual turbidity generated from open-water disposal of dredged material. The dredged material was disposed in 20 m of water at the New Haven disposal site in Long Island Sound. The material, consisting primarily of marine silt (silt - clay concentrations up to 90 %) with high water content (70 to 75 %), was instantaneously released from scows of 1,200 and 2,000 m^3 capacities. Based on a series of turbidity measurements, Gordon estimated the amount of fines (i.e., silt and clay particles) lost to the water column to be approximately 1 % of the material discharged.

- San Francisco Bay

In a dredged material disposal study at the Carquinez Site in San Francisco Bay (Sustar and Wakeman, 1977), the U.S. Army Engineer District, San Francisco used transmissometer and gravimetric analysis to measure water column suspended solids concentrations resulting from disposal of silty clay material from twin 994 m^3 hopper dredges in 13.7 m of water. Mass balance calculations suggest the amount of sediments lost to the upper water column to be in the range of 1 to 5 % of the material released.

- Dredged Material Research Program Sites

As part of the U.S. Army Corps of Engineers' (USACE) Dredged Material Research Program (DMRP), Bokuniewicz et al. (1978) investigated the mechanics of

the placement of dredged material at six open-water disposal sites in which disposal operations were performed from stationary barges. With release times ranging from 10 to 100 s, water depths from 15 to 67 m, and fall velocities on the order of 1 m/s, the majority of discharges at these sites are described as semi-continuous jets of dense fluid which entrain large volumes of ambient water as they descend to the bottom. The authors hypothesize that under these shallow-water disposal scenarios, the inward circulation caused by the descending jet serves to confine the released material to a narrow zone and to inhibit the stripping of fine materials into the surrounding water column. They estimated the material lost to the ambient water to be less than 5 % of the original material and surmised that this material represented additional sediment released from the dredge after the jet phase is completed (i.e., material that never makes it into the initial "jet").

- Mud Dump Site, New York Bight

Tavolaro (1984) performed a sediment dry mass study of 1980 clamshell dredging and sediment disposal activities at the Mud Dump Site, located in 15 - 24 m of water. The operations involved disposal of 658,500 m^3 of New York Harbor sediment, consisting predominantly of silt and clay. Using pre- and post-disposal bathymetric data, Tavolaro compared the estimated total dry mass of sediment deposited at the site to the dry mass of sediment in the barges and estimated the loss of fines to be 3.7 %.

- Foul Area Disposal Site, Massachusetts Bay

During 1982 - 1983 disposal activities at the Foul Area Disposal Site, currently known as the Massachusetts Bay Deep Water Disposal Site, the USACE New England Division undertook a study to determine the plume behavior of silt material disposed from hopper dredges in 90 m of water compared to that previously observed during clamshell/scow operations, which produced relatively small plumes (SAIC, 1984). Studies of acoustic backscatter measurements revealed that the convective flow to the bottom removed most of the sediment material from the water column within a

few minutes, and a mass balance estimate indicated that sediment concentrations in the remaining plume (5 to 12 mg/l) represented approximately 3 % of the total load.

- Rockland Disposal Site, Rockland, Maine

The USACE New England Division conducted multiple sediment plume measurements in 1985 at the Rockland Disposal Site, Rockland, Maine (SAIC, 1988), involving three separate discharges of silty clay material (1,205 to 2,780 m^3) from towed scows into approximately 65 m of water. Mass balance calculations using acoustic profiling sediment concentration data indicated that approximately 6 % of the released material would be transported out of the disposal area during maximum flood tide, compared with only 1 % if disposal occurred evenly throughout the tidal period.

- Field Data Collection Project, Mobile, Alabama

Further insight into sediment plume dynamics was gained during the Mobile, Alabama Field Data Collection Project (Kraus, 1991) conducted by the USACE Waterways Experiment Station (WES) as part of the Dredging Research Program (DRP). In this study, sediments were discharged into shallow water (7.6 m and 12 m depths) over a 10 to 20 s period from barges traveling at 4 to 6 knots. Field observations from 18 disposal events indicated that only a small portion of the fine-grained particles was lost to the water column, as a thin surface plume, with the bulk of the material rapidly convected downward as a coherent mass. The surface plumes appeared to be the result of shearing effects and dispersion caused by the moving barge during release, suggesting that the amount of material remaining in the water column was largely a function of the relative velocities of the ambient current and discharge vessel. Results similar to the Mobile, Alabama study were obtained by WES in the laboratory using 1:50 scale models of split-hull and multi-hopper disposal vessels under both moving and stationary conditions (Johnson et al., 1993). Some of the discharged silt material was sheared off into an upper water column plume during tests with moving vessels; such shearing was not observed during stationary experiments in quiescent water.

Chapter 3

Experimental Methods

The majority of this work is based on a series of flow visualization experiments performed with non-cohesive particles. Manufactured spherical glass beads and natural ground silica silt were used for these experiments. A limited number of experiments was also conducted using Boston Blue Clay, a cohesive material. A cross-reference table is provided in Appendix A, which summarizes the particle sizes and other salient features of all experiments conducted for this work. The particle types, equipment, image processing techniques, and experimental procedure used for these experiments are described in the following sections.

3.1 Particle Types

For the majority of particle cloud experiments, pre-sorted non-cohesive particles consisting of four different sizes of glass beads and one nominal size of ground silica silt were used. The glass beads, manufactured by Potters Industries, Inc. (Valley Forge, Pennsylvania) under the trade name Ballotini Impact Beads, are composed of soda-lime silica glass with a density of 2.5 $\frac{g}{cm^3}$. The high reflectivity of the beads (refractive index: 1.51 - 1.52) provided a strong imaging signal for the flow visualization system discussed later in this chapter. The density of the ground silica silt, provided by U.S. Silica Company (material code: SIL-CO-SIL 40 - 0.005 mm), was measured to be approximately 2.67 $\frac{g}{cm^3}$. In contrast to the spherical glass beads, the silica silt is

Particle Type	*Mean d_s (mm)*	*Range (mm)*	*True Round*	$w_s(\frac{cm}{s})$
Silica Silt	0.010 ± 0.011	0.001 - 0.045	–	9.1×10^{-3}
Glass Bead	0.024 ± 0.006	0.012 - 0.038	> 85 %	4.7×10^{-2}
Glass Bead	0.129 ± 0.019	0.075 - 0.148	> 85 %	1.36
Glass Bead	0.264 ± 0.018	0.208 - 0.290	> 65 %	3.2
Glass Bead	0.556 ± 0.033	0.445 - 0.597	> 60 %	7.1

Table 3.1: Particle specifications for non-cohesive particles.

known to have a very angular shape due to the grinding process.

Specifications, including the mean, range, and standard deviation associated with each particle diameter (d_s), are included in Table 3.1. For the two largest glass bead sizes, the d_s statistics were calculated from a randomly chosen group of 50 particles for which the diameters were measured using a micrometer. For the two smallest glass bead sizes, the d_s statistics were derived from a randomly chosen set of 20 particles for which the diameters were measured using a calibrated microscope. The minimum percent round data shown in Table 3.1 were provided by the manufacturer. The mean d_s value shown for the silt is actually the median value taken from the grain size distribution provided by the manufacturer. The standard deviations associated with this value were also estimated from the grain size distribution data using the estimated mean value of 0.014 mm.

Also included in Table 3.1 are the settling velocities (w_s) of the particles. The fall velocities of the two largest size glass beads were measured from settling column tests (Socolofsky, 2000), and the fall velocities for the smaller beads and silica silt were calculated using Stokes' Law (i.e., $w_s = \frac{{d_s}^2(\rho_s - \rho)g}{18\mu}$) with $\mu = 1 \times 10^{-6}$ based on a water temperature of 20°. The Boston Blue Clay is an illitic marine clay containing about 60 % clay-sized particles ($< 0.002\ mm$) with the remaining fraction consisting mostly of silt particles with diameters less than 0.01 mm (Zreik, 1994).

3.2 Sediment Release and Capture Mechanisms

A release apparatus, shown in Figure 3.1, was design and constructed to enable both wet and dry sediments (to be defined later) to be released in a controlled, repeatable manner. Another design objective was to create a very rapid release device (i.e., instantaneous) that would facilitate a smooth discharge of material with minimal disturbance associated with the opening of an orifice (i.e., via a valve, stopper, or moving door). The release mechanism is constructed from aluminum and was designed to hold a cylindrical Lexan^{TM} tube in which the material to be released is placed. The cylinders were fitted with a rubber gasket inside of the bottom rim to make them water-tight. Particles are released when a thin Lexan^{TM} lever arm, or "trap door," connected to a spring, is allowed to swing open. The arm is held in place by the cylinder itself, which is clamped down with a horseshoe-shaped aluminum arm mounted on the top of the apparatus. The "trap door" swings open when the tension on the release cylinder is relieved by turning a screw holding the aluminum arm in place. The "trap door" was equipped with an electronic switch that automatically triggers the image acquisition system described in the next section. Video images indicate that the spring-loaded arm opens in less than one video frame (i.e., $< \frac{1}{30}$ s). As will be discussed in later chapters, the release mechanism produced axisymmetric "thermal-like" particle clouds with no signs of "lopsidedness" caused by opening of the trap door. As verification that the release mechanism was not skewing the cloud behavior in some manner, experiments conducted with the position of the release mechanism rotated 180° produced virtually identical cloud shapes.

Cylinders with five different diameters (D) were constructed to fit into the sediment release mechanism as shown below:

- 1.91 cm (0.75 in)
- 2.54 cm (1.00 in)
- 3.18 cm (1.25 in)
- 3.81 cm (1.50 in)

- 4.45 cm (1.75 in)

The above cylinder sizes were used with the same initial volume of particles, resulting in different height-to-diameter ($\frac{H}{D}$) aspect ratios. After several trial experiments, the smallest cylinder size was abandoned because the very large aspect ratio resulted in semi-continuous releases that produced elongated clouds with "plume-like" features.

A sediment "trap" was constructed to facilitate quantification of particles not initially incorporated into the cloud or stripped away from the cloud as it descended. As discussed in Chapter 5, in some of the experiments, a "stem" of particles\fluid formed behind the main cloud as it descends. The trap was suspended inside the glass tank in a horizontal position by ropes (Figure 5.1 shows cross-sectional view). As shown in Figure 3.2, the trap is constructed of an aluminum frame fitted with a pre-rolled extendible curtain (i.e., a modified window shade) that is closed via an attached string fed to the top of the tank. The shade is supported by a cross brace and several strings which span the width of the aluminum frame. The cross brace and strings did not appear to influence the motion of the descending cloud. A fluorescent "flag," constructed from a plastic fastener, was attached to one of the strings (shown in Figure 5.1) to indicate the precise time at which the curtain was pulled across the trap (i.e., chops off the "stem"). Following passage of the cloud through the trap, the shade was pulled to isolate particles in the main cloud from those left behind in the water column, which subsequently settled on top of the shade. Video footage of the moving flag showed that the curtain traversed the width of the "stem" (1 - 8 cm) within one to four video frames (0.03 - 0.13 s). After the "stem" particles had settled on top of the curtain, the tank was drained, and the mass of particles on the shade measured after drying.

3.3 Flow Visualization

Flow visualization experiments were conducted in a 3,600 liter glass-walled tank measuring 1.22 m on each side and 2.44 m high, as shown in Figure 3.3. The glass is constructed of two fully tempered laminated lites, each 16 mm thick, separated by a

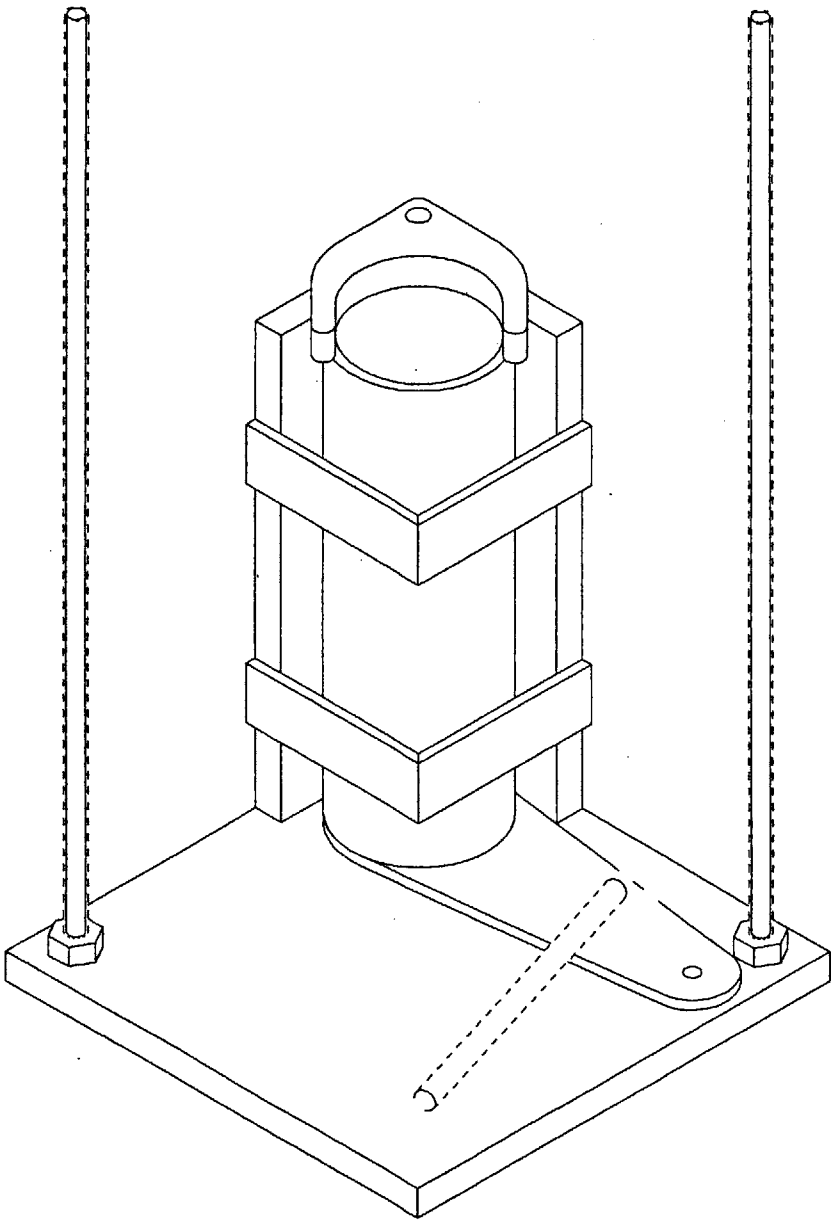

Figure 3-1: Sediment release mechanism (scale: base is 15.2 cm x 15.2 cm).

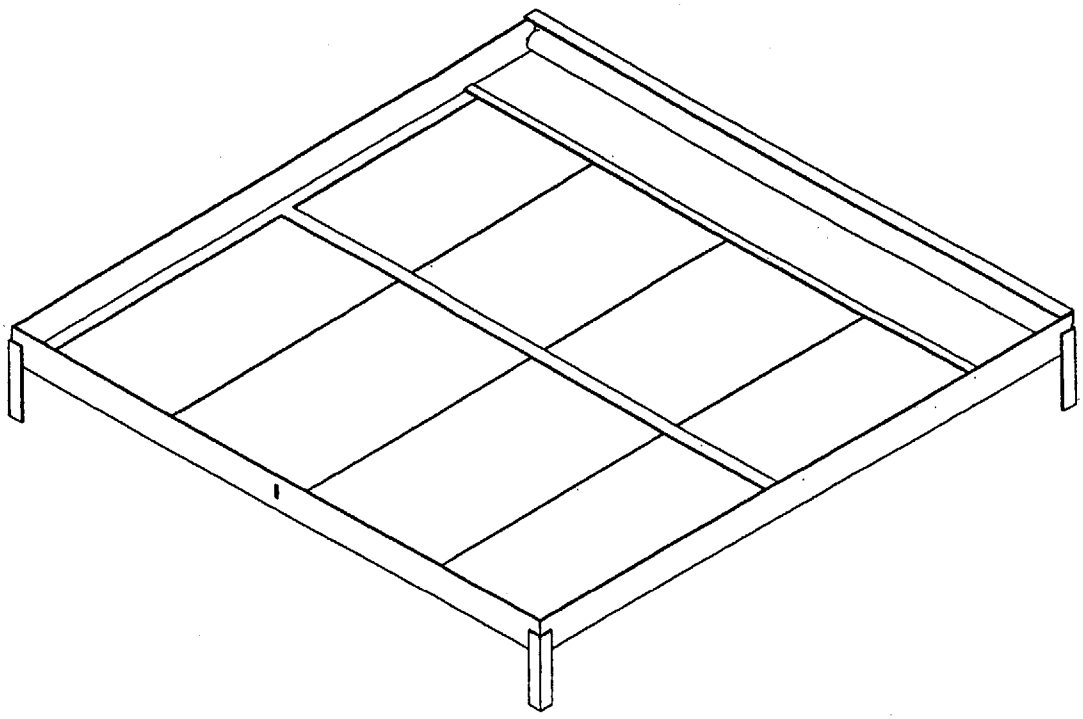

Figure 3-2: Sediment trap mechanism (scale: frame is 92 cm x 92 cm).

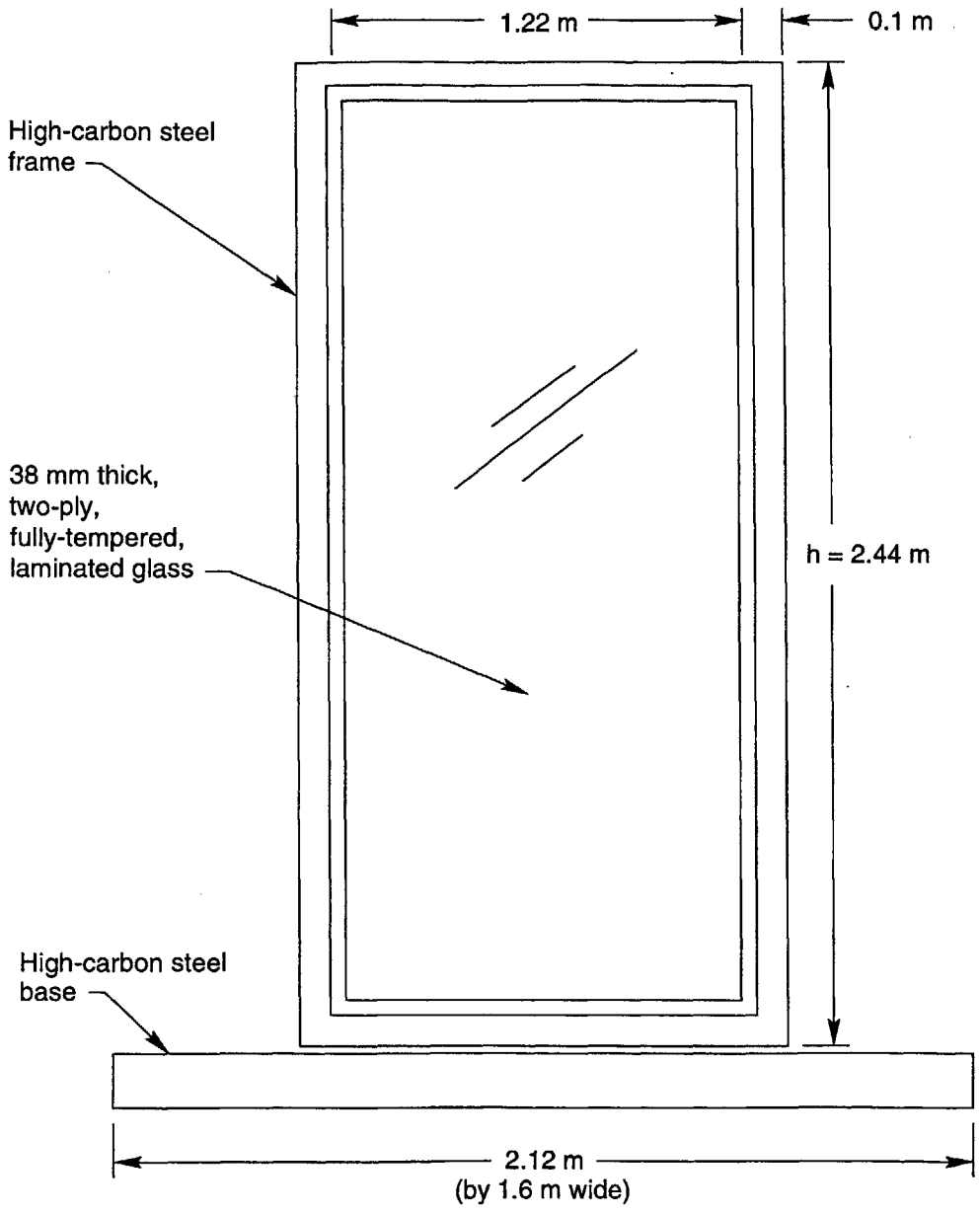

Figure 3-3: Flow visualization tank (after Socolofsky, 2000).

6 mm thick clear layer of polyvinylbutyral. The frame and base are constructed of structural C1010 carbon steel with an epoxy coating.

Flow visualization was accomplished by illuminating a thin vertical cross-section of the particle clouds. Azimuthal symmetry of the cloud enabled its volume and center of mass position to be calculated from a cross-sectional image, as explained in the next section. The cross-sections were illuminated with a 20 mm thick vertical sheet of blue-green laser light (488 nm and 514 nm primary wavelengths) produced by a 6 watt argon-ion laser (Coherent, Inc. Model Innova 70). The light sheet was created by first feeding the laser beam through a fiber optic cable and then passing it through a cylindrical lens mounted at the end of the cable.

The argon-ion laser provided very good illumination of the glass bead particles contained within the thickness of the light sheet, which easily penetrated the entire width of the particle cloud. The silt particles, however, significantly attenuated the light sheet as it passed through the cloud, resulting in a very dim image on the far side of the cloud and making edge detection difficult. To alleviate this problem, a small amount of rhodamine 6G dye, which fluoresces under the laser light, was added to the silt solutions to brighten the cloud images. Numerous trial experiments were performed to determine the optimal camera settings and lighting conditions necessary for performing subsequent edge detection analysis.

Cloud images were recorded using a data acquisition system consisting of a black-and-white charge-coupled device (CCD) progressive scan camera (Pulnix TM9701-AN), computer frame-grabber board (Matrox, Inc., Model Pulsar PCI), and associated image acquisition driver software (LabView Advanced IMAQ) provided by Graftek Imaging, Inc. A schematic of the image acquisition system is shown in Figure 3.4. The frame-grabber board captures gray-scale analog images from the CCD camera at a maximum frequency of 30 frames per second and converts them to binary images with a 764 x 484 pixel resolution. The frame-grabber is controlled manually by either the computer mouse or via an external trigger which reads an analog signal (i.e., battery voltage) generated by the electronic switch mounted on the sediment release mechanism. The captured images, each recorded into its own file (bitmap

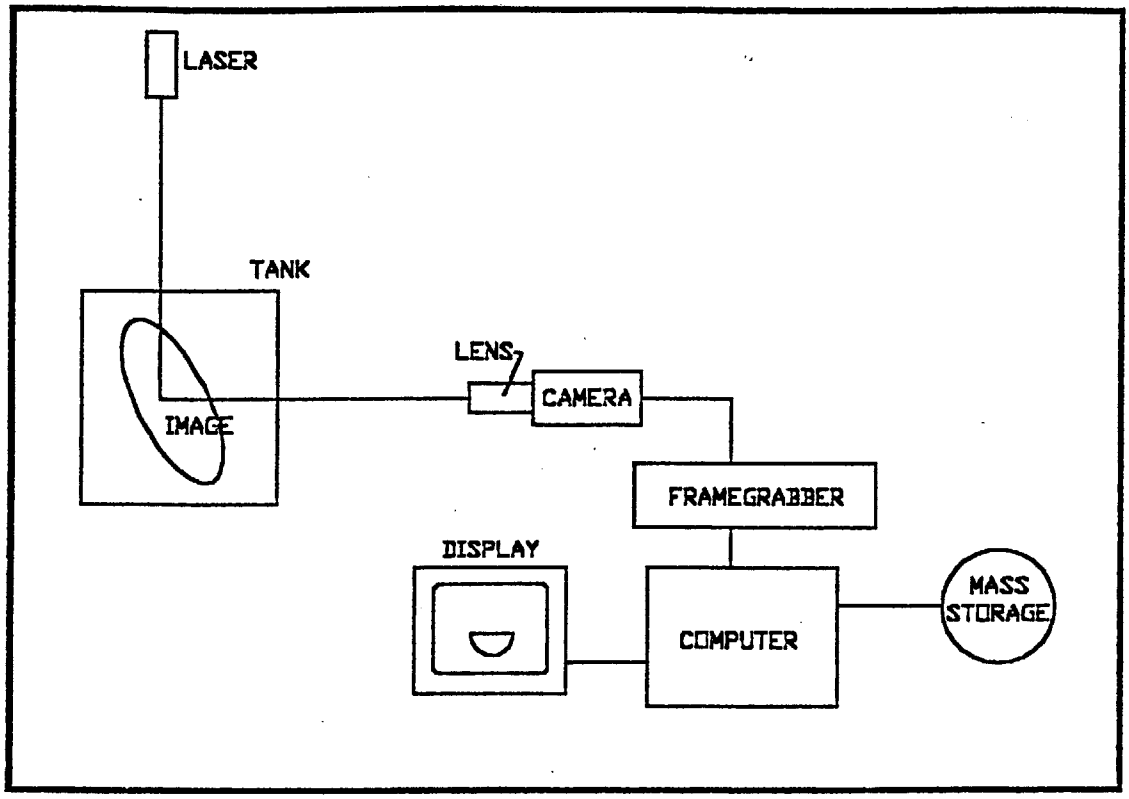

Figure 3-4: Image acquisition system (after Bruce, 1998).

format), were first stored on the computer hard drive and then transferred onto compact disks (CDs) for subsequent processing, as described in the following section.

The recorded images were calibrated using a 0.9 m by 1.2 m vertical sheet consisting of a grid pattern of 5 cm x 5 cm squares. The calibration sheet was constructed by sandwiching the grid pattern, plotted on a sheet of mylar, between two 3 mm thick sheets of plexiglass. For each experiment, the grid pattern is placed inside the tank (filled with water), aligned with the laser light sheet, and then recorded. The grid provides a repeatable means of calibrating the horizontal and vertical dimensions of the digital image (measured in pixels) to actual dimensions.

3.4 Image Processing

Processing of recorded images was conducted using customized computer programs written in the MATLAB^{TM} numeric computing environment and utilizing commands contained in the MATLAB Image Processing Toolbox (The Math Works, Inc., 1997). For each recorded image, the intensity of each pixel is mapped to a grey-scale ranging from 1 to 256, with a value of 1 corresponding to a totally dark (black) pixel and 256 representing a fully illuminated (white) pixel. The first image processing step was a frame-by-frame analysis of the cross-sectional area of the cloud using edge detection methods. Edge detection was accomplished by first observing the grey-scale intensity values associated with the cloud image, as well as those for the ambient fluid (i.e., background intensity), and then selecting an appropriate threshold to distinguish the cloud material from background fluid (i.e., threshold intensity level greater than twice the background intensity level). Representative horizontal and vertical intensity profiles from a recorded image from one of the 0.264 mm glass bead experiments are provided in Figure 3.5.

Because CCD camera positions and lighting conditions (e.g., shutter speed and f-stop settings) varied for different groups of experiments, threshold limits were selected on a case-by-case basis, but were generally held constant for a particular group of experiments utilizating the same camera location and settings. An automated

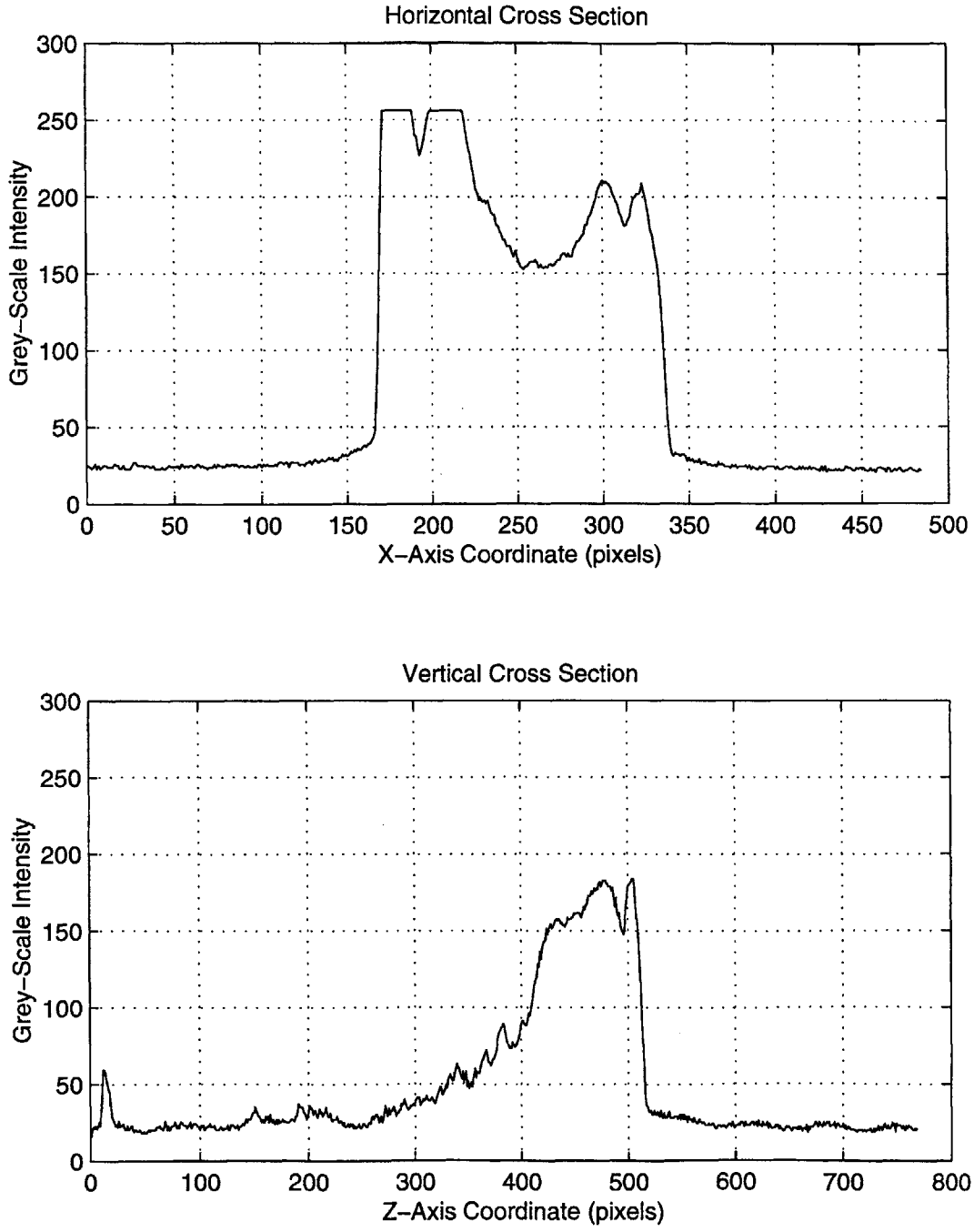

Figure 3-5: Grey-scale intensity profiles for representative horizontal and vertical cross sections of a 0.264 mm particle cloud image.

MATLAB^{TM} program was developed to determine the maximum cloud diameter and leading edge position using a pre-selected threshold value. These parameters were calculated by cycling through the rows and columns of pixels comprising the image matrix while keeping track of the minimum and maximum horizontal and vertical (i.e., x, z) locations of the pixels exceeding the threshold limit in each row and column of pixels.

The horizontal center of mass location ($\bar{x}$) associated with the illuminated cross-sectional area is determined by dividing the first spatial moment (mean displacement in the horizontal direction) by the zeroth moment (cross-sectional area) as follows:

$$\bar{x} = \frac{\sum_{ij} x_{ij} v_p}{\sum_{ij} v_p} \tag{3.1}$$

where x_{ij} and v_p are the pixel location and pixel volume, respectively.

The cloud volume is calculated by spatially integrating pixel volumes as follows:

$$V = \sum_{ij} v_p \pi (x_{ij} - \bar{x}) \tag{3.2}$$

In the above equation, the horizontal summation adds up concentric semi-circular rings of pixels for each side of the cloud (relative to the axis of symmetry) to form a disc-shaped horizontal slice with a thickness of one pixel. The horizontal slices are then summed in the vertical direction to obtain the total cloud volume. The vertical center of mass location of the cloud volume ($\bar{z}$) is then determined by dividing the first spatial moment (mean displacement in the vertical direction) by the zeroth moment (cloud volume) as follows:

$$\bar{z} = \frac{\sum_{ij} v_p \pi (x_{ij} - \bar{x}) z_{ij}}{V} \tag{3.3}$$

MATLAB^{TM} functions allow exact pixel locations associated with a displayed video image to be determined digitally using a point-and-click method with the computer mouse. The cross-sectional dimensions (i.e., maximum diameter, leading edge position) and the center of mass locations calculated by the automated MATLAB^{TM}

program were verified using this procedure.

To accommodate time variations in cloud shape (i.e., elongation and flattening) and corresponding changes in maximum radius, which may not necessarily be associated with entrainment mechanisms, cloud growth rates (i.e., entrainment coefficients) were estimated using the radius of an equivalent spherical volume calculated as follows:

$$r = \left(\frac{3V}{4\pi}\right)^{\frac{1}{3}} \tag{3.4}$$

Using the equivalent radius defined above, the entrainment coefficient is calculated from Equation 2.4 as follows:

$$\alpha = \frac{\Delta r}{\Delta z} \tag{3.5}$$

where Δr is the change in equivalent radius associated with a given change in center of mass position (Δz).

In Equation 3.5, $\frac{\Delta r}{\Delta z}$ represents the slope of the curve produced from the $(r, \bar{z})$ data pairs for a given experiment. Hereafter, all discussions of the cloud radius will refer to the equivalent radius unless otherwise noted.

With respect to determining equivalent radius values and center of mass locations for the parent cloud, the experiments that produced "stems" of particles trailing behind the cloud required "image cropping," in which the material behind the cloud is excluded from the calculations. To accomplish this in an automated and objective manner, the MATLAB^{TM} image processing program "crops" the "stem" by omitting a portion of the image above a certain elevation (depth), which the program calculates by subtracting a multiple (i.e., 100 % or 150 %) of the maximum cloud diameter from the maximum leading edge position. For the glass bead experiments, 150 % of the maximum diameter was used to calculate this elevation, whereas for the silt experiments, 100 % of the maximum diameter was used. The 150 % value was used for the glass bead experiments to avoid "chopping off" the rear portions of some of the particle clouds that experience an elongation during the first part of descent. The

100 % value was used for the silt clouds since they did not elongate, and remained roughly spherical in shape, and tended to have larger "stems" that should not be counted as part of the parent cloud.

The two different percentages used for the "image cropping" had a relatively minor effect (10 % variation) on the calculated α values for the glass bead experiments, but had a more pronounced impact (28 % variation) on the α values measured for the silt experiments. Entrainment coefficient values calculated using both percentages are provided in Appendix D. The large variations in α associated with the silt experiments were the result of the rather "fat stems" attached to the clouds. As discussed in Chapter 5, the measured mass of particles in these "stems" was not proportional to thickness of the stem in the recorded images because of the added fluorescent dye. The two different percentages used for the "image cropping" had little influence on the calculated velocity profiles for the silt and glass bead experiments.

The velocity of the cloud's center of mass is calculated by simply taking the slope of the volumetric center of mass versus time curve as follows:

$$w = \frac{\Delta z}{\Delta t} \tag{3.6}$$

The calculated center of mass positions exhibited small variations (i.e., "noise") associated mainly with variations in light intensity of the laser light sheet. Nonuniformities in the laser light sheet may have been caused by corruption of the collimated laser beam within the fiber optic cable. The center of mass positions for the group of twelve experiments discussed in Chapter 4 are provided in Appendix C. To filter out (i.e., smooth) some of the experimental variations in the center of mass postions, the velocity was calculated by taking the slope of a 5-point moving linear regression of the center of mass versus time data. In Figure 3.6, the velocity profiles generated by this approach are compared to those produced by taking frame-by-frame changes in center of mass position (i.e., using $\Delta t = \frac{1}{30}\ s$ in Equation 3.6) as well as those generated with a 3-point moving linear regression. As shown in Figure 3.6, the 5-point regression eliminates a significant degree of the variability within the deceleration

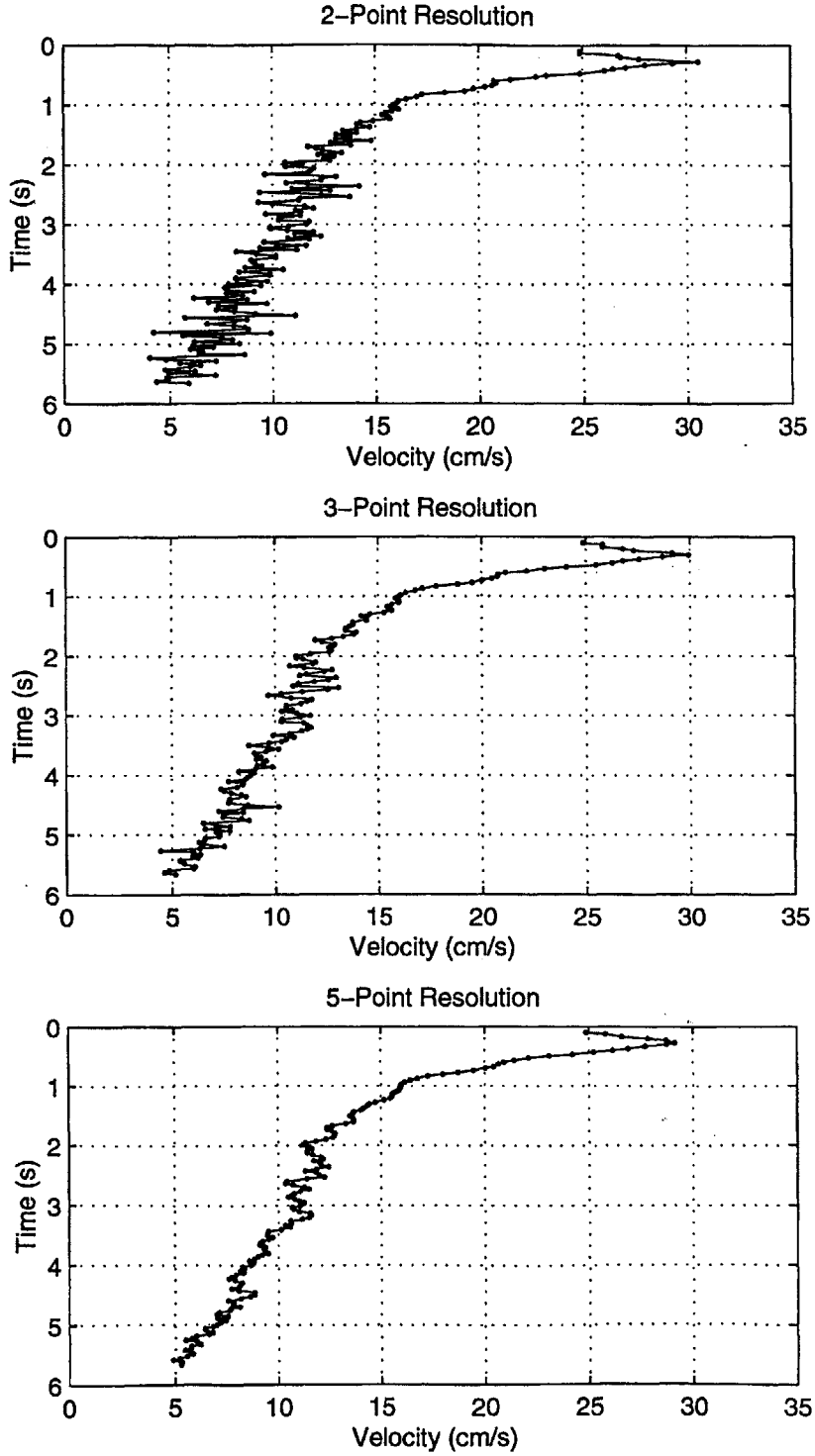

Figure 3-6: Representative velocity profiles for a 0.264 mm particle cloud based on 2-point, 3-point, and 5-point resolutions.

region without a significant loss in resolution within the initial acceleration phase.

3.5 Experimental Procedure

To quantify the repeatability of the experiments and the uncertainties in calculated velocities and growth rates associated with experimental variability, each experiment using the non-cohesive particles (glass beads and silica silt) was repeated a minimum five times. Representative images of the five repetitions for the twelve experiments analyzed in Chapter 4 are included in Appendix B. The entrainment coefficients and cloud velocities were calculated using Equations 3.5 and 3.6 and the mean equivalent radius and center of mass position values calculated for the five repetitions performed for each experiment. For the majority of experiments, all five realizations were used to calculate the mean equivalent radius and center of mass position values. In four of the experiments, only four of the five realizations were used to derive the mean values, and in one experiment, only three realizations were selected. The realizations were excluded from the calculations for these experiments for one of two reasons: (1) either their behavior (i.e., shape, velocity, growth rate) differed significantly from the other three or four experiments because the particles failed to form well-mixed, axisymmetic clouds; or (2) the light intensity of the recorded images contained an abnormal amount of "noise," resulting in radius and center of mass profiles containing gross errors. One possible reason for why the particles did not form well-mixed, axisymmetic clouds in some cases is "clumping of the particles" due to interlocking or adhesion.

Chapter 4

Particle Cloud Experiments

The results of particle cloud experiments are presented in terms of growth rate, velocity, and circulation characteristics in Sections 4.2, 4.3, and 4.4, respectively. Trends in these characteristics, with respect to the various initial conditions, are analyzed in Section 4.5. Of the twenty-six experiments performed, a subset of twelve experiments was selected for in-depth presentation and discussion. The results of six other experiments are also presented, but in less detail. The rationale for this approach is discussed in the following section. The remaining eight experiments were performed using the 0.556 mm glass beads, the results of which are provided in Appendix E. Analysis of these experiments was complicated by the fact that the beads began to settle out of the cloud after 2 - 3 s of descent, resulting in a very short period of self-similarity. Clouds formed from these large beads, which scale to 3 - 6 cm cobbles in real world dimensions based on N_c, quickly became laminar, as inter-particle collisions effectively dampened turbulent motion. Nevertheless, within the first 1 - 2 s of descent the behavior of the 0.556 mm particle clouds closely resembled that of the 0.264 mm clouds, therefore supporting conclusions discussed herein but providing no additional insight.

Initial Condition	*Group I*	*Group II*	*Group III*
Water Content	x	x	
Initial Momentum	x	x	x
Compaction		x	
Cloud Number			x

Table 4.1: Initial condition variables – experimental Groups I, II, and III.

4.1 Approach

For presentation and comparison purposes, the twelve experiments have been organized into three groups, denoted Group I, Group II and Group III. The initial conditions varied for each group are shown in Table 4.1.

The salient features of each experiment are provided in Table 4.2. The experiment nomenclature in Table 4.2 is used throughout this chapter to distinguish only the differences between the experiments in each group, which are shown in boldface type in Table 4.2. The initial dry mass of particles was maintained at 40 g for all experiments, yielding a constant initial buoyancy (B_o) of $23,520\ gms^{-2}$. Only the 0.264 mm glass beads were used for experiments in Groups I and II, whereas, the 0.010 mm silica silt and 0.024 mm glass beads were used for Group III. The 3.18 cm diameter and 4.45 cm diameter release cylinders were used in the Group I experiments, while the Group II and Group III experiments employed only the 4.45 cm diameter release cylinder. The opening of the release mechanism in the experiments was positioned either immediately above the water surface (i.e., within 2 mm) or was completely submerged so that the height of material in the cylinder coincided with the ambient water elevation in order to release the material without any initial potential energy (i.e., initial momentum). In the tables and figures presented herein, the former types of releases are denoted by an "AW" abbreviation, and the latter by a "BW." Particles were either released in a settled state, denoted as "Set.," or as a suspension, abbreviated "Sus.," by stirring them with a glass rod prior to releasing them.

The particles in all of the Group I experiments were released in a settled state. For the Group I experiments denoted as "wet," the glass beads were supersaturated

Experiment	$d_s(mm)$	$D_o(cm)$	$\frac{H_o}{D_o}$	$H_2O(cm^3)$	*Pos.*	*Sus./Set.*
Group I Experiments						
3.18 cm Cyl., Dry	0.264	**3.18**	**1.1**	**0**	AW	Set.
3.18 cm Cyl., Wet	0.264	**3.18**	**1.3**	**17**	AW	Set.
4.45 cm Cyl., Dry	0.264	**4.45**	**0.4**	**0**	AW	Set.
4.45 cm Cyl., Wet	0.264	**4.45**	**0.5**	**17**	AW	Set.
Group II Experiments						
40 cm^3 H_2O, Sus., AW	0.264	4.45	**0.8**	**40**	**AW**	**Sus.**
40 cm^3 H_2O, Sus., BW	0.264	4.45	**0.8**	**40**	**BW**	**Sus.**
40 cm^3 H_2O, Set., AW	0.264	4.45	**0.8**	**40**	**AW**	**Set.**
17 cm^3 H_2O, Sus., AW	0.264	4.45	**0.5**	**17**	**AW**	**Sus.**
Group III Experiments						
0.024 mm Beads, AW	**0.024**	4.45	0.8	40	**AW**	Sus.
0.024 mm Beads, BW	**0.024**	4.45	0.8	40	**BW**	Sus.
0.010 mm Silt, AW	**0.010**	4.45	0.8	40	**AW**	Sus.
0.010 mm Silt, BW	**0.010**	4.45	0.8	40	**BW**	Sus.

Table 4.2: Release condition matrix – experimental Groups I, II, and III.

with 17 cm^3 of water, compared to the approximately 10 cm^3 required to just saturate the initial 26 cm^3 of dry beads. The additional water was added to accommodate any volumetric measurement errors and to ensure that all beads in the test cylinder were completely submerged before release. All particles in Group III were supersaturated with 40 cm^3 of water and released as a suspension (Sus.). Group II experiments consisted of both settled and suspended releases with either 17 cm^3 or 40 cm^3 of water added as indicated in Table 4.2

In addition to the twelve experiments, six other experiments were conducted using the 0.264 mm beads to determine whether differences in cloud behavior between the 3.18 and 4.45 cm cylinder sizes resulted from differences in initial potential energy (i.e., height of material above water surface) or initial release geometry characterized by the aspect ratio of the height of material in the cylinder (H_o) to the cylinder diameter (D_o). Three of the experiments (Group IV) involved changing H_o while keeping $\frac{H_o}{D_o}$ constant, whereas, the other three (Group V) involved varying $\frac{H_o}{D_o}$ while holding the elevation of particles with respect to the water surface constant. In all six experiments, the glass beads were released in a "settled" state. The release conditions

Experiment	$d_s(mm)$	$D_o(cm)$	$\frac{H_o}{D_o}$	$H_2O(cm^3)$	*Pos.*
Group IV Experiments					
4.6 cm AW, 0.0 cm BW	0.264	4.45	1.0	33	AW
2.3 cm AW, 2.3 cm BW	0.264	4.45	1.0	33	AW/BW
0.0 cm AW, 4.6 cm BW	0.264	4.45	1.0	33	BW
Group V Experiments					
$\frac{H_o}{D_o}$ = 0.8, 1.2 cm BW	0.264	**3.81**	**0.8**	17	AW/BW
$\frac{H_o}{D_o}$ = 1.1, 1.6 cm BW	0.264	**3.18**	**1.1**	17	AW/BW
$\frac{H_o}{D_o}$ = 2.6, 4.8 cm BW	0.264	**2.54**	**2.6**	17	AW/BW

Table 4.3: Release condition matrix – experimental Groups IV and V.

of these experiments are summarized in Table 4.3.

4.2 Cloud Growth Analysis

In this section, cloud growth rates are analyzed in terms of the entrainment coefficient (α) calculated by taking the slope of measured equivalent radius versus depth curves, as discussed in Section 3.4. Based on the behavior of these curves, the clouds are characterized as either well-mixed "thermals" or "circulating thermals."

4.2.1 "Thermal" Phase

One distinguishing feature of the Group I particle clouds compared to the other experiments is the additional time required for the Group I clouds to become turbulent. Representative images depicting the initial 0.6 s of descent for the two Group I "wet" experiments are provided in Figure 4.1. Representative images showing the entire recorded descent duration for Groups I - III are given in Figures 4.2 - 4.4. Representative images from the five repetitions performed for these experiments are provided in Appendix B.

Initial cloud conditions for the twelve experiments are included in Table 4.4. In Table 4.4, z_o and z_1 refer to the cloud center of mass positions at times t_o (i.e., prior to release) and t_1, respectively, where t_1 refers to the time required for the majority

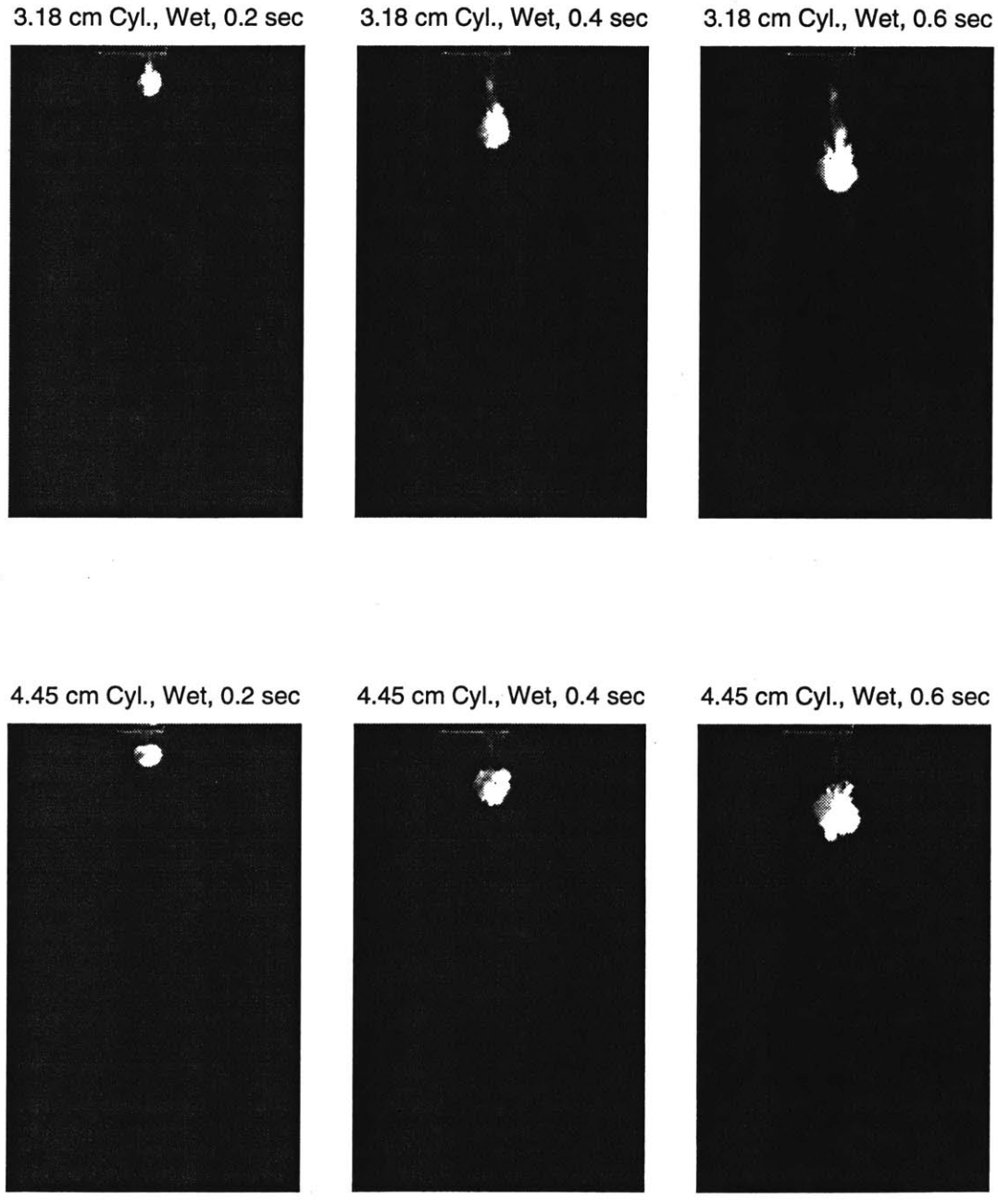

Figure 4-1: Selected cloud images for first 0.6 s of descent - Group I "Wet" experiments. Actual size of frames is approx. 64 cm x 87 cm.

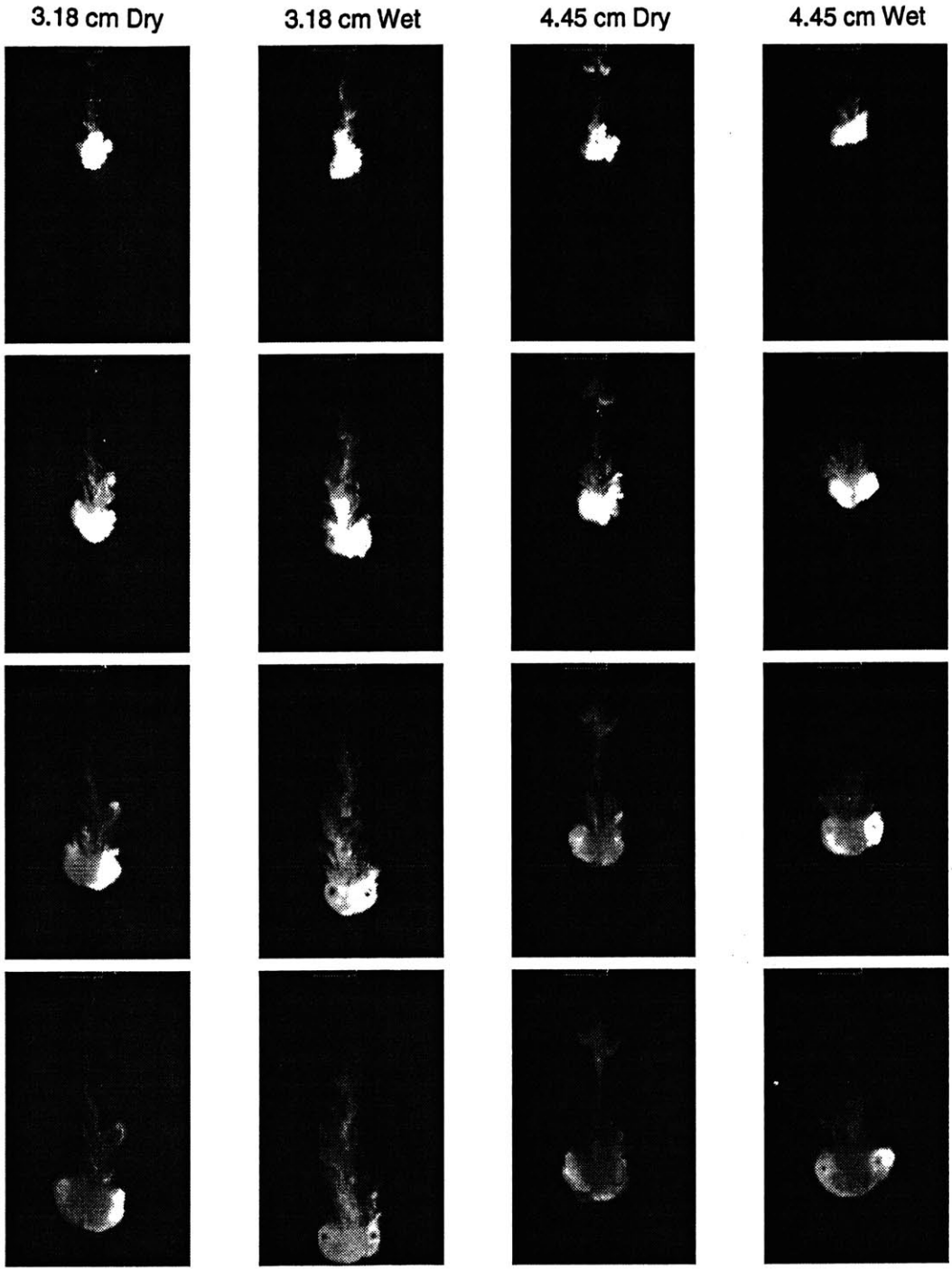

Figure 4-2: Selected cloud images at 1 s, 2 s, 3 s, and 4 s - Group I experiments. Actual size of frames is approx. 64 cm x 87 cm.

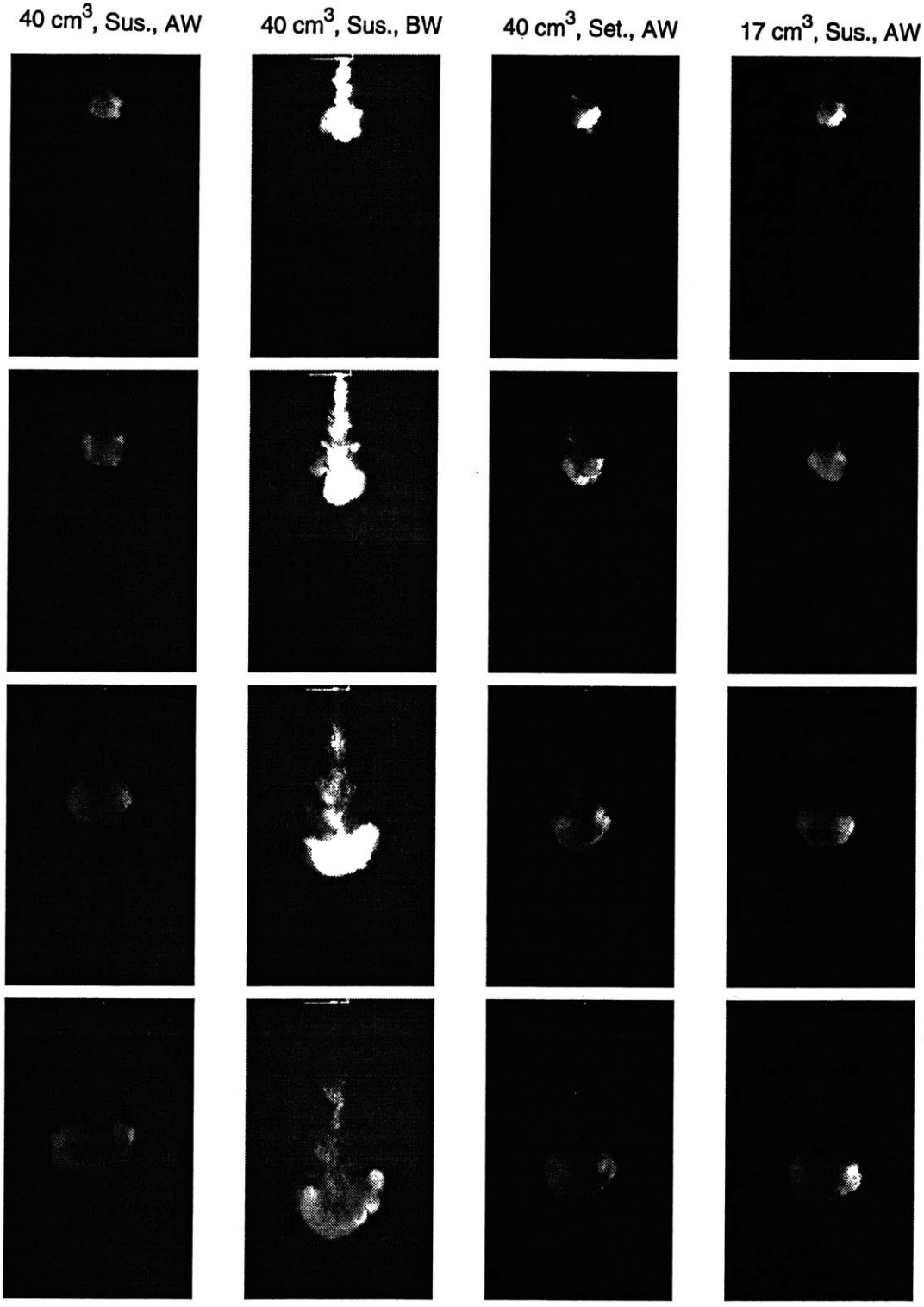

Figure 4-3: selected cloud images at 1 s, 2 s, 4 s, and 6 s - Group II experiments. Actual size of "AW" frames is approx. 88 cm x 116 cm. Actual size of "BW" frames is approx. 69 cm x 91 cm.

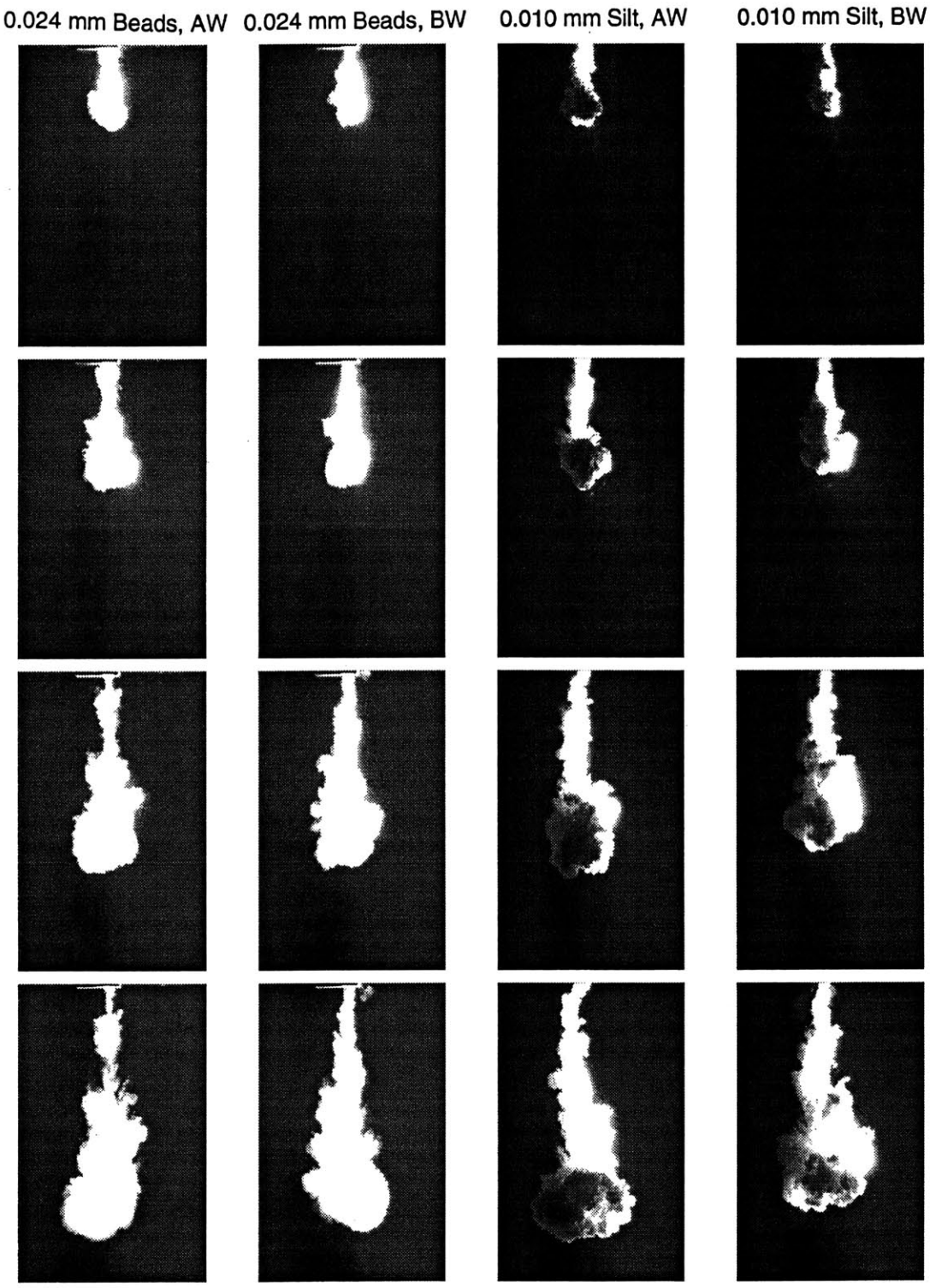

Figure 4-4: Selected cloud images at 1 s, 2 s, 4 s, and 6 s - Group III experiments. Actual size of frames is approx. 69 cm x 91 cm.

Experiment	$z_o(cm)$	$r_o(cm)$	$z_1(cm)$	$r_1(cm)$	α_o	$t_1(s)$	$t_r(s)$
Group I Experiments							
3.18 cm Cyl., Dry	-1.81	1.87	1.55	2.32	0.14	0.10	0.10
3.18 cm Cyl., Wet	-2.08	1.99	2.02	2.43	0.11	0.13	0.10
4.45 cm Cyl., Dry	-0.89	1.87	1.58	2.43	0.23	0.10	0.10
4.45 cm Cyl., Wet	-1.07	1.99	1.34	2.53	0.22	0.10	0.10
Group II Experiments							
40 cm^3 H_2O, Sus., AW	-1.81	2.37	1.07	3.01	0.22	0.10	0.10
40 cm^3 H_2O, Sus., BW	-1.81	2.37	8.08	4.57	0.22	0.40	0.10
40 cm^3 H_2O, Set., AW	-1.81	2.37	0.94	2.84	0.17	0.10	0.10
17 cm^3 H_2O, Sus., AW	-1.07	1.99	0.93	2.75	0.38	0.10	0.10
Group III Experiments							
0.024 mm Beads, AW	-1.81	2.37	2.76	4.30	0.42	0.20	0.10
0.024 mm Beads, BW	-1.81	2.37	5.01	3.92	0.30	0.40	0.10
0.010 mm Silt, AW	-1.77	2.36	2.18	3.59	0.25	0.13	0.10
0.010 mm Silt, BW	-1.77	2.36	2.95	3.24	0.19	0.27	0.10

Table 4.4: Initial cloud conditions – experimental Groups I, II, and III.

of the particle mass to exit the release cylinder, based on visual observations of recorded images. For all experiments, the bottom of the release mechanism base was taken as elevation $z = 0$, resulting in negative z_o values. As expected, t_1 values are higher for the "BW"' experiments in which the particles had less initial potential energy than for their "AW" counterparts. The r_o and r_1 values in Table 4.4 denote cloud radius (based on an equivalent spherical volume) at times t_o and t_1, respectively. The α_o values in Table 4.4, to be discussed later in this chapter, represent initial "entrainment" coefficient values, calculated as $\frac{r_1 - r_o}{z_1 - z_o}$.

The release times, t_r, estimated from the actual cloud images, are also shown in Table 4.4. The t_r times represent the time required for the main particle cloud to exit the cylinder. As shown in Figures 4.3 and 4.4 and described in detail in Chapter 5, the Group III experiments and the "40 cm^3 H_2O, Sus., BW" Group II experiment produced particles clouds with an attached "stem" of particles trailing behind the main cloud. For the other experiments, which generated little or no "stem," t_1 is essentially identical to t_r. For the clouds with an attached "stem," the t_1 values are longer than the t_r values because they include additional time required for most of

the "stem" particles to exit the cylinder.

The theoretical releases times for the "AW" and "BW" were calculated by equating the mass of initial material times its acceleration with the sum of the buoyancy and gravitational forces as follows:

$$\text{"AW" Release: } \rho H_o A_o \frac{dz}{dt} = \rho H_o A_o g - \rho_a A_o g z \tag{4.1}$$

$$\text{"BW" Release: } \rho H_o A_o \frac{dz}{dt} = \rho H_o A_o g - \rho_a A_o g H_o \tag{4.2}$$

where z is the center of mass depth relative to the water surface; A_o is the release cylinder cross-sectional area; and ρ and ρ_a are the densities of the initial material and ambient fluid, respectively. Using the initial conditions, $z = -\frac{H_o}{2}$ and $\frac{dz}{dt} = 0$, the above equations were solved as follows:

$$\text{"AW" Release: } z = H_o \left[-\frac{1}{2} + \frac{\rho}{\rho_a} \left(1 - \cos\left(\sqrt{\frac{\rho_a g}{\rho H_o}} t \right) \right) \right] \; ; \; -\frac{H_o}{2} \leq z \leq \frac{H_o}{2} \tag{4.3}$$

$$\text{"BW" Release: } z = \frac{1}{2} \left(\frac{\rho - \rho_a}{\rho} \right) g t^2 + \frac{H_o}{2} \tag{4.4}$$

The theoretical release times for the twelve experiments were calculated using the initial density and H_o values for the various initial conditions. The average theoretical release time for the nine "AW" experiments was calculated to be 0.09 s, compared to the actual average t_r value of 0.10 s for these experiments. The average theoretical release time for the three "BW" experiments was calculated to be 0.16 s, which is identical to the actual average t_r value estimated for these three experiments.

Prior to release, the 0.264 mm glass beads used in the Group I experiments were mechanically homogenized in the cylinder (i.e., stirred with a glass rod) and then allowed to settle, which occurred almost instantaneously due to their high fall velocity (2.3 $\frac{cm}{s}$). While not tightly packed, such as in a sandy soil or other porous medium, the close spacing of the beads caused sufficient interlocking and internal

friction to result in initially smooth-edged particle clouds exhibiting no signs of turbulence (Figure 4.1, 0.2 s images). Since no turbulent eddies are present with which to entrain ambient fluid, particle cloud growth in this initial phase is likely the result of inter-particle collisions and associated random particle velocity fluctuations. In the literature, the breakup of similar particle suspensions has been referred to as hydrodynamic diffusion (Eckstein et al., 1977; Davis, 1996) and hydrodynamic dispersion (Powell and Mason, 1982; Nitsche and Batchelor, 1997). Whether viewed as a diffusive or dispersive process, it appears that a certain degree of inter-particle spacing must be achieved before destabilizing forces associated with density discontinuities can overcome internal friction. Though difficult to discern in Figure 4.1, the development of a waviness around the cloud perimeter and subsequent cauliflower-like protuburences can be seen in larger video display images. The time required for the onset of turbulence, characterized by the wave-like structures was observed visually for all experiments and is recorded as t_t in Table 4.5.

As indicated in Table 4.5, the initially "dry" Group I clouds took slightly longer (about 0.2 s) to exhibit turbulence than did their "wet" counterparts. This delay is attributed to the presence of trapped air within the "pore" spaces of the particle cloud, which increased the internal friction by inhibiting particle motion and the flow of water into the cloud and between particles. In essence, the trapped air temporarily locks the particles in place until it fully escapes from the cloud. In the "dry" experiments, air bubbles on the order of 1 mm in diameter were observed flowing out of the cloud during the first 0 - 1 s of descent.

All clouds in Group III and one Group II cloud were basically turbulent upon their release (i.e., $t_t = t_1$). As one might expect, suspending the beads by stirring them before release sped up the transition to turbulence. Furthermore, the addition of excess water (23 cm^3) to the settled beads produced the same effect. In other words, the bulk of the excess water, or supernatant, becomes incorporated into the cloud as it exits the cylinder, dispersing the beads and reducing internal particle friction. As discussed in Chapter 5, the amount of this excess water that becomes incorporated into the cloud was quantified using a silt tracer.

Experiment	α_1	α_2	$t_t(s)$	$t_c(s)$	$z_c(cm)$	$\frac{r_c}{r_t}$	$\frac{r_c}{r_o}$
Group I Experiments							
3.18 cm Cyl., Dry	0.18	0.14	0.5	1.7	38.8	2.0	4.5
3.18 cm Cyl., Wet	0.17	0.08	0.27	2.3	50.7	3.3	5.1
4.45 cm Cyl., Dry	0.20	0.16	0.47	1.3	30.9	1.9	4.1
4.45 cm Cyl., Wet	0.22	0.14	0.30	1.3	26.4	2.3	3.9
Group II Experiments							
40 cm^3 H_2O, Sus., AW	0.27	0.18	0.13	1.0	19.0	2.3	3.3
40 cm^3 H_2O, Sus., BW	0.29	0.18	0.40	1.4	23.2	2.0	3.8
40 cm^3 H_2O, Set., AW	0.23	0.16	0.20	1.4	28.2	2.4	3.9
17 cm^3 H_2O, Sus., AW	0.31	0.19	0.17	1.1	21.5	2.7	4.0
Group III Experiments							
0.024 mm Beads, AW	0.23	0.12	0.20	3.0	37.5	2.8	5.4
0.024 mm Beads, BW	0.28	0.20	0.40	2.7	29.0	2.6	4.5
0.010 mm Silt, AW	0.27	0.20	0.13	5.2	54.9	6.8	6.8
0.010 mm Silt, BW	0.29	0.24	0.27	2.6	33.4	4.8	4.8

Table 4.5: Cloud growth parameters – experimental Groups I, II, and III. Time t_c and depth z_c denote the time and depth associated with the transition to "circulating thermal."

It is evident in Figure 4.1, as the Group I clouds become turbulent, they also undergo an elongation in the vertical direction, which is more pronounced in the experiments with the higher $\frac{H_o}{D_o}$ aspect ratio. The elongation occurs from approximately 0.3 to 0.7 s for the smaller aspect ratios and from 0.3 to 1.0 s for the larger $\frac{H_o}{D_o}$ ratio. This phenomenon is likely caused by the fact that the interior of the cloud retains more of its initial momentum than does the outer region, which shares its momentum with entrained ambient fluid. As a result, the denser interior core falls through the outer turbulent region, which ends up towards the rear of the cloud causing the observed elongation. The elongation process dies out as the developing eddies penetrate into the interior of the cloud, at which point the cloud is fully mixed. The significance of the elongation effect, which was not observed the Group II and Group III clouds, is related to the circulation produced, to be discussed later in this chapter.

Once the clouds are fully mixed, whether immediately upon release or after a short dispersive phase, they enter the classic "thermal" phase in which velocity and

Group IV			Group V		
Experiment	α_1	α_2	*Experiment*	α_1	α_2
4.6 cm AW, 0.0 cm BW	0.18	0.12	$\frac{H_o}{D_o} = 0.8$	0.21	0.17
2.3 cm AW, 2.3 cm BW	0.21	0.14	$\frac{H_o}{D_o} = 1.1$	0.21	0.16
0.0 cm AW, 4.6 cm BW	0.23	0.13	$\frac{H_o}{D_o} = 2.6$	0.29	0.23

Table 4.6: Entrainment coefficient values – experimental Groups IV and V.

buoyancy profiles across the width of the cloud are assumed to be self-similar and the cloud radius is proportional to depth (i.e., $r = \alpha z$), as described in Chapter 2. As will be shown, all clouds depicted in Figures 4.2 - 4.4 at the 1 s time frame have entered the "thermal" phase.

One measure of self-similarity in thermals is the linearity of r versus z (i.e., constant slope, α). The measured equivalent radius data are plotted against their respective cloud center of mass positions in Figures 4.5 - 4.7 for Groups I - III. The data shown in these figures represent mean values calculated from the data generated by the five repetitions performed for each experiment. The radius data for each of the five realizations is provided in Appendix C. As shown in Figures 4.5 - 4.7, the radius versus depth plots have varying slopes that generally decrease with depth. However, linear segments of data points are evident in the upper and lower regions of the curves. As shown in Figures 4.5 - 4.7, linear regression lines were fit to the measured data in each region, resulting in two different entrainment coefficient values, referred to hereafter as α_1 and α_2. The α_1 and α_2 values for the twelve experiments are summarized in Table 4.5. The α_1 and α_2 values for the experimental Groups IV and V are summarized in Table 4.6.

The entrainment coefficient values in Table 4.5 were calculated from the mean radius versus depth data for the five repetitions performed for each experiment. The standard deviations in α associated with the standard deviations of the five radius versus depth curves are tabulated in Appendix D. Representative profiles depicting the mean and standard deviations of the radius versus depth curves are also provided in Appendix D. For the majority of experiments, the standard deviations associated

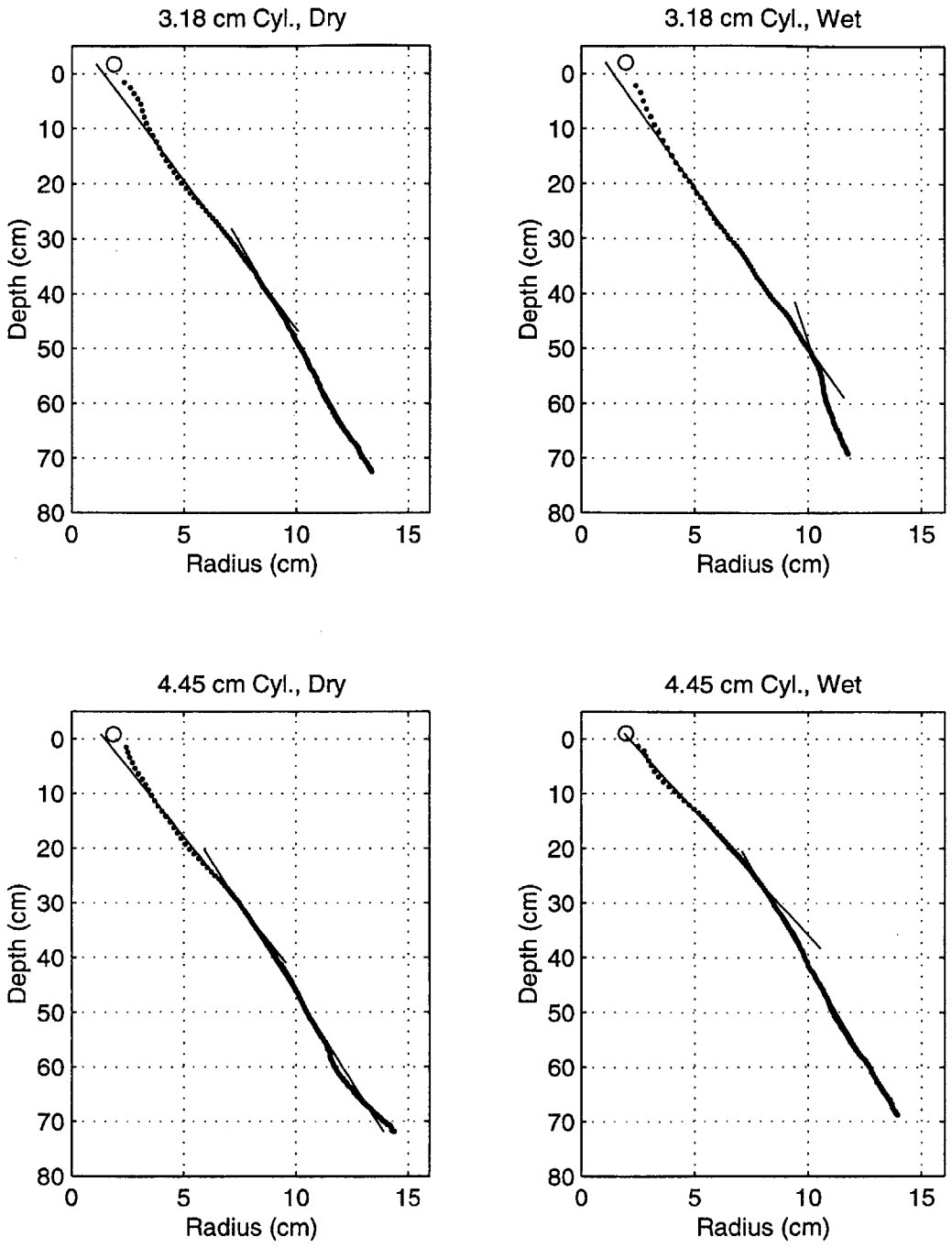

Figure 4-5: Equivalent radius versus center of mass position with fitted linear regression lines - Group I experiments. Open circles denote pre-release radius and center of mass position.

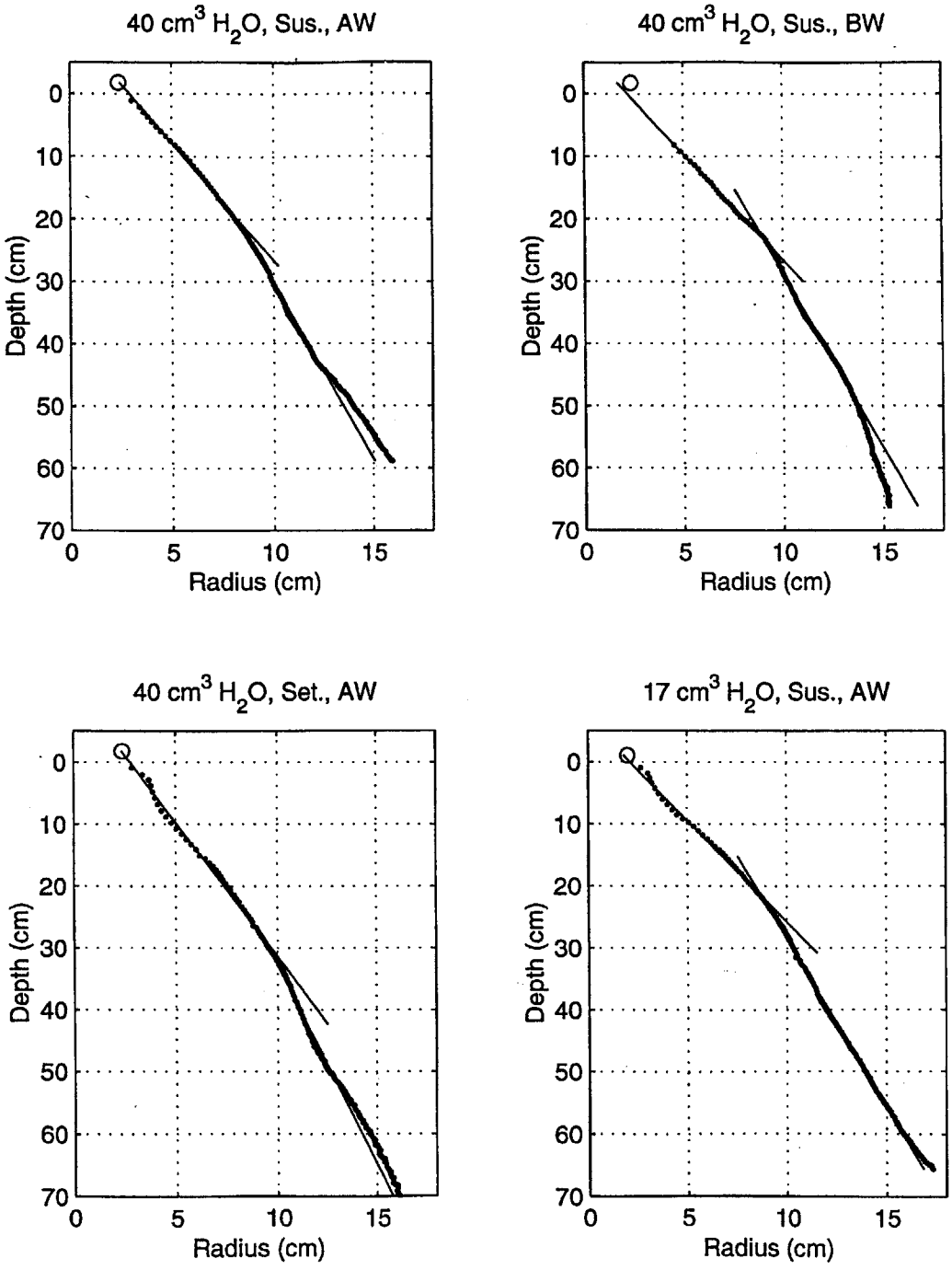

Figure 4-6: Equivalent radius versus center of mass position with fitted linear regression lines - Group II experiments. Open circles denote pre-release radius and center of mass position.

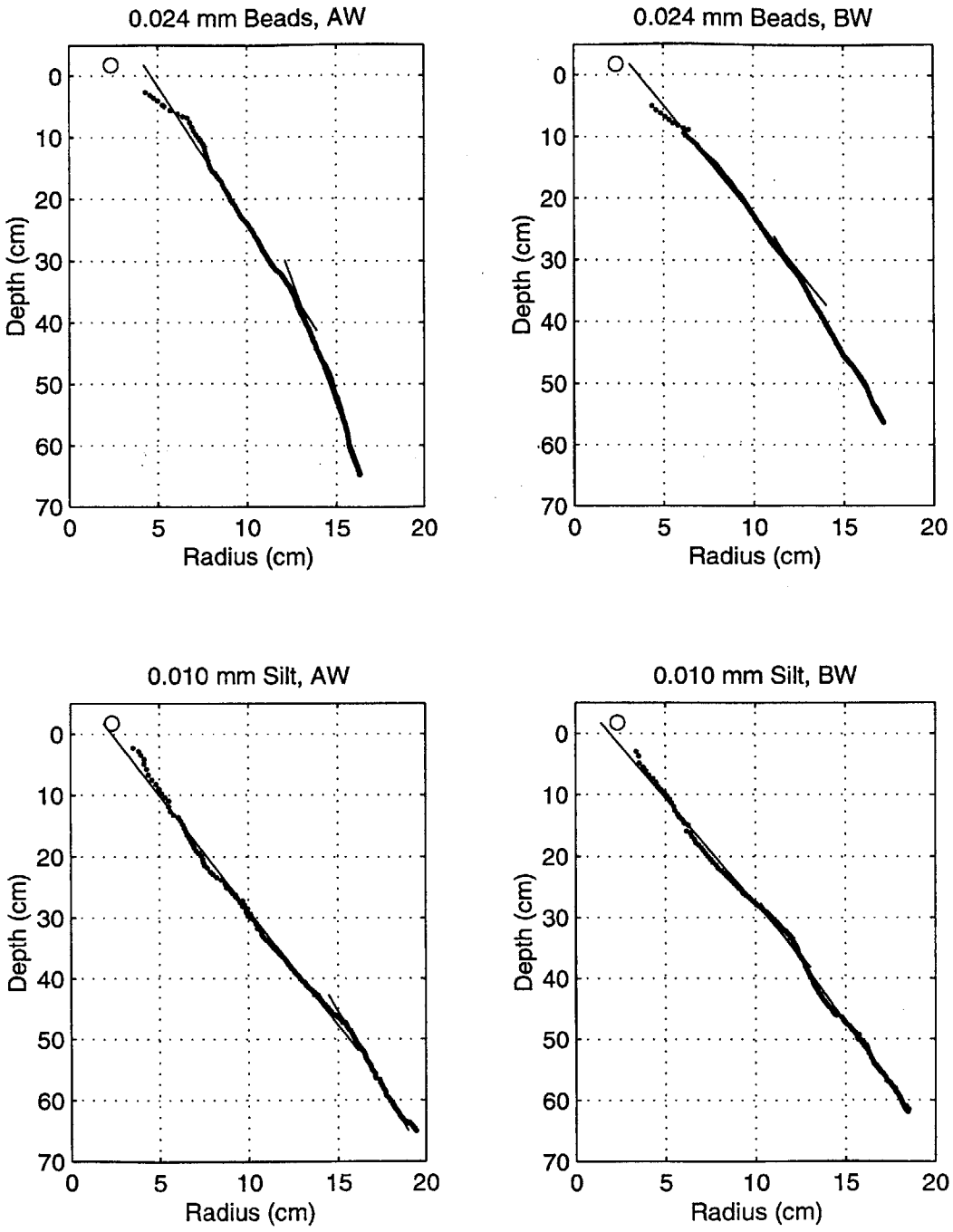

Figure 4-7: Equivalent radius versus center of mass position with fitted linear regression lines - Group III experiments. Open circles denote pre-release radius and center of mass position.

with α_1 and α_2 were less than 0.02 (10 %).

In many cases, the initial linear regression line associated with α_1 can be extrapolated back to the pre-release point (r_o,z_o), shown as open circles in Figures 4.5 - 4.7. In other words, the initial entrainment coefficient (α_0) values, characterizing cloud growth during release/formation, can be approximated by the calculated α_1 values for the well-mixed " thermal" phase. This result is clearly convenient for predictive modeling, as discussed in Chapter 6. For some of the experiments, the first few data points fail to fall on the α_1 linear regression line, suggesting that the clouds have yet to achieve self-similarity. The time corresponding to when the first data point falls on the α_1 line generally coincides with the observed turbulent transition time (t_t).

4.2.2 "Circulating Thermal" Phase

While there is clearly a smooth, continuous transition between the upper and lower portions of the radius versus depth curves and their corresponding α_1 and α_2 values, the curves often show a rather abrupt transition in slope (i.e., sharp kink), suggesting a sudden change in flow regime and related entrainment mechanisms. After evolving into well-mixed "thermals," the particle clouds formed from the 0.264 mm beads eventually organize into elements resembling a vortex ring structure, as can be seen in Figures 4.2 and 4.3, particularly in the 3.0 s and 4.0 s images from the Group I " Wet" experiments. As described in Chapter 2, a vortex ring contains counter-rotating vortices and is shaped like a torus, or doughnut, with a hollow center and cross-sectional radius, a. The vortex ring structure is first recognizable in the 3 s image for experiment "3.18 cm Cyl. Wet" and in the 2 s frame for experiment "4.45 cm Cyl., Wet." The ring is shown more clearly in Figure 4.8, depicting a top view of the "4.45 cm Cyl., Wet." experiment at 4 s. The top view and cross-sectional images show the particles concentrated in the two counter-rotating cores, in which the (negative) buoyancy and vorticity are also concentrated. The particle clouds shaped like a vortex ring are referred to herein as a "circulating thermals," to distinguish them from Turner's buoyant vortex rings, which were produced with an initial circulation, produced by the initial impulse and independent of the initial

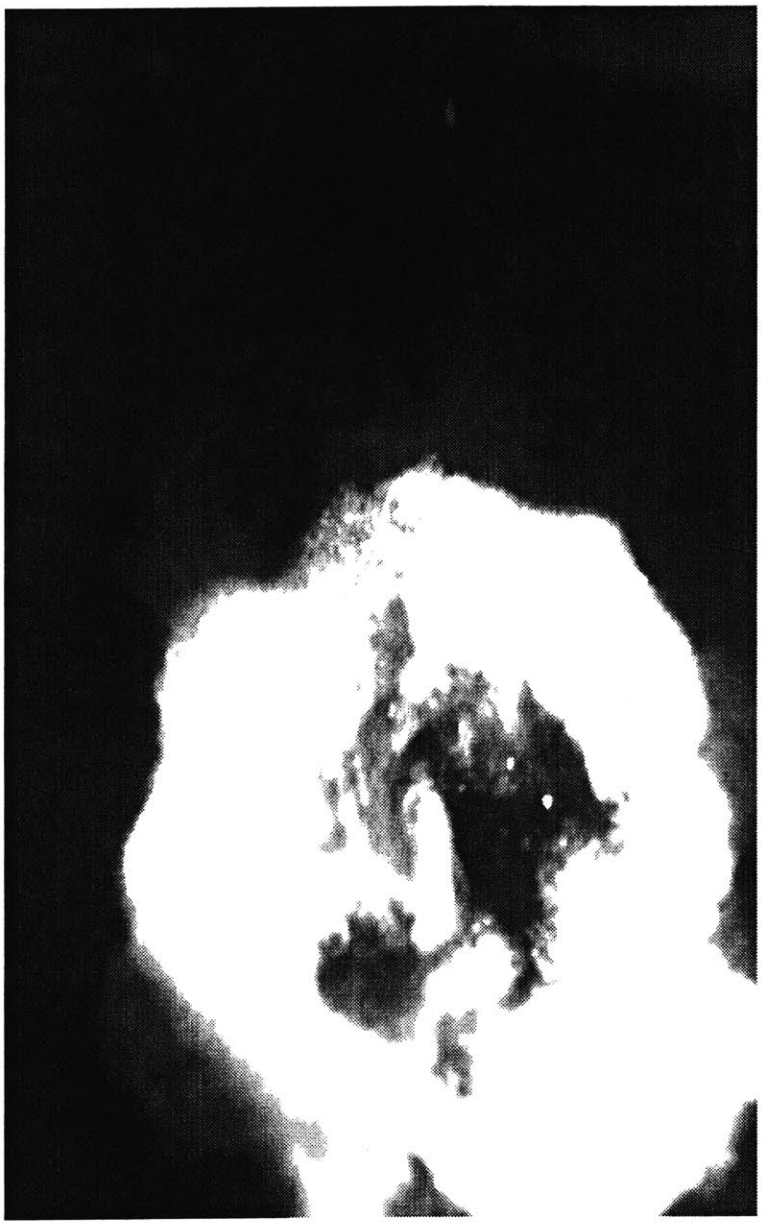

Figure 4-8: Top view of cloud at 4 s - 4.45 cm Cyl. "Wet" experiment.

buoyancy. Thus, the particle clouds are not true vortex rings in the sense that they possess little or no initial circulation, with the bulk of their circulation generated through the buoyancy force.

The intersection of the two regression lines was used as an objective means to identify the time (t_c) and depth (z_c) associated with the transition from well-mixed "thermal" to "circulating thermal", whose values are summarized in Table 4.5. The subscript "c" was used to denote the onset of circulation. The ratios of the cloud radii at times t_c and t_t (i.e., $\frac{r_c}{r_t}$) are also shown in Table 4.5 as well as the ratio of the radius at time t_c to the initial radius (r_o). A frame-by-frame analysis shows the toroidal structure emerging at 2.3 s and 1.3 s for the "3.18 cm Cyl., Wet" and "4.45 cm Cyl., Wet" experiments, respectively, coinciding with the t_c values. Thus, it appears that prior to t_c, the particle clouds behave as classic "thermals," with self-similar buoyancy profiles (i.e., tophat or Gaussian), and after this time evolve into buoyant vortex rings with bimodal buoyancy distributions. As discussed in Chapter 2, using the continuity equation and entrainment assumption, one can show that cloud radius is proportional to depth for both thermals and vortex rings, with constant spreading angles under the assumption of self-similarity, regardless of the buoyancy configuration. The constant entrainment coefficients (α_1, α_2) derived from the measured data appear to support this assumption for the "thermal" and "circulating thermal" phases.

The rather quick transition from well-mixed "thermal" to buoyant vortex ring can be explained in terms of turbulent eddy growth. As initial small-scale eddies engulf ambient fluid, they grow in the outward radial direction as well as penetrate into the cloud's interior. Thus, assuming that the inward growth rate is roughly equal to the outward rate, the eddies arising on opposite sides of the cloud should meet at the cloud's axis of symmetry when the cloud has essentially doubled in size. Excluding the two highest values, a mean value of 2.3 was computed for $\frac{r_c}{r_t}$ for the ten glass bead experiments. With respect to the initial cloud volume, a mean value of 4.3 was computed for $\frac{r_c}{r_o}$ for the ten glass bead experiments. One explanation as to why many of the $\frac{r_c}{r_t}$ ratios are slightly larger than 2.0 is that the inward and outward growth of turbulent eddies is not completely symmetric in the radial direction so that the

cloud is slightly larger than twice its size when the eddies converge in center. Another possibility is that once eddy size approaches the cloud radius, the particles and fluid require a little more time to completely organize into a well-structured vortex ring.

The large $\frac{r_c}{r_t}$ value computed for the "3.18 cm Cyl. Wet" experiment was the result of the initially large aspect ratio ($\frac{H_o}{D_o} = 1.3$), which caused the cloud to elongate for approximately 1.0 s, in turn delaying establishment of the circulation pattern by about the same amount of time. Since only minor slope transitions were observed for the 0.010 mm silt experiments, the existence and location of the "kink" remains in question. The radius versus depth curves for both experiments are rather linear, and both exhibit several small kinks over their entire depths. Hence, the validity of the large $\frac{r_c}{r_t}$ values computed from the selected "kinks" for these experiments must be questioned.

The decrease in growth rate experienced by the particle clouds as they transition from a well-mixed "thermal" to a "circulating thermal" is explained by the stabilizing effect created by the rotating cores in the vortex ring. As Turner (1957) describes, the circulating core stabilizes the motion by preventing material in the core from spreading over the entire moving region, similar to the way stable stratification suppresses the instability of shearing flows in a gravitational field, except that the gravitational force is replaced by the centrifugal force generated by rotation. In other words, in a "circulating thermal" the ability of turbulent eddies to entrain ambient fluid and mix it with interior particles is reduced by the stability of the rotating cores.

As can be seen in Figures 4.2 - 4.4, particle clouds produced with the larger 0.264 mm beads evolved into more organized, laminar-looking circulating thermals compared to the Group III clouds, generated with the smaller-sized beads and silt. As the larger beads became organized into the ring structure, they clearly had a dampening effect on the initial turbulent eddies. One can see that this dampening effect is much less effective with the 0.024 mm particle clouds and still less, or virtually nonexistent, with the 0.010 mm silt clouds. Hence, the 0.264 mm particle clouds formed laminar "vortex rings", while the smaller particle clouds produced turbulent "vortex rings". As noted by Turner (1973), laminar vortex rings tend to have a

constant volume, becoming thinner as the ring expands laterally, whereas in turbulent rings, the cross-sectional radius, a, remains proportional to the ring radius, R. The laminar ring observation appears to also hold true for the particles clouds from the "4.45 cm Wet" experiment in Group I in the "circulating thermal" phase (Figure 4.2).

Using the ratio $\frac{r_c}{r_o} = 4.3$ and $\alpha_1 = 0.25$, the transition depth (z_c) associated with the particle cloud transition from well-mixed "thermal" to "circulating thermal" was estimated for three real-world barge volumes as follows:

- volume = 100 m^3: $z_c = 49.5m$
- volume = 1,000 m^3: $z_c = 107m$
- volume = 5,000 m^3: $z_c = 182m$

4.3 Velocity Analysis

Velocity profiles were generated by computing the slope of the center of mass position versus time curves as described in Chapter 3. The resulting profiles are shown in Figures 4.9 - 4.11 for experimental Groups I - III. The profiles shown in these figures were calculated from the mean center of mass versus time curve of the five repetitions performed for each experiment. The center of mass versus time curve for each of the five realizations is provided in Appendix C. The velocity parameters for the three experimental groups are summarized in Table 4.7. The standard deviations associated with the initial (w_1) (i.e., first measured) and maximum (w_{max}) velocity values are tabulated in Appedix D. Representative profiles depicting the mean and standard deviations of the velocity profiles are also provided in Appendix D. For the majority of experiments, the standard deviations associated with w_1 and w_{max} were less than 10 %. The initial acceleration phase is apparent in all Group I profiles (Figure 4.9), whereas for most of the Group II and III clouds, the first calculated velocity point falls immediately in the deceleration phase. For these latter experiments, the initial acceleration duration, t_a, is less than the release time, t_1. The duration of the initial acceleration phase was extremely short, with a mean t_1 or t_a of 0.25 s calculated for

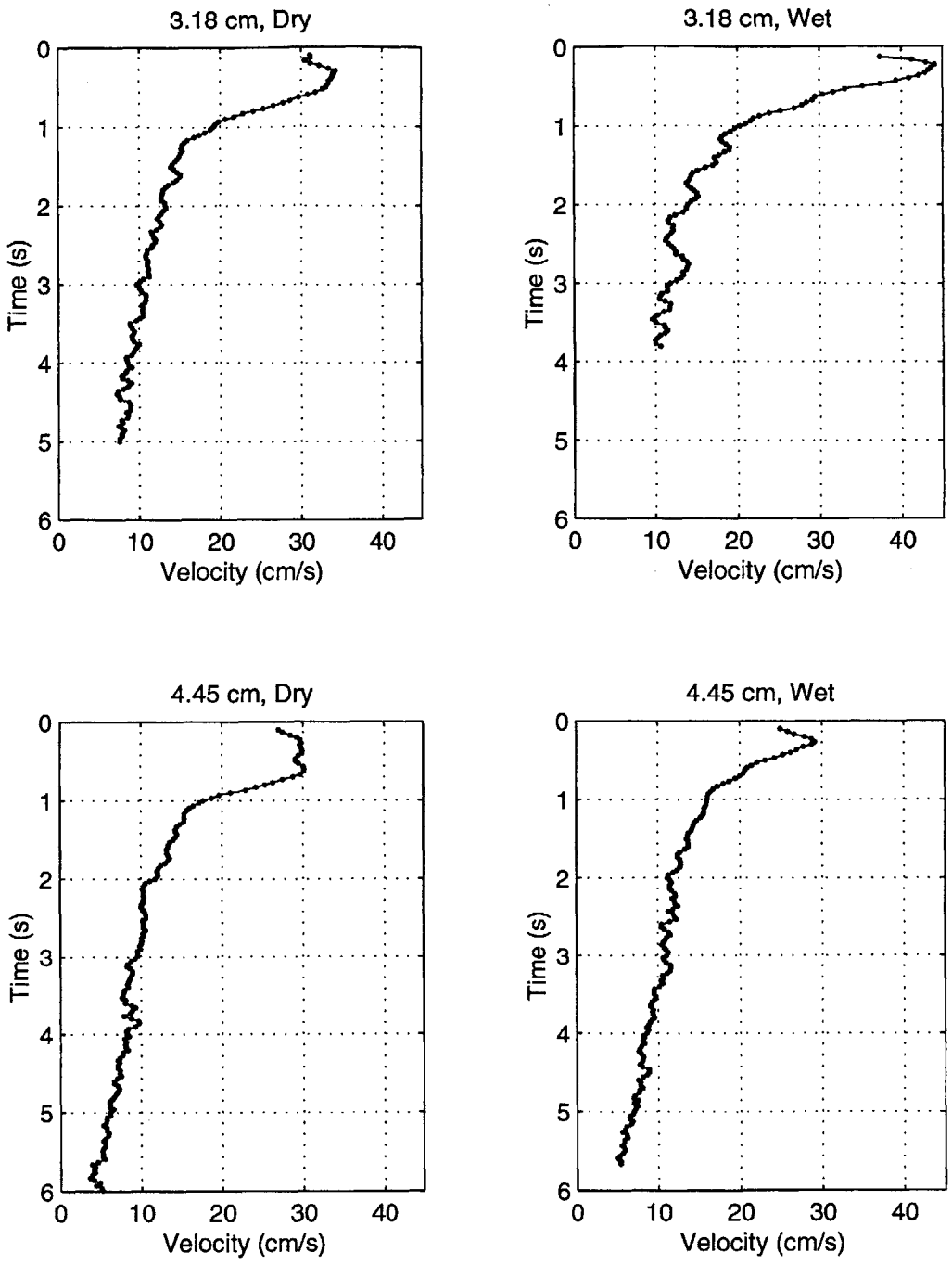

Figure 4-9: Center of mass velocity versus time - Group I experiments.

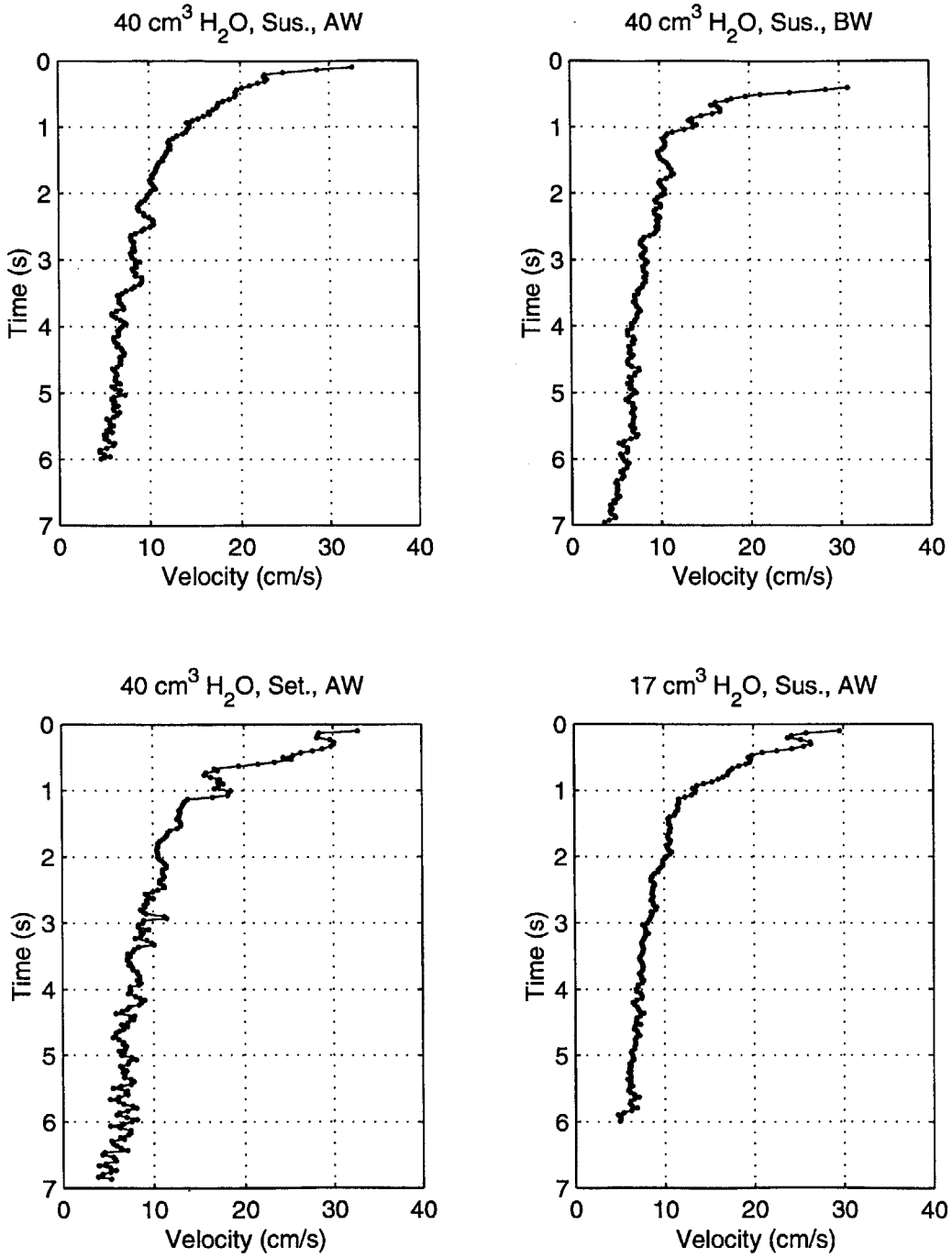

Figure 4-10: Center of mass velocity versus time - Group II experiments.

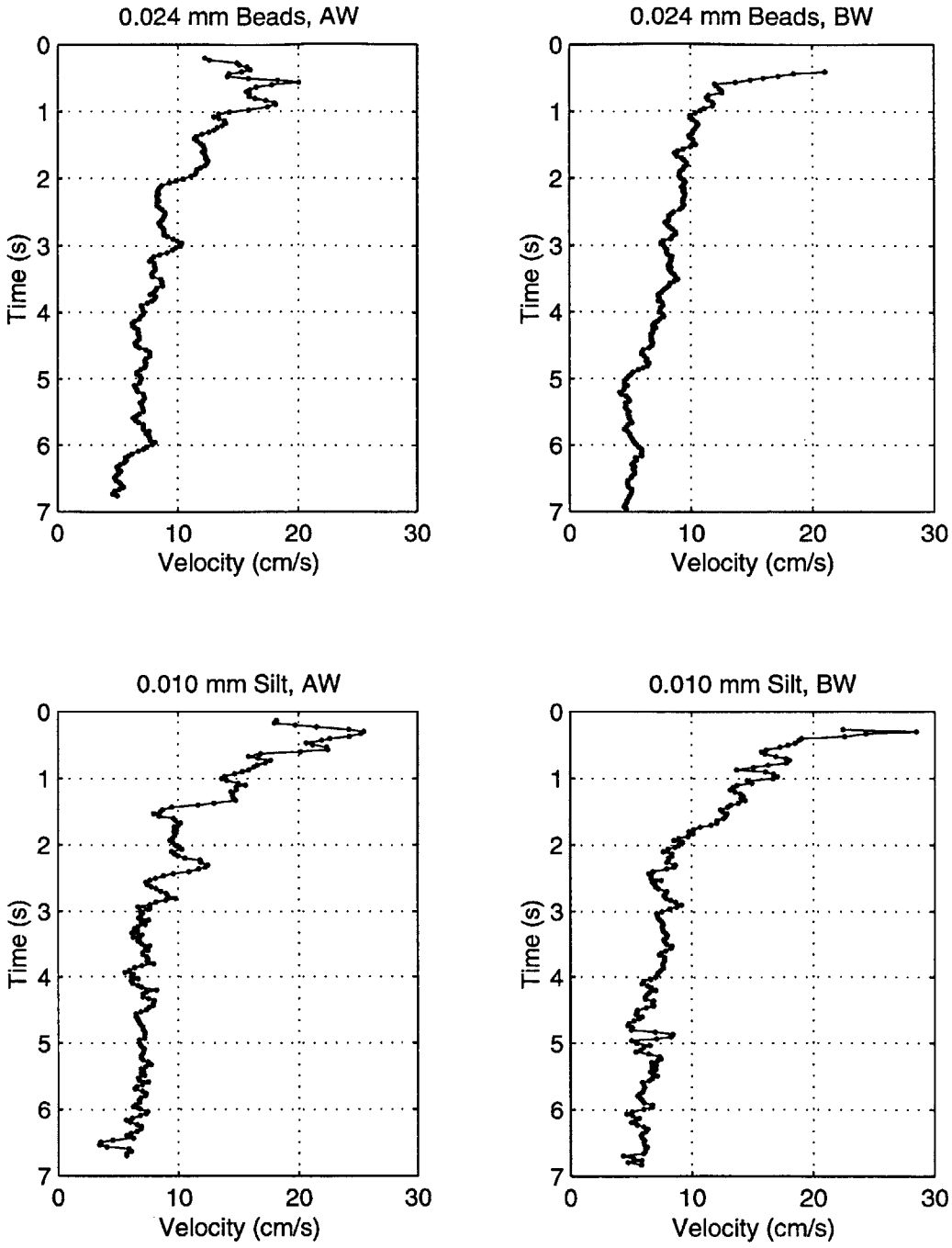

Figure 4-11: Center of mass velocity versus time - Group III experiments.

Experiment	$w_o(\frac{cm}{s})$	$w_1(\frac{cm}{s})$	$w_{max}(\frac{cm}{s})$	$t_a(s)$	$\frac{z_a}{D_o}$	m
Group I Experiments						
3.18 cm Cyl., Dry	82.1	31.1	34.2	0.30	2.1	-0.55
3.18 cm Cyl., Wet	77.1	37.4	44.1	0.23	1.6	-0.53
4.45 cm Cyl., Dry	82.1	27.0	29.9	0.37	2.5	-0.58
4.45 cm Cyl., Wet	77.1	24.9	29.1	0.27	1.5	-0.45
Group II Experiments						
40 cm^3 H_2O, Sus., AW	64.8	32.6	32.6	0.10	0.2	-0.51
40 cm^3 H_2O, Sus., BW	64.8	31.0	31.0	0.40	1.7	-0.46
40 cm^3 H_2O, Set., AW	64.8	32.8	32.8	0.10	0.2	-0.51
17 cm^3 H_2O, Sus., AW	77.1	29.6	29.6	0.10	0.2	-0.48
Group III Experiments						
0.024 mm Beads, AW	64.8	12.2	16.0	0.20	0.6	-0.47
0.024 mm Beads, BW	64.8	21.0	21.0	0.40	1.1	-0.49
0.010 mm Silt, AW	65.0	18.1	25.4	0.30	1.2	-0.47
0.010 mm Silt, BW	65.0	22.4	28.5	0.30	0.8	-0.50

Table 4.7: Velocity parameters – experimental Groups I, II, and III.

the twelve experiments. For scaling purposes, the ratio of the cloud depth measured at t_a, to the initial diameter (d_o) was calculated. As shown in Table 4.7., most particle clouds attained their maximum velocity after traveling a distance of less than two initial cloud diameters, consistent with findings of previous researchers (Escudier and Maxworthy, 1973; Baines and Hopfinger, 1984). The very low $\frac{z_a}{D_o}$ ratios are the result of the initial shape of the particle cloud, which resembles an oblate spheriod with a height to width ratio of about 0.4.

The velocity profiles were plotted on log-log scales to investigate how closely the cloud deceleration rates resemble the theoretical velocity decay rate for a true thermal (i.e., $w \sim t^{-0.5}$). For comparison, the theoretical linear line of slope $m = -0.5$ was superimposed on these profiles, as shown in Figure 4.12. The curves in this figure indicate that once the particle clouds enter the "thermal" phase, their deceleration rate closely resembles that of the true heavy thermal (i.e., dense liquid). Unlike the radius versus depth profiles, no change in slope is evident to mark the transition from well-mixed "thermal" to "circulating thermal," consistent with the fact that buoyant vortex rings also decelerate according to $t^{-0.5}$, as discussed in Section 2.2. The sudden

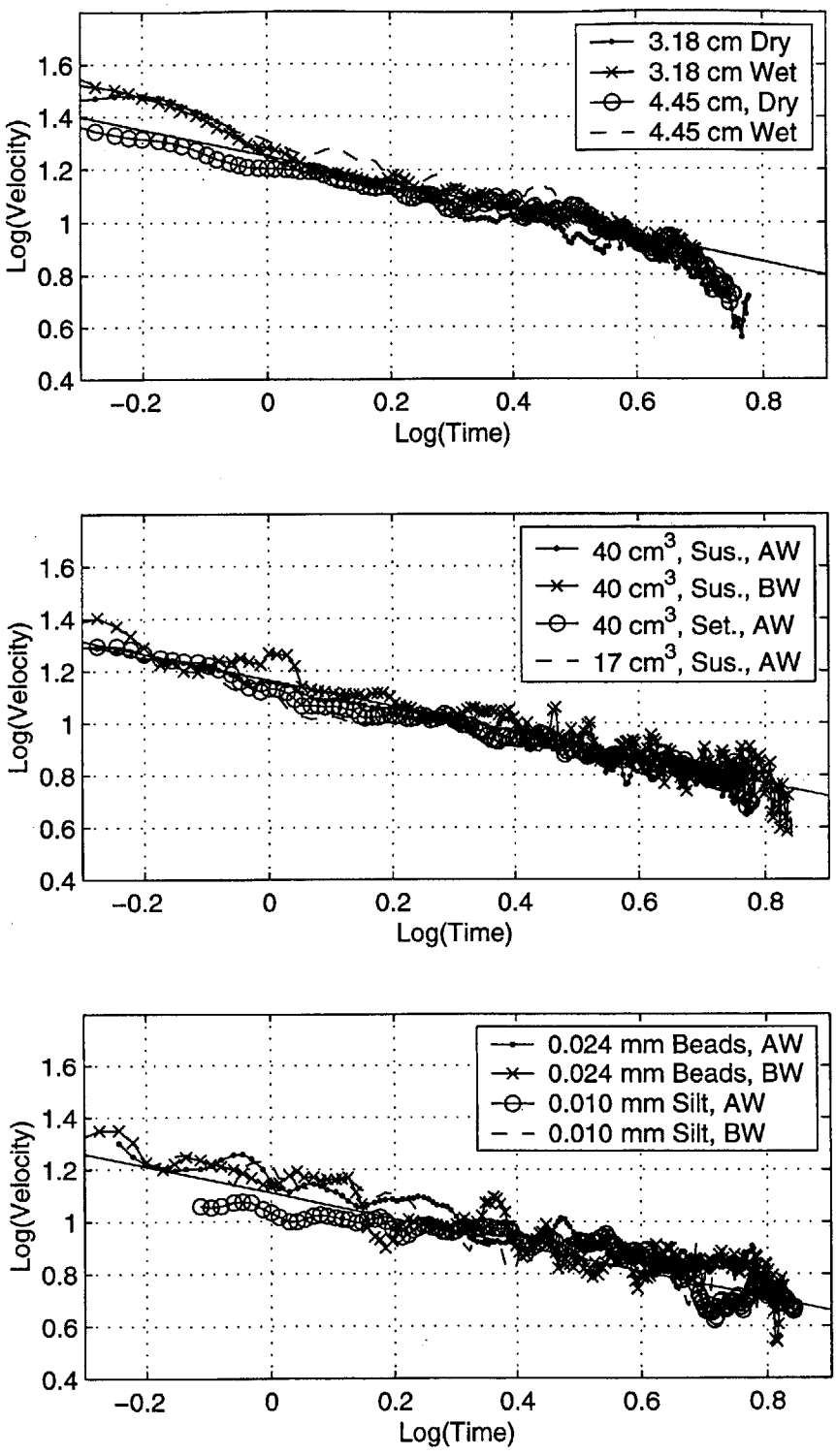

Figure 4-12: Log-log plots of center of mass velocity versus time - experimental Groups I, II, and III. Straight lines are fitted linear regression lines with -0.5 slope.

Experiment	$w_o(\frac{cm}{s})$	$\frac{w_1}{w_o}$	$\frac{w_{max}}{w_o}$	$\frac{w_{1.0s}}{w_o}$	$\frac{w_{2.0s}}{w_o}$
3.18 cm Cyl., Wet	77.1	0.49	0.57	0.264	0.18
4.45 cm Cyl., 4.6 cm AWS	92.5	0.47	0.54	0.29	0.19

Table 4.8: Normalized velocity comparison.

decrease in slope for the Group I clouds at $t = 5.0s$ (i.e., $\log t = 0.7$) is attributed to the settling of particles from the cloud (i.e., beginning of the dispersive phase), in which the particle settling velocity (mean $w_s = 3.2\frac{cm}{s}$) begins to approach the cloud velocity ($w = 7\frac{cm}{s}$). For each experiment, a least squares linear regression line was fit to the measured data falling within the deceleration region. The majority of the slopes of these lines, denoted by "m" and tabulated in Table 4.7, fall close to the -0.5 mark predicted from thermal theory.

Included in Table 4.7 is the characteristic velocity, $w_o = (\frac{B_o}{\rho_a r_o^2})^{0.5}$, derived in Chapter 2. The utility of w_o as a scaling factor can be seen by comparing normalized velocities from the "4.45 cm Cyl., 4.6 cm AWS" Group IV experiment ($B_o = 57,036\ gms^{-2}$) to the "3.18 cm Cyl., Wet" Group I experiment ($B_o = 23,520\ gms^{-2}$), as shown in Table 4.8. The data in Table 4.8 show that the four normalized velocities calculated for the Group I experiment fall within about 10 % of the corresponding Group IV velocities. The small discrepancies may be due to the 30 % difference in initial aspect ratio between the experiments.

4.4 Circulation Analysis

The final characteristic of cloud behavior to be analyzed in this chapter is the circulation (K). As discussed in Section 2.2, the circulation can be calculated via simple dimensional analysis or by integrating the tangential velocity component around a closed circuit containing one of the two rotating cores (as viewed in a two-dimensional cross section) resulting in the following expression:

$$K = \frac{1}{c} wr \tag{4.5}$$

where Turner's (1957) form for the proportionality term $\frac{1}{c}$ has been adopted. As will be discussed, the value of c, referred to herein as the "circulation coefficient," is related to the geometry of the vortex ring, or more specifically, the region in which the bulk of the vorticity is contained. As outlined in Chapter 2, Turner derived the following expression for the entrainment coefficient:

$$\alpha = \frac{B_o}{2\pi c K^2 \rho_a} \tag{4.6}$$

Combining Equations 4.5 and 4.6 and solving for c yields:

$$c = \frac{2\pi\alpha w^2 r^2 \rho_a}{B_o} \tag{4.7}$$

Using Equation 4.7, time-varying values for c were calculated using the equivalent radius, velocity and entrainment coefficient data obtained for the twelve experiments. Time-varying K values were then computed by inserting the coefficient, radius, and velocity data back into Equation 4.5. Two representative plots for c and K are shown in the upper two plots in Figure 4.13 for two of the Group I experiments. The discontinuities shown in Figure 4.13 are the result of using a step function for the entrainment coefficient (i.e., α_1 and α_2). Though small oscillations are present due to experimental "noise," the values of c and K appear to remain relatively constant within the "thermal" and "circulating thermal" phases. However, only data calculated within the "circulating thermal" phase can be considered valid since Equations 4.5 - 4.7 apply only to a vortex ring structure with bimodal distributions of buoyancy and vorticity.

Time-averaged values of c and K within the "circulating thermal" phase were calculated for the twelve experiments, as shown in Table 4.9. "Theoretical" entrainment coefficients, denoted α_{2c} were calculated using Equation 4.6 as shown in Table 4.9. The α_2 values are also included in Table 4.9 for comparison. The K and α_{2c} values included in Table 4.9 were derived using the average value of c for all the experiments

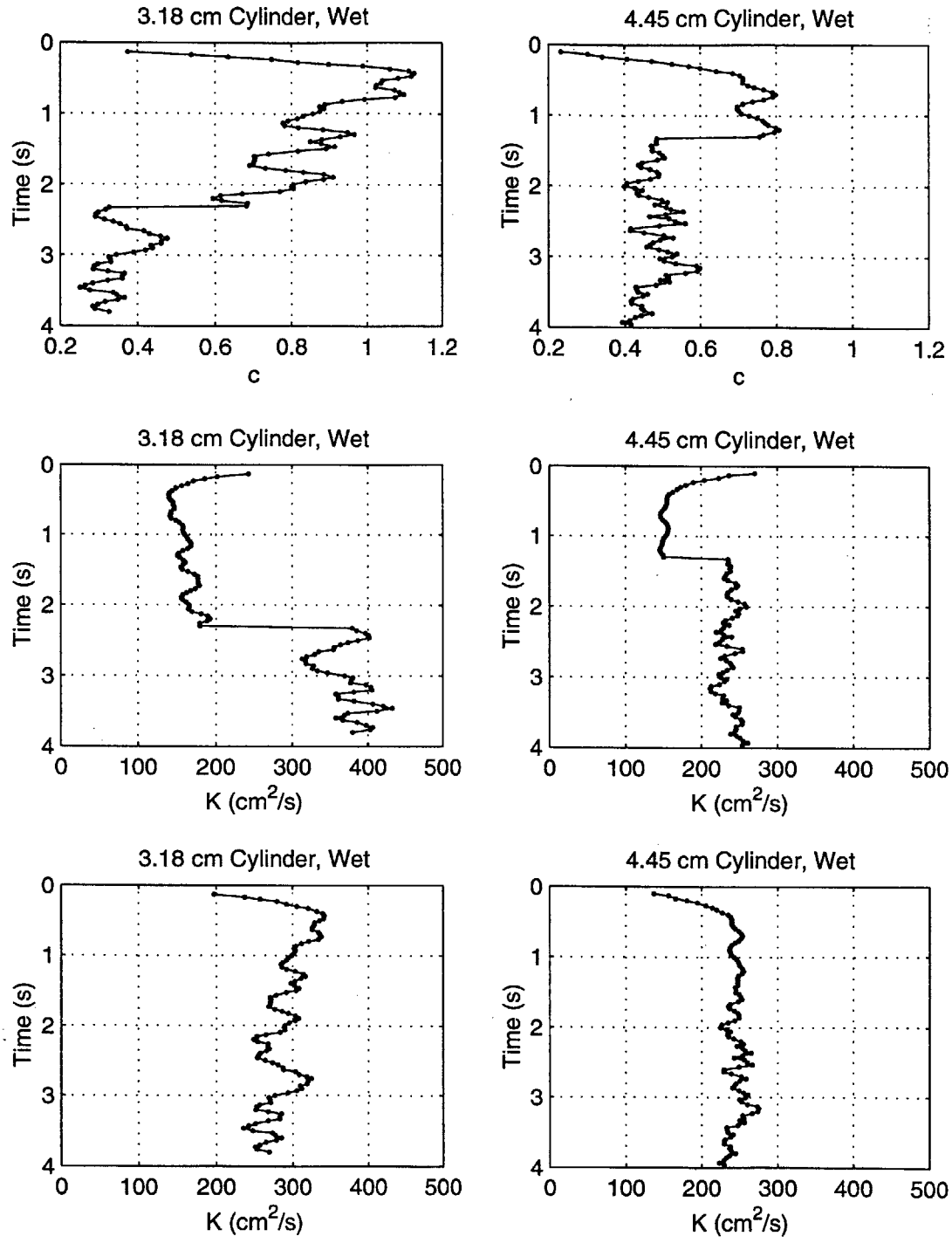

Figure 4-13: Circulation coefficients and circulation versus time - Group I "Wet" Experiments. Middle K plots based on time-varying c; lower K plots based on $c = 0.46$.

Experiment	$t_{th}(s)$	$\frac{z_{th}}{D_o}$	$\bar{c}$	$\bar{K}(\frac{cm^2}{s})$	α_2	α_{2c}
Group I Experiments						
3.18 cm Cyl., Dry	0.30	2.1	0.46	240	0.14	0.13
3.18 cm Cyl., Wet	0.37	3.1	0.38	276	0.08	0.10
4.45 cm Cyl., Dry	0.33	2.2	0.42	216	0.16	0.16
4.45 cm Cyl., Wet	0.37	2.2	0.48	245	0.14	0.12
Group II Experiments						
40 cm^3 H_2O, Sus., AW	0.27	1.1	0.46	202	0.18	0.18
40 cm^3 H_2O, Sus., BW	0.40	1.7	0.37	210	0.18	0.18
40 cm^3 H_2O, Set., AW	0.20	0.8	0.52	231	0.16	0.14
17 cm^3 H_2O, Sus., AW	0.23	1.1	0.51	212	0.19	0.17
Group III Experiments						
0.024 mm Beads, AW	0.43	1.3	0.43	234	0.12	0.14
0.024 mm Beads, BW	0.40	1.1	0.38	183	0.20	0.22
0.010 mm Silt, AW	0.40	1.7	0.66	239	0.20	0.14
0.010 mm Silt, BW	0.67	2.3	0.55	200	0.24	0.20

Table 4.9: Circulation parameters – experimental Groups I, II, and III.

(i.e., $c = 0.46$), since there currently is no a prior means of determining a value of c from the initial conditions. The 0.46 value for c is the mean for the 10 glass bead experiments. The lower two plots in Figure 4.13 show K values calculated using $c = 0.46$. With the exception of the "AW" silt experiment, the calculated α_{2c} values fall within 20 % of the measured α_2 data. Compared to the other experiments, the radius versus depth curves for the five repetitions performed for the "AW" silt experiments exhibited a high degree of variability (see Appendix C), resulting in a standard deviation of 0.08 for the calculated α_2 value.

Circulation versus time plots were developed for all twelve experiments using $c = 0.46$. Representative profiles for two of the Group I experiments are shown in Figure 4.13. Following an initial phase, the circulation remains relatively constant for the life of the particle cloud as it should since $K \sim wr$ and $w \sim t^{-0.5}$ and $r \sim t^{0.5}$. Though K does not have a true physical meaning within the "thermal" phase, the time when K becomes constant can be used to signal the point when the cloud enters this phase and $w \sim t^{-0.5}$ and $r \sim t^{0.5}$ both hold. Thus, the time required for the

product wr to reach a steady-state value can be regarded as the "thermal" formation time (t_{th}). The estimated t_{th} times for the three experimental groups are listed in Table 4.9 along with the corresponding $\frac{z_{th}}{D_o}$ ratios. The range of $\frac{z_{th}}{D_o}$ values (1.1 - 3.1) is slightly higher than the range of $\frac{z_a}{D_o}$ values (0.2 - 2.5) shown in Table 4.7. The mean values of 0.36 s and 1.7 for these parameters are close the values of 0.25 s and 1.6 for t_a and $\frac{z_a}{D_o}$, respectively, suggesting that the assumption of self-similarity at the time of deceleration is more or less valid; i.e., the deceleration and "thermal" phases begin at roughly the same time and depth.

The geometric significance of the circulation coefficient can be seen by equating the right hand side of Equation 4.5 with the integral of the tangential velocity taken around a closed circuit containing one the cores of radius, a , (i.e., $2\pi wa$) to yield:

$$c \sim \frac{r}{2\pi a} \tag{4.8}$$

Hence, c can be viewed as a type of scaling parameter between the overall cloud radius and the core radius. Equation 4.8 was derived under the assumption that the tangential velocity can be approximated by the cloud velocity (w) (i.e., $K = 2\pi wa$), which has not been verified. Under this assumption and using the values of c derived from Equation 4.7, Equation 4.8 was solved for a . In addition, the diameter of the center hole in the vortex ring (D_{hole}) was estimated by:

$$D_{hole} = 2(r_{max} - 2a) \tag{4.9}$$

where r_{max} is the maximum cloud radius.

Using Equations 4.8 and 4.9, a and D_{hole} were estimated for two Group I and two Group II experiments as shown in Table 4.10. Representative images for these experiments, taken at 4 s, are provided in Figure 4.14. Superimposed on these images are vertical lines depicting the diameters of the rotating cores (i.e, $2a$), with the distance between the two inner lines equivalent to D_{hole}. As shown in Figure 4.14, the diameter boundaries associated with the calculated a values essentially align with the width of rotating cores. The "3.18 cm Cyl., Wet" image in Figure 4.14,

Experiment	$a(cm)$	$r_{max}(cm)$	$d_{hole}(cm)$
3.18 cm Cyl., Wet	5.0	11.0	1.0
4.45 cm Cyl., Wet	4.0	13.9	5.9
40 cm^3 H_2O, Sus., AW	4.5	15.6	6.6
17 cm^3 H_2O, Sus., AW	4.2	14.4	6.0

Table 4.10: Predicted geometric parameters for circulating thermals.

showing the poorest agreement between calculated and visual core radii, was actually the most organized of the five repetitions performed for this experiment. The four other realizations resulted in larger, more diffuse cores indicative of the large a and small D_{hole} shown in Figure 4.14.

4.5 Discussion and Summary

Compared to saturated conditions, the release of initially dry particles results in slightly lower entrainment rates in both the turbulent and circulating thermal phases. Air trapped in the pore spaces increases internal friction and decreases turbulence in the first phase and interferes with the circulation of particles in the next phase. The dry particles resulted in clouds that were less organized than the saturated clouds in the circulating thermal region. The trapped air in the initially "dry" clouds appeared to disrupt establishment of the vortical flow pattern, resulting in cores that were less dense and more poorly defined than their "wet" counterparts. In the "wet" clouds, the momentum associated with the inner core of more tightly packed particles appears to serve as a vortex generator by inducing counter rotation as it falls through the outer, less dense layers of the cloud. The net result was a well-organized vortex ring structure with a high degree of circulation (average $\bar{K} = 261\frac{cm^2}{s}$) and lower entrainment coefficient in the circulation phase. In contrast, the air trapped in initially dry beads prevents organization of the particles, reducing the amount of circulation generated (average $\bar{K} = 228\frac{cm^2}{s}$) and increasing the spreading rate. Hence, on average, there was only a 24 % difference between α_1 and α_2 for the "dry" experiments compared

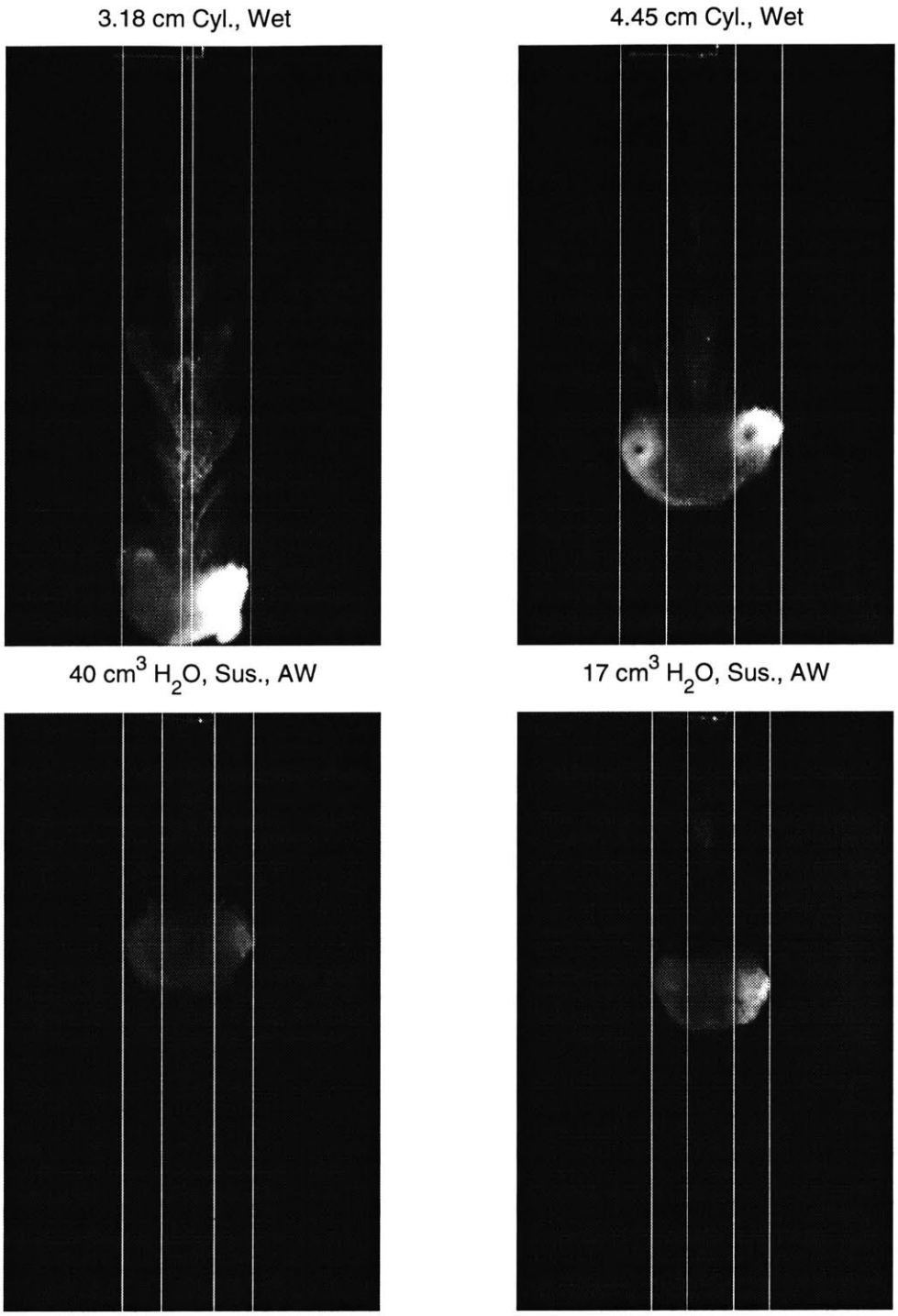

Figure 4-14: Predicted vortex ring core and hole diameters superimposed on selected cloud images at 4 s.

to a 58 % difference for the "wet" experiments.

The addition of excess water appears to have a similar effect on cloud behavior in that it lowers circulation and increases the entrainment. For example, for the 0.264 mm glass bead experiments, the average α_2 and $\bar{K}$ values for the three initially suspended bead experiments were 0.18 and 208 $\frac{cm^2}{s}$, respectively, compared to 0.13 and 251 $\frac{cm^2}{s}$ for the three settled bead experiments. Suspending the beads by stirring also enhanced the initial amount of turbulence and associated entrainment rate, increasing the value of α_1 by 25 %. The growth rates and velocity profiles for the "40 cm^3 H_2O, Sus., AW " and "40 cm^3 H_2O, Set., AW " experiments were very similar (i.e., within 15 %), suggesting that the same amount of excess water, whether initially mixed with the beads or present as a supernatant, became incorporated into the cloud as the material entered the ambient water. The amount of excess water that becomes incorporated into the cloud was investigated using a silt tracer, as discussed in Chapter 5.

Only minor variations in particle growth rates were observed due to changes in initial momentum resulting from differences in the potential energy associated with initial height of material above the water surface. For the three pairs of "AW \BW" experiments included in Groups II and III, releasing the particle slurry above the water surface lowered α_1 by 6 - 18 % compared to the "BW" experiments. This decrease in α_1 appears to be due to the fact that the clouds possessing initial momentum travel slightly farther than those without initial momentum in the same amount of time, resulting in a larger Δz. No trends in α_2 were observed for the "AW/BW" pairs of experiments, suggesting that the clouds have lost all memory of their initial momentum by the time they have entered the "circulating thermal" phase.

The data for the Group IV experiments (Table 4.6) reveal the same trend in α_1 as observed in the other "AW/BW" experiments. That is, providing the clouds with an initial impulse results in a slightly lower entrainment coefficient in the thermal phase (about 25 % lower in this case) compared to releasing the material from rest. The data for the Group V experiments (Table 4.6), as well as the "4.45 cm Cyl., Wet" Group I experiment ($\frac{H_o}{D_o} = 0.5$) indicate that the release geometry (i.e., $\frac{H_o}{D_o}$)

N_c	$d_s(cm)$	α_1	α_2
$4x10^{-2}$	0.2640	0.28	0.18
$7x10^{-4}$	0.024	0.264	0.16
$5x10^{-5}$	0.010	0.28	0.22

Table 4.11: Entrainment coefficient comparison based on N_c.

has a minor effect (i.e., < 15 %) on entrainment rates. The larger α_1 and α_2 values calculated for the "$\frac{H_o}{D_o} = 2.6$" experiment most likely resulted from the fact that the beads in the narrowest cylinder required a substantially longer release time than they did with the wider cylinders (i.e., 0.4 s versus. 0.17 s), significantly reducing the initial momentum.

The influence of particle size, or cloud number (N_c), on cloud growth rates can be seen in Table 4.11, in which the average α_1 and α_2 values are compared for the three pairs of "AW/BW" experiments using the 0.264 mm, 0.024 mm, and 0.010 mm particle sizes. The particle clouds produced with the larger glass beads differed in appearance from the 0.024 mm bead and 0.010 mm silt clouds, in that they possessed smaller "stems" and evolved into more organized, laminar vortex ring structures. The "stem" of particles associated with these particle clouds will be discussed in Chapter 5. Despite these differences, there appears to be no statistical difference between their corresponding entrainment coefficients given their standard deviations, which ranged from $\pm$ 0.02 to $\pm$ 0.08 (see Appendix D.1). Thus, these results suggest that the basic entrainment mechanisms for the three particle sizes are similar.

Chapter 5

Sediment Trap Experiments

Using the sediment trap apparatus described in Section 3.2, a series of experiments was conducted to evaluate particle stripping mechanisms associated with convective descent. Three general types of experiments were performed. The first experimental group involved the release of well-mixed suspensions of different particle sizes from above and below the water surface ("AW" and "BW"). The second group involved releasing initially "dry" and "wet" settled 0.264 mm beads from above the water surface. The third group of experiments consisted of an "AW" and "BW" release of 0.264 mm beads in which the beads were mixed with excess water and allowed to settle prior to release, producing an initial "supernatant" layer of fluid on top of the beads. Results from the three suites of experiments are discussed in Sections 5.1 - 5.3 with conclusions summarized in Section 5.4.

5.1 Suspended Particles

5.1.1 Quantification of "Stem" Particles

The objective of this group of experiments was to investigate the influence of particle size, or cloud number (N_c), and initial potential energy ("AW" versus. "BW") on particle stripping mechanisms. As with the experiments discussed in Chapter 4, five repetitions were performed for each experiment. The following four particle sizes and

associated initial cloud numbers were used:

- 0.010 mm silt ($N_c = 1$ x 10^{-4})
- 0.024 mm beads ($N_c = 7$ x 10^{-4})
- 0.129 mm beads ($N_c = 2$ x 10^{-2})
- 0.264 mm beads ($N_c = 5$ x 10^{-2})

For each experiment, 40 g of particles were mixed with 40 cm^3 of water and agitated prior to release. The 4.45 cm release cylinder was used for all experiments in this group, which was positioned either immediately above the water surface("AW") or below the water surface ("BW") so that the top of the particle suspension was flush with the water surface. For each experiment, the sediment trap was positioned at either a shallow depth (i.e., 13.3 cm below release cylinder) or deep depth (i.e., 34.3 - 36.8 cm below release cylinder). The slight variation in trap positions for the deeper depth was due to knot slippage in the ropes suspending the trap, which occurred over the 5-day experimental period. The two trap depths were used to evaluate the time variation of particle concentration in the stem. In other words, to determine whether the stem was gaining particles (i.e., by detrainment from the cloud) or losing particles (i.e., by re-entrainment into the cloud) as the cloud descended.

For most of the suspended releases discussed in Chapter 4, a plume, or "stem"of particles attached to the cloud can be observed, as shown in Figures 4.3 and 4.4. The objective in each experiment was to isolate as much of this "stem"as possible from the main cloud without disturbing or "chopping off" any of the particles near the rear of the cloud. Hence, the entire clouds were allowed to pass through the trap before the stem was separated by closing the trap curtain. This procedure resulted in separation points located approximately 1.1 - 1.3 cloud diameters above the leading edge of the cloud. To ensure proper closure time, all experiments were recorded to verify the precise time of trap closure using the fluorescent trap flag, as described in Section 3.2. The curtain was closed 1.2 - 1.5 s after release for the shallow trap depth and 4.0 - 5.1 s after release for the deep depth. Figure 5.1 includes sample images

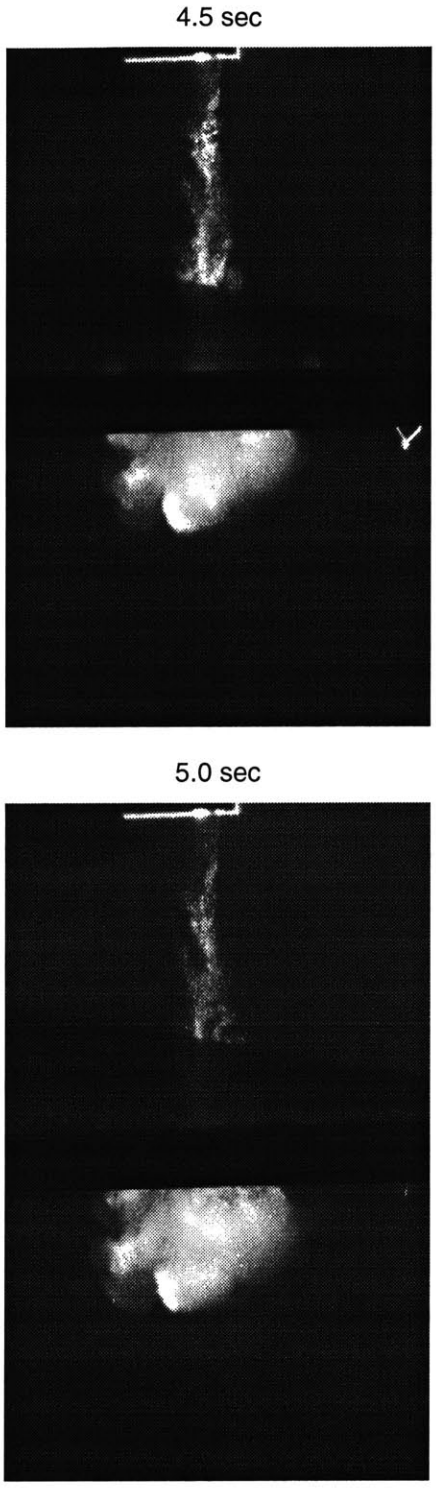

Figure 5-1: Before and after images of 0.264 mm particle cloud descending through sediment trap.

Trap Depth/Closure Time (cm)/(s)	0.010 *mm*	0.024 *mm*	0.129 *mm*	0.264 *mm*
	"AW" Experiments			
13.3 / 1.2 - 1.5	7.9 $\pm$ 2.7 %	5.8 $\pm$ 4.4 %	5.7 $\pm$ 1.1 %	1.6 $\pm$ 0.4%
34.3 / 4.0	3.5 $\pm$ 0.7 %	–	–	–
	"BW" Experiments			
13.3 / 1.2 - 1.6	22 $\pm$ 7 %	21 $\pm$ 5 %	31 $\pm$ 7 %	21 $\pm$ 5 %
34.3 - 36.8 / 4.4 - 5.1	8.4 $\pm$ 1.2 %	13 $\pm$ 3 %	18 $\pm$ 4 %	9.2 $\pm$ 1.8 %

Table 5.1: Sediment trap results – suspended particle experiments. Trap depth denotes elevation of sediment trap. Closure time denotes time shade was drawn after release of particles. Percentages denote mass of "stem" particles retained on shade expressed as the percent of original mass.

from one of the 0.264 mm particle cloud experiments showing the cloud descending through the trap as well as the presence and disappearance of the trap flag before and after closure of the curtain. The release apparatus was removed from the top of the tank approximately 10-15 s following release of the particles. Following closure of the curtain, the trap was removed from the tank after waiting approximately 3 - 5 minutes to ensure that the stem of particles had collapsed onto the trap curtain. The mass of particles retained on the curtain was subsequently measured as described in Section 3.2.

All particle sizes were released "AW" and "BW" with the trap located at the shallow (13.3 cm) depth (i.e., eight experiments). For the deep trap experiments, only the 0.010 mm silt suspensions were released from both "AW" and "BW" positions. The larger beads were released only from below the water surface, resulting in a total of five experiments at this trap depth. The results of all thirteen experiments are summarized in Table 5.1. The percentages shown represent the percent of original mass of solids (40 g) retained on the curtain. The data in Table 5.1 represent the mean value of the five repetitions conducted for each experiment. Standard deviations for each experiment are included in Table 5.1.

When experimental variability indicated by the standard deviations is taken into account, little trend in the data is discernible with respect to particle size or cloud number (N_c). The percentages of particles retained on the curtain for the four particle

sizes essentially fall within the same range for a given trap depth and release condition. The one exception is the 0.264 mm bead "AW" experiment for which only 1.6 % of the original material was captured on the trap. The discrepancy here is attributed to the very short release time (0.1 s) for this experiment compared to 0.2 - 0.4 s for the other releases. Unlike the smaller glass beads and silt, the 0.264 mm beads did not cling to the cylinder side walls, allowing them to accelerate very rapidly when released above the water surface. Thus, the entry speed and associated release time appear to have played a dominant role in determining how much of the initial material made it into the cloud during release and formation. Averaging results from the three smaller particle sizes, one finds that approximately 25 % of the initial material failed to become incorporated into the cloud when it was released below the water surface compared to only 6.5 % when released in the "AW" position. The average release time for the "BW" experiments was 0.36 s compared to 0.18 s for the "AW" releases.

To verify that the percentage of material in the "stem" was independent of N_c, one additional sediment trap experiment was conducted in which 20 g of the 0.010 mm silt and 20 g of 0.264 mm beads were released below the water surface ("BW"). As with the other "suspended" experiments, 40 cm^3 of water was added to the particles and the mixture stirred prior to release. The sediment trap was positioned 34.3 cm below the water surface, and the shade was closed 5 s after release. The quantities of 0.010 silt and 0.264 mm beads retained on the shade, expressed in terms of mass retained and percent of original mass (shown in parentheses), are shown below:

- 0.010 mm silt: 1.78 g (4.5 %)
- 0.010 mm beads: 1.75 g (4.4 %)
- Total: 3.53 g (8.8 %)

As shown above, the measured distribution of silt and beads in the "stem" was almost identical to the original silt/bead ratio in the pre-released material. This result suggests that the cloud and "stem" are well-mixed, and that there are no size-dependent "stripping" mechanisms associated with either the "parent" cloud or

"stem" that would cause fine particles to detrain from larger particles descending within either of these elements.

Comparison of the shallow (1.2 - 1.5 s) and deep (4.0 - 5.1 s) sediment trap results (Table 5.1) indicates that a large percentage of the material contained in the "stem" eventually "caught up" to the cloud and became re-entrained. For the "BW" releases, an average of 24 % of the original solids mass was retained on the shallow trap compared to 12 % on average on the deep trap. The same trend is evident for the "AW" releases for the 0.010 mm silt slurries in which the percentage decreased from 7.9 % to 3.5 %. Hence, after the cloud descended a distance equivalent to about seven initial diameters, about half of the material that failed to make it into the cloud upon formation had sufficient density and momentum to catch up to the main cloud. The narrow "stem" of particles trailing behind the cloud, with its small frontal area, experienced less drag and lateral growth than did the main cloud. In addition, the circulation set up by the main cloud helped to advect the "stem." The "stem" therefore decelerated at a slower rate than the cloud enabling the material closest to the cloud to become re-entrained.

5.1.2 Mass Distribution of Particles in "Stem"

To determine the distribution of particles within the "stem" of the 0.010 mm silt "BW" experiment from an Eulerian standpoint, four experiments were conducted in which the sediment trap was positioned at four different depths(13.3 cm, 20.3 cm, 27.9 cm, and 34.3 cm), as shown in Figure 5.2. In each experiment, the trap curtain was closed after 4.4 s to investigate how the total 8.4 % (3.35 g) of material not incorporated in the cloud at $t = 4.4s$ (see Table 5.1) was distributed in the "stem" as well as in the release cylinder. The results of these experiments are provided in Table 5.2.

As shown in Table 5.2, an estimated 0.7 g of material remained in the cylinder after 4.4 s. To determine how quickly material was discharged from the release cylinder, a set of experiments was performed in which the cylinder trap door was closed at various times following release of silt suspension. The closed cylinder was then removed from

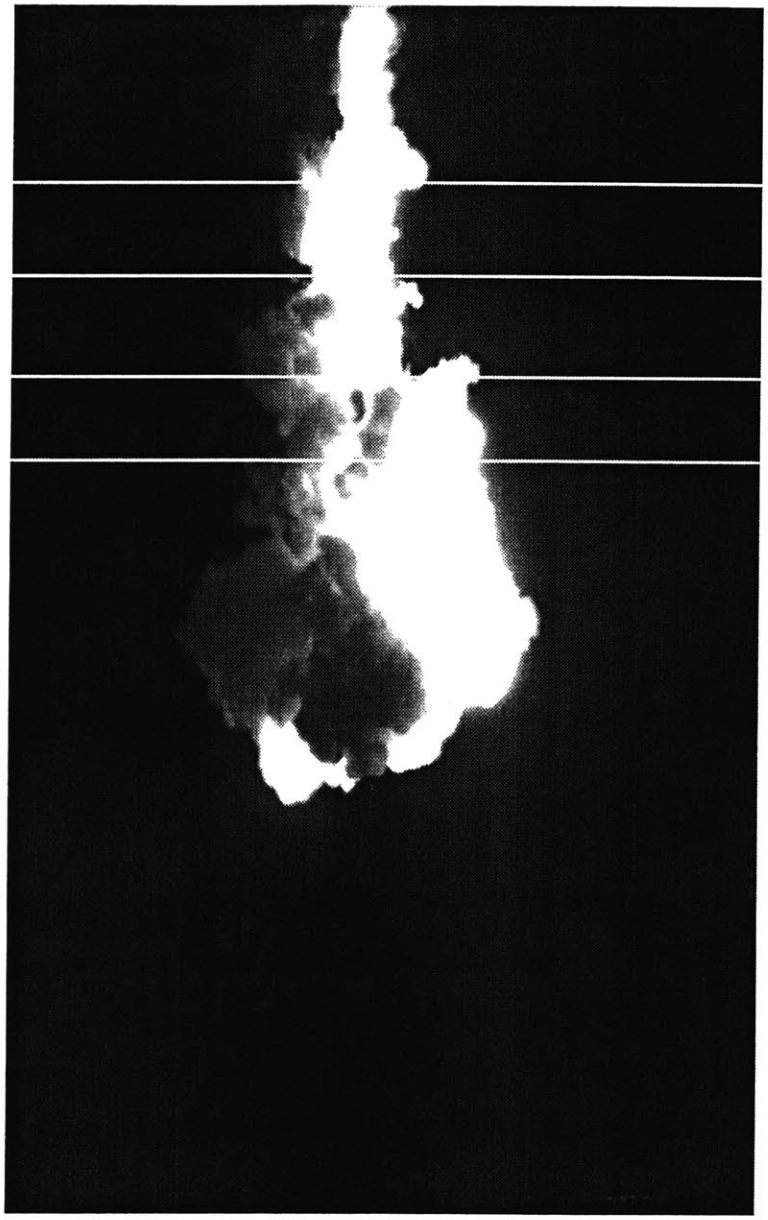

Figure 5-2: Sediment trap locations for determining "stem" mass distribution for 0.010 mm "BW" silt experiment.

Depth Interval	*Mass (g)*	*Percent*	*Mass/Depth (g/cm)*
< 0 cm (Cylinder)	0.7	1.8	–
0.0 - 13.3 cm	0.9	2.3	0.068
13.3 - 20.3 cm	0.8	2.0	0.114
20.3 - 27.9 cm	0.5	1.3	0.066
27.9 - 34.3 cm	0.4	1.0	0.063

Table 5.2: Mass distribution in "stem" – 0.010 mm silt "BW" experiment. Percent values denote the amount of mass contained within the depth interval relative to the total mass in "stem."

the water and the isolated mass of particles measured. This set of experiments was also conducted using the larger 0.264 mm glass beads. The results of both sets of experiments are plotted in Figure 5.3 along with fitted exponentially decaying functions extrapolated back to the original mass at time zero (40 g). As shown in Figure 5.3, the glass bead suspension was released from the cylinder at a much faster rate than the silt slurry, which tended to cling to the cylinder side walls. Approximately 8 g of silt remained in the cylinder after 1 s compared to 2 g of glass beads at this time.

The data in Table 5.2 indicate that at time $t = 4.4s$, the distribution of mass over the length of the "stem" was nearly uniform. This result appears to contradict the image in Figure 5.2, depicting a wider stem near the cloud, as well as the exponential release of material shown in Figure 5.3, suggesting that the concentration of particles in the stem should decrease with distance away from the cloud. This apparent inconsistency can be explained by examining the behavior of motion occurring at opposite ends of the "stem" from a Lagrangian viewpoint. As the cloud descended, material towards the front of the "stem," possessing an appreciable amount of momentum, caught up to and became re-entrained into the cloud, as suggested by the shallow and deep sediment trap data in Table 5.1. At the same time, new material, possessing less momentum, was fed into the rear of the "stem" from the release cylinder. Thus, as time progressed, the particle concentration profile within the "stem" changed from one that initially increased with depth (e.g., before 1 s) to a more uniform (i.e.,

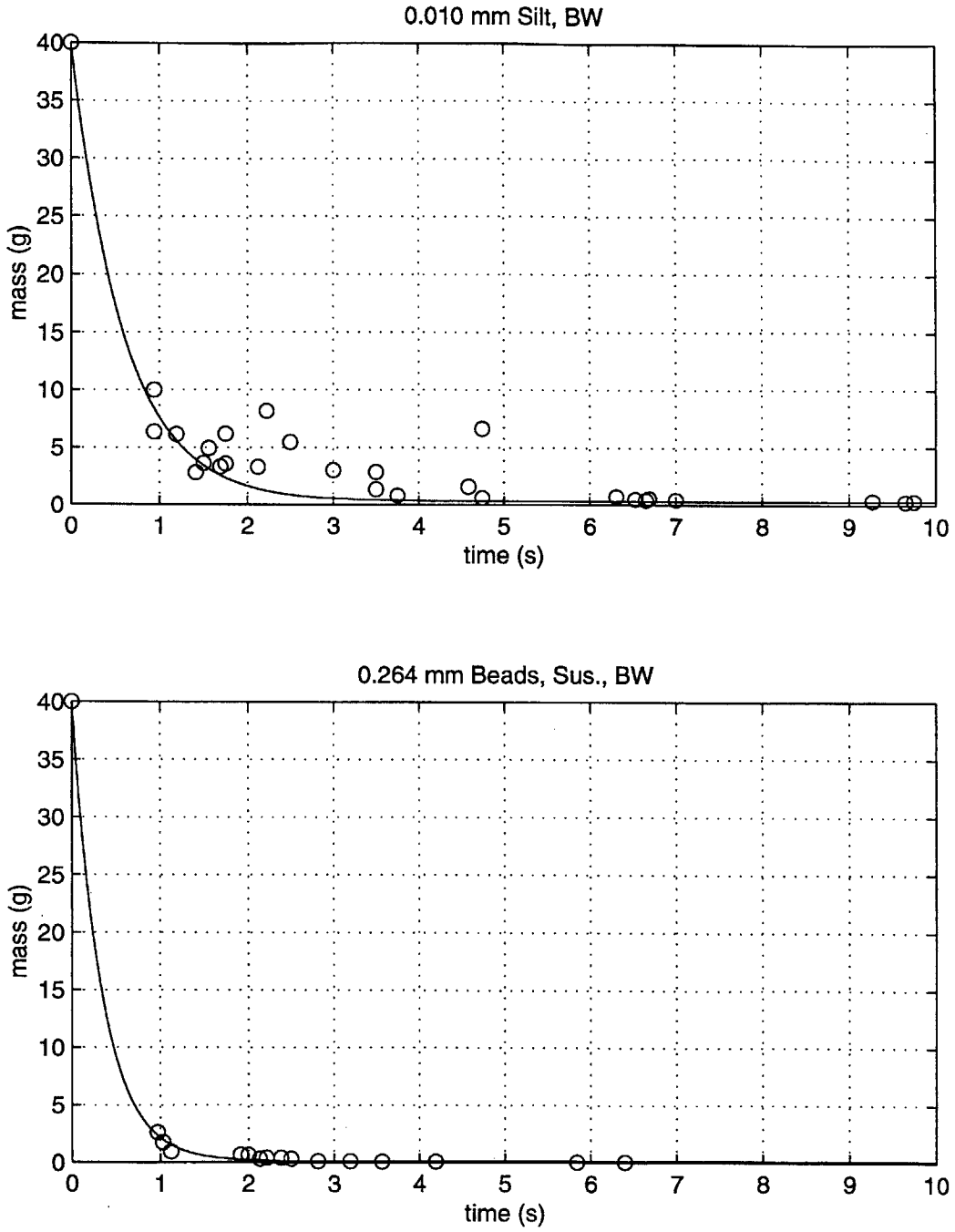

Figure 5-3: Time-variation of particle mass remaining in release cylinder for 0.010 mm silt and 0.264 mm bead "BW" experiments. Open circles denote measured data. Solid lines show fitted exponentially decreasing functions.

constant) profile (e.g., after 4 s).

The fact that particles near the front of the stem fell faster than those near the rear caused the portion of stem nearest to the cloud to thin out, as particles were re-entrained, eventually resulting in the detachment of the upper portion of the "stem" from the main cloud. This process is evident in the images shown in Figure 5.4 for the 0.264 mm glass bead experiment. The horizontal lines in Figure 5.4 represent the approximate location of the the shallow and deep sediment trap positions. The light intensity from the larger glass beads appears to give a truer indication of particle concentration than does the intensity generated by the 0.010 mm silt, which contained a small fraction of fine colloidal material as well as the rhodamine 6G dye added to the initial suspension. The light intensity of the large glass beads rapidly diminishes with decreasing concentration. In contrast, there is no correlation between the concentrations of silt particles and associated light intensity. For this reason, it is quite possible that the lower "fat" portion of the silt "stem" shown in Figure 5.2 contained a smaller amount of particles than the upper portion, consistent with the sediment trap findings.

The "thinning out" of the lower portion of the "stem" (Figure 5.4, 3 s image) reveals the separate, secondary plume of particles falling behind the cloud. Formation and detachment of this secondary plume may have resulted from, or at least be influenced by, the flow of water around the cloud after the initial slug of material had exited. Water initially displaced by the main slug flowed back around the rear of the descending cloud with upward velocity components, mixing with the "stem" material and retarding its descent. For the "BW" releases, the displaced water may have actually swept some of the particles back into the release cylinder, while for the "AW" releases, the material was simply pushed towards the water surface. This process may explain the secondary release of particles that is observed exiting the cylinder from about 0.2 - 0.5 s. Example images depicting the "head" of the secondary plume, just after emergence from the cylinder, are provided in Figure 5.5. In each image, the plume "head" can be identified by noting the roundish mass of material located directly above the contraction in the "stem."

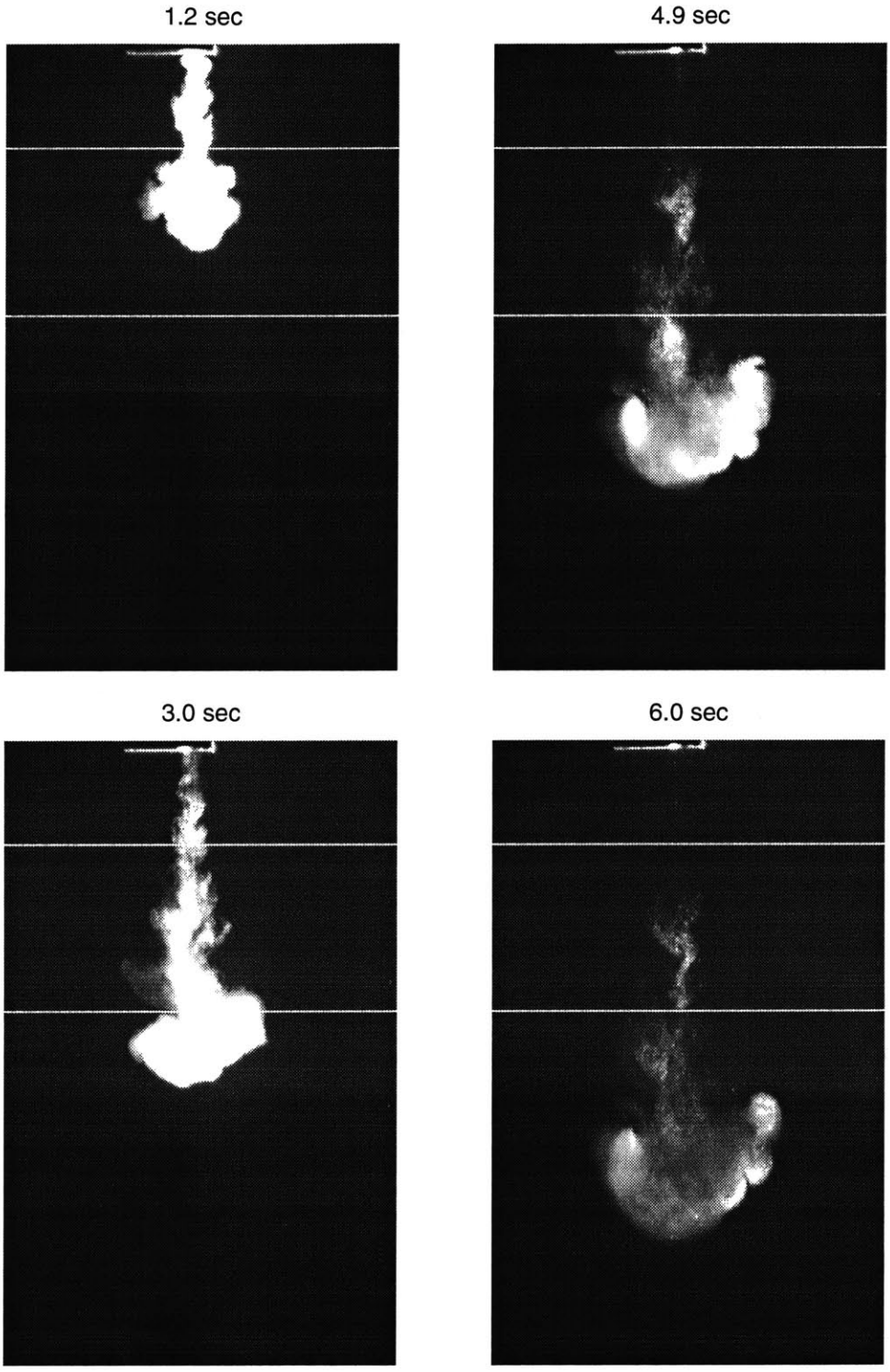

Figure 5-4: Selected images from 0.264 mm bead "BW" experiment showing shallow and deep sediment trap locations.

Time Interval (s)	*Silt Cloud*	*Silt "Stem"*	*Bead Cloud*	*Bead "Stem"*
1.5 - 2.0	10.6	5.0	10.0	8.1
2.0 - 2.5	9.3	6.7	8.8	7.6
2.5 - 3.0	8.4	5.7	8.0	7.9
3.0 - 3.5	7.8	5.5	7.3	7.4
3.5 - 4.0	7.2	5.7	6.8	8.6
4.0 - 4.5	6.8	6.2	6.4	7.4
4.5 - 5.0	6.4	5.2	6.1	8.1
5.0 - 5.5	6.1	6.0	5.8	8.3
Mean $\pm$ Std. Dev.	5.8 ± 0.5	7.9 ± 0.4	–	–

Table 5.3: Comparison of cloud center of mass velocity and secondary plume leading edge velocity for 0.010 mm silt and 0.264 mm bead "BW" experiments. Units for all velocities are $\frac{cm}{s}$.

The leading edge velocities of the secondary plumes formed from the "BW" 0.010 mm silt and 0.264 mm bead releases were estimated by manually determining the leading edge position at 0.5 s intervals. As shown in Figure 5.5, the secondary plume is quite discernible in the 0.264 mm bead experiments. Identification of the leading edge of the plume in the silt experiments was more difficult; however, the approximate location of the leading edge could be determined in one of the five repeated experiments. Four representative images from this "BW" silt experiment are included in Figure 5.6, with the approximate leading edge location indicated by the superimposed horizontal lines. The estimated leading edge velocities of the secondary plumes associated with the 0.010 mm silt and 0.264 mm bead experiments are compared to the "smoothed" mean center of mass velocities for their respective "parent" clouds in Table 5.3. The "smoothed" cloud center of mass velocities shown in Table 5.3 were derived by fitting a smooth curve to the measured data (i.e., $w = 14.0t^{-0.5}$ for 0.010 mm silt and $w = 13.2t^{-0.5}$ for 0.264 mm beads). As shown in Table 5.3, by 1.5 s, each secondary plume has apparently reached a fairly constant terminal velocity which eventually exceeds that of the main cloud (e.g., after 6 s for 0.010 mm silt cloud after 3 s for 0.264 mm bead cloud), allowing it to ultimately catch up and become re-entrained (at approximately 23 s for 0.010 mm silt cloud and 11 s for 0.264 mm

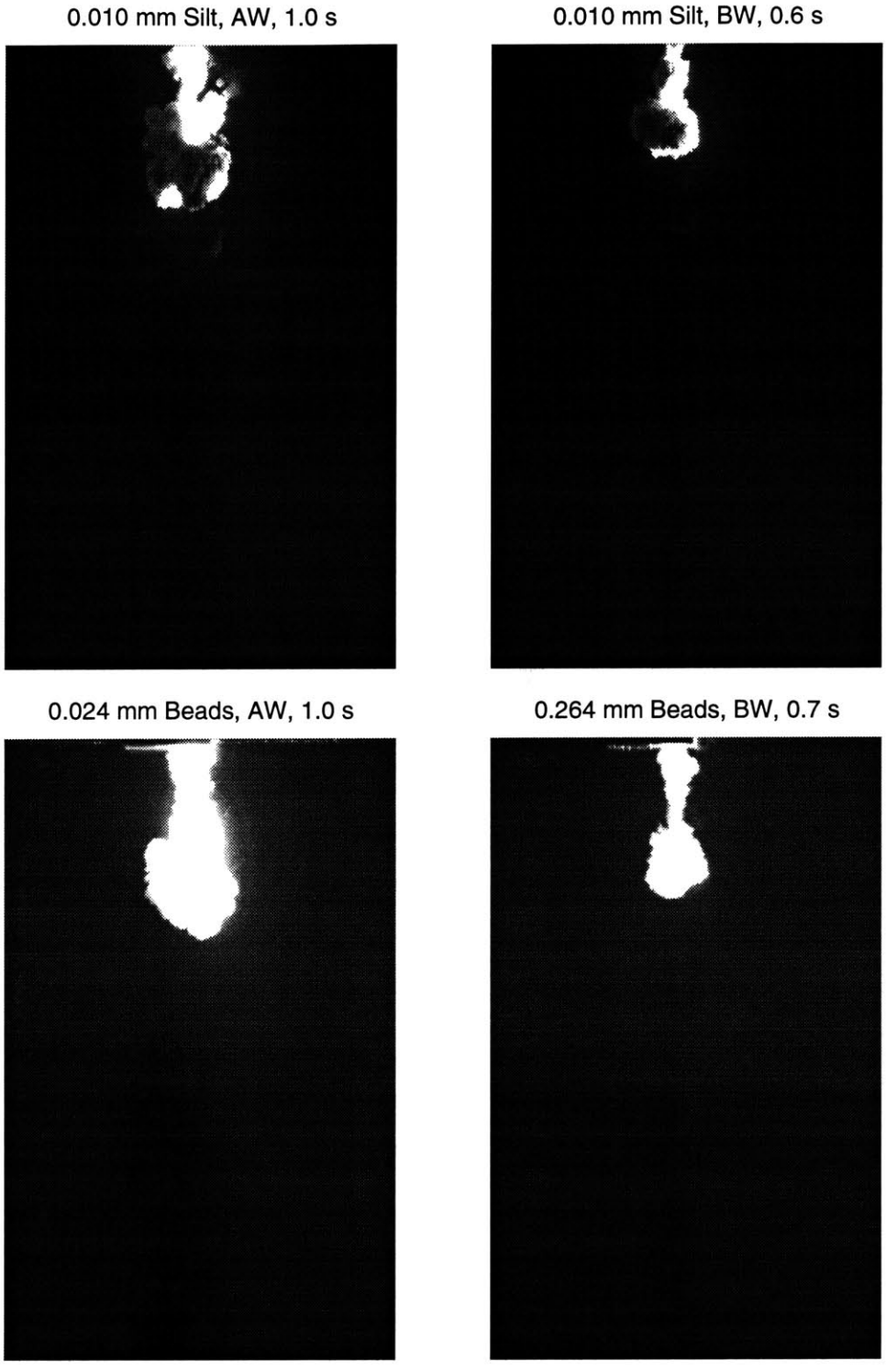

Figure 5-5: Selected images showing emergence of secondary plume in sediment trap experiments.

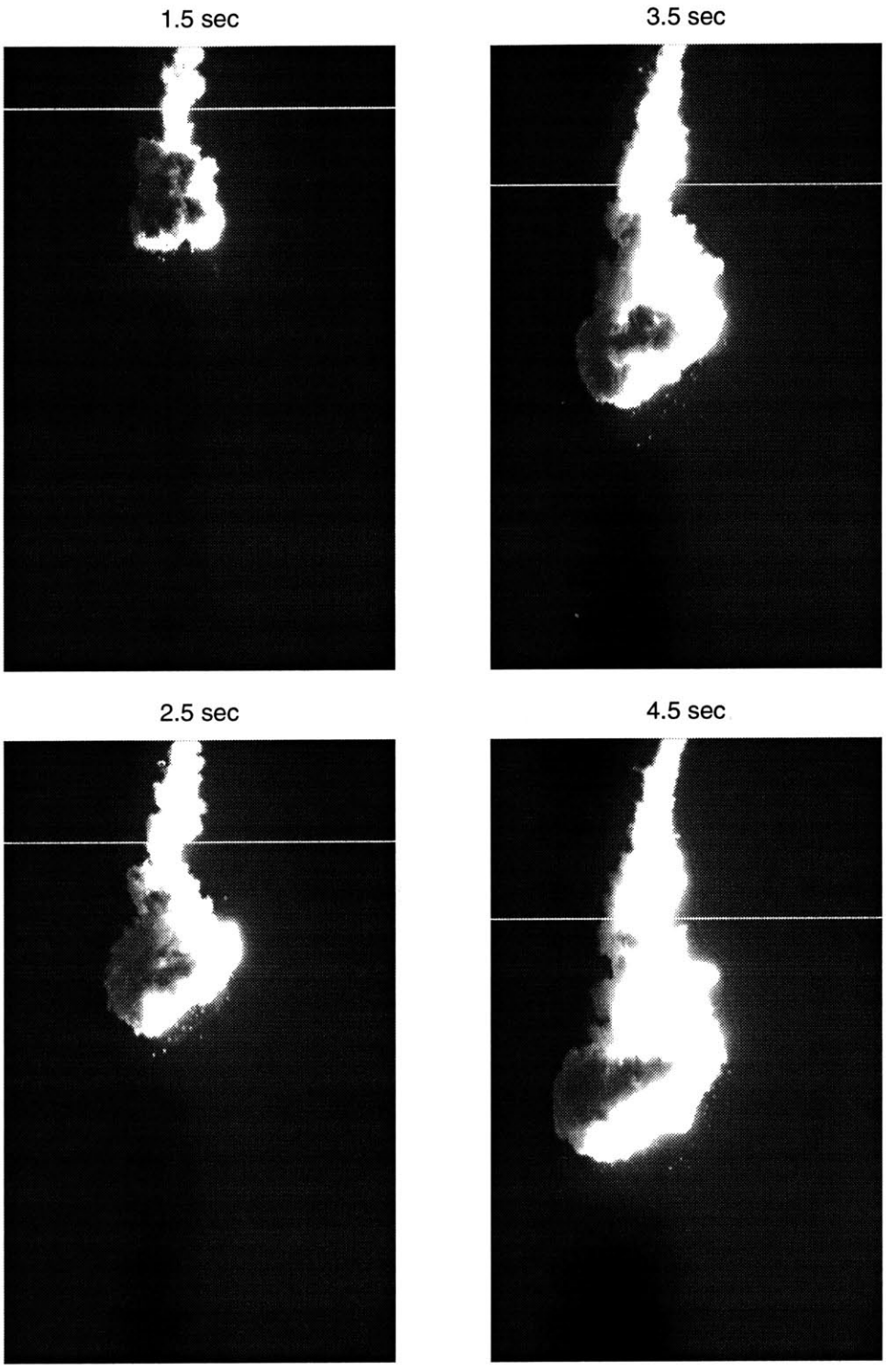

Figure 5-6: Selected images from 0.010 mm silt "BW" experiment showing approximate leading edge locations of secondary plumes.

bead cloud). The faster velocity calculated for the glass bead plume was most likely the result of its larger initial momentum (i.e., faster release time from the cylinder). The faster particle settling velocity of the individual beads ($3.2\frac{cm}{s}$) compared to the silt ($0.009\frac{cm}{s}$) may have also contributed to the quicker plume descent.

5.1.3 Mass of Particles Excluded from "Stem"

As discussed in the previous section, the "stem" of particles and fluid that forms behind some clouds descends at a velocity that greatly exceeds the particle settling velocity (w_s), allowing it to either become re-entrained into the "parent" cloud or impact the bottom shortly after it. Thus, material that may be "lost" to the environment during convective descent (e.g., carried away by ambient currents) consists primarily of particles and fluid that fail to become incorporated into the "stem." Visual observations from the various experiments discussed in Section 5.1 suggest that the amount of this material was a very small fraction of the total "stem" material and likely represented less than 1 % of the original sediment mass. To quantify this percentage, one additional sediment trap experiment was conducted in which the "0.010 mm silt BW" experiment discussed in Section 5.1 (i.e., 40 g silt with 40 cm^3 of water) was repeated but with a longer shade closure time (i.e., 30 s instead of 4.4 - 5.1 s). In this experiment, the shade was pulled 30 s after release of the silt suspension to allow the "stem" of material to completely pass through the sediment trap and to capture only the fraction of material suspended in the water column; that is, material that was last to exit the cylinder and failed to be transported with the "stem"). Thus, any "stem" material descending with a velocity greater than about 1 $\frac{cm}{s}$ would have passed through the trap before the shade was pulled at 30 s. After allowing the silt material suspended in the water column (i.e., falling with average $w_s = 0.009\frac{cm}{s}$) to settle on top of the shade, the shade was then removed from the tank and the mass of silt measured. The mass of silt retained on the shade was approximately 0.1 g or 0.25 % of the original mass. The amount of material that fails to become incorporated into the "stem" is likely to be less than this amount for initially "settled" sediments, since the "stems" associated with these particle clouds (Table 5.4) contained considerably

Trap Depth / Closure Time	*"Dry" Beads*	*"Wet" Beads*
12.7 cm / 1.0 - 1.5 s	5.0 ± 0.7 %	1.6 ± 0.2 %
63.5 cm / 7.0 - 8.0 s	5.8 ± 1.5 %	1.9 ± 0.4 %

Table 5.4: Sediment trap results – settled particle experiments. Trap depth denotes elevation of sediment trap. Closure time denotes time shade was drawn after release of particles. Percentages denote mass of "stem" particles retained on shade expressed as the percent of original mass.

less material than those produced by the "suspended" particles (Table 5.1).

5.2 Settled Particles

The objective of this group of experiments was to investigate the influence of water content and settling on particle stripping mechanisms. As with the suspended experiments, 40 g of particles and the 4.45 cm release cylinder were used for all experiments in this group. For the "wet" experiments, 17 cm^3 of water was added to the beads prior to release. The release cylinder was positioned immediately above the water surface("AW") for all experiments. The sediment trap was positioned at either a shallow depth (i.e., 12.7 cm below release cylinder) or deep depth (i.e., 63.5 cm below release cylinder), yielding a total of four experiments. As with the other experiments, five repetitions were performed for each experiment. The results of the four experiments are summarized in Table 5.4. The percentages shown again represent the means and standard deviations of the percent of original mass of solids (40 g) retained on the curtain.

As can be seen in the images in Figure 4.2, clouds formed from the "wet" particles fell as discrete volumes with little or no material trailing behind them as a "stem." Thus, virtually all ($>$ 98 %) of the initial material became incorporated into the cloud upon release. In contrast, when the beads were released in a "dry" state, approximately 94 - 95 % of the initial material made it into the cloud during formation. The material that did not make it into the cloud formed a small "stem" as evident in Figure 4.2. In addition, following release of the main cloud, a secondary "puff" of

material emerged from the cylinder, similar to the secondary plume discussed in the previous section. Based on visual observation, it appears that the bulk of the 5 - 6 % of the original mass not incorporated into the cloud was present in this secondary "puff." The absence of this secondary release in the "wet" experiments suggests that the added water helps to keep the initial volume intact, possibly through interparticle cohesion.

Taking into account the experimental variability indicated by the standard deviations, the data in Table 5.4 show that little or no mass was lost to the water column (i.e., stripped from the cloud) during descent. That is, once particles were incorporated into the cloud during initial formation, they remained in the cloud until they settled out of the cloud when the cloud velocity approached the particle settling velocity (i.e., $N_c \rightarrow 1$). The entrainment mechanisms essentially sequestered the material within the cloud during descent. The results presented in the previous section suggest that any "stem" attached to the cloud was generated from material that failed to make it into the cloud upon release, rather than from some type of "stripping" mechanism acting as the cloud descends.

5.3 Settled Particles with Excess Water

This set of experiments consisted of "AW" and "BW" releases of 0.264 mm bead mixtures produced by adding 42 cm^3 of water to 40 g of beads and allowing them to settle prior to release, producing an initial "supernatant" layer of fluid on top of the beads. The goal of these experiments was to determine how much of the supernatant becomes incorporated into the cloud during formation and how much is left behind in the "stem." This information is important from an environmental perspective, because real-world dredged sediments may contain an appreciable amount of water (generated by using a closed "environmental" bucket) mixed with fine particles to which toxic contaminants are adsorbed. To measure these quantities, 10 g of the 0.010 mm silt was added to the water\bead mixture to serve as a tracer for the initial water. The entire mixture was first homogenized and then allowed to settle 2 - 3 s

Release Type/Closure Time	*% of Total Mass*	*% of Supernatant*
"AW" / 5.0 - 6.0 s	5.1 ± 1.7 %	7.0 ± 2.4 %
"BW" / 7.5 - 8.5 s	15 ± 2.3 %	20 ± 3.2 %

Table 5.5: Sediment trap results using silt tracer – settled particles/excess water experiments. The % of total mass denotes the amount of captured silt relative to the total added silt. The % of supernatant denotes the amount of captured silt relative to the silt contained in the overlying water.

before release, enabling the beads to settle while keeping the silt particles suspended in the water. Based on a bead porosity of 0.4, approximately 11.5 cm^3 of the added water was contained within the beads as "pore water," with the remaining 30.5 cm^3 present as a supernatant. Hence, of the initial 10 g of silt, approximately 2.7 g was contained within the beads and 7.3 g in the overlying water.

Only one sediment trap depth (63.5 cm) was used for the "AW" and "BW" experiments, with five repetitions conducted for each experiment. The results of the two experiments and the associated standard deviations are given in Table 5.5. Two percentages are included in Table 5.5, the first representing the percent of the total mass of silt (10 g) retained on the curtain, and the second expressing the mass on the curtain as the percent of silt contained in the original supernatant (7.3 g).

The results shown in Table 5.5 indicate that the particles were capable of incorporating a large percentage of overlying water (80 - 93 %) into the cloud upon their release. Consistent with the sediment trap results for the suspended particles, the data show that speeding up their release (i.e., decreasing release time from 0.4 s to 0.1 s) by increasing their height above the water surface (i.e., potential energy) significantly increased the amount of material that became incorporated into the cloud. The ability of the particles to incorporate the majority of any overlying water and transport it downward with the descending cloud clearly has positive benefits for real-world disposal/capping projects in which the water may contain dissolved and particulate contaminants from dredging operations.

5.4 Discussion and Summary

Sediment trap results using both suspended and settled particles suggest that material incorporated into the cloud during initial formation is sequestered via entrainment mechanisms until the dispersive phase, in which solid particles begin to settle out of the cloud.

The amount of material not initially incorporated into the cloud is directly dependent on the initial potential energy and associated release time, with quicker releases resulting in more material being incorporated into the cloud. Material not incorporated into the cloud ranged from 2 - 8 % of the initial mass for the "AW" experiments compared to 21 - 31 % for the "BW" releases. The large percentage of "stem" material produced by the "BW" releases was likely a result of the "stalling effect" caused by ambient fluid flowing, and carrying particles, back into the submerged cylinder after the bulk of the particles was released. Though sediments from real barges and scows are released below the water surface (due to their hydrostatic equilibrium elevation), the "stalling effect" would not be expected in a real barge because of the decrease in the vessel's draft (i.e., rise in elevation) as the material is released. Thus, the two ranges of percentages associated with the "AW/BW" experiments may bracket the amount of "stem" material the would be expected under real-world release conditions.

Particle size, or cloud number (N_c), does not appear to have a major influence on the ability or inability of particles to become incorporated into the cloud upon formation. By reducing sidewall cohesion, large particles (i.e., $N_c > 10^{-2}$) may be more easily incorporated into the cloud than smaller particles that tend to adhere to the release vessel walls.

By increasing inter-particle cohesion, saturating particles prior to release improves the ability of the particles to remain intact during their release, particularly with respect to the last particles to exit the release vessel, which have the most difficulty being incorporated into the cloud.

The material that fails to enter the cloud upon formation forms a "stem" of material behind the descending cloud. For the experiments conducted here, approximately

half of the material located near the front of the "stem" possesses sufficient momentum to enable it to become re-entrained into the main cloud within a distance equal to about seven initial diameters. The other half of the material in the stem falls more slowly as a separate density plume that, in some cases, detaches from the main cloud. This rather narrow secondary plume decelerates more slowly than the main cloud, allowing it to either become re-entrained into the main cloud, with sufficient water depth, or impact the bottom soon after the collapse of the main cloud. The motion and distribution of particles in the "stem" may be influenced by the flow of displaced ambient fluid around the falling cloud, serving to sweep particles upward retarding their descent.

Failure of the last particles and fluid that exit the release vessel to become incorporated into the falling "stem" is the predominant mechanism by which material is lost to the environment. The amount of this material was quantified to be less than 1 % of the original sediment mass (0.25 %) for the 0.010 mm silt "BW" suspension. The amount of material that fails to become incorporated into the "stem" is likely to be less than this amount for initially "settled" sediments, since the "stems" associated with these particle clouds (Table 5.4) contained considerably less material (1.6 - 5.8 %) than those produced by the "suspended" particles (Table 5.1). Thus, sediment trap results from the 0.010 mm silt "BW" experiment represents a "worst case" scenario.

Settled particles in the cylinder appear capable of incorporating a large percentage of overlying water into the cloud upon release. The amount of supernatant fluid incorporated into the cloud upon formation is dependent on the initial potential energy of the material and resulting entrance velocity. Approximately 93 % and 80 % of the excess water was incorporated into the cloud for material released above and below the water surface, respectively.

Chapter 6

Integral Model Analysis

In this chapter, application of a numerical integral model to eight of the twelve Group I, II, and III particle cloud experiments, described in Chapter 4, is discussed. The integral model was applied in the "normal" mode in which cloud characteristics (i.e., size and velocity) were determined by solving the conservation laws using user-specified "calibration" parameters, namely the entrainment (α), drag (C_D), and added mass (k) coefficients. When used in this traditional mode, the integral model will be referred to herein as the "forward model." In addition to the "forward" mode, the integral model was run in a backward, or "inverse" mode, in which the momentum equation was rewritten to solve for either the drag or added mass coefficient using measured entrainment and velocity data. When used in this backward mode, the integral model will be referred to herein as the "inverse model." As will be discussed, the inverse model was formulated to solve for the apparent mass coefficient (C_m), which was then used to calculate the added mass coefficient.

The first section of this chapter outlines the governing equations on which the forward and inverse models are based. The next section includes the results of a brief analysis of the forward model's sensitivity to the three "calibration" coefficients. The third section provides the results of the inverse model analysis, including time-varying relationships for the added mass coefficient. In the next section, results of the forward model simulations using both constant and time-varying calibration coefficients is presented. In the final section, the forward model is applied to two

shallow-water case study simulations: (1) Boston Harbor, representing a very shallow sediment disposal scenario (15 - 20 m); and (2) Massachusetts Bay, representing a deeper (100 m) disposal site. In addition, the final section includes a brief analysis of particle cloud mechanics under the influence of density stratification at a generic deep-water (610 m) site. The STFATE model (Johnson and Fong, 1995) was used for this analysis.

6.1 Model Development

The forward model essentially solves the initial value problem posed by the mass, momentum, and buoyancy conservation equations (presented in Chapter 2) by converting the ordinary differential equations into difference equations using Euler's method. Since the mass of solid particles in the cloud was assumed constant (i.e., no stripping or settling) and only an ambient fluid of uniform density was used in the experiments, the forward model tracks the growth in cloud volume (V) using the entrainment assumption and volume conservation equation as follows:

$$V_t = V_{t-1} + 4\pi r_{t-1}^2 w_{t-1} \alpha \Delta t \tag{6.1}$$

where the subscripts t and $t-1$ refer to the discretized times separated by the interval Δt. A Δt of 0.01 s was used in all forward and inverse model simulations, which yielded converged solutions.

The change in momentum (M) is tracked by summing the buoyancy (B) and drag (D) forces as follows:

$$M_t = M_{t-1} + (B_{t-1} - D_{t-1})\Delta t \tag{6.2}$$

where $M_{t-1} = C_m m_{t-1} w_{t-1}$, $D_{t-1} = 0.5\rho_a C_D \pi {r_{t-1}}^2 {w_{t-1}}^2$, and $B_{t-1} = B_o = V_{t-1}(\rho_{t-1} - \rho_a)g$, as discussed in Chapter 2. For the simulations discussed herein, the initial momentum (M_o) is given a value of zero, since the forward model is run with the cloud starting from rest. The cloud velocity is then computed by dividing the momentum

by the cloud's apparent mass:

$$w_t = \frac{M_t}{C_m m_t} \tag{6.3}$$

Using the experimental velocity and radius values to compute M and the force terms in the inverse model, Equation 6.2 can be solved for either C_D or k, while holding the other coefficient constant. A time-varying drag coefficient is computed from the measured data by rearranging Equation 6.2 as follows:

$$C_{D_t} = 2\left(B_o - \frac{M_t - M_{t-1}}{\Delta t}\right)\left(\frac{1}{w_t^2 r_t^2}\right) \tag{6.4}$$

A time-varying apparent mass coefficient is computed by reformulating Equation 6.2 as follows:

$$C_{m_t} = \left(1 - \frac{(mw)_t - (mw)_{t-1}}{(mw)_{t-1}}\right) + \frac{(B-D)\Delta t}{(mw)_{t-1}} \tag{6.5}$$

The initial value for C_m is calculated by holding it constant over the first time step yielding:

$$C_{m_o} = \frac{(B-D)\Delta t}{(mw)_t - (mw)_{t-1}} \tag{6.6}$$

The added mass coefficient can be computed from C_m as follows:

$$k_t = \frac{\rho_t}{\rho_a}(C_{m_t} - 1) \tag{6.7}$$

After the cloud descends about two initial diameters, $\frac{\rho}{\rho_a} \simeq 1$ and $k \simeq C_m - 1$.

6.2 Sensitivity Analysis

As discussed in Chapter 2, researchers have proposed values for the entrainment, drag, and added mass coefficients that generally fall within the following ranges:

- α: 0.1 - 0.5

- C_D: 0.01 - 0.5

- k: 0.01 - 0.5

The entrainment coefficient values shown above represent the approximate range of values determined experimentally, encompassing values measured for heavy thermals (i.e., dense liquids), buoyant vortex rings, and particle clouds. The upper value of 0.5 for the added mass and drag coefficients is based on the theoretical value derived for a solid sphere. The lower limit of 0.01 for C_D and k is based on estimates made from thermal experiments as well as from heuristic arguments as discussed in Chapter 2.

The sensitivity analysis was performed for the entrainment coefficient by running the forward model using the upper and lower limits on α while holding C_D and k constant at a " mean" value of 0.25. The model's combined sensitivity to C_D and k was evaluated by running the model with $C_D,\ k = 0.01$ and $C_D,\ k = 0.5$, while holding α constant at 0.25. For all sensitivity analysis simulations, the initial buoyancy and volume were held constant at the values used for the 0.010 mm silt experiments (i.e., $B_o = 23,520\ gms^{-2},\ V_o = 56\ cm^3$). In addition, all particle volumes were started from rest (i.e., $w_o = 0$) and from a submerged state ("BW"). The results of the sensitivity analysis, as characterized by predicted cloud velocities, radii, and center of mass positions as functions of time, are shown in Figure 6.1.

As depicted in Figure 6.1, the forward model is far more sensitive to variations in α than it to changes in C_D and k. The upper and lower limits for α resulted in velocity variations ranging from 74 % to 100 %, and a radius variation of about 40 % after 6 s of descent. In contrast, the upper and lower values for C_D and k resulted in velocity variations ranging from about 10 % to 19 %, and a radius variation of about 11 % after 6 s of descent. When the center of mass locations are taken into account, and velocities are compared on a depth basis, the variation becomes considerably larger (i.e., 21 % compared to 10 %).

The lack of model sensitivity to the added mass and drag coefficients is a direct result of the feedback mechanism between the entrainment and momentum equations.

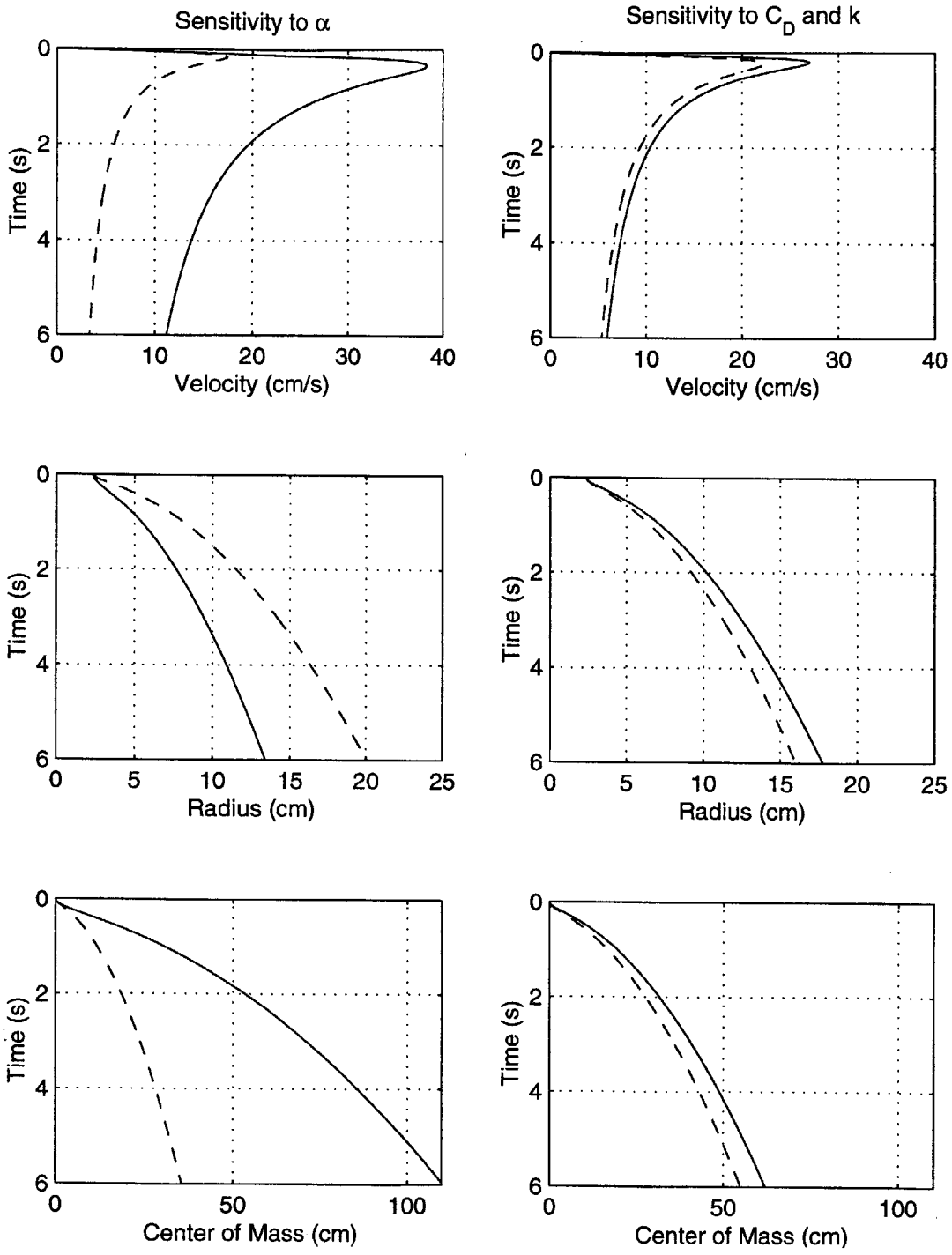

Figure 6-1: Forward model sensitivity analysis results. In left column plots, $C_D, k = 0.25$ and $\alpha = 0.1$ and $\alpha = 0.5$ denoted by solid and dashed lines, respectively. In right column plots, $\alpha = 0.25$ and $C_D, k = 0.01$ and $C_D, k = 0.5$ denoted by solid and dashed lines, respectively.

To a large extent, any increase in the drag force caused by a higher C_D is offset by a corresponding decrease in the radius resulting from the smaller entrainment velocity caused by the increased drag force (due to C_D). Similarly, any increase in the apparent mass caused by a higher k is offset to a large degree by a corresponding decrease in actual mass resulting from the smaller entrainment velocity caused by the increase in k. In essence, the cloud dynamics are dominated by the entrainment mechanisms.

6.3 Inverse Modeling Results

Eight of the twelve Group I, II, and III particle cloud experiments, described in Chapter 4, were selected for application of the forward and inverse model as listed below:

- 4.45 cm Cylinder, Wet (0.264 mm beads set., 17 $cm^3 H_2O$)
- 40 $cm^3 H_2O$, Settled, "AW" (0.264 mm beads, 4.45 cm cyl.)
- 40 $cm^3 H_2O$, Suspended, "AW" (0.264 mm beads, 4.45 cm cyl.)
- 40 $cm^3 H_2O$, Suspended, "BW" (0.264 mm beads, 4.45 cm cyl.)
- 0.024 mm beads, "AW" (4.45 cm cyl., 40 $cm^3 H_2O$)
- 0.024 mm beads, "AW" (4.45 cm cyl., 40 $cm^3 H_2O$)
- 0.010 mm silt, "AW" (4.45 cm cyl., 40 $cm^3 H_2O$)
- 0.010 mm silt, "BW" (4.45 cm cyl., 40 $cm^3 H_2O$)

The eight selected experiments provide a good representation of the major initial conditions investigated in Chapter 4; that is, potential energy ("AW" versus "BW"), settled versus suspended particles, and particle size (cloud number, N_c). The above list includes the nomenclature used in Chapter 4 for the various experiments with additional descriptive details shown in parentheses. All experiments involved the

release of "wet" beads from the 4.45 cm cylinder, and 40 cm^3 was added to the particles in all cases with the exception of the first experiment.

The first objective of the inverse model analysis was to determine actual values for C_D and k using Equations 6.3, 6.4, and 6.5 and the measured velocity and radius data from the eight experiments. To reduce the "noise" associated with the random fluctuations in the measured velocity and radius data, smooth functions were fit to the data, from which discrete values were entered into the model instead of the raw data. Functions with a $t^{-0.5}$ dependency were fit to the velocity data within the deceleration region. Because of the nonlinear radius versus depth profiles (i.e., dual α), single functions with a $t^{0.5}$ dependency could not be fit to the entire radius versus time data sets. For this reason, the radius data were fit using 6th-order polynomials. Two examples of the fitted velocity and radius data are included in Figure 6.2. To verify that the inverse model was properly coded, the forward model was run with the actual k values generated by the inverse model, which produced velocity and radius profiles identical to smooth functions used to fit the experimental data.

6.3.1 Determination of Drag Coefficient

The inverse model was first used to compute time-varying C_D values using Equation 6.3 and the fitted velocity and radius curves from the eight experiments. The fitted curves were sampled at a 0.01 s time step (i.e., $\Delta t = 0.01s$). For these model simulations, the added mass coefficient was held constant at either the lower ($k = 0.01$) or upper limit ($k = 0.5$) used in the sensitivity analysis. Results of these model simulations are shown in Figures 6.3 and 6.4. As shown in these figures, the higher value of k produces lower values for C_D and vice versa since both coefficients have a similar effect on cloud velocity; that is, higher values both decrease velocity.

For the four 0.264 mm bead experiments shown in Figure 6.3, the average time associated with the transition from well-mixed "thermal" to "circulating thermal" (t_c) was 1.2 s, as can be seen in Table 4.5. Regardless of the k value used, the inverse model yielded negative C_D values for this time period. Most of the inverse model simulations for the 0.024 mm bead and 0.010 mm silt experiments (Figure 6.4) also produced

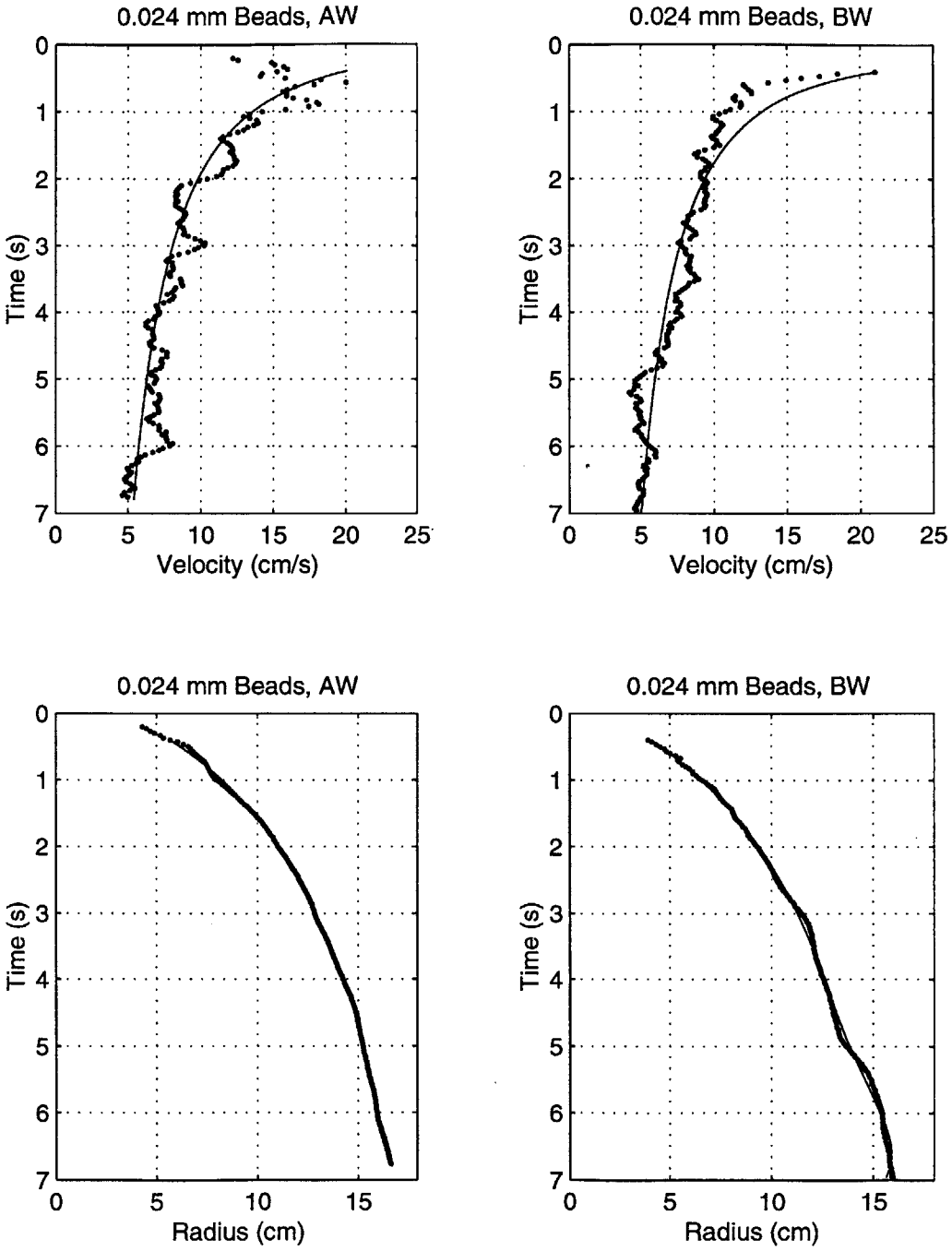

Figure 6-2: Examples of smooth curves fitted to measured velocity and radius data using $t^{-0.5}$ functions and 6th-order polynomials, respectively.

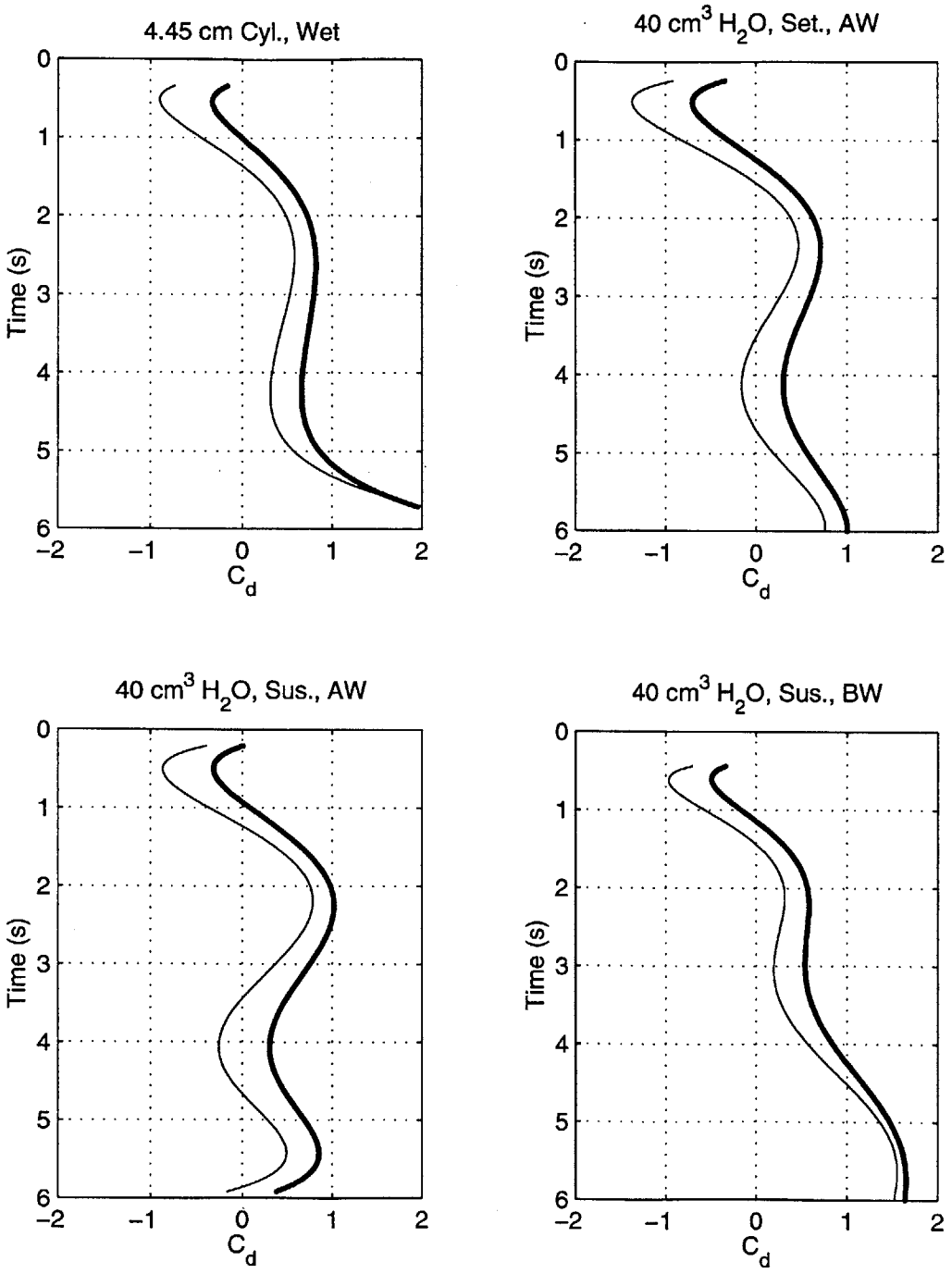

Figure 6-3: Inverse model results for drag coefficient (C_D) for 0.264 mm bead experiments. Results using $k = 0.01$ and $k = 0.5$ denoted by thick and thin lines, respectively.

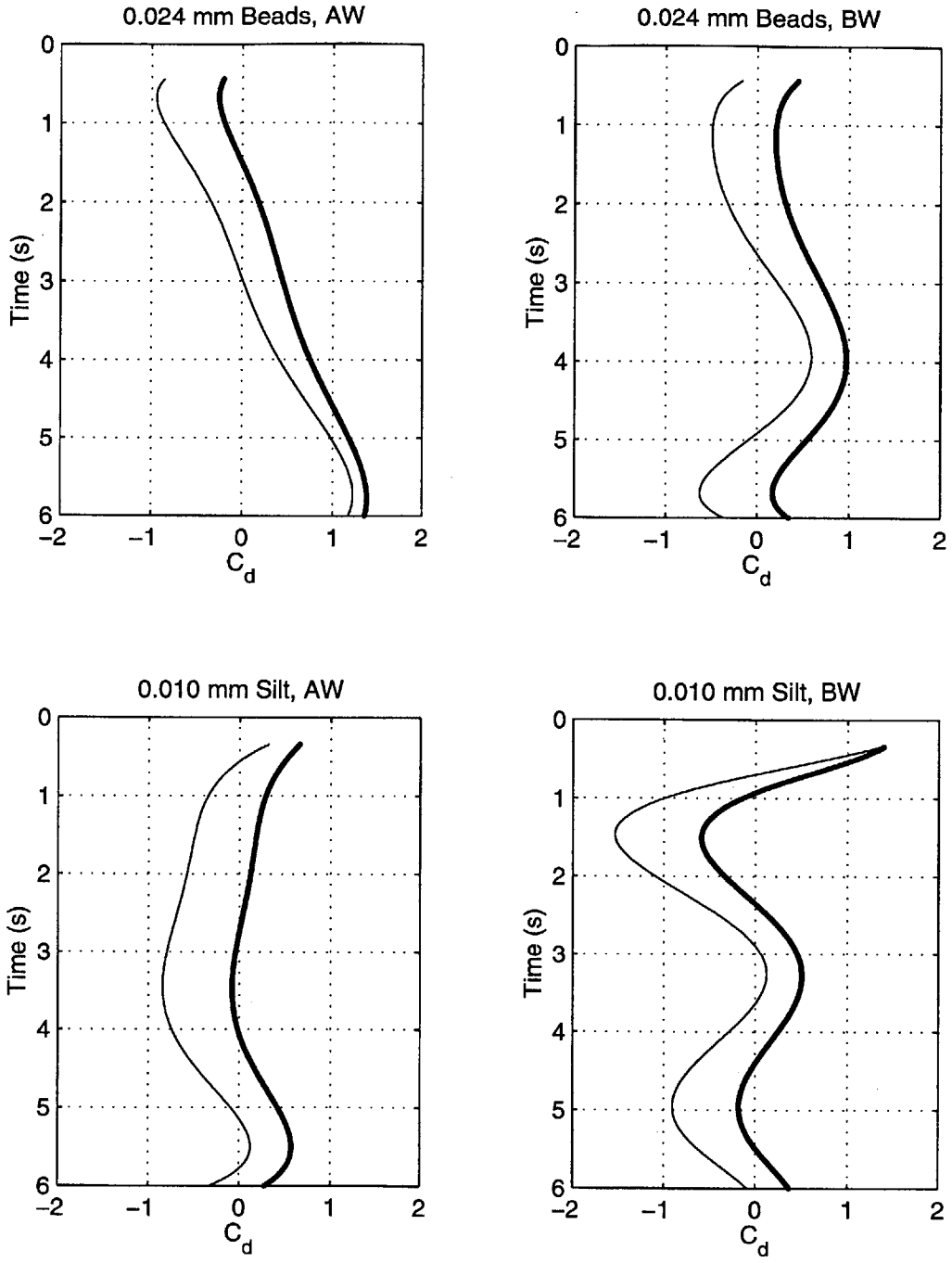

Figure 6-4: Inverse model results for drag coefficient (C_D) for 0.024 mm bead and 0.010 mm silt experiments. Results using $k = 0.01$ and $k = 0.5$ denoted by thick and thin lines, respectively.

negative C_D values for the majority of the "thermal" phase. The negative values, while having no physical meaning, suggest that the drag force is extremely small, with a C_D value close to zero. The negative values are a result of the inverse model's hypersensitivity to the magnitude of the cloud's velocity and radius, which appear as squared quantities in the denominator of Equation 6.3. This sensitivity can be seen by comparing the fitted velocity and radius curves for the "AW" and "BW" experiments with the 0.024 mm glass beads shown in Figure 6.5. The velocity profiles for these two experiments are very similar. The radius profiles are also similar with respect to slope but differ by about 1.6 cm in magnitude. With $k = 0.01$, this difference results in negative values during the first 1.5 s for the "AW" experiment (i.e.,$-0.2 < C_D < 0$) and positive values for the "BW" experiment (i.e.,$0.2 < C_D < 0.5$). Given the inverse model's sensitivity to the measured data coupled with the inherent variability of the measured data, firm conclusions cannot be drawn from the shape, or functionality, of the C_D curves for individual experiments. When taken as a whole, the C_D data within the "thermal" phase for the eight experiments do suggest a value of C_D close to zero rather than the 0.5 value for an equivalent solid sphere. This result is consistent with arguments made by Turner (1973) and Escudier and Maxworthy (1971) that the drag on thermals should be quite small because there is no flow separation at the cloud's boundary and thus no form drag.

One trend that is apparent in the C_D results for the six glass bead experiments is an increase in magnitude near the transition time (t_c), marking the transition from α_1 to the lower α_2 values. With a constant entrainment coefficient, the product w^2r^2 in the denominator of Equation 6.3 should remain constant, since velocity decreases as $t^{-0.5}$, while radius increases as $t^{0.5}$. However, this product does not remain constant but decreases as the entrainment coefficient decreases from α_1 to α_2, essentially causing the radius profile to shift to a new $t^{0.5}$ curve. The resulting decrease in cloud radius does not produce an associated increase in velocity, which remains on the same asymptotic $t^{-0.5}$ curve. The resulting decrease in w^2r^2 is not offset by the decrease in the $\frac{\Delta M}{\Delta t}$ term in Equation 6.3, since the time derivative of the cloud volume (and mass) scales with $t^{-0.5}$ and r^2 scales with t. Hence, C_D must increase in some fashion,

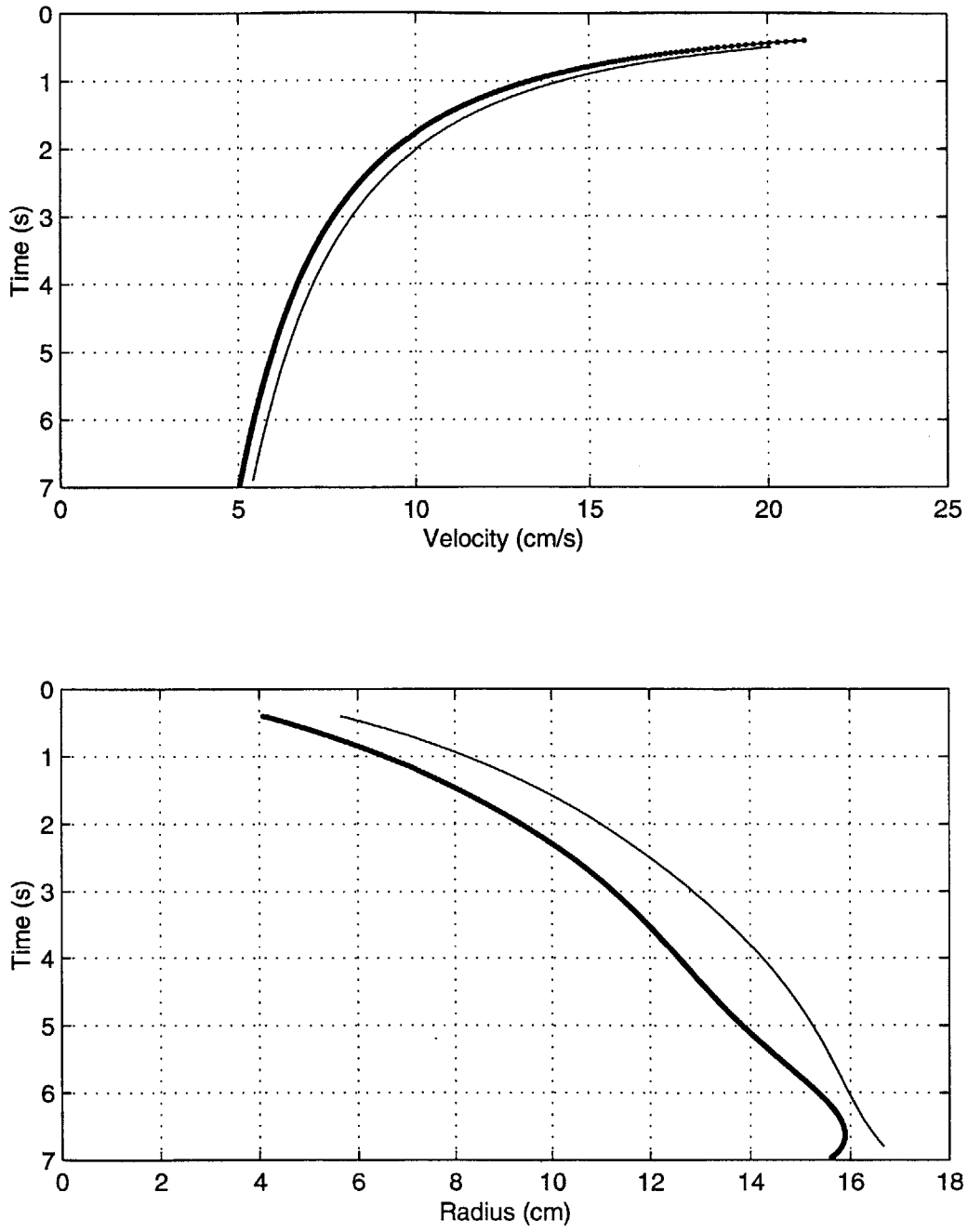

Figure 6-5: Comparison of smooth curves fitted to measured velocity and radius data for 0.024 mm bead "AW" and "BW" experiments.

the rate of which is dependent on the transition from α_1 to α_2.

As shown in Figure 6.4, the inverse model results for the two silt experiments did not show the increasing trend in C_D, a result of the relatively constant entrainment coefficients compared to the glass bead experiments. Regardless of the k value, most of the C_D values fall near or below zero, supporting the case for a very small drag coefficient.

6.3.2 Determination of Added Mass Coefficient

The inverse model results depicting time-varying added mass coefficients based on Equations 6.4 and 6.5 are included in Figures 6.6 and 6.7 for the eight experiments. As with the drag coefficient calculations, the "k" version of the inverse model was run using either the upper or lower limit of C_D, which was held constant for a given simulation. Similar to the behavior of the drag coefficient, computed k values also show a high degree of sensitivity to the measured radius and velocity data, which determine the values of the denominator terms in Equation 6.4. Again, the results from the 0.024 mm bead experiments illustrate the model's sensitivity to cloud radius, as k varied from -0.2 for the "AW" experiment to 0.4 for the "BW" experiment.

Similarly to the drag coefficient results, the time-varying behavior of k exhibits increasing trends for the glass bead experiments, associated with the α_1/α_2 transitions, and more constant values for the two silt experiments, reflective of the rather constant entrainment coefficients. In total, the results for the eight experiments for the "thermal" phase suggest that the added mass associated with turbulent particle clouds is closer to zero than to the theoretical 0.5 value for a corresponding solid sphere. These results, which are consistent with the findings of Neves and Almeida (1991), suggest that the volume of surrounding fluid being accelerated by the moving cloud is much less than the volume associated with a solid sphere, which must be due to the entrainment mechanisms. Much of the work being done on the surrounding fluid is shared with the kinetic energy of the turbulent eddies that are engulfing ambient fluid on all sides of the cloud. This interaction between the cloud eddies and the displaced fluid results in the reduced added mass as well as drag.

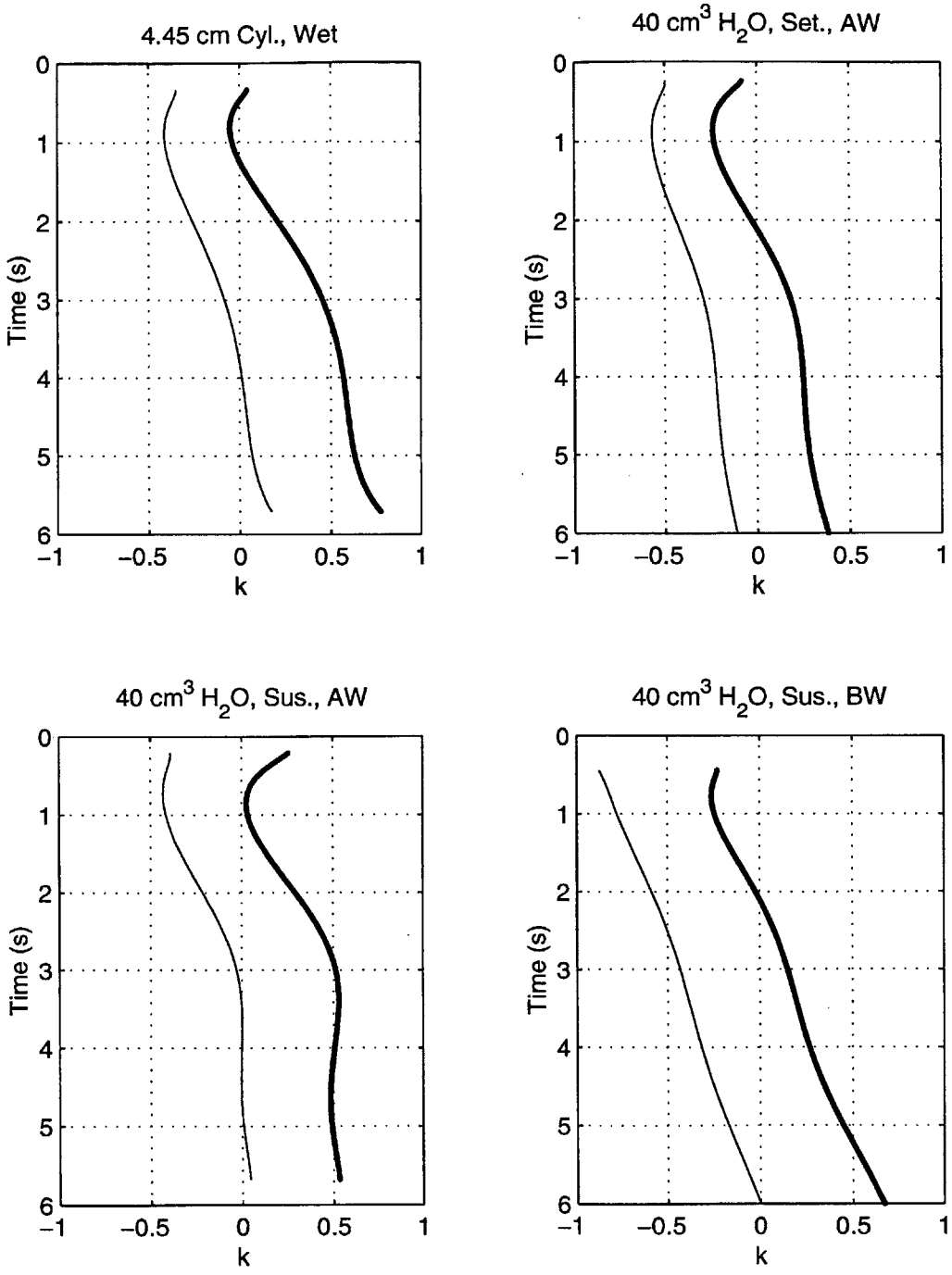

Figure 6-6: Inverse model results for added mass coefficient (k) for 0.264 mm bead experiments. Results using $C_D = 0.01$ and $C_D = 0.5$ denoted by thick and thin lines, respectively.

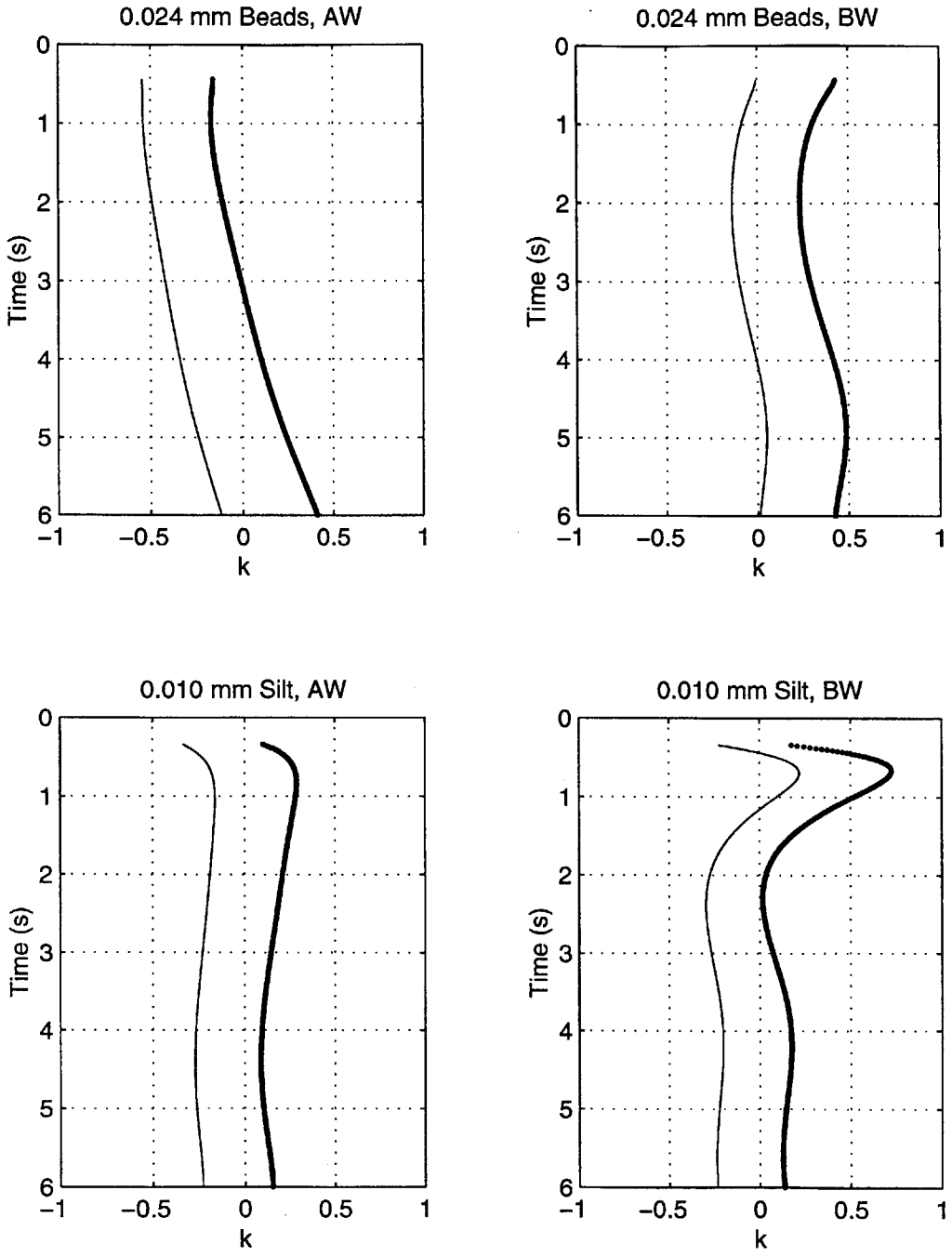

Figure 6-7: Inverse model results for added mass coefficient (k) for 0.024 mm bead and 0.010 mm silt experiments. Results using $C_D = 0.01$ and $C_D = 0.5$ denoted by thick and thin lines, respectively.

The increase in the added mass coefficient caused by the lower entrainment in the "circulating thermal" phase for the glass bead experiments may be associated with the suppression of turbulent eddies within this phase. In contrast to the silt clouds, which remain highly turbulent, energy dissipation from inter-particle collisions of the glass beads causes the clouds to appear more laminar with time, with smoother boundaries. The suppression of entraining eddies and the resulting smoothing of cloud boundaries may provide a physical explanation for why the inverse model tends to increase k to values approaching 0.5 for a solid sphere.

6.4 Forward Model Analysis

The forward model was first calibrated to the subset of eight experiments using constant coefficients (i.e., α, C_D, and k) followed by a more complicated suite of simulations using time-varying functions for the entrainment and added mass coefficients. The objective here was to first evaluate the performance of the simplest "baseline" model employing constant coefficients, and then determine what improvements, if any, could be gained by using time-varying coefficients. For both cases, selected coefficient values were based on the measured radius data presented in Chapter 4 and the inverse modeling results discussed in the previous section.

6.4.1 Model Simulations Using Constant Coefficients

The forward integral model was first applied to the eight experiments using constant coefficients, as outlined in Table 6.1. Based on the inverse model results, the drag and added mass coefficients were held constant at 0.01. With respect to the entrainment coefficient, two α_1 values were used for the glass bead experiments; the mean α_1 value of the "settled" experiments (0.22), and the mean α_1 value of the "suspended" experiments (0.27). The α_1 values were used to obtain the optimum performance within the "thermal" phase and to determine how well the model performs in the "circulating thermal" region while holding α_1 constant. An average of the α_1, α_2 values could have been used in lieu of this approach, which possibly would yield

Experiment	α	C_D	k	$m_s(g)$
4.45 cm Cyl., Wet	0.22	0.01	0.01	40.0
40 cm^3 H_2O, Set., AW	0.22	0.01	0.01	40.0
40 cm^3 H_2O, Sus., AW	0.27	0.01	0.01	39.4
40 cm^3 H_2O, Sus., BW	0.27	0.01	0.01	34.0
0.024 mm Beads, AW	0.27	0.01	0.01	39.0
0.024 mm Beads, BW	0.27	0.01	0.01	33.2
0.010 mm Silt, AW	0.25	0.01	0.01	37.7
0.010 mm Silt, BW	0.25	0.01	0.01	33.9

Table 6.1: Forward model parameters - constant coefficients.

improved model performance in the "circulating thermal" phase at the expense of performance in the "thermal" phase. For comparison purposes, model results using this second approach are presented for the two settled experiments. Because of the uncertainty in the t_c transition points selected for the two silt experiments and the associated α_1, α_2 values, mean entrainment coefficients were calculated for these experiments by fitting linear lines over the entire depths. This approach resulted in a mean α of 0.25 for both silt experiments.

With respect to initial conditions, the z_o and r_o values shown in Table 4.4 were used to define the initial cloud depth and volume. In all simulations, the cloud was started from rest assuming it was completely submerged. No special provisions were added to the model to account for differences in release times or initial potential energy (i.e., "AW" versus "BW"), since no velocity differences based on these factors were observed. Furthermore, no special provision was made to account for possible differences in the initial growth rate associated with the release of particles from the cylinder (i.e, is was assumed that $\alpha_0 = \alpha_1$). As shown in Table 6.1, the initial mass of solids was adjusted based on the sediment trap data presented in Chapter 5. The adjustments were made by subtracting the average of the mass quantities captured in the shallow and deep sediment trap experiments from the initial solids mass (40 g). For the deep sediment trap experiments performed only with the 0.010 mm silt (i.e, "BW" releases), it was assumed for the larger particles, that the same percentage decrease in stem material would occur between the shallow and deep trap locations as

observed in the silt experiments. Thus, the loss of initial material from the cloud was handled in a rather crude manner, with no mechanisms added to the model to account for the motion of the trailing "stem" or subsequent re-entrainment of "stem" material into the cloud at some time later in its descent. In short, application of the integral model under the conditions in Table 6.1 represents the most simplistic modeling approach and provides a baseline against which potential model enhancements can be compared.

The results of the forward model simulations for the eight experiments are provided in Figures 6.8 - 6.11. As shown by the velocity profiles, the forward model performs quite well in capturing cloud velocity for the entire deceleration phase. The majority of predicted velocities fall within 10 % of the experimental data. Agreement between measured and predicted velocities in the initial acceleration phase is considerably more variable between the eight experiments, with absolute differences between measured and predicted maximum velocities falling between 4 % and 30 %. This agreement is still quite good considering the simple assumptions made for the release conditions.

Perhaps a better measure of model performance is how well the model tracks the cloud center of mass position over time, which basically accumulates errors in predicted velocities. With the exception of the "$40cm^3H_2O$, Sus., BW" experiment (Figure 6.9), at the 6 s mark, simulated center of mass positions fell within 5 % of the measured data. The 14 % difference in center of mass positions for "40 cm^3H_2O, Sus., BW" experiment was caused by the slight underprediction of velocity for this experiment.

As can be seen from the radius versus time profiles, the forward model performs well in capturing the radial growth rates in the initial "thermal" region but, as expected, begins to diverge from the measured data (i.e., overshoot) as the clouds transition into the "circulating thermal" phase. The divergence is essentially due to the differences between the α_1 and α_2 values. For the glass bead experiments, predicted radius values exceed measured values by 9 - 24 % after 6 -7 s of descent. As shown in Figure 6.11, the forward model simulates radial cloud growth extremely well for both

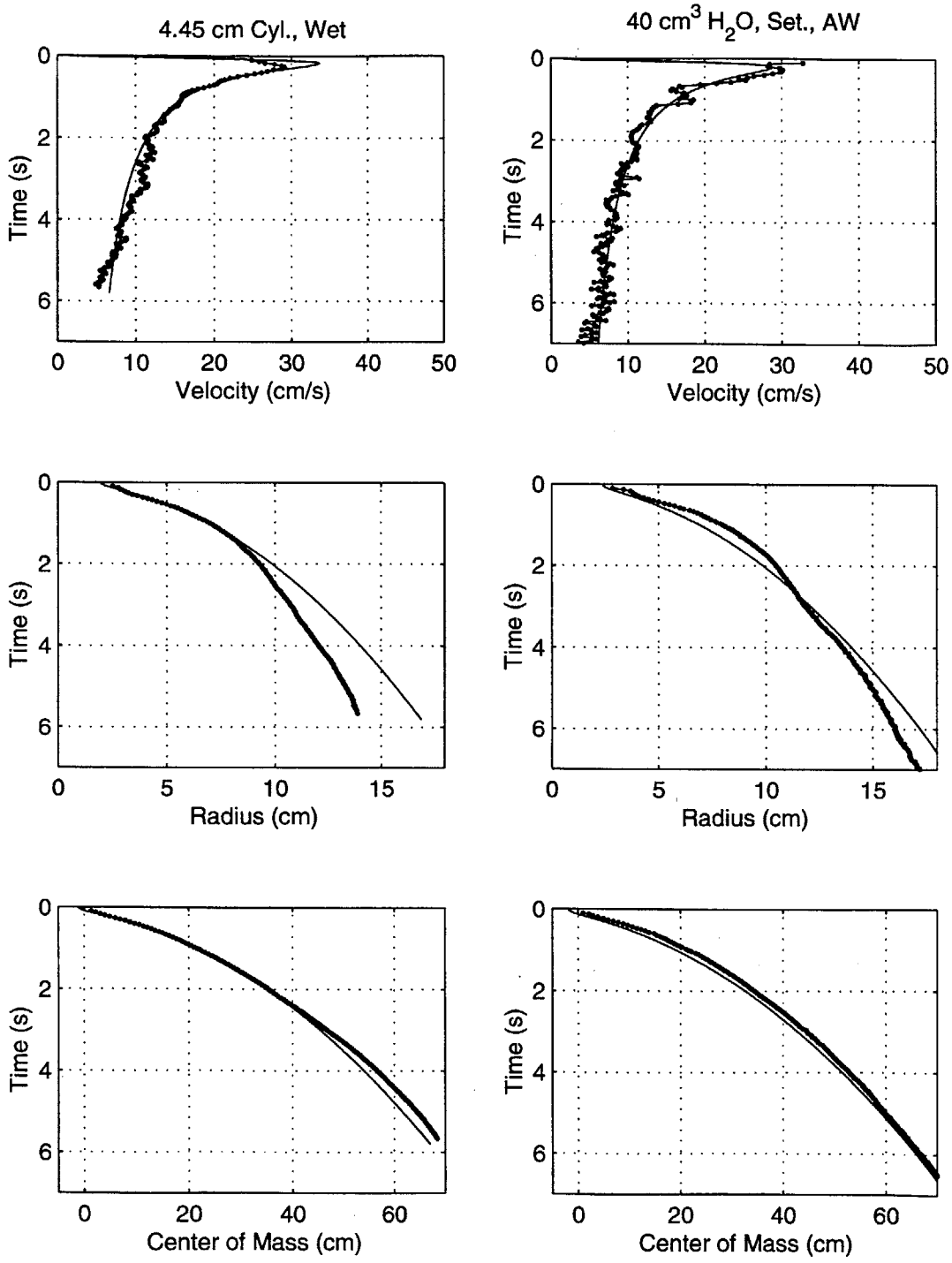

Figure 6-8: Forward model results using constant coefficients for 0.264 mm bead "Settled" experiments. Simulation results denoted by thin lines.

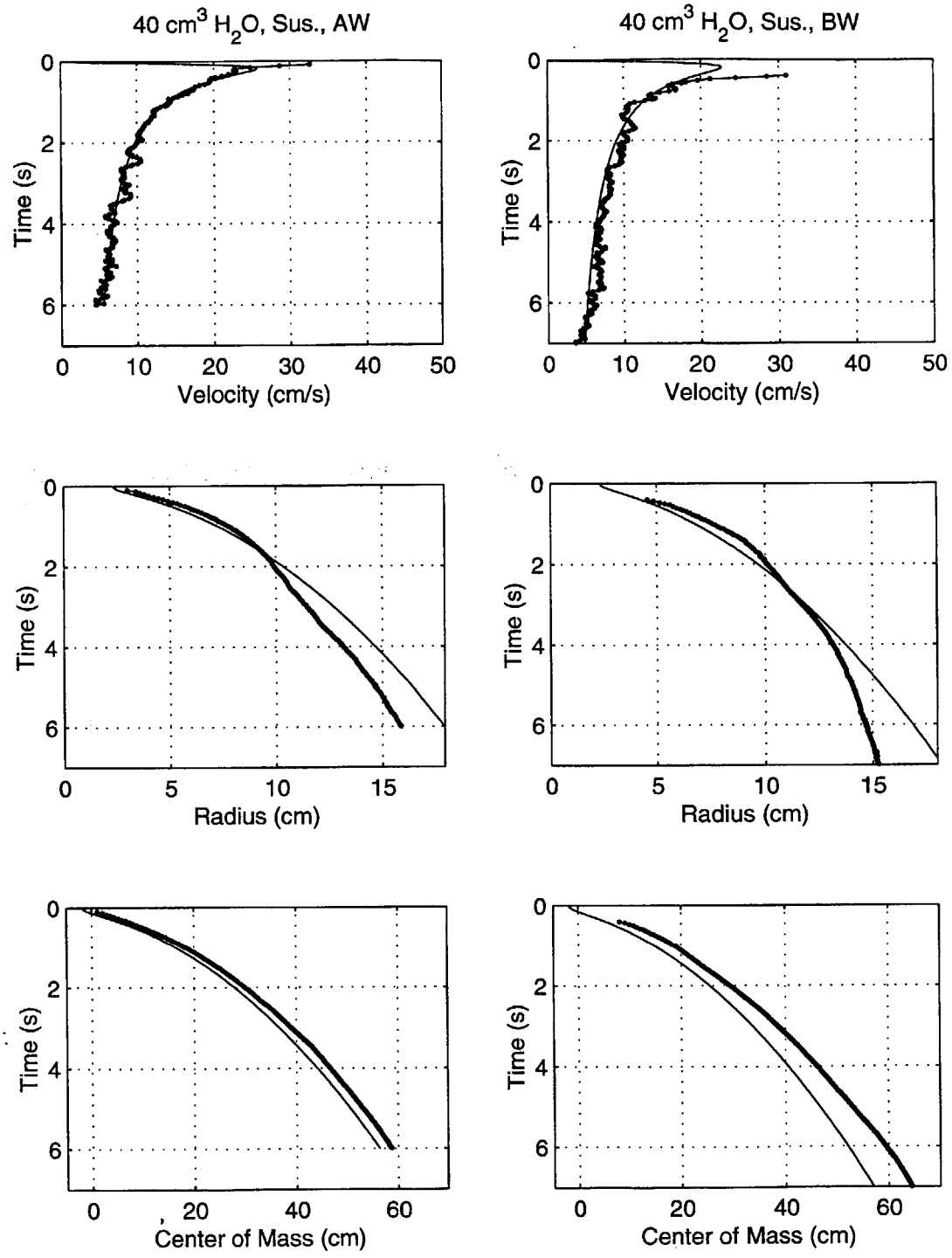

Figure 6-9: Forward model results using constant coefficients for 0.264 mm bead "Suspended" experiments. Simulation results denoted by thin lines.

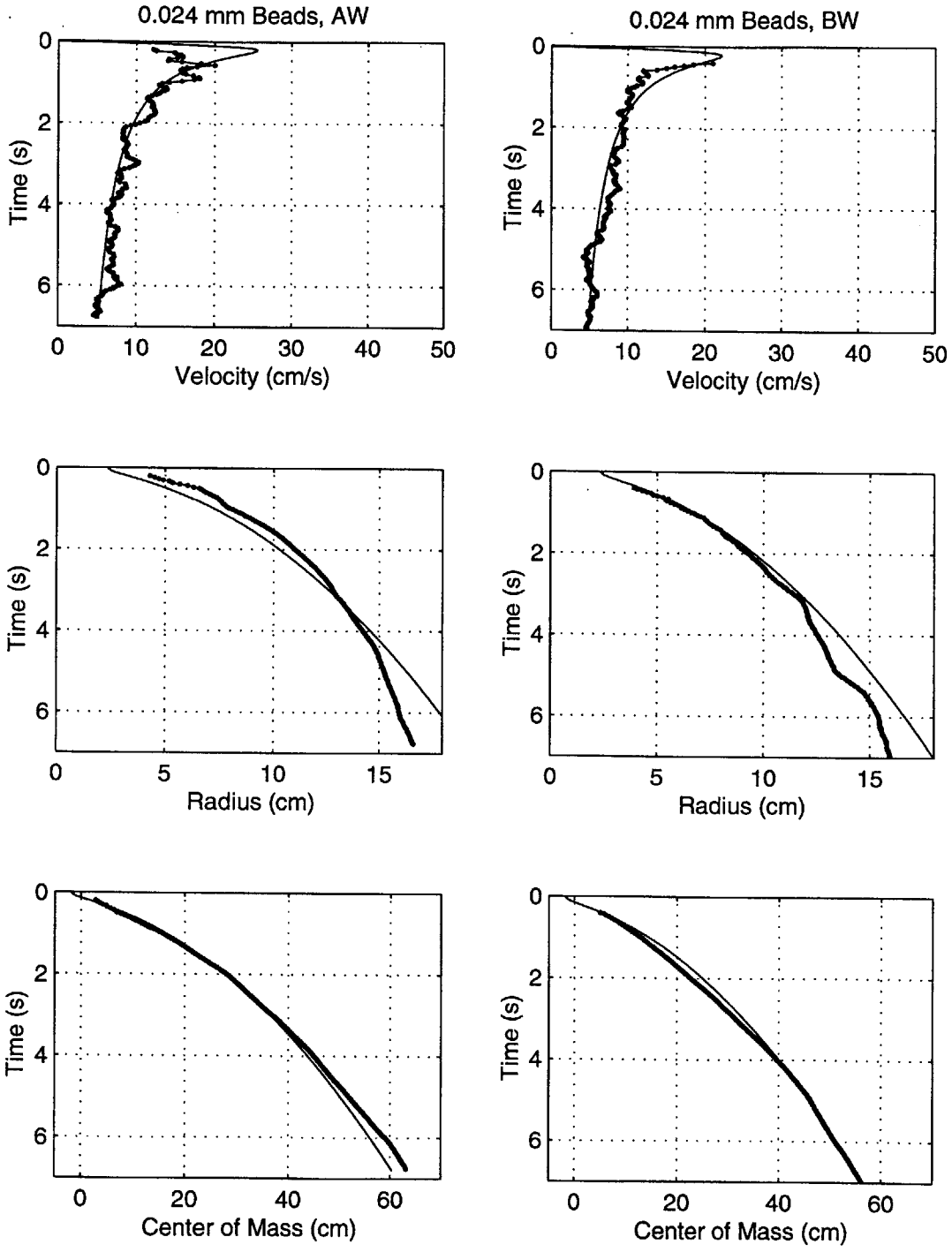

Figure 6-10: Forward model results using constant coefficients for 0.024 mm bead "AW" and "BW" experiments. Simulation results denoted by thin lines.

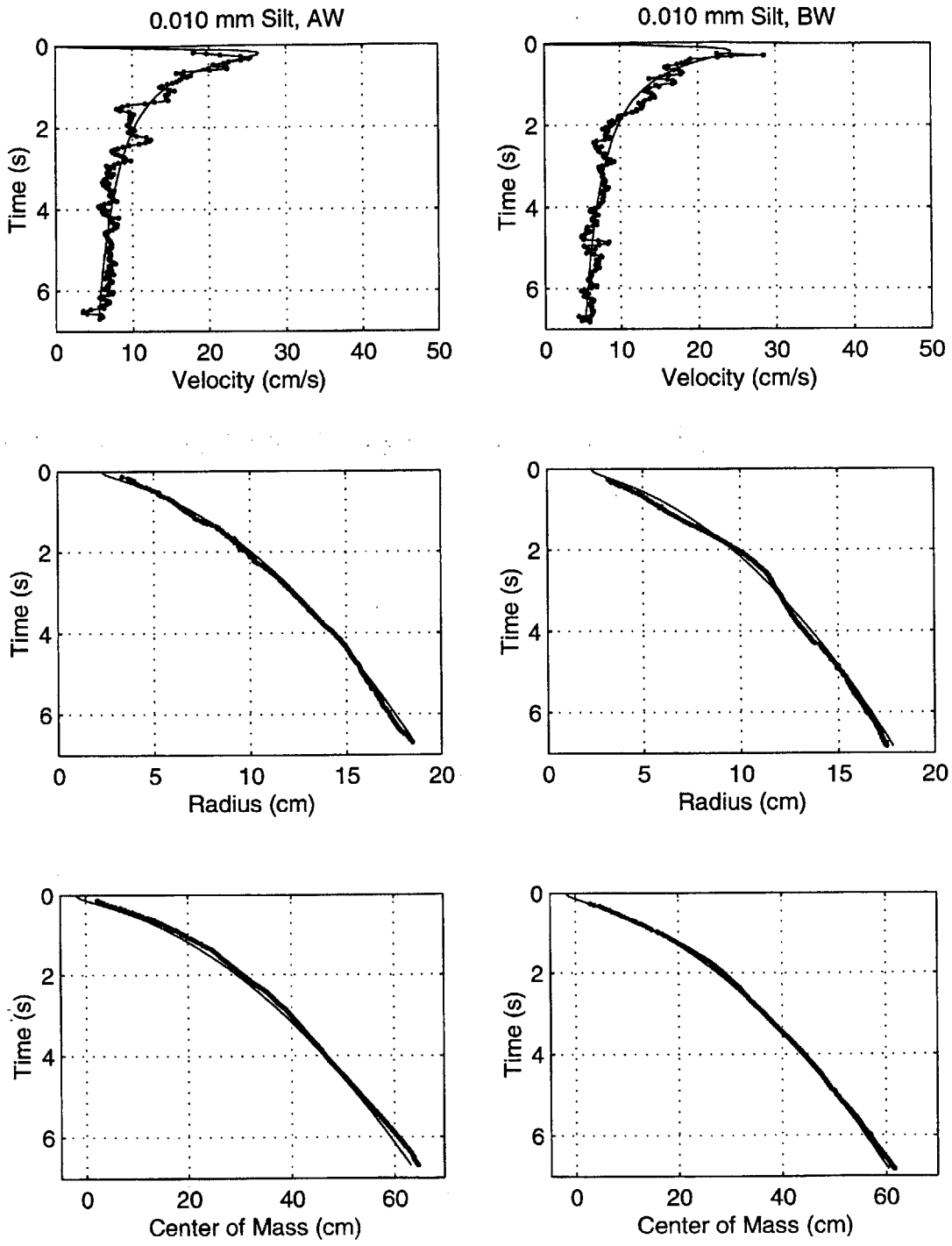

Figure 6-11: Forward model results using constant coefficients for 0.010 mm silt "AW" and "BW" experiments. Simulation results denoted by thin lines.

the "AW" and "BW" silt experiments. The lack of divergence between the measured and predicted curves suggests a constant entrainment coefficient (i.e., $\alpha = 0.25$) as opposed to the α_1 and α_2 values shown in Table 4.5.

As noted earlier, rather than using the α_1 values for the constant entrainment coefficient for the glass bead experiments, the mean values for α_1 and α_2 cloud have been used. Forward model results using this approach are shown in Figure 6.12 for the two "settled" 0.264 mm bead experiments in which an average value of 0.185 was used for α. As one might expect, employing this approach produces slightly better performance in radial cloud growth predictions at the expense of predictions in velocity and center of mass locations.

6.4.2 Model Simulations Using Time-Varying Coefficients

As discussed in the previous section, for the six glass bead experiments, the forward model overpredicts cloud growth during the "circulating thermal" phase when a constant entrainment coefficient is used. To overcome this problem, the mean α_1 and α_2 values for the "settled" and "suspended" experiments were used in conjunction with the forward model, as shown in Table 6.2. As discussed in Section 4.2, the transition from "turbulent" to "circulating thermal" occurs when the cloud radius has approximately doubled with respect to its size when turbulence arises (i.e., $\frac{r_c}{r_t} = 2$). For modeling purposes, the transition to "circulating thermal" must be related to the initial size, or cloud radius (r_o). The $\frac{r_c}{r_o}$ ratios for the six modeled experiments are included in Table 6.2. The average of the six ratios is approximately 4 (i.e., 4.1), indicating that the initial diameter approximately quadruples in size when the cloud transforms into a "circulating thermal." To simulate a smooth, continuous transition from α_1 to α_2, centered around the time and depth corresponding with $\frac{r_c}{r_o} = 4$, the following hyperbolic tangent function was adopted:

$$\alpha = \frac{\alpha_1 + \alpha_2}{2} + \left(\frac{\alpha_1 - \alpha_2}{2}\right) tanh\left(2(4 - \frac{r}{r_o})\right) \tag{6.8}$$

The factor 2 within the *tanh* function in the above equation controls the slope of

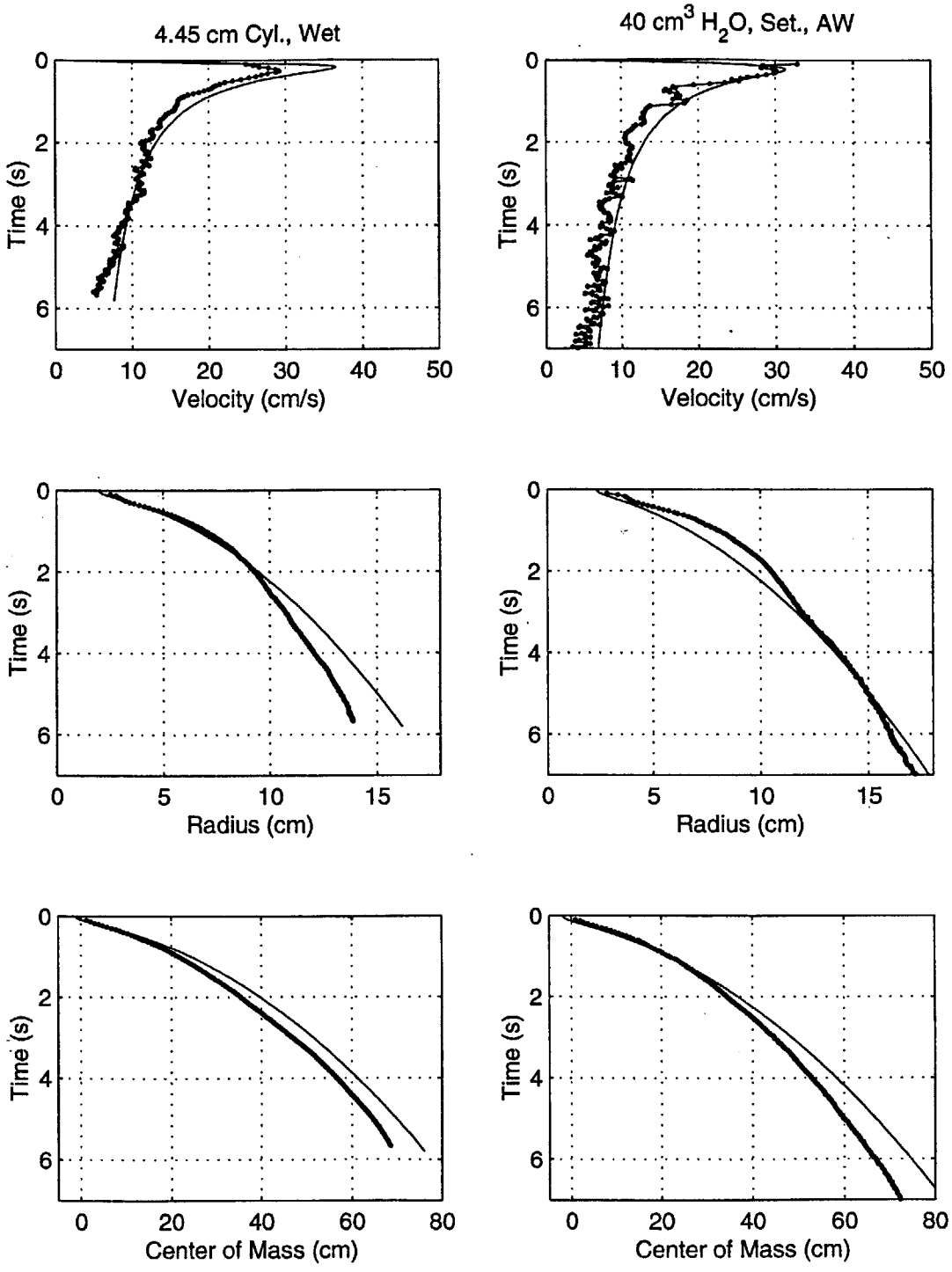

Figure 6-12: Forward model results using constant coefficients with mean α for 0.264 mm bead "Settled" experiments. Simulation results denoted by thin lines.

Experiment	α_1	α_2	C_D	k_1	k_2	$m_s(g)$	$\frac{r_c}{r_o}$
4.45 cm Cyl., Wet	0.22	0.15	0.01	0.01	0.5	40.0	3.9
40 cm^3 H_2O, Set., AW	0.22	0.15	0.01	0.01	0.5	40.0	3.9
40 cm^3 H_2O, Sus., AW	0.27	0.17	0.01	0.01	0.5	39.4	3.3
40 cm^3 H_2O, Sus., BW	0.27	0.17	0.01	0.01	0.5	34.0	3.8
0.024 mm Beads, AW	0.27	0.17	0.01	0.01	0.5	39.0	5.4
0.024 mm Beads, BW	0.27	0.17	0.01	0.01	0.5	33.2	4.5

Table 6.2: Forward model parameters - time-varying coefficients.

the line passing through the inflection point located at $\frac{r_c}{r_o} = 4$, with small values corresponding to a gentle slope and large values yielding a sharper transition.

The revised model prompts the user for the upper and lower limits for α (i.e., α_1 and α_2) and then uses Equation 6.8 to force a smooth transition with an inflection point occurring when $\frac{r}{r_o} = 4$. The variations in entrainment coefficients with respect to $\frac{r}{r_o}$ and time are shown in Figure 6.13 for the "settled" and "suspended" bead experiments.

To illustrate the effect of using a time-varying entrainment coefficient with the forward model, the model was run for two "settled" 0.264 mm bead experiments using Equation 6.8 while holding C_D and k constant at 0.01. As shown in Figure 6.14, incorporation of the time-varying α improves the model's ability to simulate proper cloud growth compared to using a constant α (Figure 6.8) but precludes the model's ability to maintain correct deceleration once the entrainment rate begins to change. The overpredictions in velocity shown in Figure 6.14 result from the fact that the time rate of change in cloud momentum, arising from a constant buoyancy force and comparatively small drag, remains fairly constant (i.e., $\sim t$) while the cloud mass decreases in accordance with the time-varying α). The net result is an increase in the computed velocity based on Equation 6.4. Hence, one approach for maintaining the correct deceleration rate (i.e., $\sim t^{-0.5}$) in this case is to increase the added mass, which basically is what the inverse model did when the velocity and data were "hard-wired" with the measured data.

To determine an appropriate time-varying function for k, the inverse model was

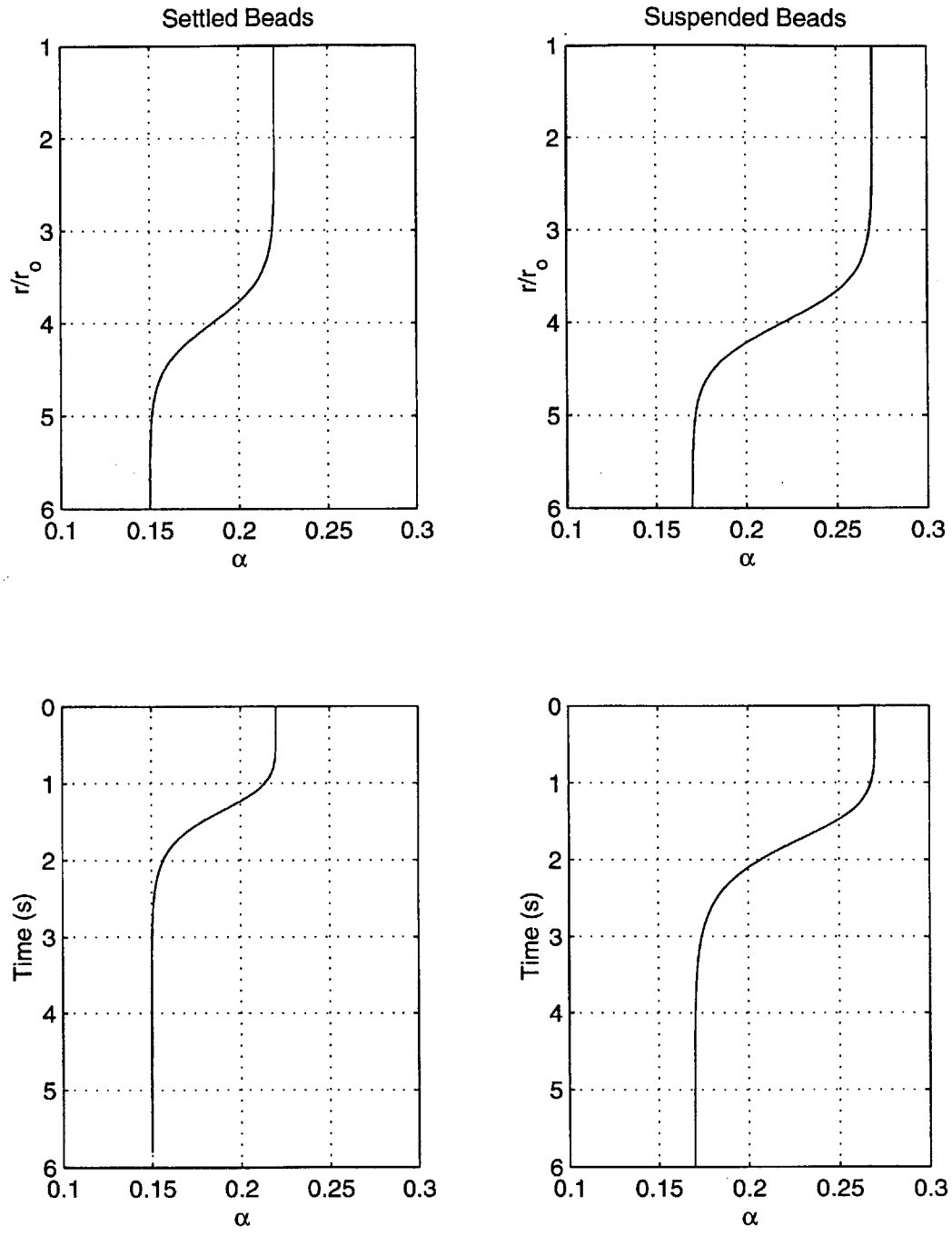

Figure 6-13: Hyperbolic tangent functions for α for "Settled" and "Suspended" bead experiments.

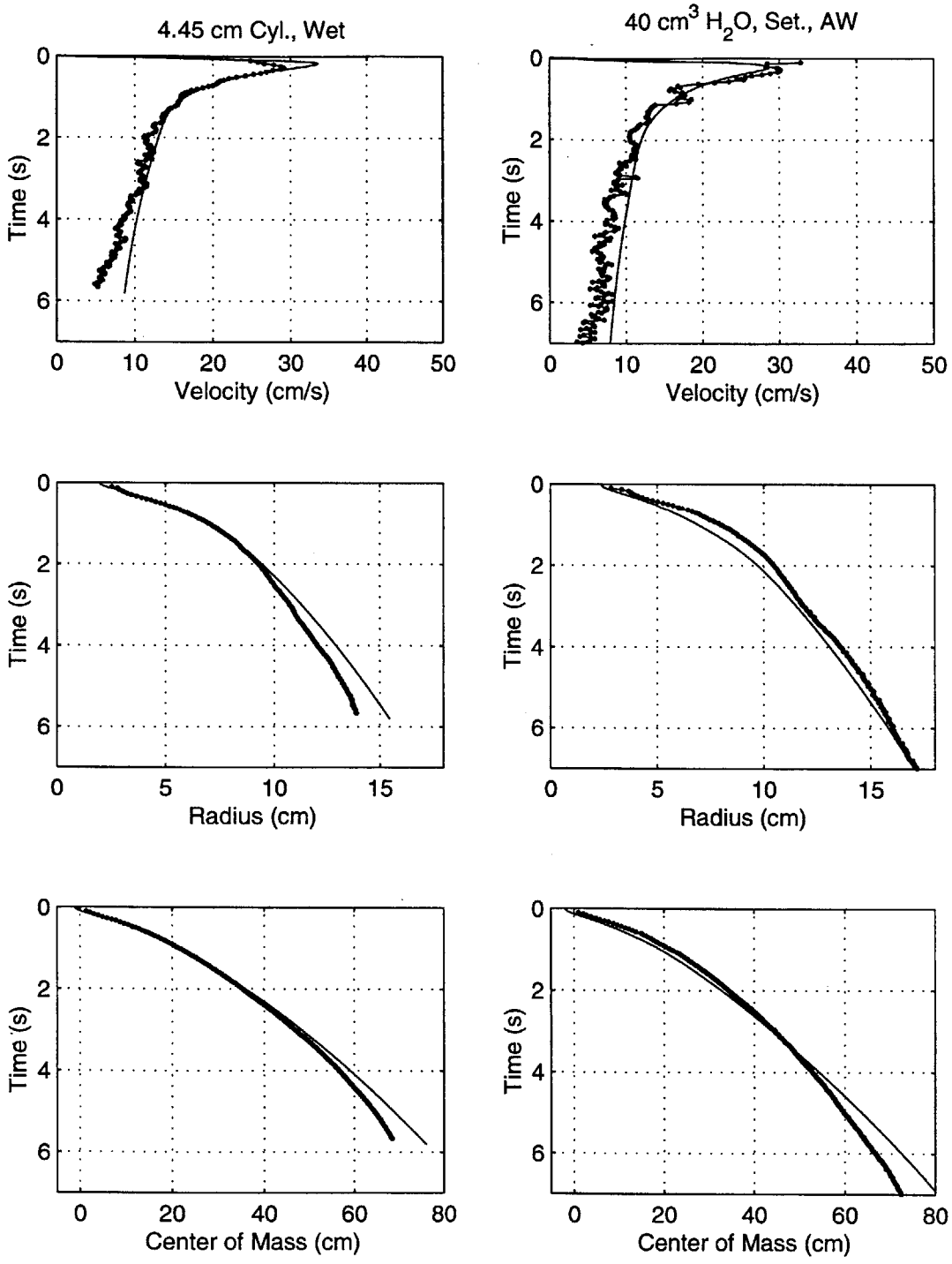

Figure 6-14: Forward model results using time-varying α and constant k for 0.264 mm bead "Settled" experiments. Simulation results denoted by thin lines.

run using Equations 6.1 and 6.8 to compute cloud growth rather than importing the actual measured radius data (i.e., fitted radius curves) as was previously done. As evident in Figure 6.15, this approach resulted in a new set of time-varying k values exhibiting different time variations but overall increasing trends, similar to the values generated from the actual (smoothed) radius data. As shown in Figure 6.15, in some cases, the inverse model again generated negative k values within the "thermal" phase as well values exceeding 0.5 in the "circulating thermal" region.

For modeling purposes, the curves in Figure 6.15 were approximated with a hyperbolic tangent function similar to Equation 6.8, using an inflection point at $\frac{r}{r_o} = 4$ but a with a more gentle transition produced by decreasing the coefficient inside the *tanh* function from 2 to 1 as shown below.

$$k = \frac{k_1 + k_2}{2} + \left(\frac{k_1 - k_2}{2}\right) tanh\left(1.0(4 - \frac{r}{r_o})\right) \tag{6.9}$$

The above equation was added to the forward model allowing the user to specify the upper and lower limits for k (i.e., k_1 and k_2), which, as shown in Table 6.2, were taken as 0.5 and 0.01 for simulating the six glass bead experiments using both time-varying α and k. The variation in k with respect to $\frac{r_c}{r_o}$ and time, using Equation 6.9, is shown in Figure 6.16. The upper and lower values selected for k basically bracket the range of plausible values with physical significance. As previously hypothesized, the increase in added mass in the glass bead experiments may be related to the transition from highly turbulent flow to more laminar motion resulting from energy dissipation due to particle collisions.

The results of the forward model simulations using the time-varying added mass and entrainment coefficients are presented in Figures 6.17 - 6.19. First comparing the results with time-varying α only (Figure 6.14) to those with variable α and k (Figure 6.17), one can see that the addition of the time-varying k function helps to correct the velocity decay rate, bringing the predicted profile closer to the measured data and improving the agreement in the center of mass positions. With respect to cloud growth, use of the time-varying k improved model performance for the "4.45

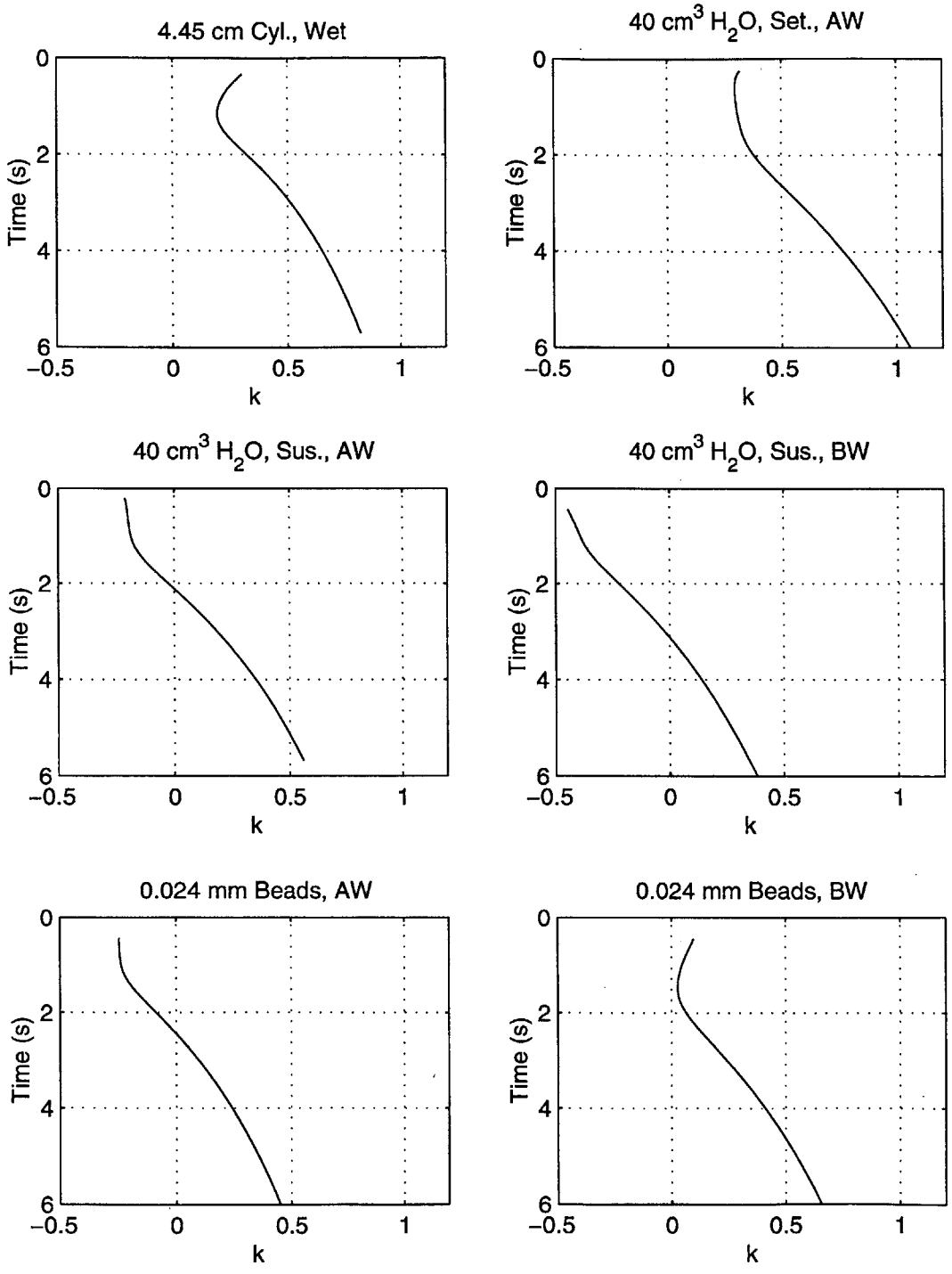

Figure 6-15: Inverse model results for added mass coefficient (k) using tanh function for α.

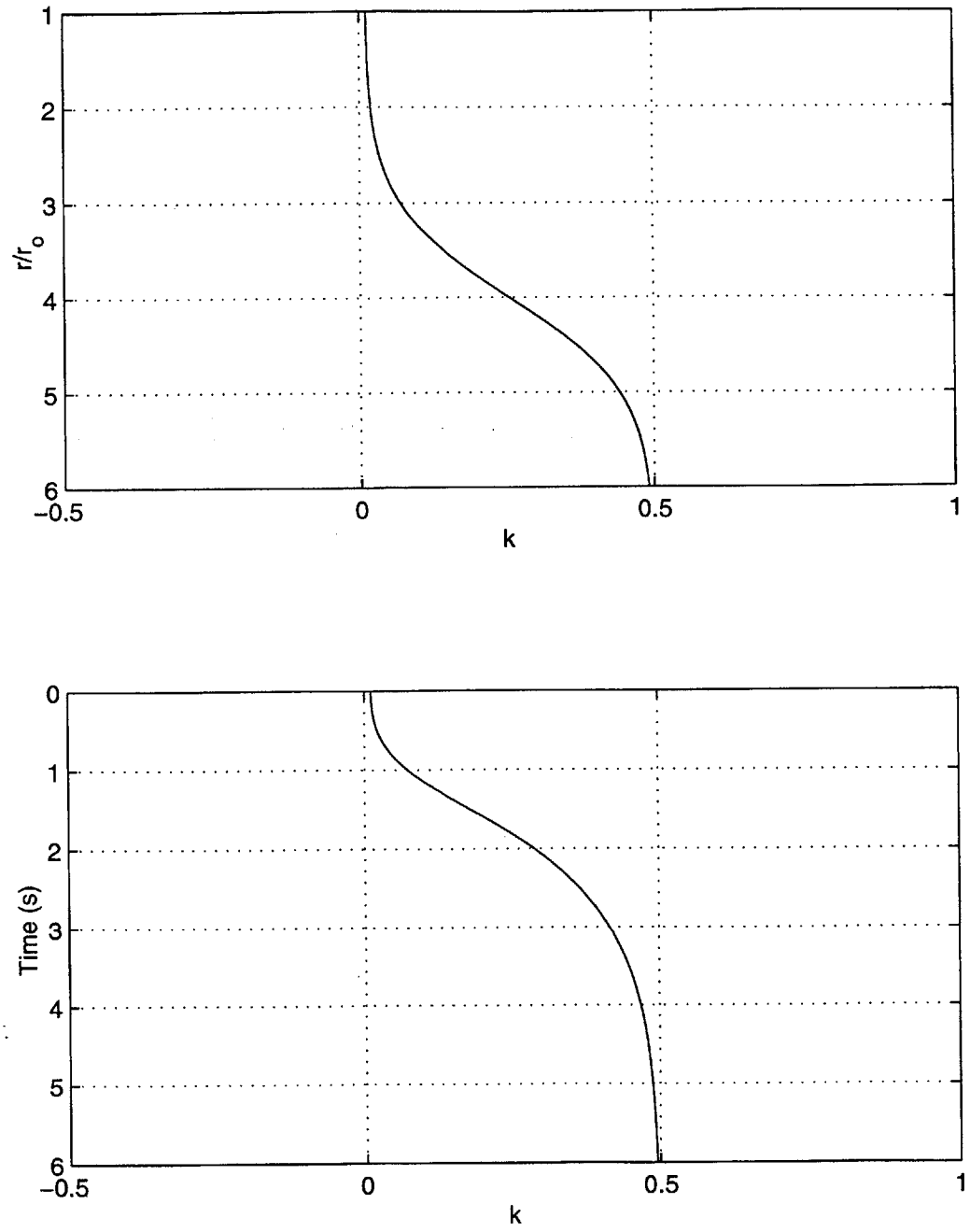

Figure 6-16: Hyperbolic tangent functions for k for glass bead experiments.

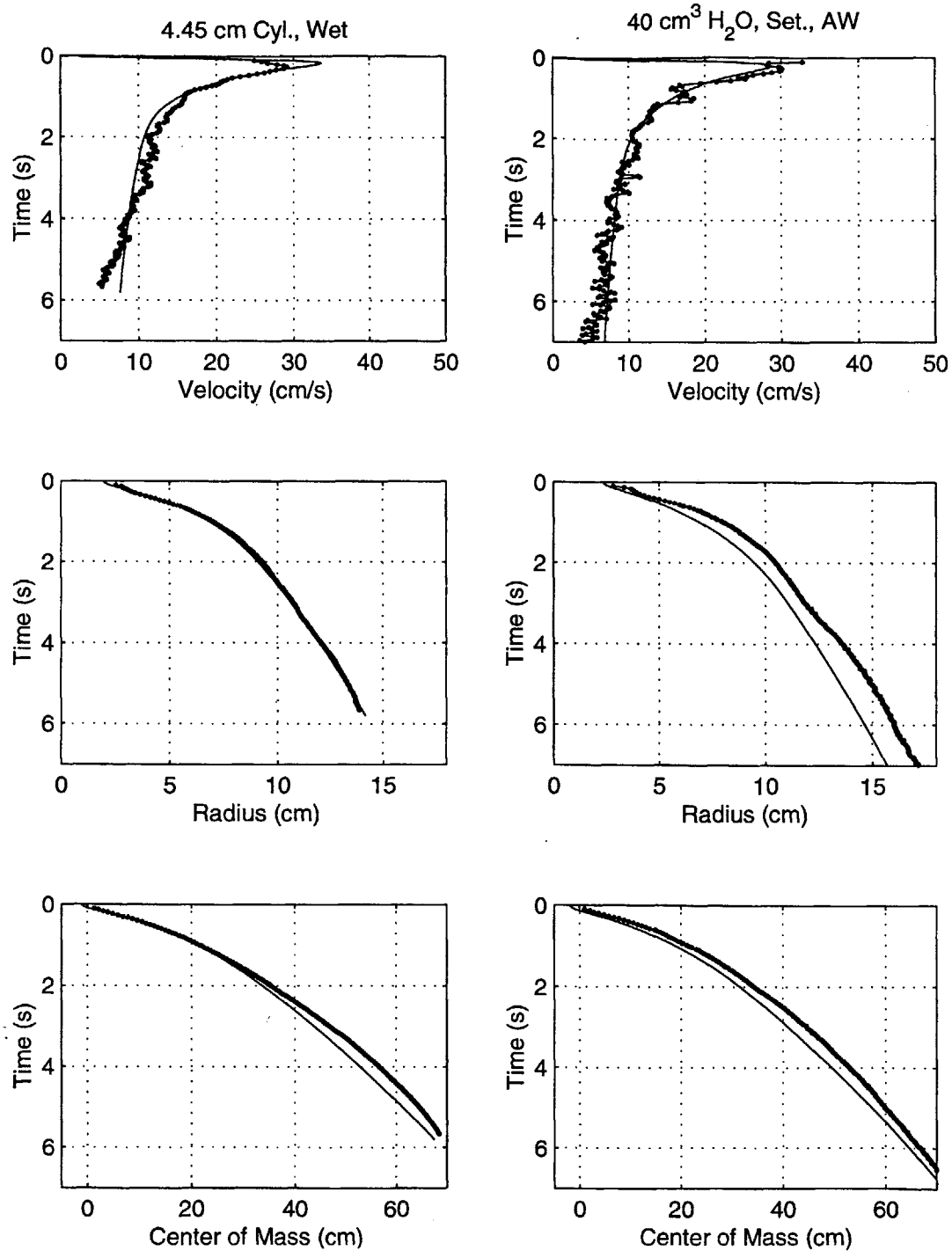

Figure 6-17: Forward model results using time-varying α and k for 0.264 mm bead "Settled" experiments. Simulation results denoted by thin lines.

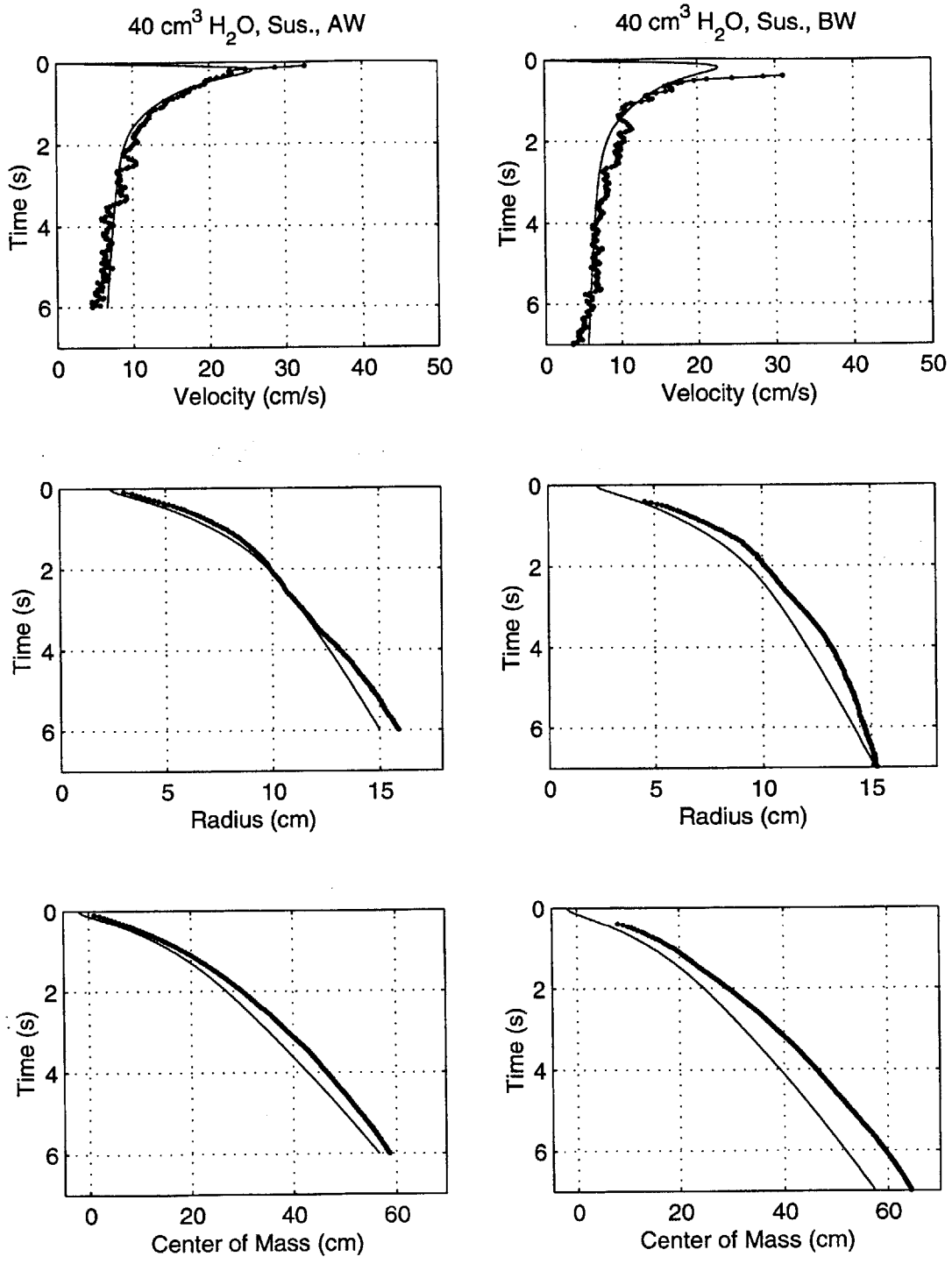

Figure 6-18: Forward model results using time-varying α and k for 0.264 mm bead "Suspended" experiments. Simulation results denoted by thin lines.

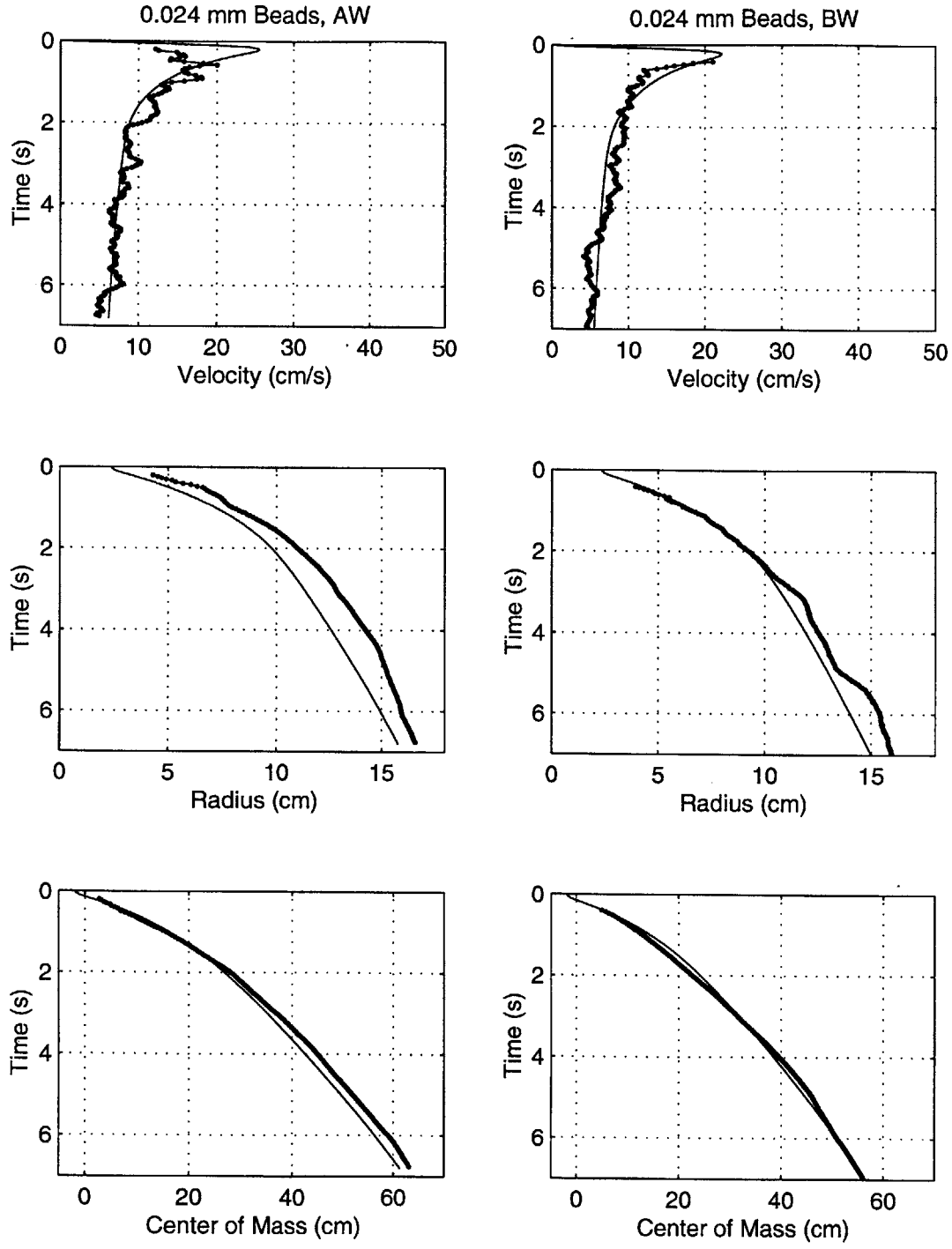

Figure 6-19: Forward model results using time-varying α and k for 0.024 mm bead "AW" and "BW" experiments. Simulation results denoted by thin lines.

cm Cyl., Wet" experiment while causing the model to underpredict cloud radius for the "40 $cm^3 H_2O$ Set., AW" experiment (Figure 6.17).

The addition of Equations 6.8 and 6.9 to the forward model improved radius predictions for some of the experiments by as much as 20 % compared to the constant coefficient simulations (Figures 6.8 - 6.10) with little sacrifice in the model's capability for simulating cloud velocity. As evident in Figures 6.8 - 6.10, the velocity profiles do not precisely follow a $t^{-0.5}$ type function as they did with constant α and k. In general, however, the velocity and center of mass values generated by the time-varying model are within 10 % of the measured data. The discrepancies are the result of approximating the time-varying k values shown in Figure 6.15 with the hyperbolic tangent function (Equation 6.9).

6.5 Real-World Scaling – Case Study Simulations

To provide insight into how the experimental data and associated model simulations scale to real-world dimensions, the "calibrated" forward model was applied to a 500 m deep disposal site. The ambient water was assumed to have a uniform density for this disposal depth, as it did in the laboratory experiments.

The results of the 500 m deep model simulations were analyzed from the perspective of three case studies: Boston Harbor, corresponding to a very shallow disposal scenario (15-20 m); Massachusetts Bay, representing a 100 m depth disposal scenario; and a third generic "deep-water" (500 m) disposal scenario.

The model simulations were conducted using both constant coefficients (i.e., α, C_D, and k) and time-varying α and k using the hyperbolic tangent functions described in Section 6.4.2 and the associated α_1/α_2 and k_1/k_2 limits. The initial conditions and model parameters used for the real-world simulations are summarized in Table 6.3. Representative initial barge volumes of 1,00 m^3, 1,000 m^3, and 5,000 m^3 were selected to bracket the range of split-hull barge sizes most commonly used in dredged material disposal operations. The initial density was chosen under the assumptions that sediment contained 50 % solids by weight prior to release. The α_1 and α_2 values

Simulation	α_1	α_2	C_D	k_1	k_2	$\rho_o(\frac{kg}{m^3})$
Constant α and k	0.25	0.25	0.01	0.01	0.01	1.43
Time-varying α and k	0.25	0.16	0.01	0.01	0.5	1.43

Table 6.3: Model parameters and initial conditions - shallow-water simulations.

were selected to represent their average values based on the twelve Group I, II, and III experiments discussed in Chapter 4.

Model results for the three barge volumes are shown in Figure 6.20. In Figure 6.20, the predicted velocities and radii are plotted against center of mass depth to show how these characteristics compare at the shallow Boston Harbor depth (15-20 m), the deeper Massachusetts Bay disposal site (100 m), and the generic deep-water (500 m) disposal site.

As discussed in Section 4.2, the depth (z_c) associated with the particle cloud transition from well-mixed "thermal" to "circulating thermal" was estimated for the three representative barge volumes as follows:

- barge volume = 100 m^3: $z_c = 49.5m$
- barge volume = 1,000 m^3: $z_c = 107m$
- barge volume = 5,000 m^3: $z_c = 182m$

As shown in Figure 6-20, the velocity profiles generated using both constant values and time-varying functions for α and k are very similar for all three barge volumes, particularly at depths less than 100 m, corresponding the Boston Harbor and Massachusetts Bay disposal sites. With respect to the predicted equivalent radius, the two curves generated with the constant and time-varying α and k values begin to diverge at the above transition z_c depth calculated for each barge volume. Hence, for disposal projects involving large volumes of sediment (i.e., $> 1,000\ m^3$) released at relatively shallow depths (i.e., $< 100\ m$), the use of a time-varying α and k does not appear to be justified, given their rather minor influence on predicted cloud velocities

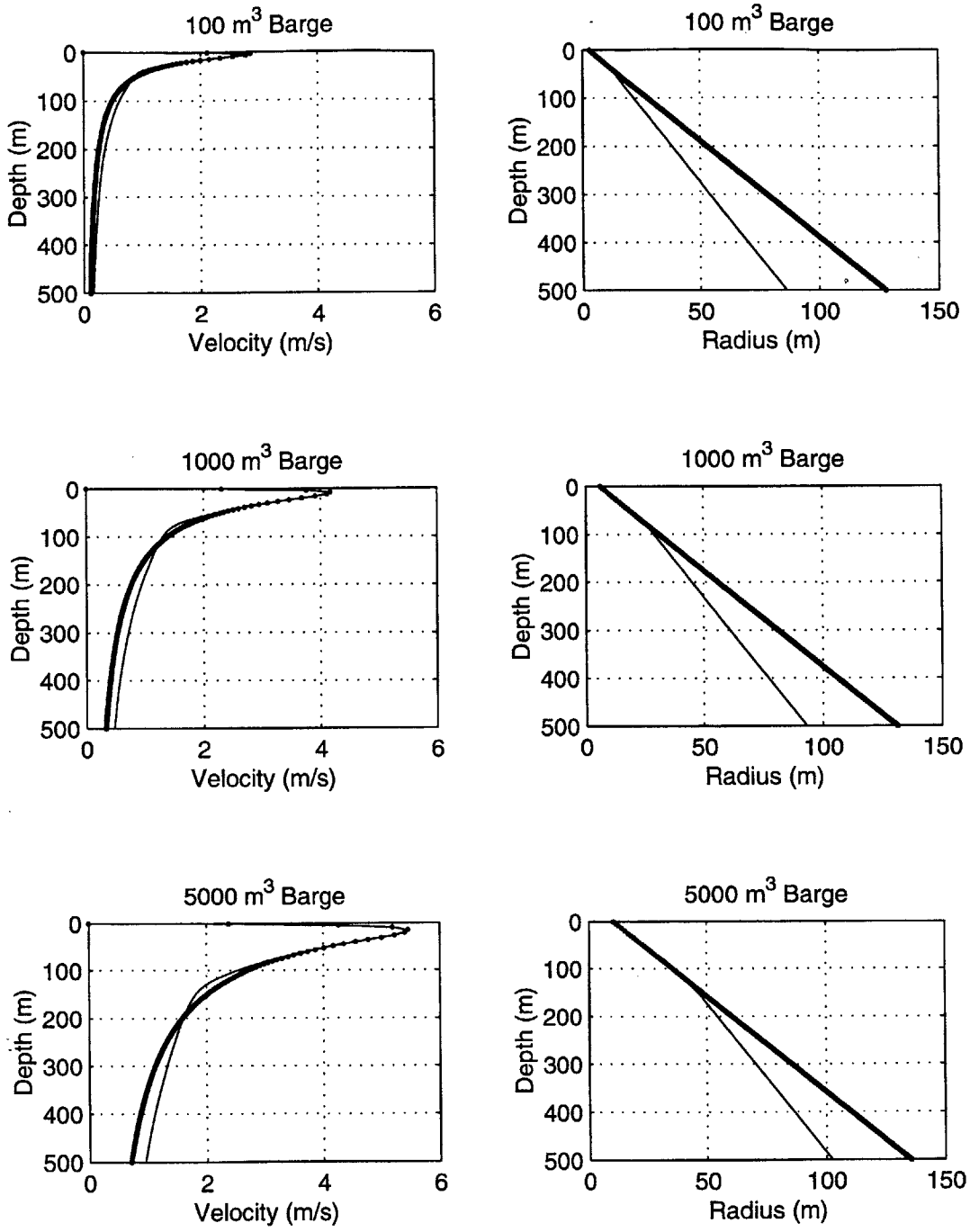

Figure 6-20: Real-world model simulation results using constant and time-varying coefficients for $100m^3$, $1,000m^3$, $5,000m^3$ barge volumes. Model results for constant and time-varying coefficients (α and k) denoted by thick and thin lines, respectively.

and radii at these depths. As the disposal depth increases beyond 100 m, the benefit of using time-varying α and k functions increases accordingly. At a 500 m deep site, for example, differences in predicted radius values using the constant and time-varying coefficients ranged from 28 % for the 5,000 m^3 volume to 39 % for the 100 m^3 volume, suggesting that use of constant α and k for deep-water sites would yield predicted radius values with similar accuracies.

As previously mentioned, the real-world model simulations were performed using a uniform density environment. Stratification regimes in temperate climates under fully stratified conditions (i.e., late August in the Northern Hemisphere) typically have a uniform density profile (i.e., well-mixed layer) within the upper 50 - 100 m of water (McLellan, 1965). Hence, the assumption of uniform density is valid for Boston Harbor and possibly also for Massachusetts Bay. Depending on the strength of stratification, the omission of ambient density stratification may not be justified at deeper sites, since the density gradient would decrease the (negative) buoyancy of the cloud and may ultimately cause it to collapse if the cloud reaches neutral buoyancy.

6.6 Conclusions

Sensitivity analysis results using the forward model indicate that predicted cloud velocities and growth rates are far more sensitive to variations in α than it is to changes in C_D and k. Variations in α resulted in velocity variations of more than 100 % compared to velocity variations of 10 - 20 % for similar changes in C_D and k.

Inverse model results using measured cloud radius and velocity data suggest that values of the drag (C_D) and added mass (k) coefficients are close to zero for particle clouds within the "thermal" phase in contrast to their values for an equivalent solid sphere (0.5). The small C_D value can be explained by the lack of flow separation around the cloud and associated form drag, as proposed by Escudier and Maxworthy (1973). The small added mass may be explained by the large entrainment rate associated with turbulent eddies. For larger particle sizes ($N_c > 10^{-4}$), the increase in k values resulting from the transition from well-mixed "thermal" to "circulating

thermal," and the corresponding reduction in α, may be explained by the dampening of turbulence by inter-particle collisions.

Forward modeling results suggest that an integral-type model, such as STFATE, used with constant coefficients, performs quite well (i.e., 10 % accuracy) in simulating particle cloud behavior (i.e., velocity deceleration and radial growth rate) in the "thermal" phase but overpredicts cloud growth in the "circulating thermal" phase by approximately 10 - 25 %. The results also suggest that time-varying entrainment and added coefficients are required to properly capture cloud velocities and growth rates for larger particle clouds ($N_c > 10^{-4}$) within the "circulating thermal" phase. These coefficients must be carefully co-varied so that velocity increases caused by decreases in α are properly offset by corresponding increases increases in k. Co-variations in α and k using hyperbolic tangent functions improved model radius predictions by 10 - 20 %.

The real-world scaling and model analysis suggest that disposal projects involving the release of large sediment volumes (i.e., $> 1,000\ m^3$) into shallow waters (i.e., $< 100\ m$) can be accurately simulated with an integral model employing constant coefficients, as the use of time-varying α and k has little impact on model performance at these depths. When N_c is greater than 10^{-4} and the depth exceeds 100 m, radius predictions in the "circulating thermal" phase can be improved by 10 - 50 % with the use of time-varying α and k.

Chapter 7

Boston Blue Clay Experiments

In addition to the experiments described in the previous chapters, performed using non-cohesive particles, a limited number of experiments was conducted with the help of Christopher Resto (1999) using natural Boston Blue Clay, a cohesive sediment excavated from Boston Harbor. The results of these experiments are compared to similar experiments performed by Bowers and Goldenblatt (1978). In their study, Bowers and Goldenblatt (1978) released silt suspensions with various water contents into tanks ranging from 0.46 m (18 in) to 2.74 m (9 ft) in depth. No information was provided with respect to particle size distribution other than to state that the materials consisted of silt sediments collected from New England and San Francisco Harbors.

7.1 Approach

The objective of this group of experiments was to investigate the influence of moisture content, or solids concentration, on the behavior of cohesive sediments. In contrast to the behavior of non-cohesive particles, Boston Blue Clay can be characterized as a Bingham plastic. A Bingham plastic will begin to deform ("flow") when the shear stress (τ) applied to the material exceeds a certain threshold, known as the yield stress (τ_o). Below τ_o, the material behaves like a solid. Once τ_o is exceeded, the shear stress and shear rate are related through the apparent viscosity (μ_a), which is not constant

for an ideal Bingham plastic. Though most clay materials are not truly ideal Bingham plastics, the behavior of many clay suspensions can be approximated by the Bingham plastic model (Brodkey, 1967). As one might anticipate, the yield stress of a clay material is inversely proportional to its water content. More specifically, Davies and Rideal (1961) demonstrate that for various types of clay suspensions (0.0004 - 0.013 mm diameters), τ_o is proportional to the cube root of the solids volume fraction and inversely proportional to the particle diameter. Based on the relationship between τ_o and solids concentration, one would expect cohesive sediments with a high water content to form "thermal-like" particle clouds, similar to the the silt particle clouds, and those with a very low water content to behave like a solid (i.e., fall as solid clump). To investigate this range of behaviors, four experiments were conducted using the solids fractions and associated water contents shown below:

- 36 % solids, 178 % moisture
- 40 % solids, 150 % moisture
- 44 % solids, 127 % moisture
- 48 % solids, 108 % moisture

The percent solids values were derived by dividing the mass of solids by the total mass, whereas, the percent moisture was calculated by dividing the mass of water by the mass of solids.

Based on experiments using natural harbor sediments with high silt contents, Bowers and Goldenblatt (1978) determine that sediments containing less than about 75 % moisture fall as one solid clump with little or no entrainment, while those containing more than about 175 % moisture form "thermal-like" particle clouds with similar entrainment coefficients ($\alpha = 0.25 - 0.30$). Between these limits, the authors observe a transition phase in which entrainment coefficient varies in a nonlinear manner. The range of solids concentrations shown above was chosen to investigate the behavior of cohesive sediments within this transition range. A handful of experiments

were performed using a 50 % solids concentration, which show the sediment falling as one solid clump.

For each experiment, the initial buoyancy was held constant ($B_o = 23,520\ gcms^{-2}$) by mixing 40 g of clay with the appropriate volume of water to produce the percent moistures shown above. The 4.45 cm release cylinder was used for all experiments in this group, which was positioned immediately above the water surface ("AW"). Before placement in the release cylinder, all clay suspensions were homogenized in a blender and then stirred inside of the cylinder prior to release.

Three repetitions were performed for each experiment. Upon release from the cylinder, the clay suspensions formed flocs and clumps of various sizes that settled out of the cloud at different times, precluding edge detection using the automated MATLAB^{TM} program described in Chapter 3. Furthermore, the greyish-colored clay suspensions significantly attenuated the laser light sheet, resulting in a poor contrast in intensity levels between the cloud and ambient water. For these reasons, cloud volumes and center of mass positions could not be calculated by the methods outlined in Chapter 3. In lieu of these methods, the leading edge position and maximum radius values were determined manually for each image using the "point-and-click" approach with the computer mouse and associated MATLAB^{TM} commands. Hence, the estimated entrainment coefficients and cloud velocities presented in the next section were based on the maximum cloud radius and leading edge position rather than the equivalent radius and center of mass. Leading edge positions were determined by estimating the approximate front edge of the parent cloud excluding any settling flocs or clumps preceding the cloud.

7.2 Cloud Growth and Velocity Results

Representative images for the four experiments, showing the descent of the particle clouds at selected time intervals, are presented in Figure 7.1. As shown in Figure 7.1, clouds formed from the most dilute clay suspension (36 % solids) are similar in appearance to the silt clouds shown in Figure 4.4. Since these clouds remained

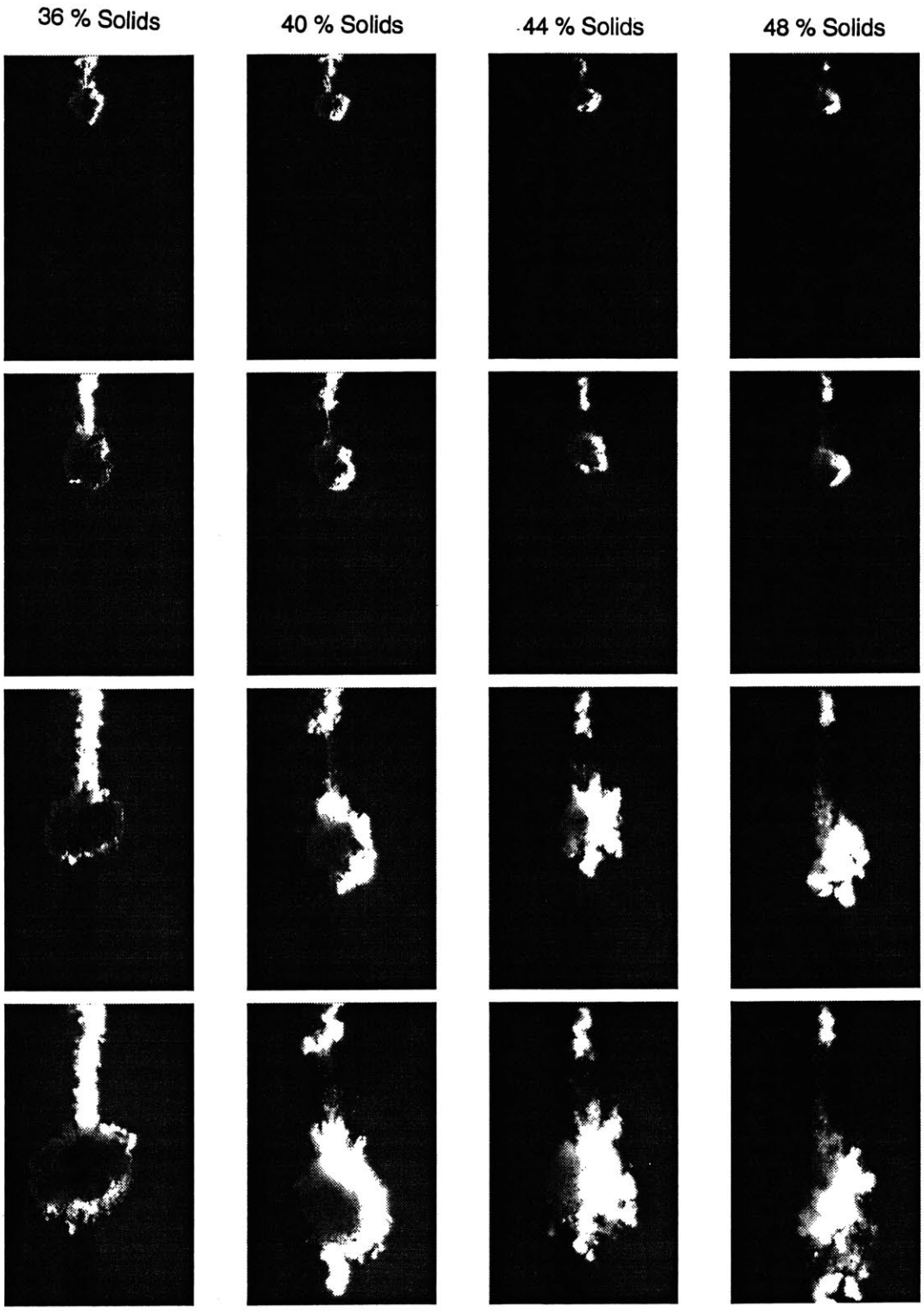

Figure 7-1: Selected cloud images at 0.5 s, 1 s, 2 s, and 3 s - Boston Blue Clay experiments.

relatively spherical in shape, the maximum radius for this experiment should roughly equal the equivalent radius. As evident in the 3.0 s image for the 36 % solids cloud in Figure 7.1, at this concentration, the clay particles aggregated into pea-sized flocs that eventually settled out of the cloud. The pea-sized flocs were not the result of inefficient mixing, as the flocculation process was observed when a small quantity of the clay slurry was added to a beaker of water. Flocculation was not observed in later experiments in which potassium hydroxide was added to the initial slurry to raise the pH and inhibit inter-particle attraction. The images for the 40 %, 44 %, and 48 % solids experiments reveal larger-sized clay clumps with increasing solids concentration. After about 2 s of descent, the clay suspensions containing 48 % solids typically broke into several (2 - 4) smaller clouds that fell very quickly with little entrainment. The radial cloud growth evident in this experiment may be mostly the result of dispersion of the clumps rather than turbulent entrainment.

Also evident in Figure 7.1, are "stems" of material trailing behind the main cloud, similar to the silt "stems" discussed in Chapter 5. Separation of these "stems" from the main cloud can be observed in the images for the 40 %, 44 %, and 48 % solids experiments. The behavior of the "stems" was likely influenced by the solids concentration in the original material. Though difficult to discern in the Figure 7.1 "snapshots," video footage shows material shearing off, or "stripping" away, from the large clay clumps falling in the 48 % solids experiment. No sediment trap experiments were performed to quantify this material.

In Figure 7.2, the mean values of the maximum radius data for the three repetitions are plotted against the mean leading edge depths for each experiment. Radius versus depth profiles for all repetitions are provided in Appendix F. Superimposed on the measured data are the corresponding least squares linear regression lines whose slopes were used to determine the mean entrainment coefficient for each experiment. The resulting mean and range of entrainment coefficients for the three repetitions are listed in Table 7.1. Also included in Table 7.1 are the approximate corresponding α values taken from the curve used by Bowers and Goldenblatt (1978) to fit their measured harbor silt data, which is provided in Figure 7.3.

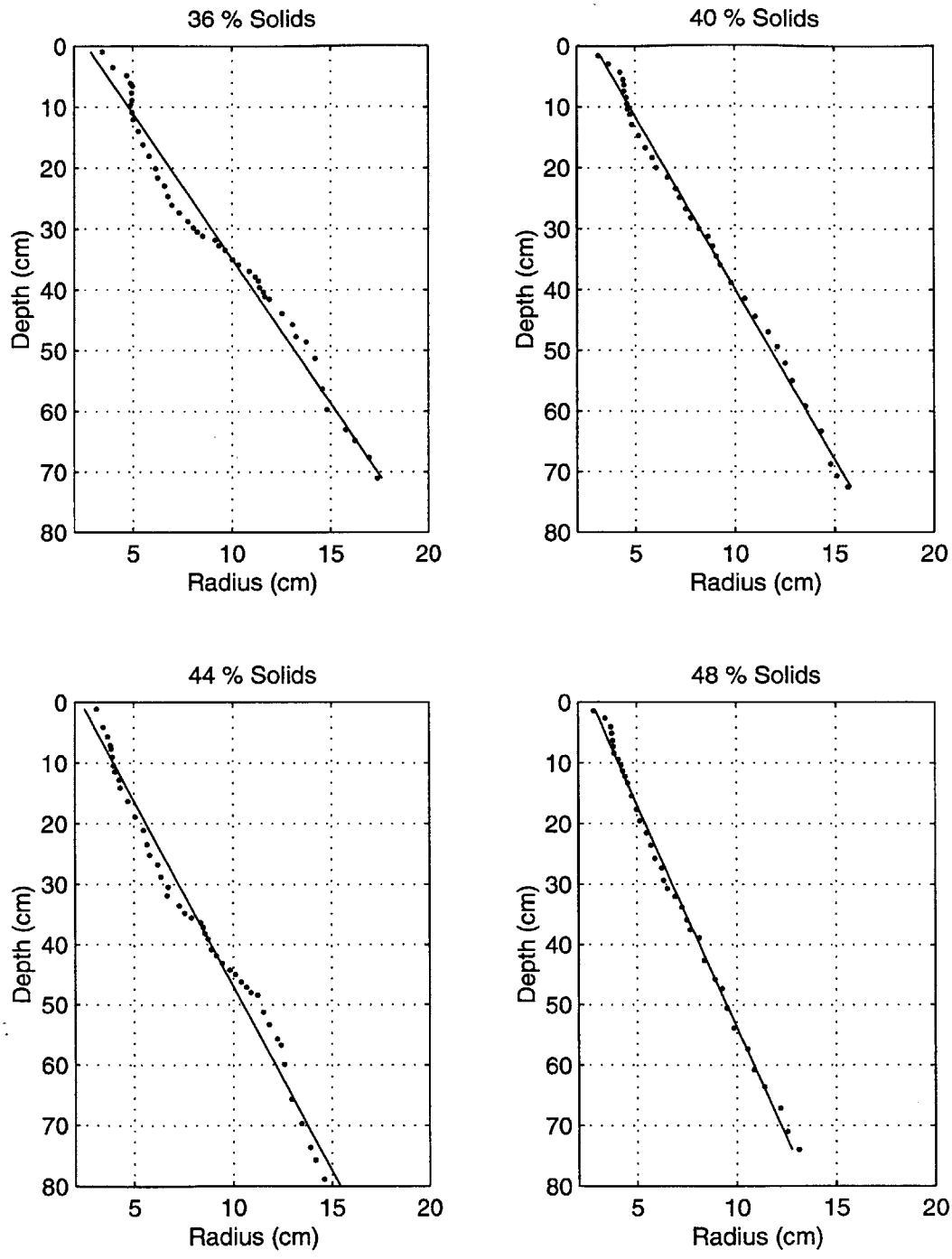

Figure 7-2: Maximum radius versus leading edge position with fitted linear regression lines - Boston Blue Clay experiments.

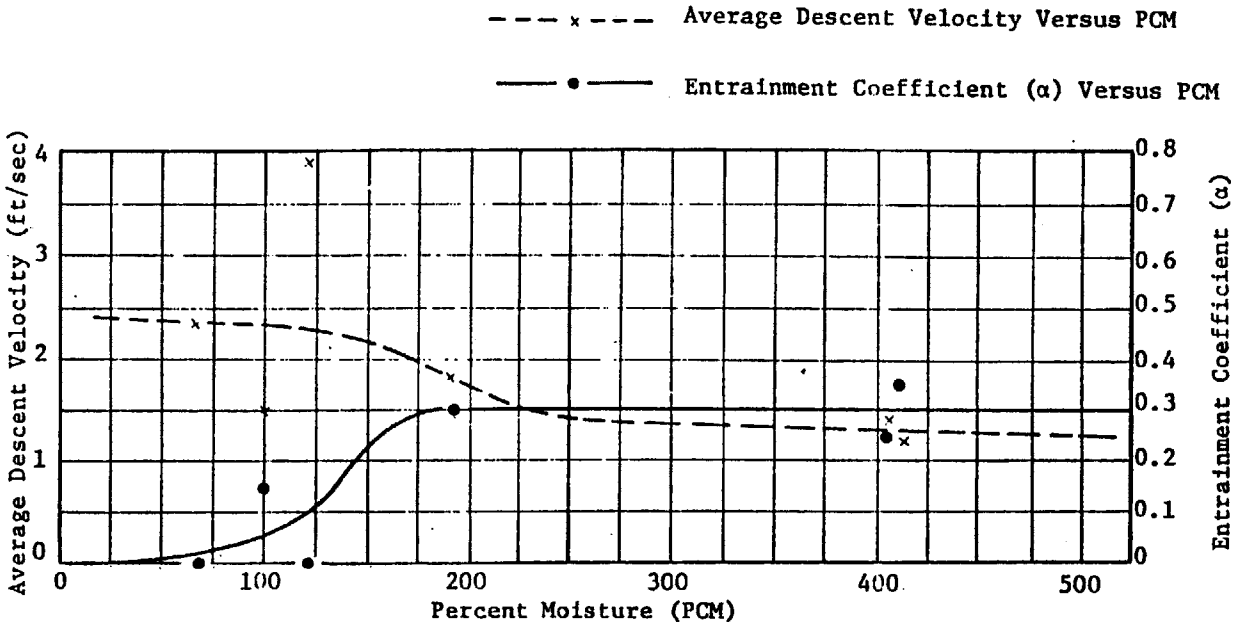

Figure 7-3: Effect of moisture content on cloud velocity and entrainment coefficient - harbor silt experiments (after Bowers and Goldenblatt, 1978).

Experiment	α *(Boston Blue Clay)*	α *(Harbor Silt)*
36 % Solids, 178 % Moisture	0.22 ± 0.02	0.30
40 % Solids, 150 % Moisture	0.18 ± 0.02	0.23
44 % Solids, 127 % Moisture	0.17 ± 0.01	0.12
48 % Solids, 108 % Moisture	0.14 ± 0.01	0.06

Table 7.1: Entrainment coefficient results – Boston Blue Clay experimental results and interpolated values based on harbor silt experiments (from Bowers and Goldenblatt, 1978).

With respect to increases in solids concentration, the entrainment coefficient results from the Boston Blue Clay and harbor silt experiments show similar decreasing trends. Differences in α values between the two sets of data may be due to differences in material composition. Bowers and Goldenblatt (1978) used larger silt particles that may have also contained organic matter. Thus, the cohesive forces between particles in their materials, and associated viscosity, may have been weaker than those in the Boston Blue Clay. As shown in Figure 7.3, there is a high degree of uncertainty associated with the form of the hyperbolic tangent-type curve used by Bowers and Goldenblatt (1978), since it is based on only a handful of sparse data points. Similarly, the limited number of α values for the Boston Blue Clay experiments do not permit formulation of an explicit function correlating α with solids concentration within the transition region, other than to show that the relationship appears to be nonlinear. A complex, nonlinear growth rate behavior in the transition region is not unexpected due to the influence of viscosity, which continually decreases as the solids concentration decreases in the entraining cloud. For dilute suspensions, the relationship between apparent viscosity (μ_a) and volume fraction solids has been shown to obey various power laws (Thomas, 1963). The mixing length associated with turbulent entraining eddies may scale in proportion to the apparent viscosity divided by the scale of velocity fluctuations. In addition to entrainment, variations in the (macro) particle size distribution in the cloud, caused by the flocculation and subsequent breakup (shearing) of particles, undoubtedly play a role the time-variation of μ_a. These factors, when taken together, result in a very complicated, material-specific

cloud behavior within the transition region.

As shown in Figure 7.4, the mean leading edge velocity profile for 36 % solids experiment resembles the typical asymptotic shape produced by the glass bead and silt particle clouds. Velocity profiles for all repetitions are provided in Appendix F. As the solids fraction increases, the deceleration rate decreases due to the decrease in entrainment rate. The mean velocity profile for 48 % solids experiment begins to resemble that of a solid sphere (i.e., constant terminal velocity). The mean velocity versus time data for each experiment were plotted on a log-log scale to compare their deceleration rates to that of a true thermal (i.e., $w \sim t^{-0.5}$). The data in these plots were fitted with linear regression lines from which the following slopes were obtained:

- 36 % solids: m = -0.44
- 40 % solids: m = -0.32
- 44 % solids: m = -0.28
- 48 % solids: m = -0.14

The above data show that cloud deceleration approaches "thermal-like" behavior as the solids fraction decreases below 36 %, while cloud velocity becomes more constant (i.e., similar to a solid) as the percent solids increases above 50 %.

7.3 Conclusions

The results from the Boston Blue Clay and Bowers and Goldenblatt (1978) experiments suggest that cohesive sediments containing less than 36 % solids by weight (percent moisture > 175 %) form "thermal-like" clouds with constant entraiment coefficients (α = 0.2 - 0.3) and asymptotic deceleration ($w \sim t^{-0.5}$). Sediments containing more than 50 % solids (percent moisture > 100 %) can be expected to fall as one or more solid clumps descending at their terminal velocities with minimal deceleration and entrainment (($\alpha < 0.1$). The lack of entrainment results in material being sheared away from the solid clumps. In between these solids fractions

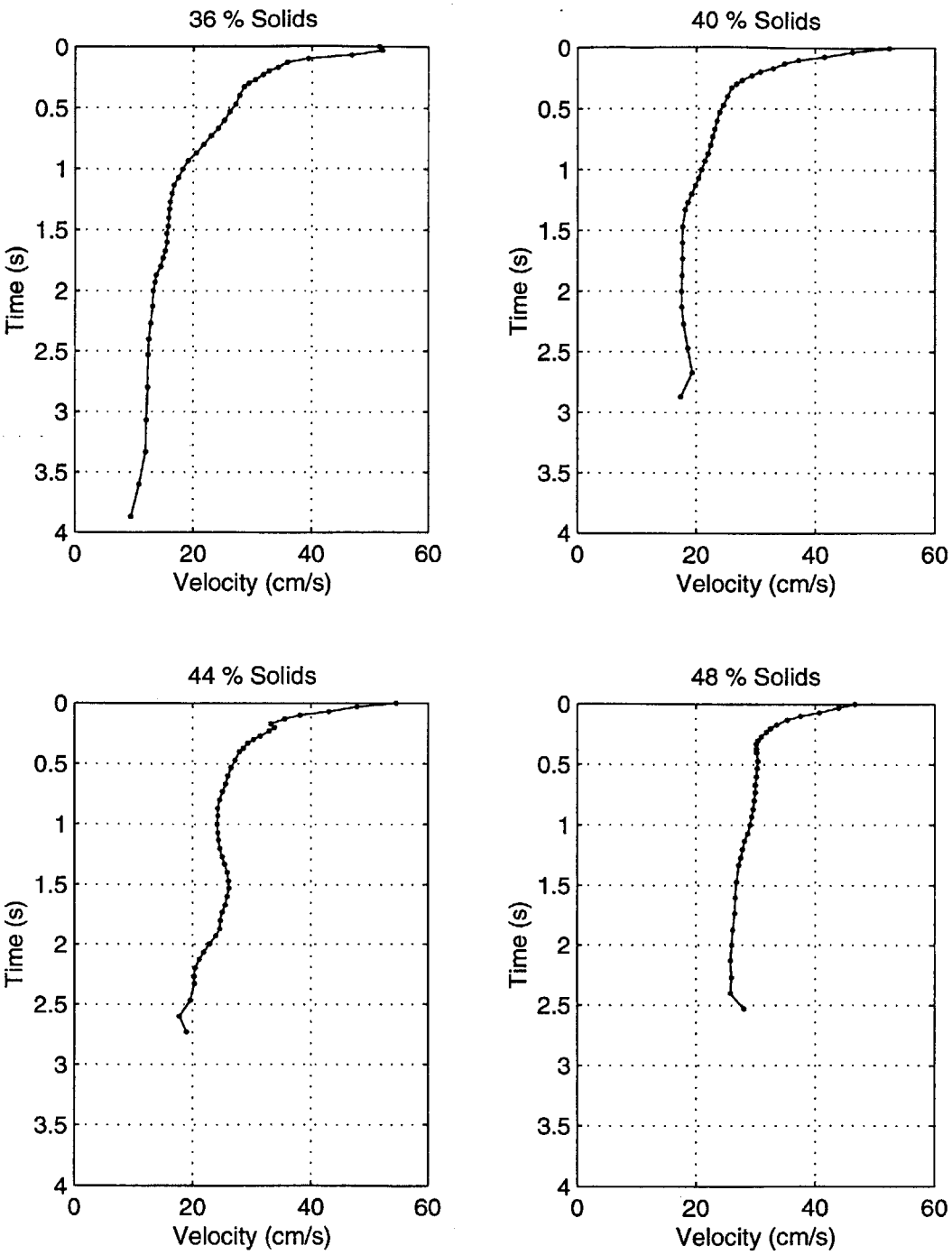

Figure 7-4: Leading edge velocity versus time - Boston Blue Clay experiments.

(36 - 50 %), particle clouds exhibit a hybrid-type behavior, breaking into several to many smaller-sized clumps with α values ranging from 0.1 - 0.2.

Chapter 8

Conclusions and Recommendations for Future Work

The general conclusions of the work are outlined in this chapter followed by a list of recommended areas for future work.

8.1 Conclusions

The overall conclusions based on the research discussed herein are summarized below.

- Non-cohesive sediments evolve rapidly into turbulent particle clouds characterized by asymptotic deceleration (velocity $(w) \sim t^{-\frac{1}{2}}$) and linear growth rates (radius $(r) \sim z$) similar to "classical thermals" with entrainment coefficients (α) in the range of 0.2 - 0.3.

- For fine-grained cohesive materials, sediments containing less than 36 % solids (by weight) form self-similar clouds with "thermal-like" characteristics ($w \sim t^{-\frac{1}{2}}; \alpha = 0.2 - 0.3$). Sediments within the transition range (36 - 50 % solids) exhibit a hybrid-type behavior with entrainment rates that vary in a non-linear manner ($\alpha = 0.1 - 0.2$). Sediments containing more than 50% solids fall as one or more solid clumps, with a constant terminal velocity and little or no entrainment.

- Once the largest eddies approach the scale of the cloud radius, particle clouds evolve from well-mixed "thermals" into "circulating thermals" characterized by a bimodal buoyancy distribution and linear growth rate predicted by buoyant vortex ring theory ($\alpha \sim \frac{B}{K^2}$). The transition to "circulating thermal" occurs when the cloud equivalent radius doubles in size relative to its initial submerged radius or quadruples in size relative to its initial (pre-release) radius.

- In the "circulating thermal" phase, large particles ($N_c > 10^{-4}$) dampen small-scale eddies, resulting in lower entrainment rates ($\alpha = 0.1 - 0.2$) and dense, rotating cores exhibiting laminar characteristics.

- Compared to cohesive sediments, which exhibit a wide range of behavior, variations in the initial conditions of non-cohesive sediments, namely water content, particle settling, and release time (momentum), produce relatively minor variations (10 - 20 %) in cloud velocities and growth rates.

- Results from sediment trap experiments suggest that there is no "stripping" mechanism associated with the convective descent of entraining particle clouds in unstratified waters, as material incorporated into the cloud during initial formation is sequestered via entrainment mechanisms. There also appears to be no size-dependent particle "stripping" mechanism that causes fine particles to separate (detrain) from larger particles in a heterogeneous cloud. Shear forces can "strip" material from cohesive sediments falling as one or more solid clumps and experiencing little or no entrainment.

- Sediments released as a suspension form a narrow "stem" of material behind the cloud, containing 2 - 8 % of the original mass for above-water releases and 21 - 31 % for below-water releases. The majority the "stem" falls as a density plume that ultimately becomes re-entrained into the cloud or impacts the bottom shortly after it (in unstratified waters). Particle size, or cloud number (N_c), does not appear to influence the "stem" formation process. The large percentage of "stem" material produced by the below-water releases appears to be due to

the "stalling effect" caused by the return flow of water and particles into the cylinder, which would not occur in actual barge releases. The "stems" generated from initially "settled" beads contained considerably less material (1.6 - 5.8 %) than those produced by "suspended" particles. Hence, the amount of "stem" material expected to form under real-world conditions is likely within the 2 - 21% range.

- The last fraction of material to exit the release vessel fails to be incorporated into the "stem" and thus may be transported by passive diffusion and ambient currents. Experimental observations and measurements suggest this fraction to be less than 1 % of the original mass for non-cohesive sediments.

When applying an integral model to particle cloud descent, the following recommendations are suggested:

- The "stripping" of particles from the cloud is best simulated by subtracting the last fraction of material to exit the vessel from the initial mass.

- The volumetric growth associated with initial cloud formation can be approximated by the "thermal" phase entrainment coefficient (α_1).

- Sediment volumes can be released from rest (i.e., with no initial momentum) without consideration of initial potential energy (release height) and associated entrance velocity since these factors have little influence on cloud mechanics in the deceleration ("thermal") phase.

- Sensitivity analysis results show that model performance in the deceleration phase is most sensitive to α and relatively insensitive to the drag (C_D) and added mass (k) coefficients. Thus, most attention should be paid to selecting the appropriate value for α.

- With small particle sizes ($N_c < 10^{-4}$) and in shallow depths (< 100 m), α value should be held constant in the range of 0.2 - 0.3, with the upper limit corresponding to loose, suspended sediments and the lower limit corresponding

to dense, settled materials. When using a constant α, small values (i.e., 0.01 - 0.1) should be used for k and C_D.

- When N_c is greater than 10^{-4} and the depth exceeds 100 m, radius predictions in the "circulating thermal" phase can be improved by 10 - 50 % by decreasing α by 33 % and increasing k to 0.5. The amount of improvement increases with water depth.

8.2 Recommendations for Future Work

Future research needs based on the findings of this work are summarized below.

- With respect to the influence of the initial conditions on the convective descent dynamics of particle clouds, cohesive characteristics (e.g., yield strength, liquid limit) of fine-grained sediments appear to play the largest role in determining the type of behavior (i.e., "thermal-like" or "solid-like") and associated particle stripping mechanisms. A better understanding is therefore needed as to how dredging techniques (e.g., clam-shell bucket type and size) and pre-release settling affect the composition of (i.e., clump sizes) and cohesive characteristics of barged sediments on a macro-scale. In conjunction with this effort, more experimental research is needed to investigate the behavior of such heterogeneous and cohesive materials.

- To better predict the amount of material that may be "lost" to the environment (i.e., transported by ambient currents), the process of "stem" formation (i.e., inclusion/exclusion of material during release) must be better understood. More insight into the convective descent dynamics of the "stem" itself is needed as well as its influence on the behavior of the parent cloud, such as subsequent re-entrainment or detachment.

- Laboratory experiments show "stem" formation to be highly dependent on how quickly the sediment is released. Most of the sediment trap experiments presented herein were performed over a limited range of release geometries (i.e.,

cylindrical vessel with $\frac{H}{D} = 0.8$) and solids concentrations (50 % solids). Thus, more research is needed on how the composition and dynamics of the "stem" are affected by the range of real-world sediment compositions and release geometries of scows and split-hull barges.

Appendix A

Experiment Cross-Reference Tables

In the table below, experimental groups refer to experiments discussed in Chapter 4. Initial particle mass denoted by m_o. Cylinder diameter denoted by D_o. Amount of water added denoted by H_2O. AW'and BW refer to releases above and below the water surface, respectively. Set. and Sus. refer to particles released from an initially settled or suspended state, respectively.

Number	*Experiment*	$m_o(g)$	$D_o(cm)$	$H_2O(cm^3)$	*Cyl. Pos.*	*Sus./Set.*
0.556 mm Glass Bead Experiments						
b001	4.45 cm Cyl., Dry	40	4.45	0	AW	Set.
b002	3.81 cm Cyl., Dry	40	3.81	0	AW	Set.
b003	3.18 cm Cyl., Dry	40	3.18	0	AW	Set.
b004	2.54 cm Cyl., Dry	40	2.54	0	AW	Set.
b006	4.45 cm Cyl., Wet	40	4.45	17	AW	Set.
b007	3.81 cm Cyl., Wet	40	3.81	17	AW	Set.
b008	3.18 cm Cyl., Wet	40	3.18	17	AW	Set.
b009	2.54 cm Cyl., Wet	40	2.54	17	AW	Set.

Number	*Experiment*	$m_o(g)$	$D_o(cm)$	H_2O	*Cyl. Pos.*	*Sus./Set.*
Group I Experiments						
d020	4.45 cm Cyl., Dry	40	4.45	0	AW	Set.
d021	4.45 cm Cyl., Wet	40	4.45	17	AW	Set.
d022	3.18 cm Cyl., Dry	40	3.18	0	AW	Set.
d023	3.18 cm Cyl., Wet	40	3.18	17	AW	Set.
Group IV and V Experiments						
d027	4.6 cm AW	97	4.45	33	AW	Set.
d028	2.3/2.3 cm AW/BW	97	4.45	33	AW/BW	Set.
d029	4.6 cm BW	97	4.45	33	BW	Set.
d030	$\frac{H_o}{D_o} = 0.8$	40	3.81	17	AW/BW	Set.
d031	$\frac{H_o}{D_o} = 1.1$	40	3.18	17	AW/BW	Set.
d032	$\frac{H_o}{D_o} = 2.6$	40	2.54	17	AW/BW	Set.
Group II Experiments						
d040	40 cm^3 H_2O, Sus.	40	4.45	40	AW	Sus.
d041	40 cm^3 H_2O, Sus.	40	4.45	17	AW	Sus.
d042	40 cm^3 H_2O, Set.	40	4.45	40	AW	Set.
d053	40 cm^3 H_2O, Sus.	40	4.45	40	BW	Sus.
Group III Experiments						
i004	0.024 mm Beads	40	4.45	40	AW	Sus.
i005	0.024 mm Beads	40	4.45	40	BW	Sus.
s003	0.010 mm Silt	40	4.45	40	AW	Sus.
s004	0.010 mm Silt	40	4.45	40	BW	Sus.
0.002 mm Boston Blue Clay Experiments						
bc09	36 % Solids	40	4.45	71.2	AW	Sus.
bc10	40 % Solids	40	4.45	60.0	AW	Sus.
bc11	44 % Solids	40	4.45	50.8	AW	Sus.
bc12	48 % Solids	40	4.45	43.2	AW	Sus.

Appendix B

Selected Images for Group I, II, and III Experiments

The following pages depict selected cloud images of the five repetitions performed for each of the twelve experiments included in Groups I, II, and III. The experiment numbers included in each group are listed in the cross-reference table provided in Appendix A.

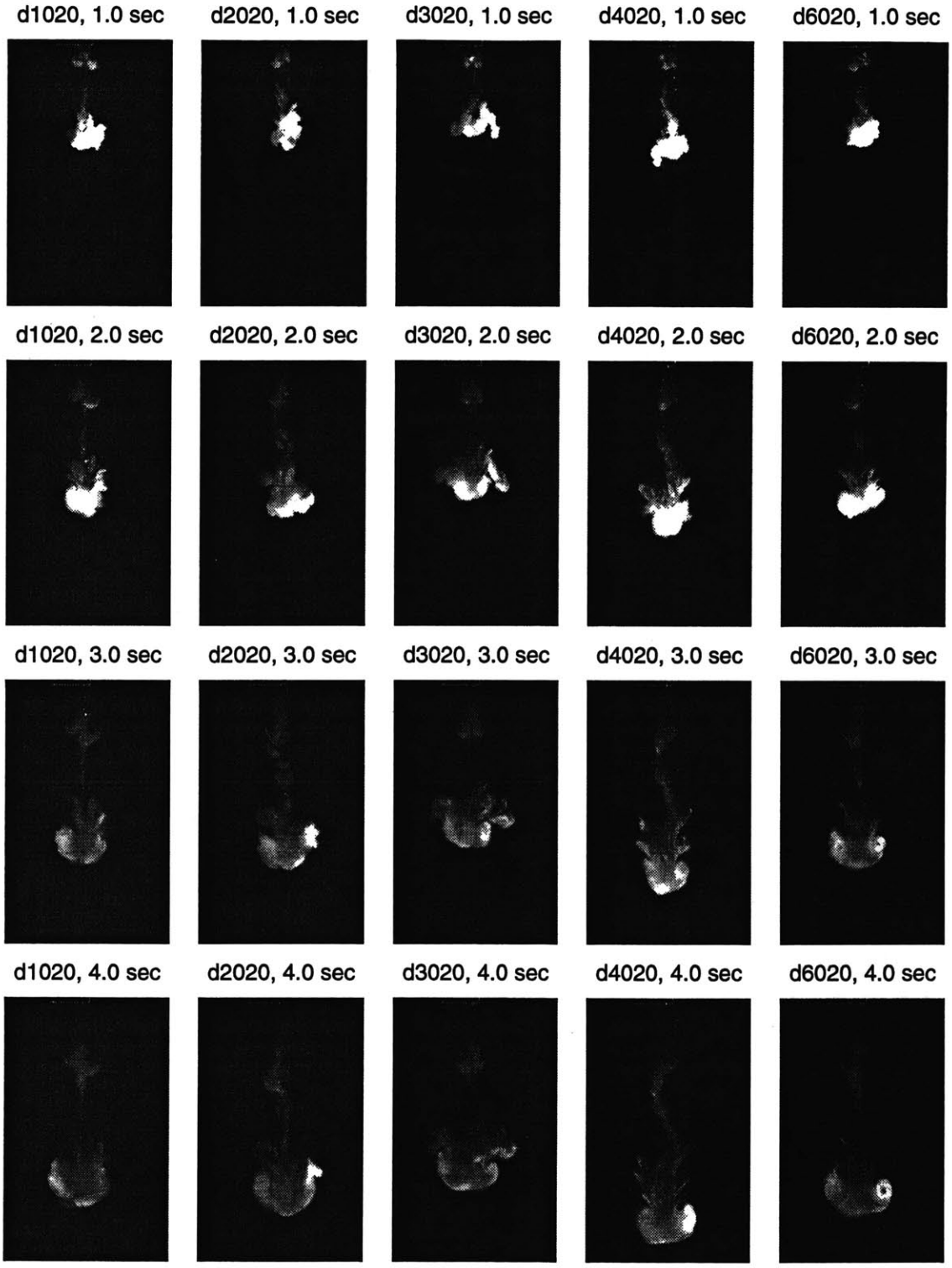
d1020, 1.0 sec
d2020, 1.0 sec
d3020, 1.0 sec
d4020, 1.0 sec
d6020, 1.0 sec
d1020, 2.0 sec
d2020, 2.0 sec
d3020, 2.0 sec
d4020, 2.0 sec
d6020, 2.0 sec
d1020, 3.0 sec
d2020, 3.0 sec
d3020, 3.0 sec
d4020, 3.0 sec
d6020, 3.0 sec
d1020, 4.0 sec
d2020, 4.0 sec
d3020, 4.0 sec
d4020, 4.0 sec
d6020, 4.0 sec

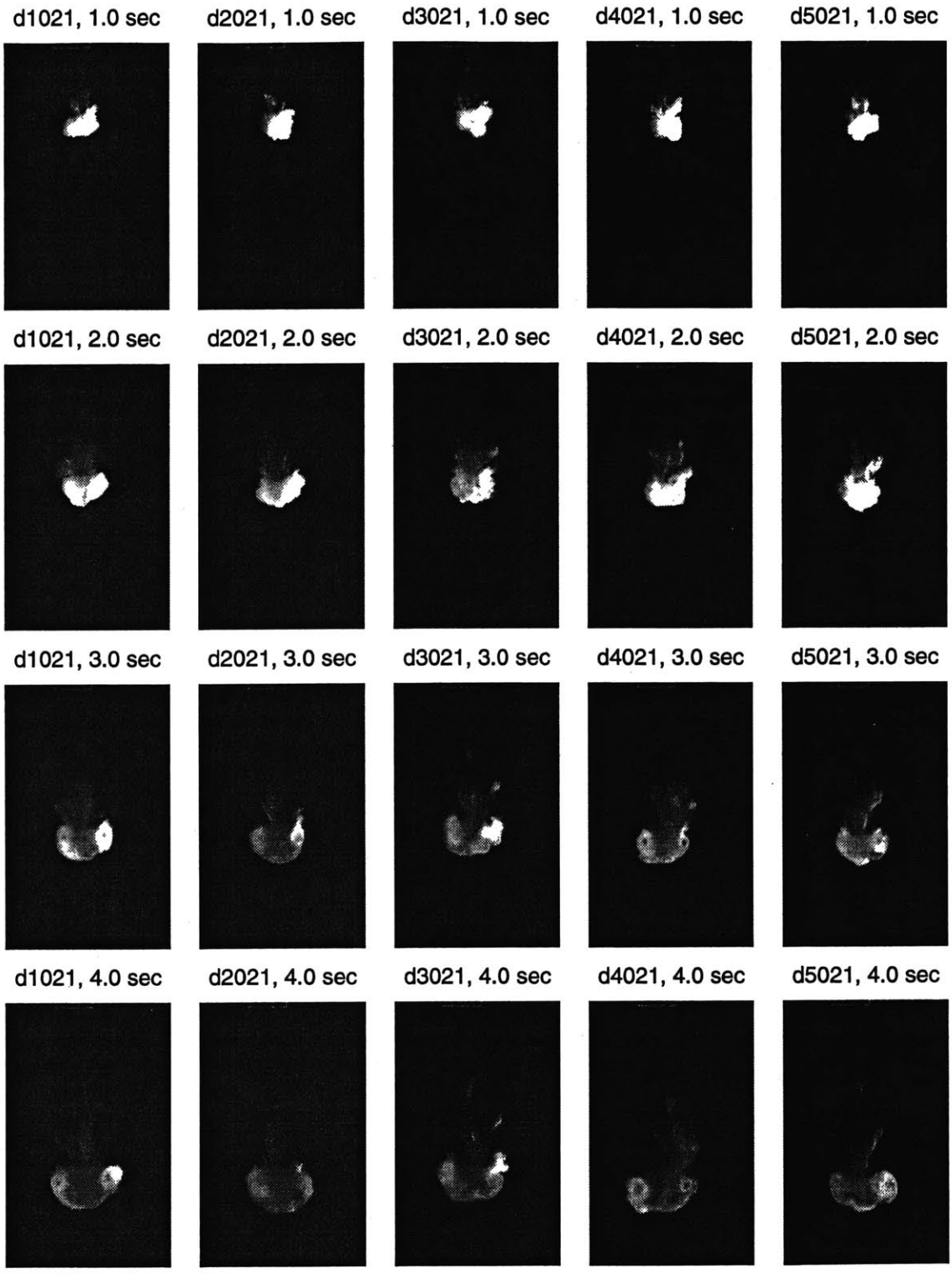
d1021, 1.0 sec
d2021, 1.0 sec
d3021, 1.0 sec
d4021, 1.0 sec
d5021, 1.0 sec
d1021, 2.0 sec
d2021, 2.0 sec
d3021, 2.0 sec
d4021, 2.0 sec
d5021, 2.0 sec
d1021, 3.0 sec
d2021, 3.0 sec
d3021, 3.0 sec
d4021, 3.0 sec
d5021, 3.0 sec
d1021, 4.0 sec
d2021, 4.0 sec
d3021, 4.0 sec
d4021, 4.0 sec
d5021, 4.0 sec

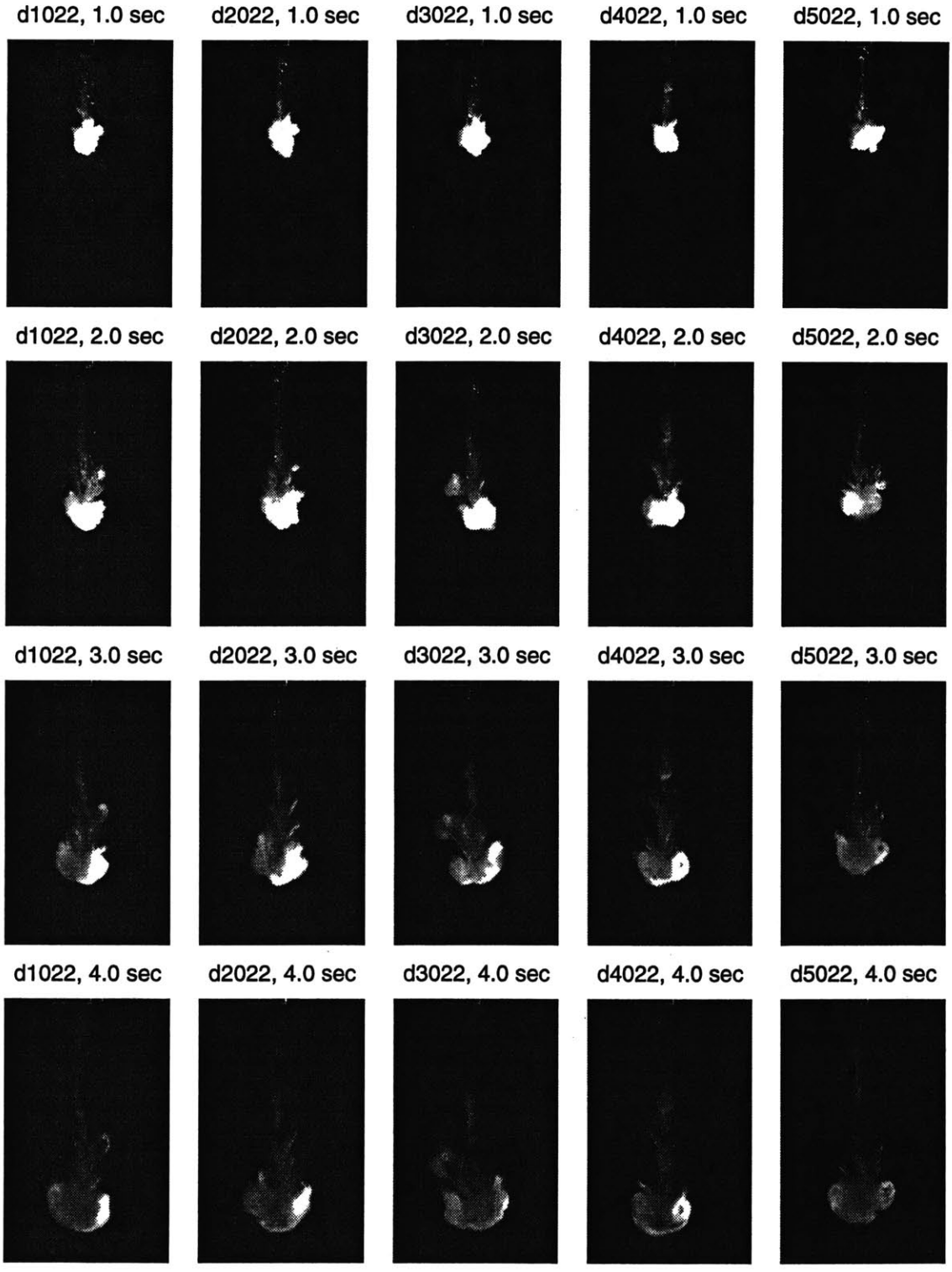
d1022, 1.0 sec
d2022, 1.0 sec
d3022, 1.0 sec
d4022, 1.0 sec
d5022, 1.0 sec
d1022, 2.0 sec
d2022, 2.0 sec
d3022, 2.0 sec
d4022, 2.0 sec
d5022, 2.0 sec
d1022, 3.0 sec
d2022, 3.0 sec
d3022, 3.0 sec
d4022, 3.0 sec
d5022, 3.0 sec
d1022, 4.0 sec
d2022, 4.0 sec
d3022, 4.0 sec
d4022, 4.0 sec
d5022, 4.0 sec

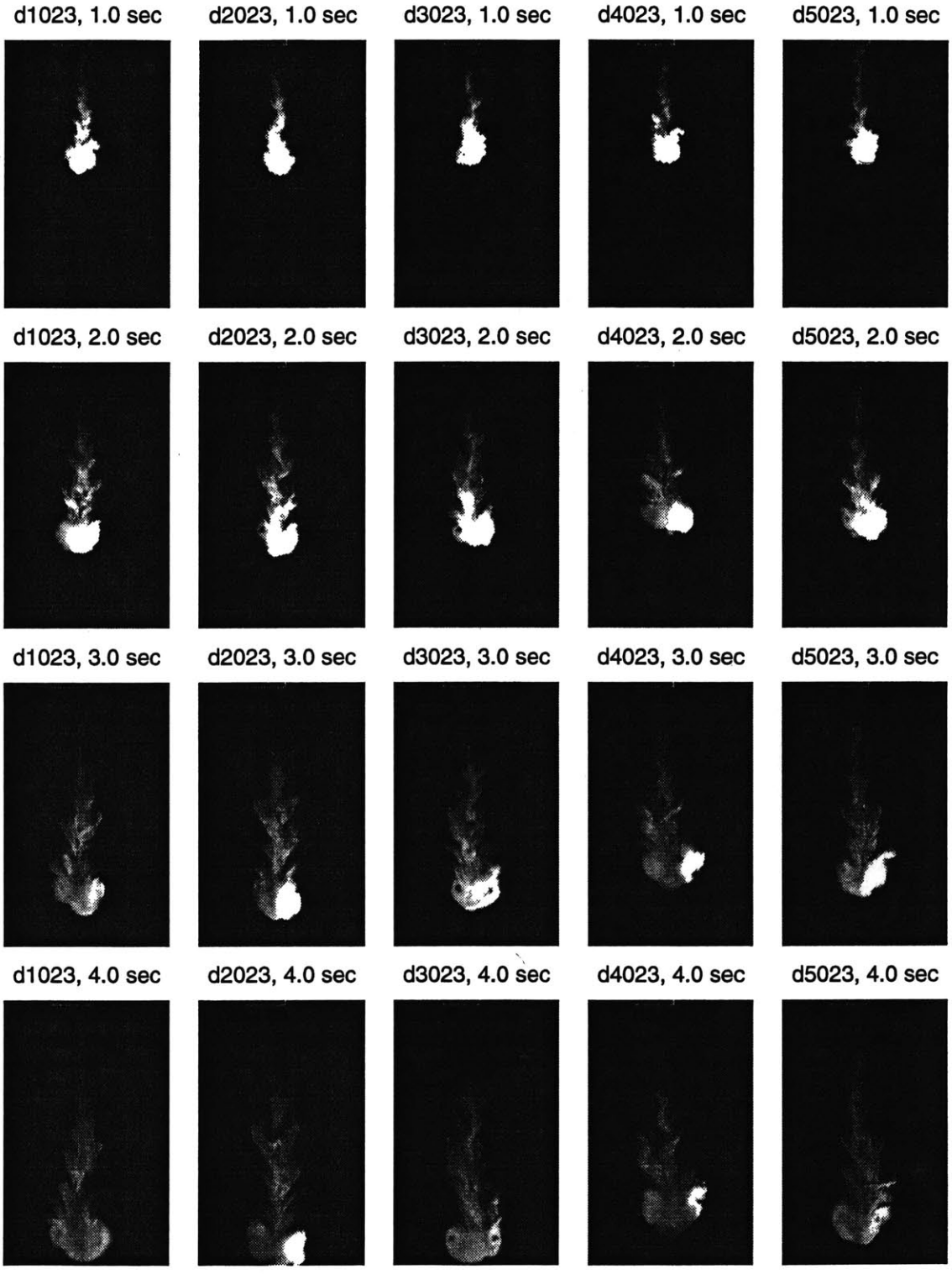
d1023, 1.0 sec
d2023, 1.0 sec
d3023, 1.0 sec
d4023, 1.0 sec
d5023, 1.0 sec
d1023, 2.0 sec
d2023, 2.0 sec
d3023, 2.0 sec
d4023, 2.0 sec
d5023, 2.0 sec
d1023, 3.0 sec
d2023, 3.0 sec
d3023, 3.0 sec
d4023, 3.0 sec
d5023, 3.0 sec
d1023, 4.0 sec
d2023, 4.0 sec
d3023, 4.0 sec
d4023, 4.0 sec
d5023, 4.0 sec

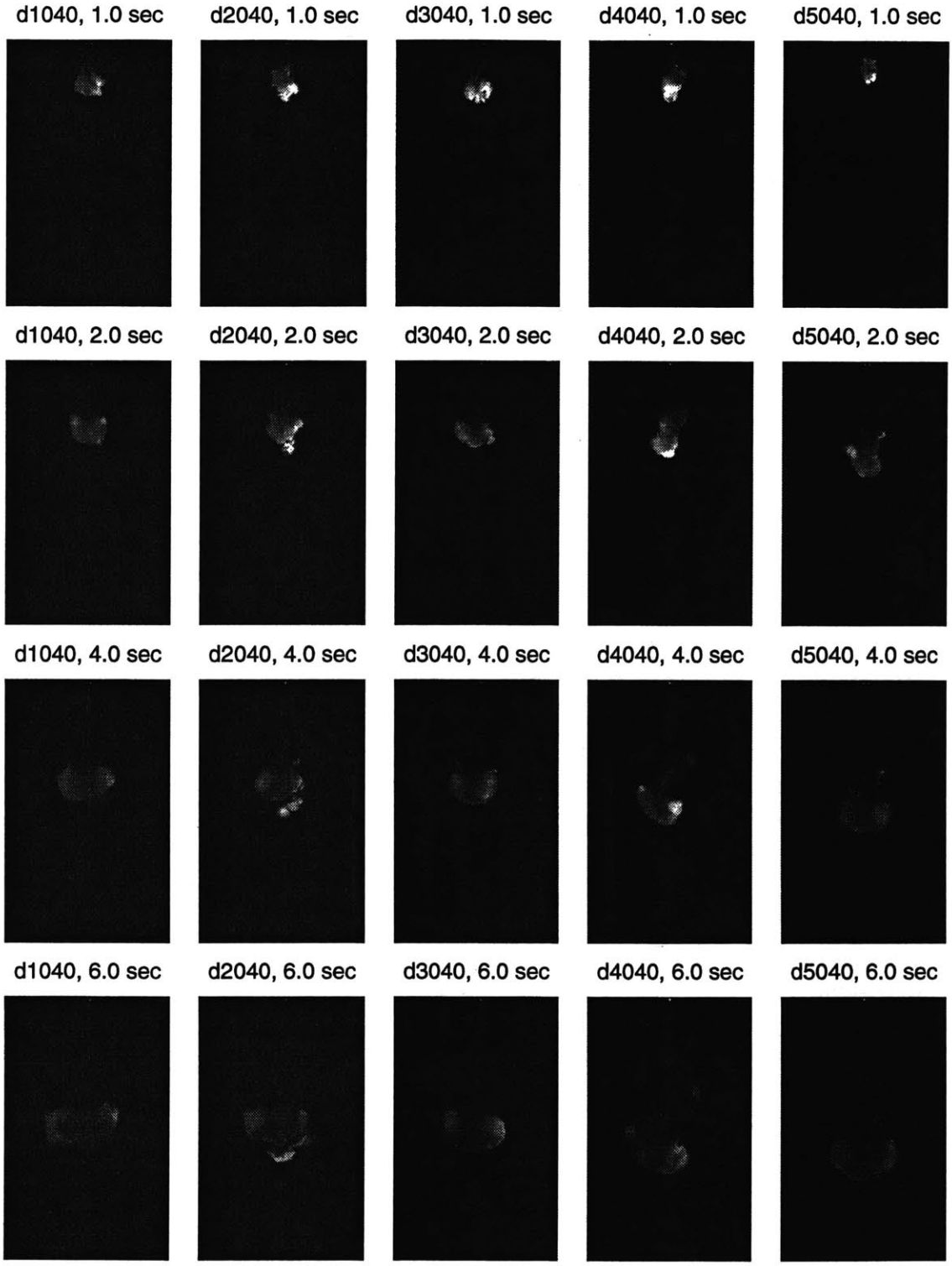
d1040, 1.0 sec
d2040, 1.0 sec
d3040, 1.0 sec
d4040, 1.0 sec
d5040, 1.0 sec
d1040, 2.0 sec
d2040, 2.0 sec
d3040, 2.0 sec
d4040, 2.0 sec
d5040, 2.0 sec
d1040, 4.0 sec
d2040, 4.0 sec
d3040, 4.0 sec
d4040, 4.0 sec
d5040, 4.0 sec
d1040, 6.0 sec
d2040, 6.0 sec
d3040, 6.0 sec
d4040, 6.0 sec
d5040, 6.0 sec

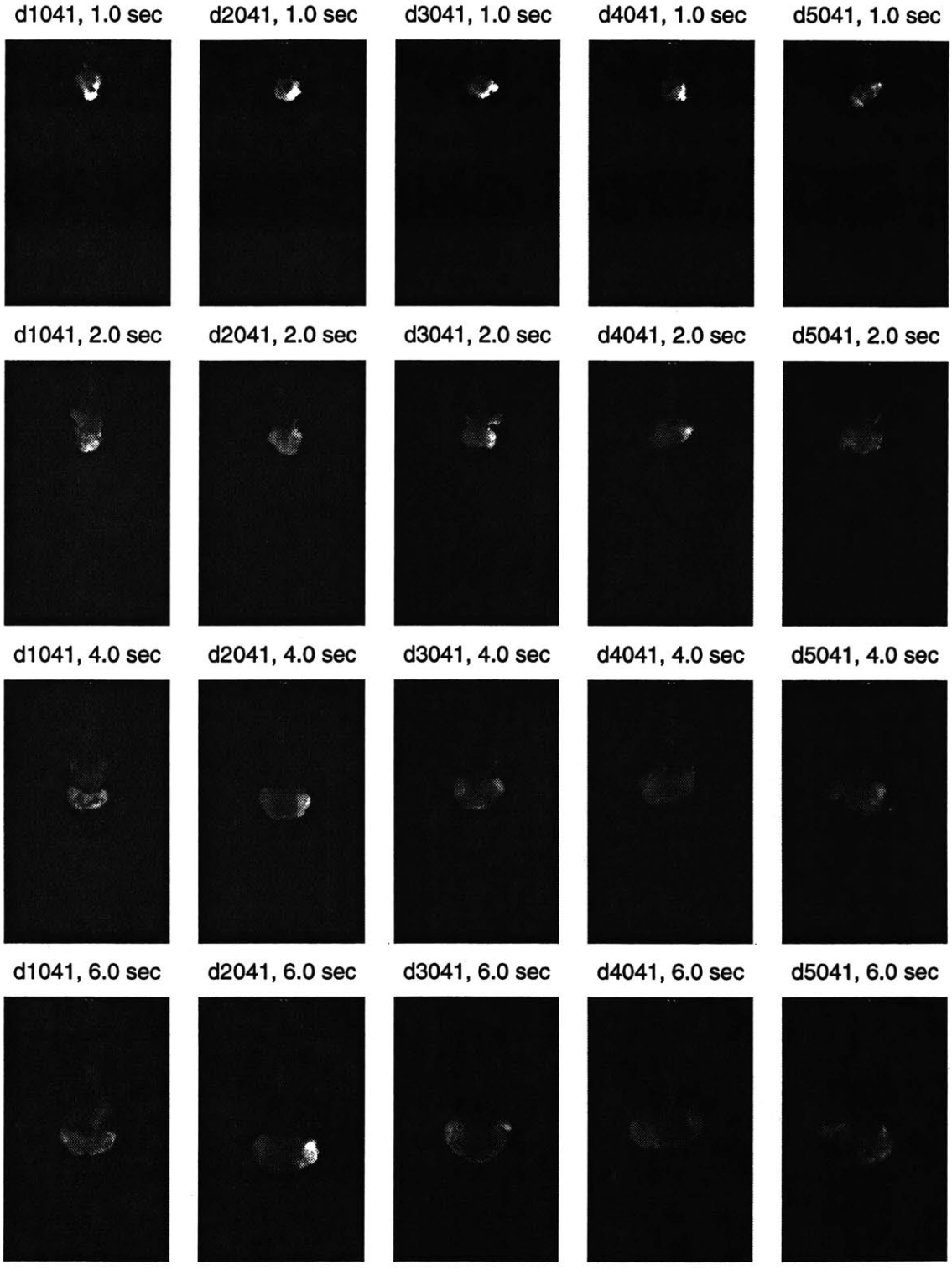
d1041, 1.0 sec
d2041, 1.0 sec
d3041, 1.0 sec
d4041, 1.0 sec
d5041, 1.0 sec
d1041, 2.0 sec
d2041, 2.0 sec
d3041, 2.0 sec
d4041, 2.0 sec
d5041, 2.0 sec
d1041, 4.0 sec
d2041, 4.0 sec
d3041, 4.0 sec
d4041, 4.0 sec
d5041, 4.0 sec
d1041, 6.0 sec
d2041, 6.0 sec
d3041, 6.0 sec
d4041, 6.0 sec
d5041, 6.0 sec

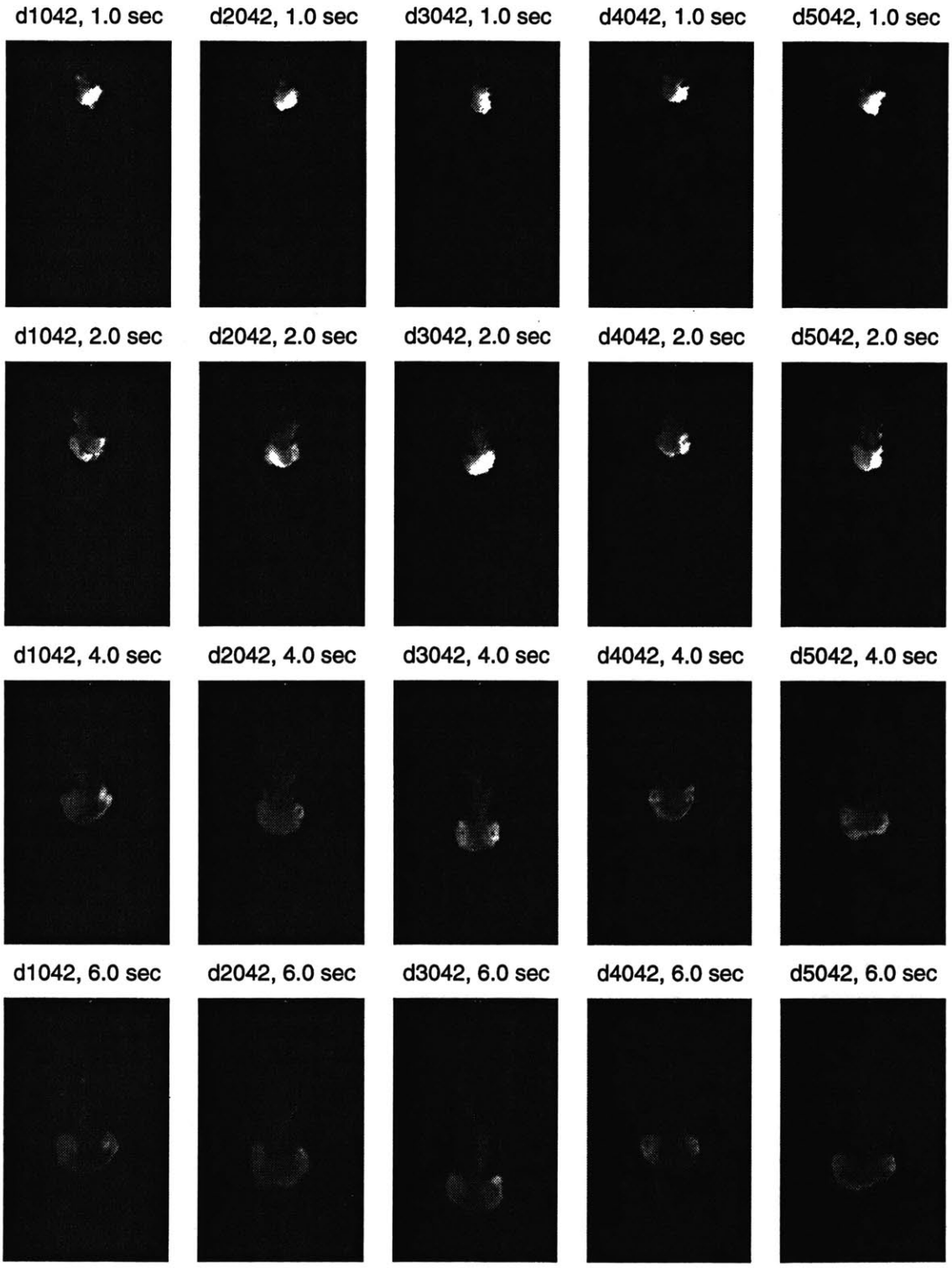
d1042, 1.0 sec
d2042, 1.0 sec
d3042, 1.0 sec
d4042, 1.0 sec
d5042, 1.0 sec
d1042, 2.0 sec
d2042, 2.0 sec
d3042, 2.0 sec
d4042, 2.0 sec
d5042, 2.0 sec
d1042, 4.0 sec
d2042, 4.0 sec
d3042, 4.0 sec
d4042, 4.0 sec
d5042, 4.0 sec
d1042, 6.0 sec
d2042, 6.0 sec
d3042, 6.0 sec
d4042, 6.0 sec
d5042, 6.0 sec

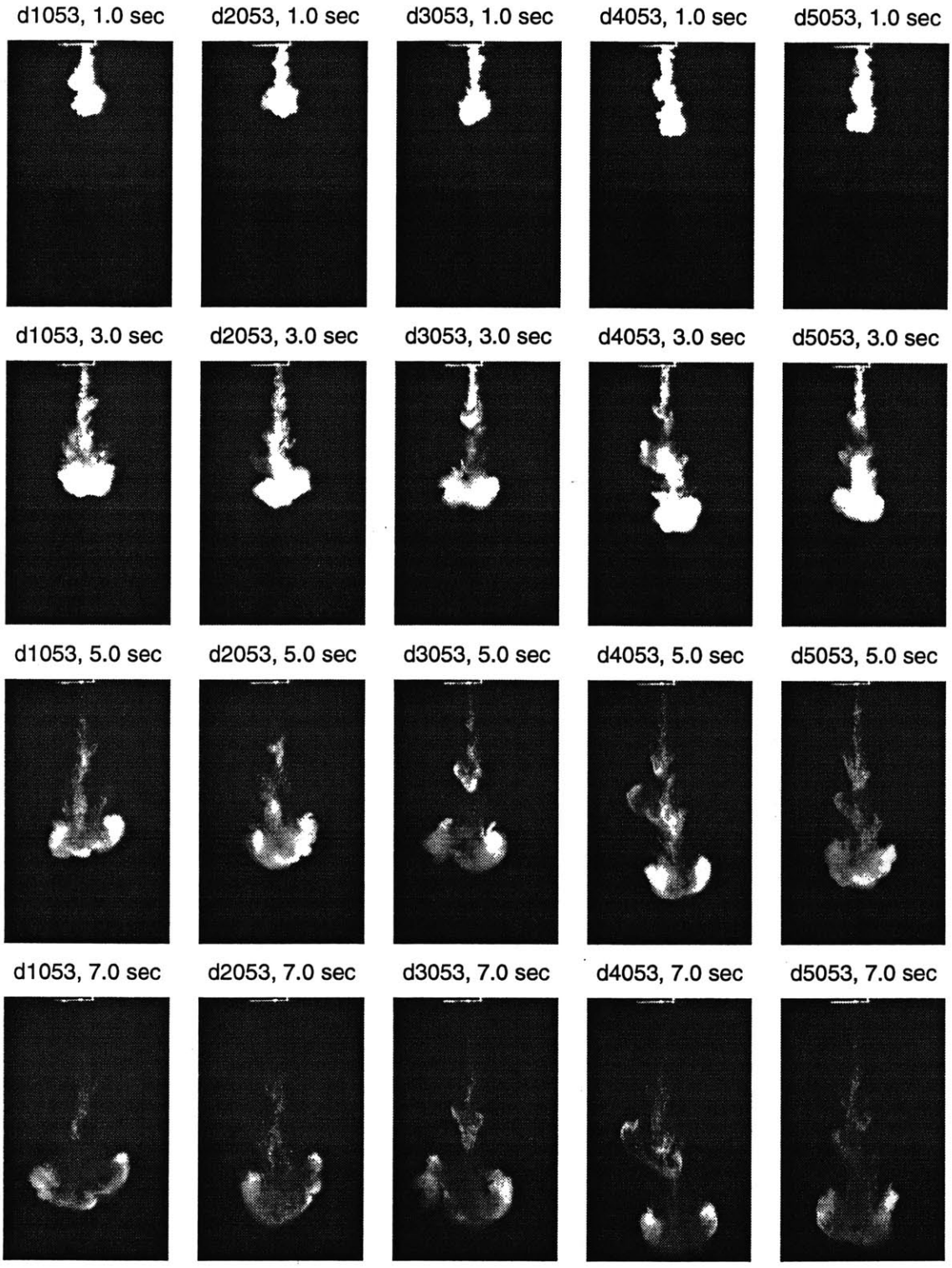
d1053, 1.0 sec
d2053, 1.0 sec
d3053, 1.0 sec
d4053, 1.0 sec
d5053, 1.0 sec
d1053, 3.0 sec
d2053, 3.0 sec
d3053, 3.0 sec
d4053, 3.0 sec
d5053, 3.0 sec
d1053, 5.0 sec
d2053, 5.0 sec
d3053, 5.0 sec
d4053, 5.0 sec
d5053, 5.0 sec
d1053, 7.0 sec
d2053, 7.0 sec
d3053, 7.0 sec
d4053, 7.0 sec
d5053, 7.0 sec

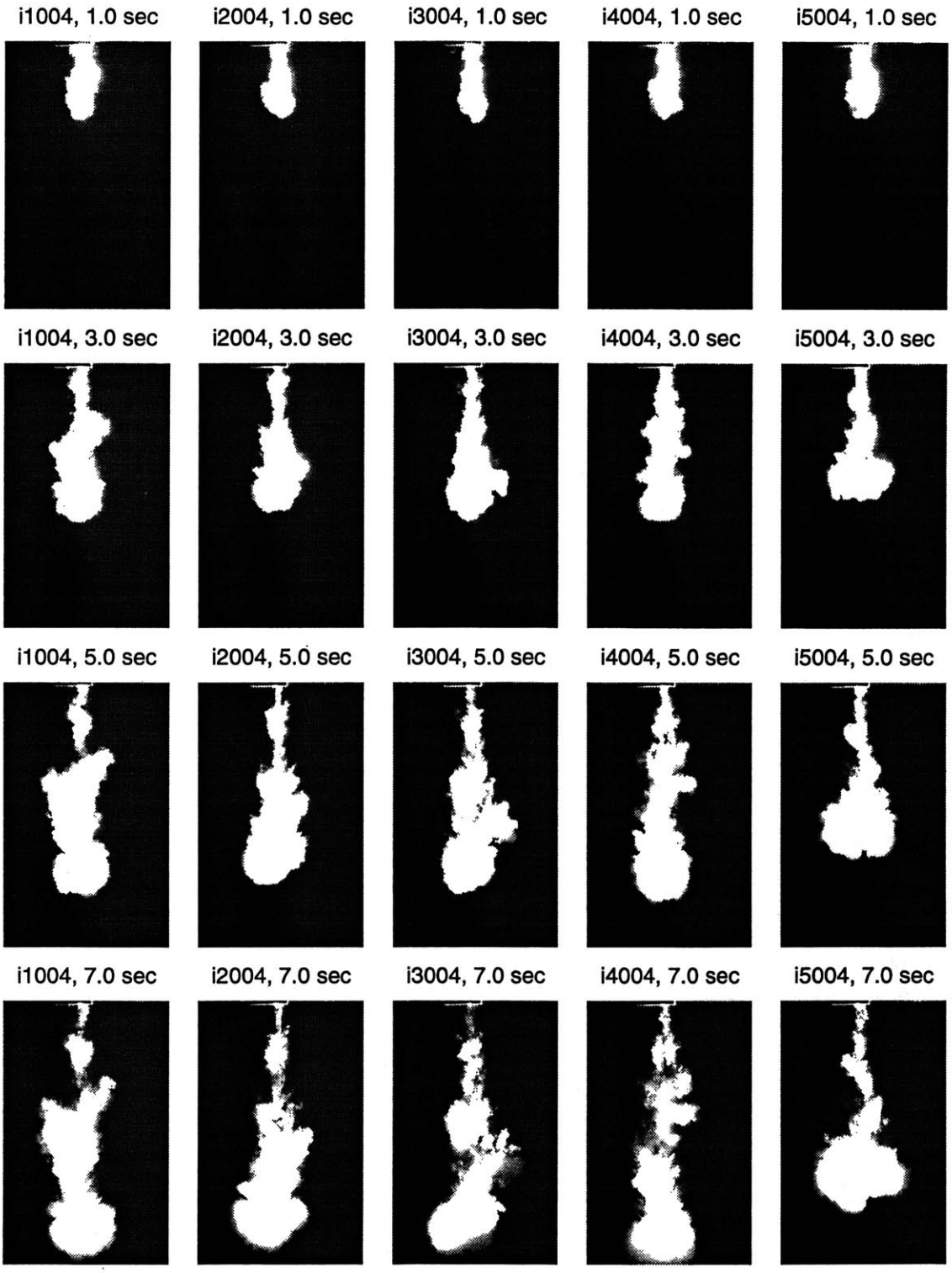
i1004, 1.0 sec
i2004, 1.0 sec
i3004, 1.0 sec
i4004, 1.0 sec
i5004, 1.0 sec
i1004, 3.0 sec
i2004, 3.0 sec
i3004, 3.0 sec
i4004, 3.0 sec
i5004, 3.0 sec
i1004, 5.0 sec
i2004, 5.0 sec
i3004, 5.0 sec
i4004, 5.0 sec
i5004, 5.0 sec
i1004, 7.0 sec
i2004, 7.0 sec
i3004, 7.0 sec
i4004, 7.0 sec
i5004, 7.0 sec

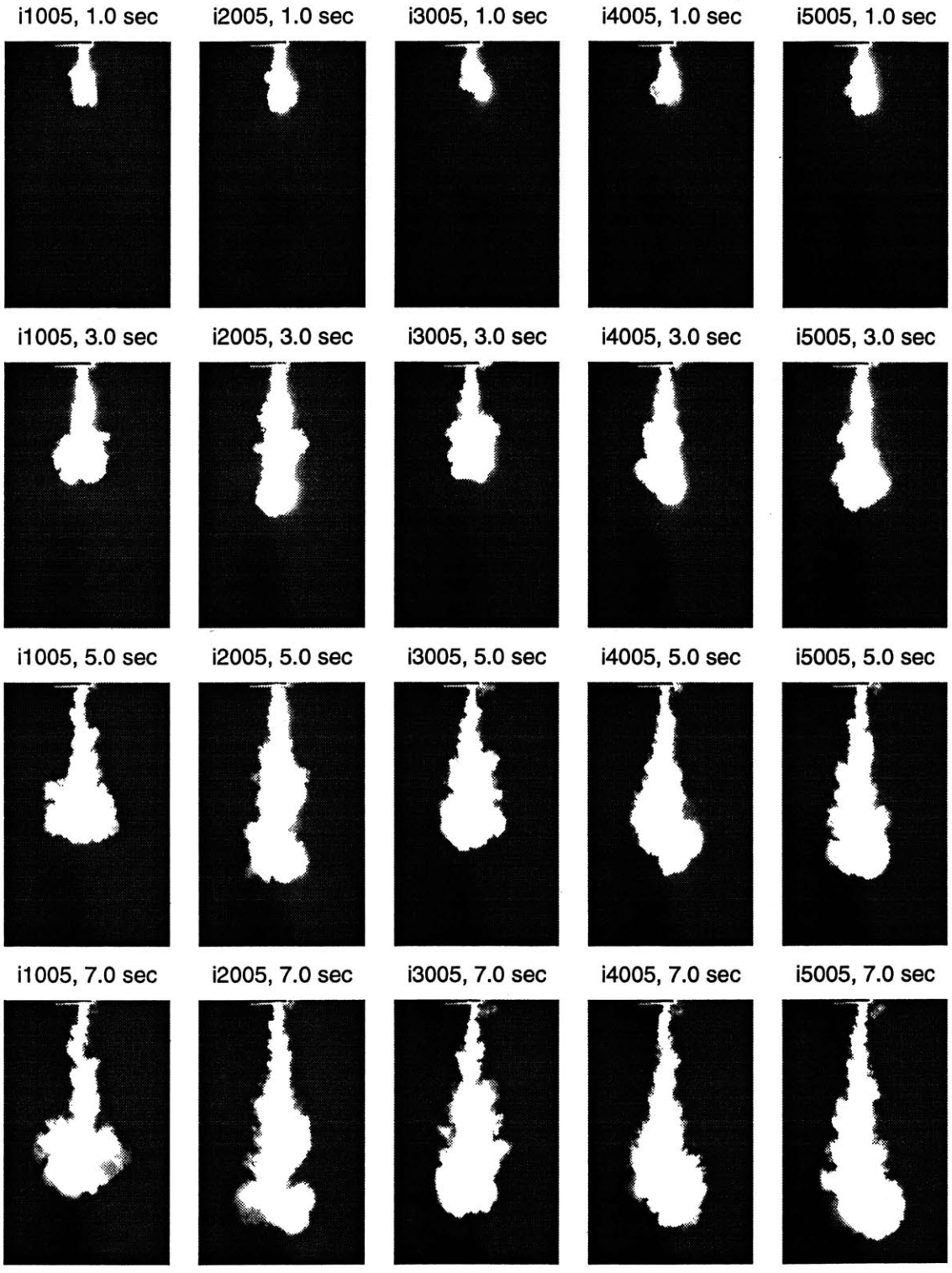
i1005, 1.0 sec
i2005, 1.0 sec
i3005, 1.0 sec
i4005, 1.0 sec
i5005, 1.0 sec
i1005, 3.0 sec
i2005, 3.0 sec
i3005, 3.0 sec
i4005, 3.0 sec
i5005, 3.0 sec
i1005, 5.0 sec
i2005, 5.0 sec
i3005, 5.0 sec
i4005, 5.0 sec
i5005, 5.0 sec
i1005, 7.0 sec
i2005, 7.0 sec
i3005, 7.0 sec
i4005, 7.0 sec
i5005, 7.0 sec

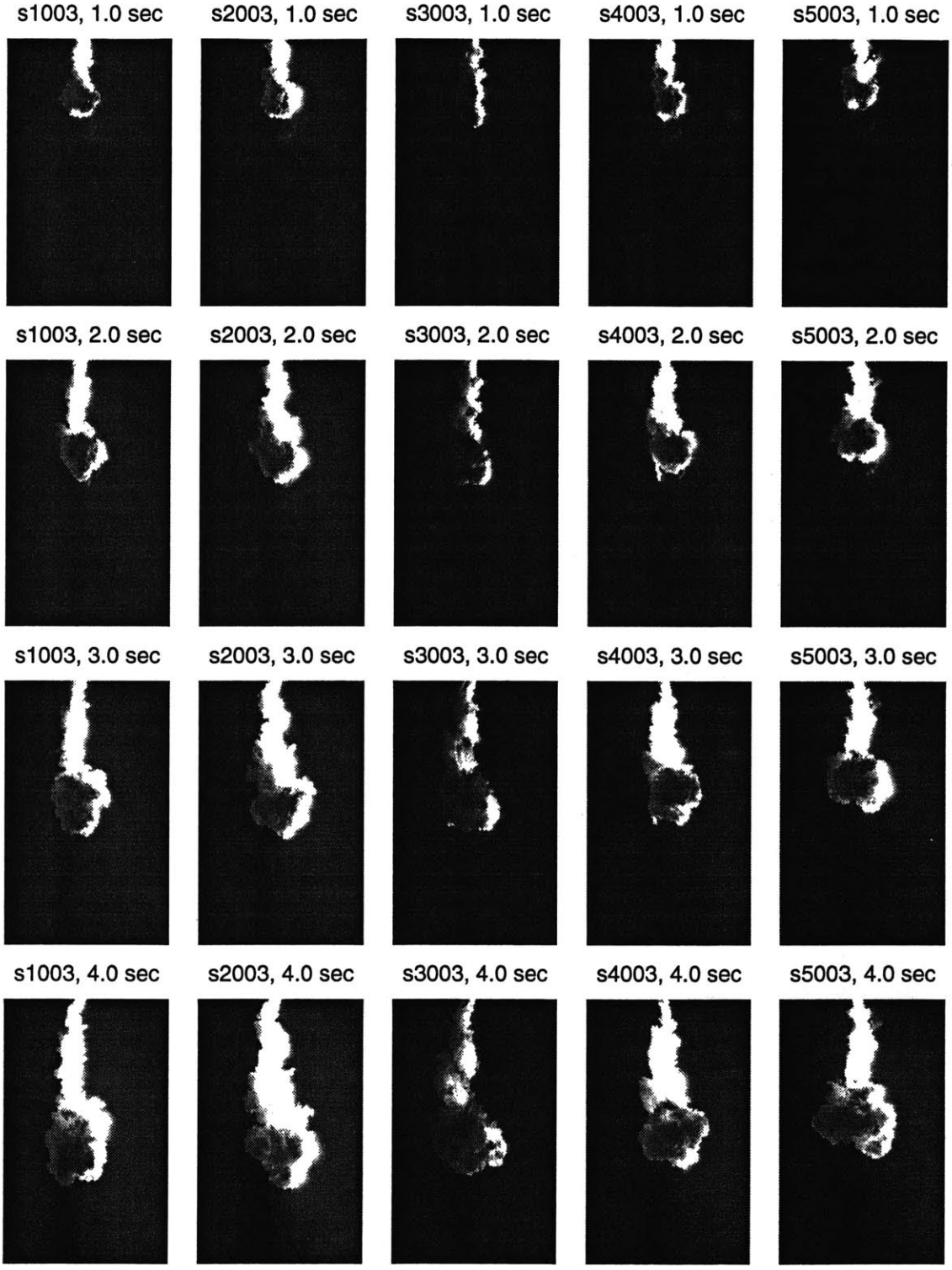
s1003, 1.0 sec
s2003, 1.0 sec
s3003, 1.0 sec
s4003, 1.0 sec
s5003, 1.0 sec
s1003, 2.0 sec
s2003, 2.0 sec
s3003, 2.0 sec
s4003, 2.0 sec
s5003, 2.0 sec
s1003, 3.0 sec
s2003, 3.0 sec
s3003, 3.0 sec
s4003, 3.0 sec
s5003, 3.0 sec
s1003, 4.0 sec
s2003, 4.0 sec
s3003, 4.0 sec
s4003, 4.0 sec
s5003, 4.0 sec

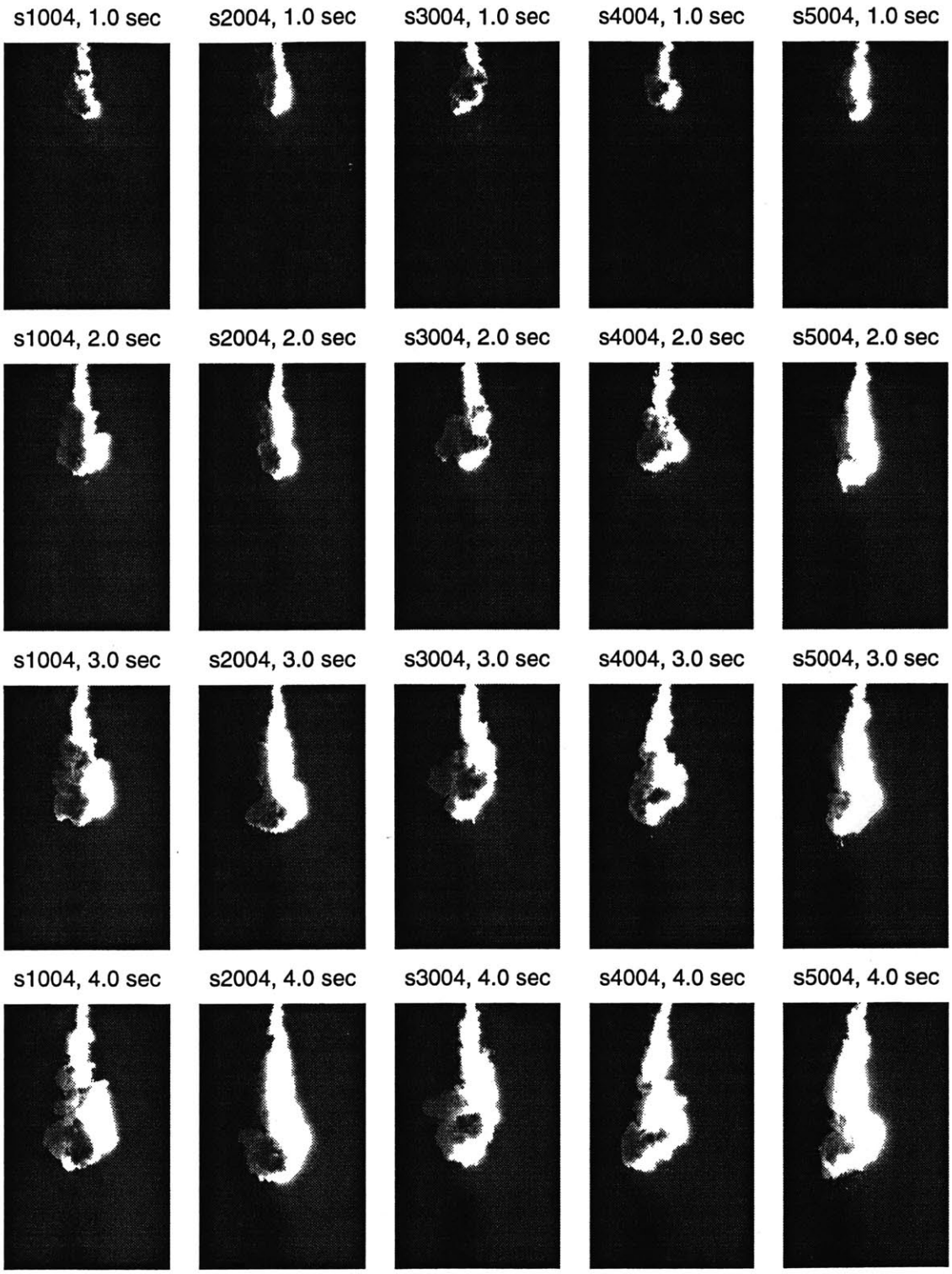
s1004, 1.0 sec
s2004, 1.0 sec
s3004, 1.0 sec
s4004, 1.0 sec
s5004, 1.0 sec
s1004, 2.0 sec
s2004, 2.0 sec
s3004, 2.0 sec
s4004, 2.0 sec
s5004, 2.0 sec
s1004, 3.0 sec
s2004, 3.0 sec
s3004, 3.0 sec
s4004, 3.0 sec
s5004, 3.0 sec
s1004, 4.0 sec
s2004, 4.0 sec
s3004, 4.0 sec
s4004, 4.0 sec
s5004, 4.0 sec

Appendix C

Radius and Center of Mass Profiles for Group I, II, and III Experiments

The following pages depict the center of mass versus time and radius versus depth data for the five repetitions performed for each of the twelve experiments included in Groups I, II, and III. The experiment numbers included in each group are listed in the cross-reference table provided in Appendix A.

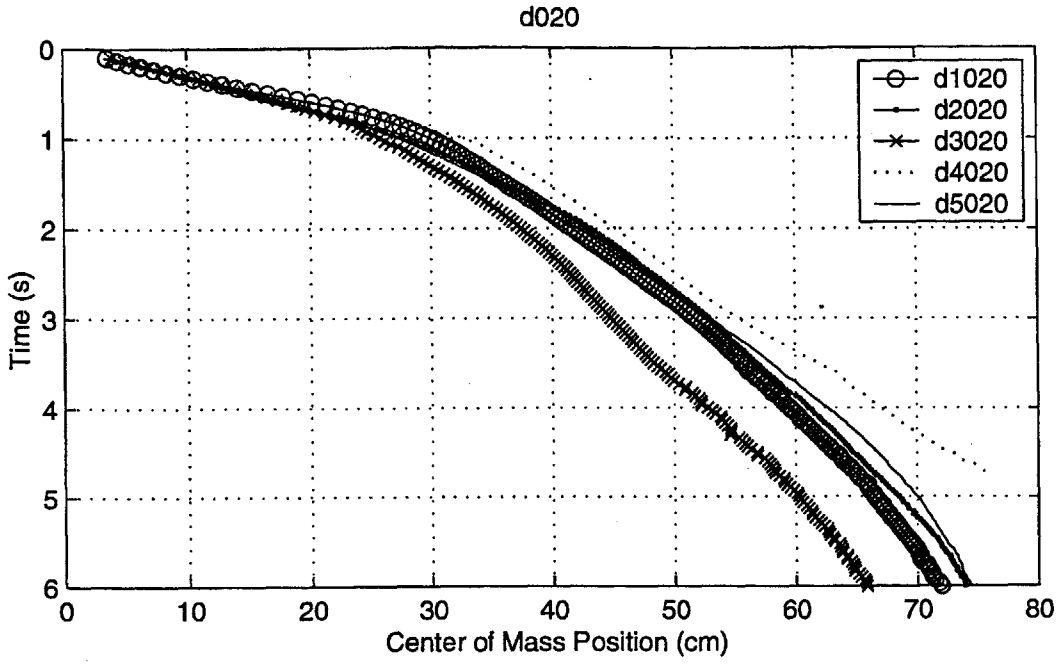
d020
d1020
d2020
d3020
d4020
d5020
Time (s)
Center of Mass Position (cm)
0
1
2
3
4
5
6
0
10
20
30
40
50
60
70
80

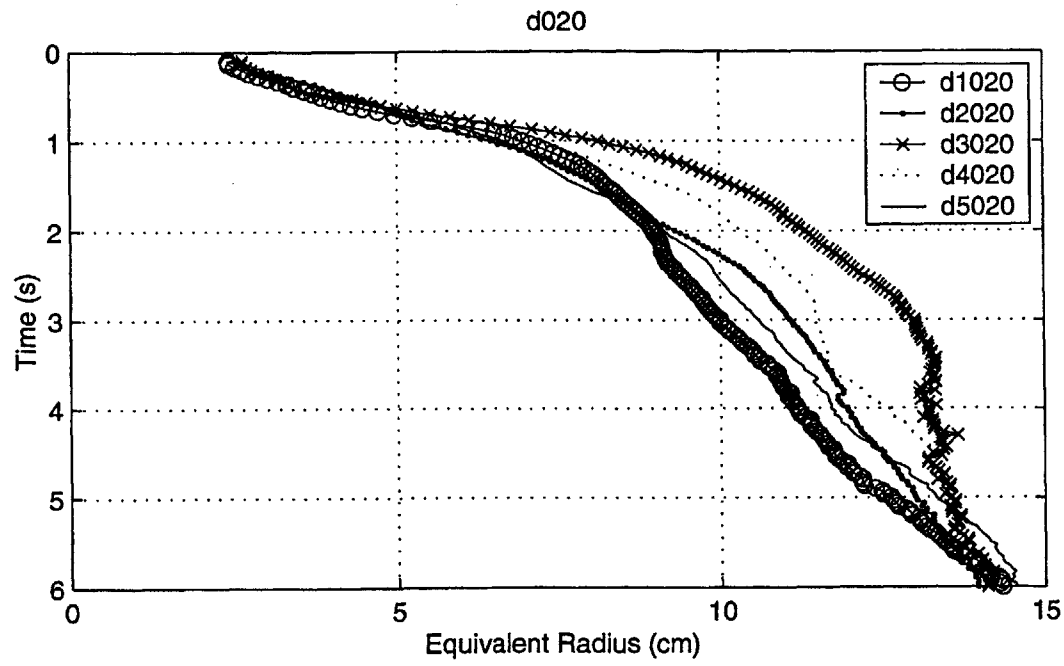
d020
d1020
d2020
d3020
d4020
d5020
Time (s)
Equivalent Radius (cm)
0
1
2
3
4
5
6
0
5
10
15

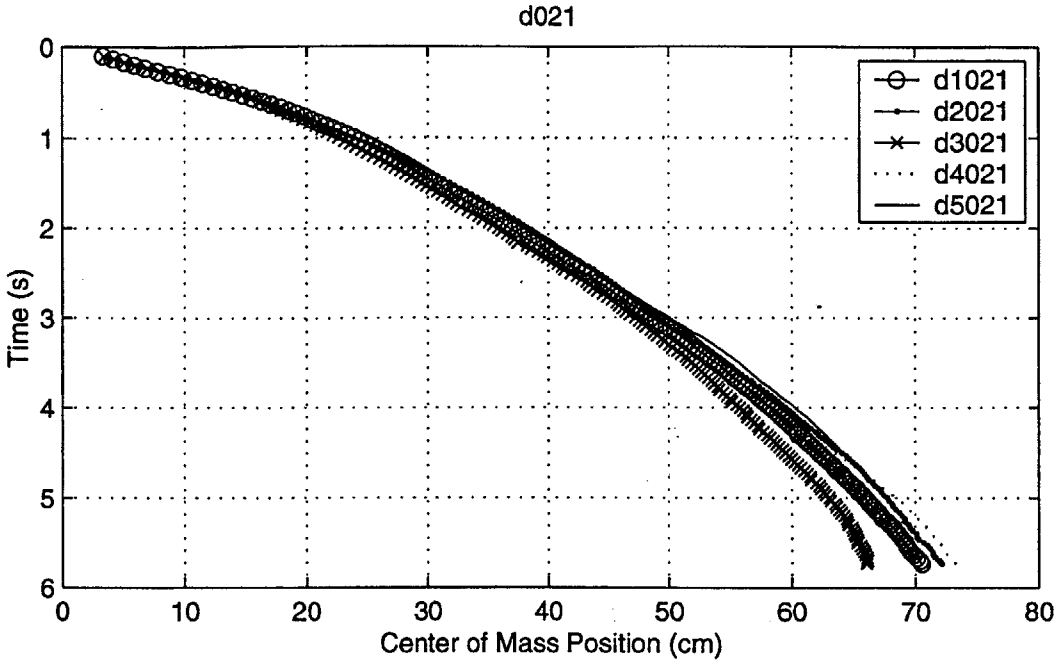
d021
d1021
d2021
d3021
d4021
d5021
Time (s)
Center of Mass Position (cm)
0
1
2
3
4
5
6
0
10
20
30
40
50
60
70
80

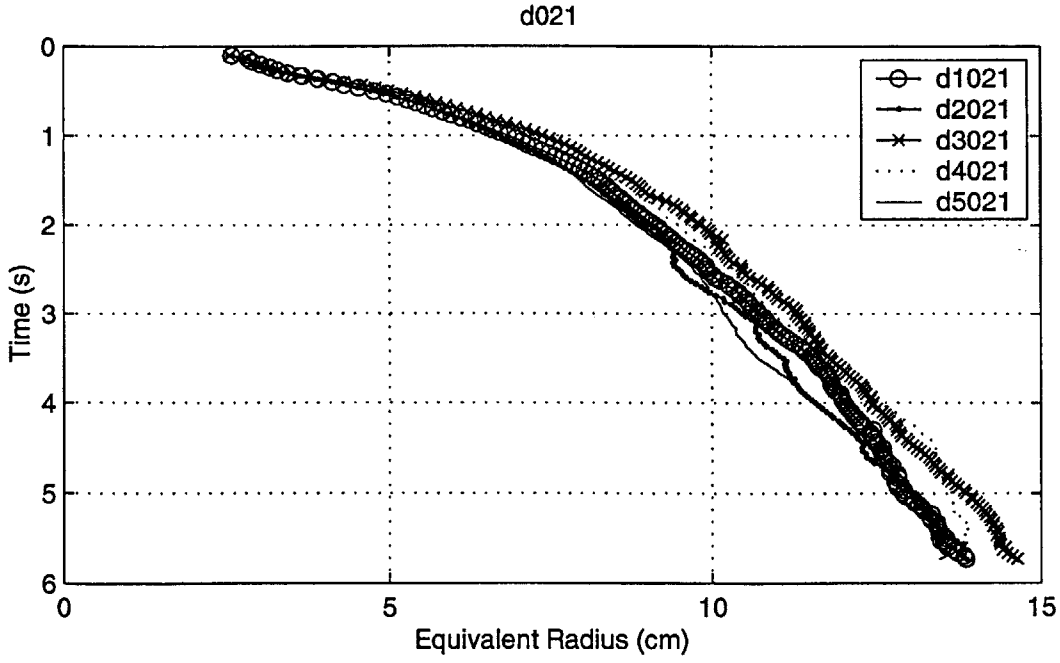
d021
d1021
d2021
d3021
d4021
d5021
Time (s)
Equivalent Radius (cm)
0
1
2
3
4
5
6
0
5
10
15

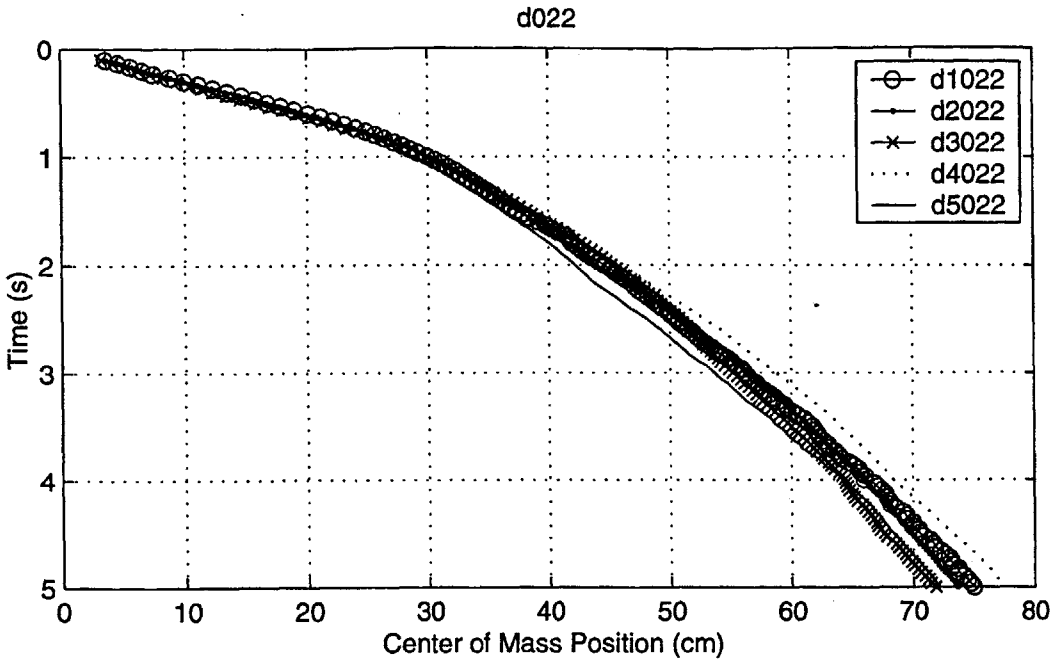
d022
d1022
d2022
d3022
d4022
d5022
Time (s)
Center of Mass Position (cm)
0
1
2
3
4
5
0
10
20
30
40
50
60
70
80

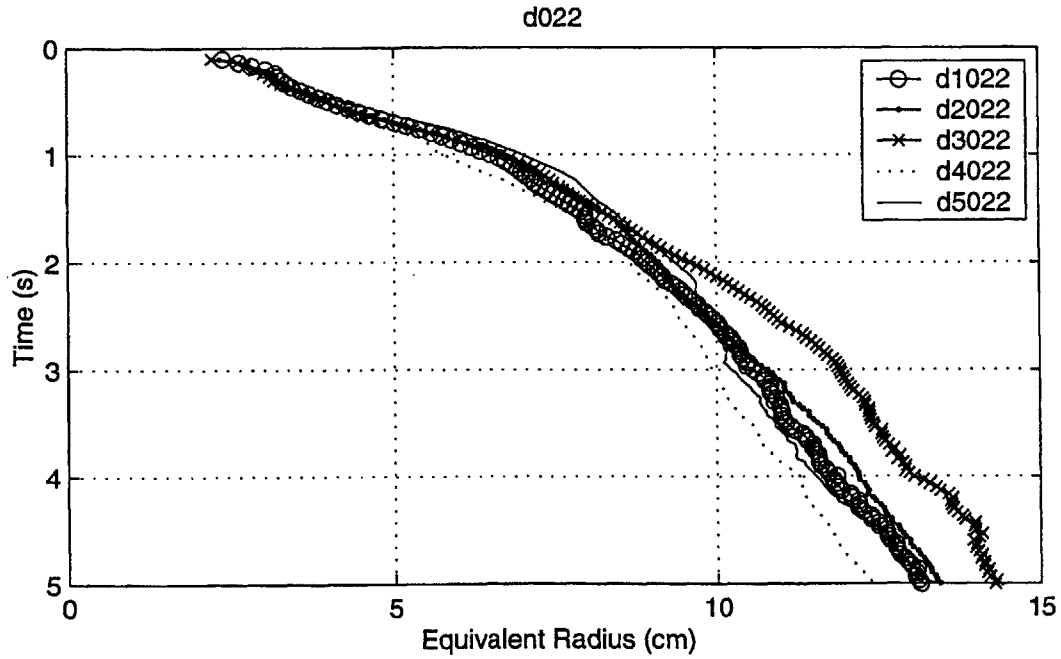
d022
d1022
d2022
d3022
d4022
d5022
Time (s)
Equivalent Radius (cm)
0
1
2
3
4
5
0
5
10
15

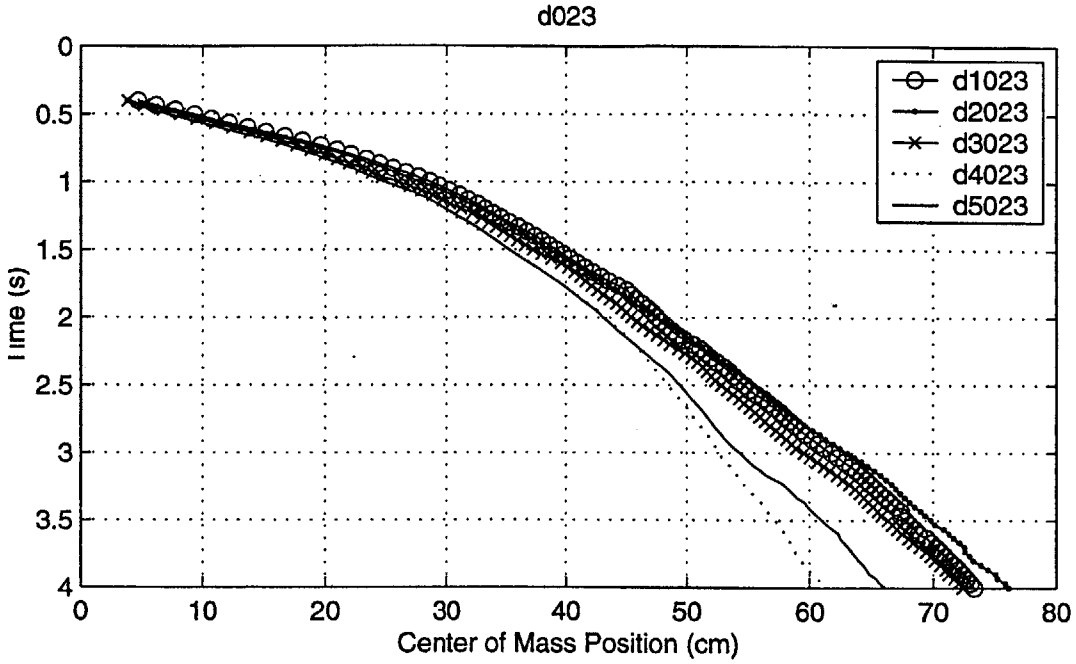
d023
d1023
d2023
d3023
d4023
d5023
Time (s)
Center of Mass Position (cm)
0
0.5
1
1.5
2
2.5
3
3.5
4
0
10
20
30
40
50
60
70
80

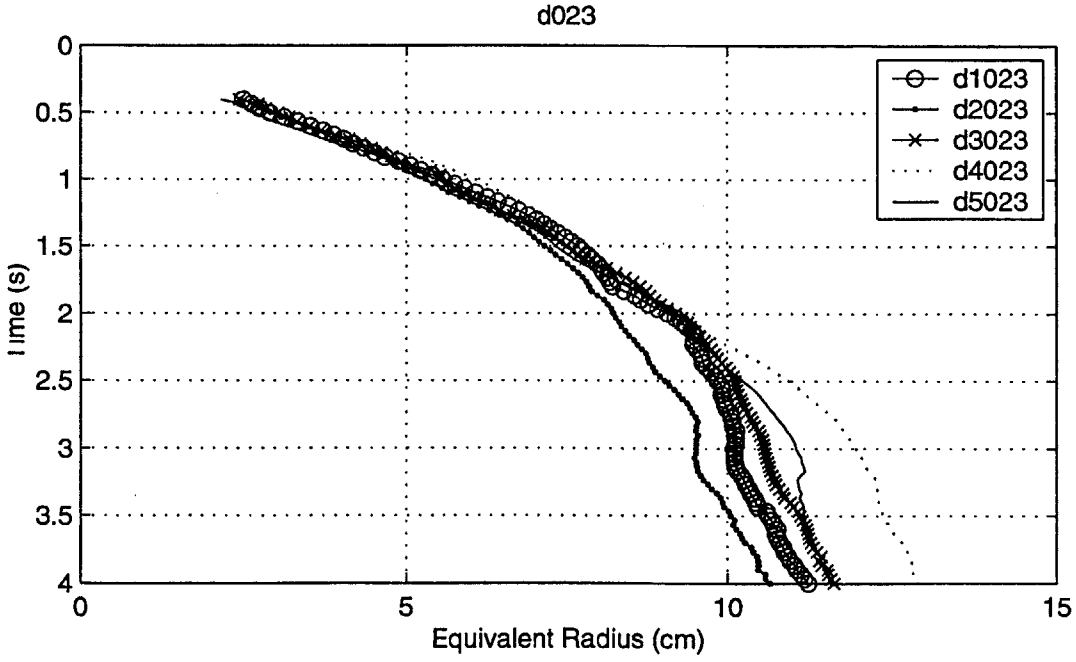
d023
d1023
d2023
d3023
d4023
d5023
Time (s)
Equivalent Radius (cm)
0
0.5
1
1.5
2
2.5
3
3.5
4
0
5
10
15

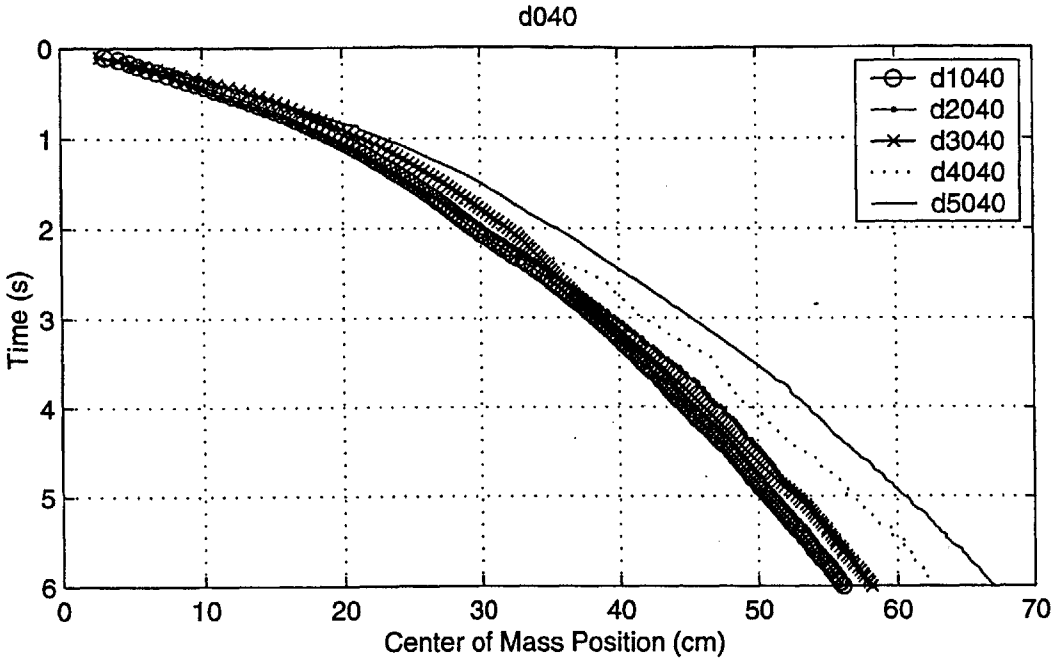
d040
d1040
d2040
d3040
d4040
d5040
Time (s)
Center of Mass Position (cm)
0
1
2
3
4
5
6
0
10
20
30
40
50
60
70

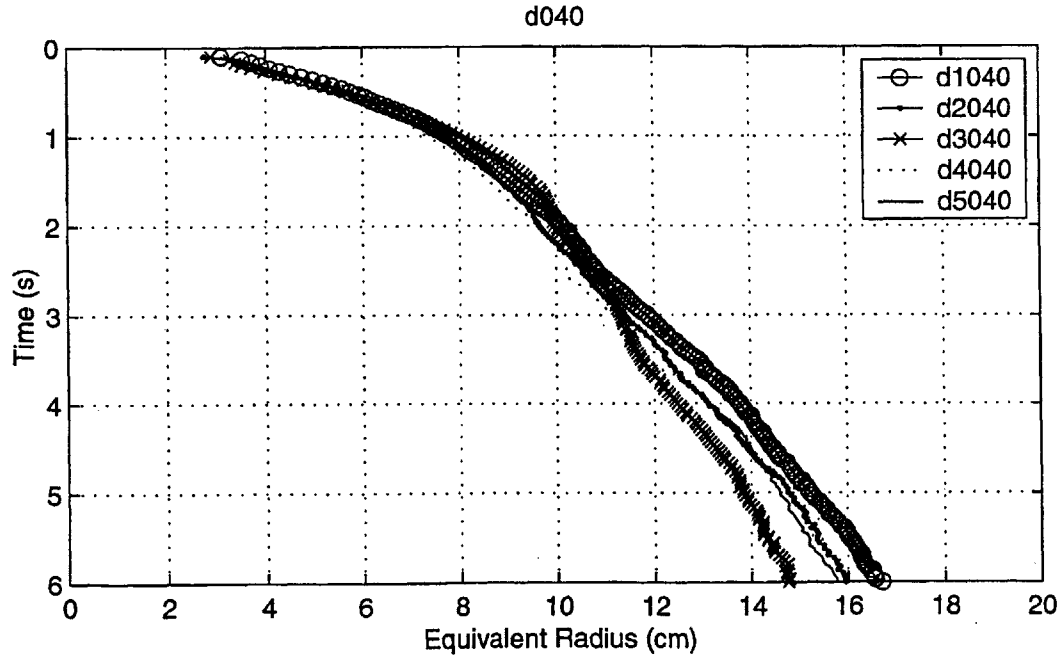
d040
d1040
d2040
d3040
d4040
d5040
Time (s)
Equivalent Radius (cm)
0
1
2
3
4
5
6
0
2
4
6
8
10
12
14
16
18
20

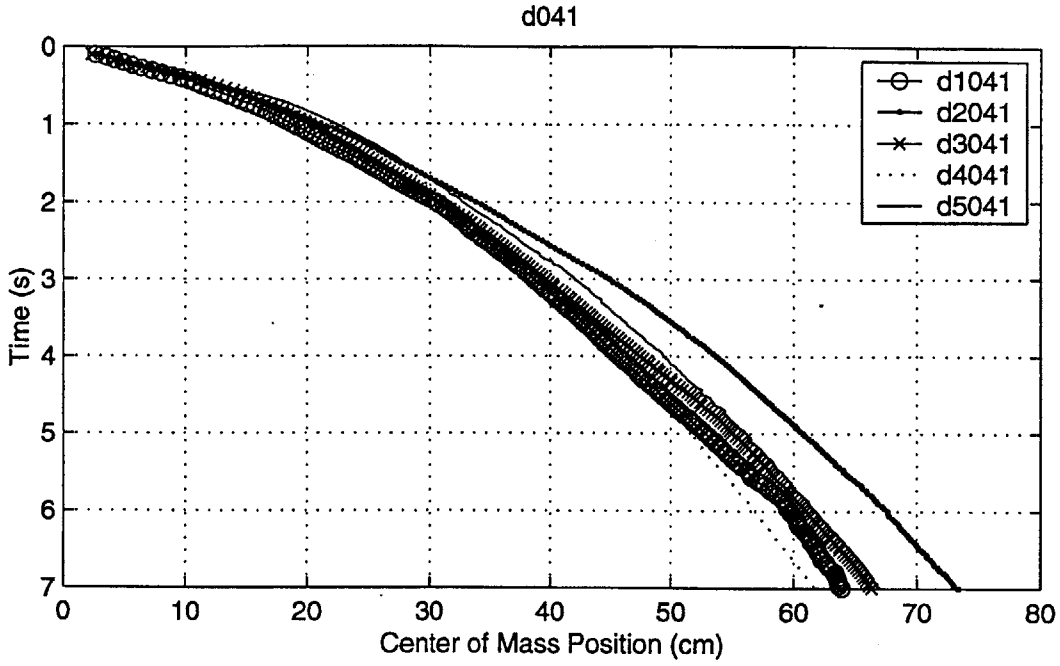
d041
d1041
d2041
d3041
d4041
d5041
Time (s)
Center of Mass Position (cm)
0
1
2
3
4
5
6
7
0
10
20
30
40
50
60
70
80

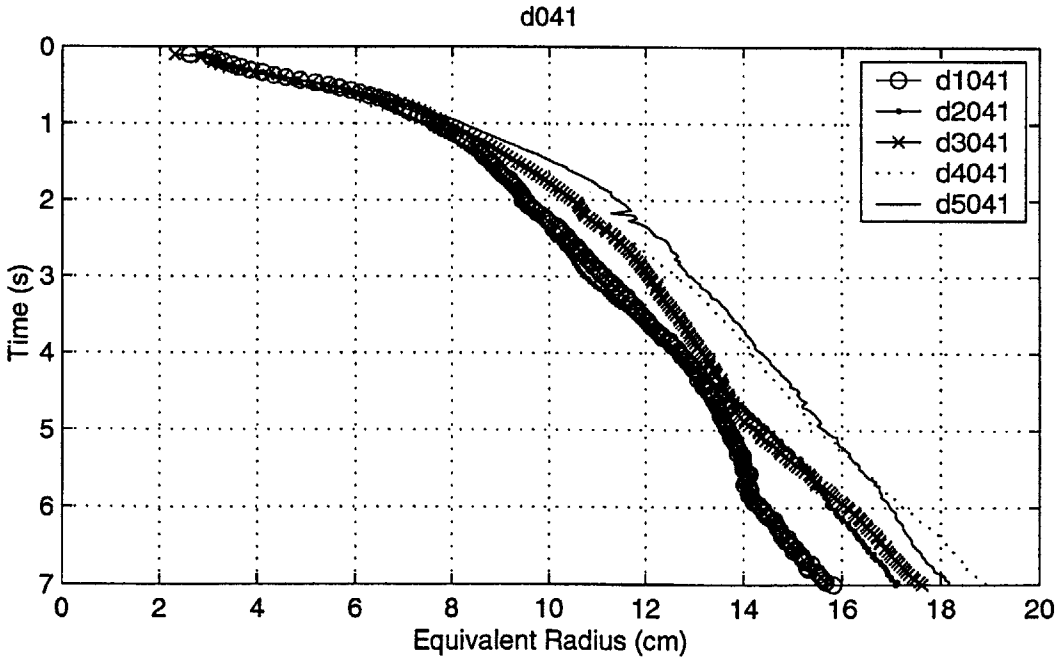
d041
d1041
d2041
d3041
d4041
d5041
Time (s)
Equivalent Radius (cm)
0
1
2
3
4
5
6
7
0
2
4
6
8
10
12
14
16
18
20

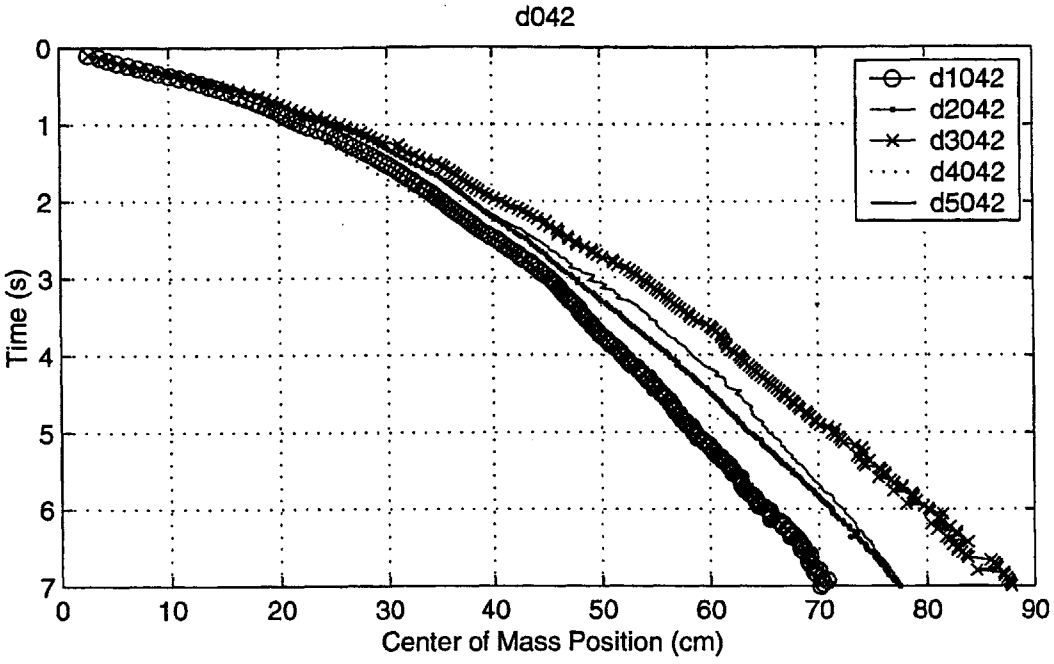
d042
d1042
d2042
d3042
d4042
d5042
Time (s)
Center of Mass Position (cm)
0
1
2
3
4
5
6
7
0
10
20
30
40
50
60
70
80
90

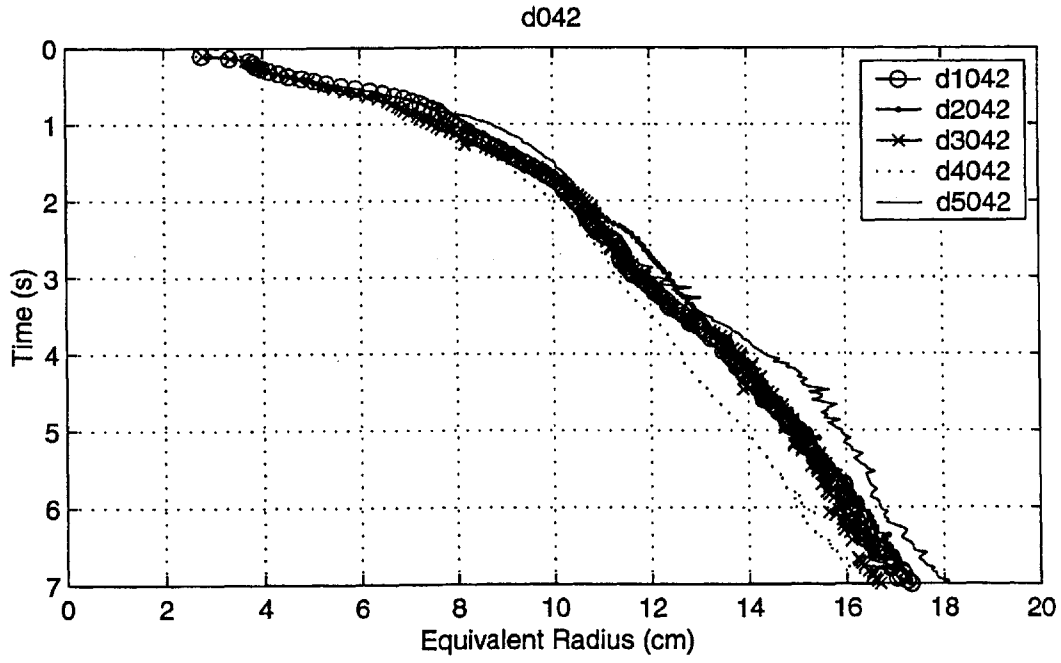
d042
d1042
d2042
d3042
d4042
d5042
Time (s)
Equivalent Radius (cm)
0
1
2
3
4
5
6
7
0
2
4
6
8
10
12
14
16
18
20

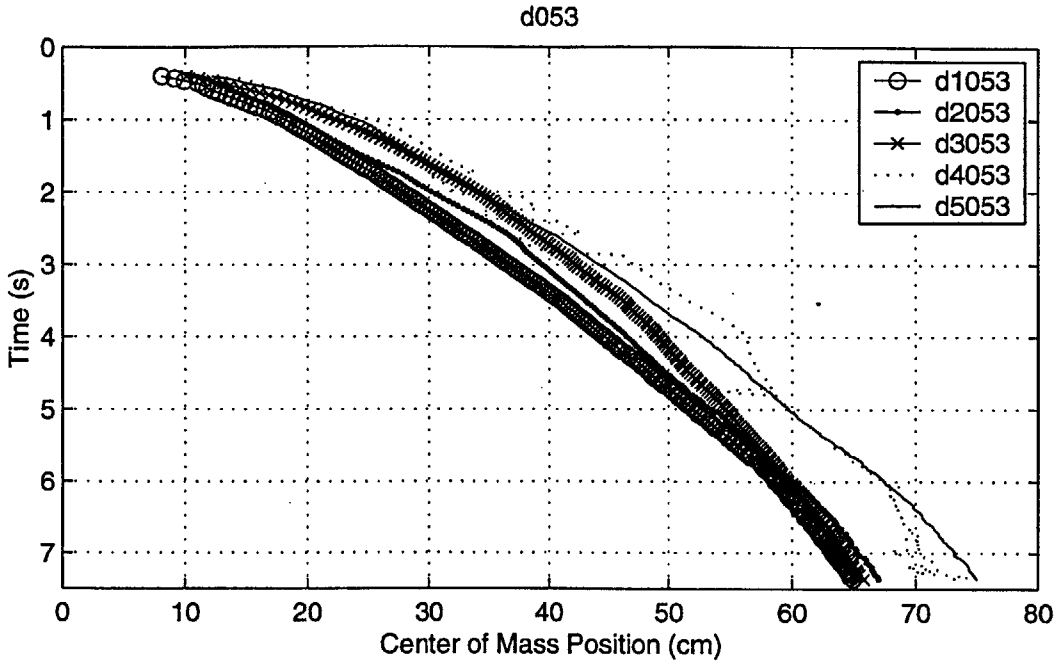
d053
d1053
d2053
d3053
d4053
d5053
Time (s)
Center of Mass Position (cm)
0
1
2
3
4
5
6
7
0
10
20
30
40
50
60
70
80

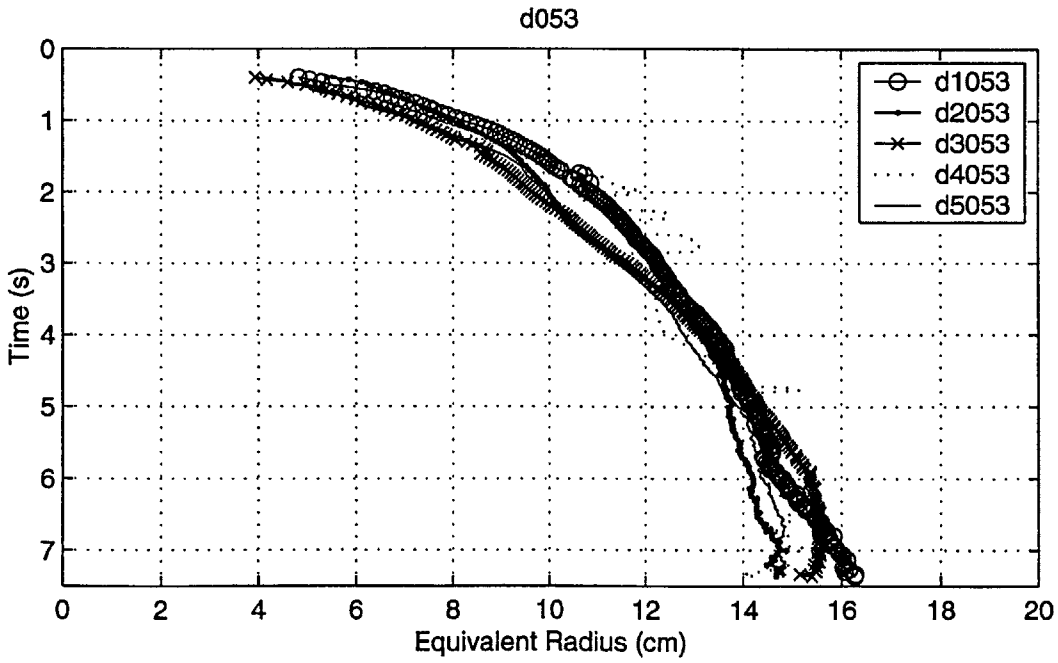
d053
d1053
d2053
d3053
d4053
d5053
Time (s)
Equivalent Radius (cm)
0
1
2
3
4
5
6
7
0
2
4
6
8
10
12
14
16
18
20

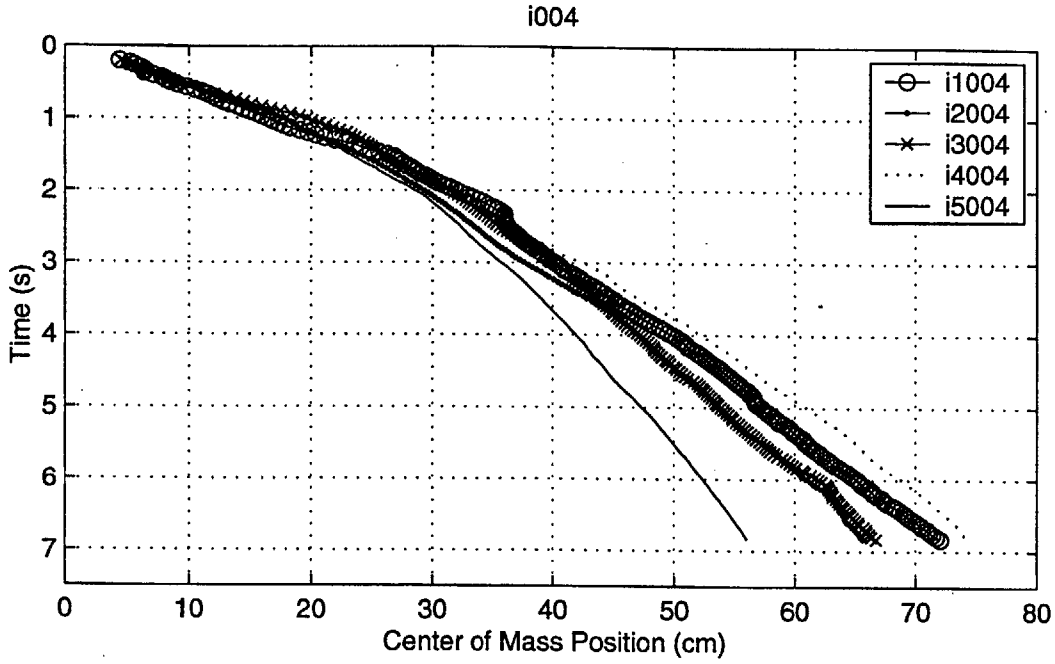
i004
i1004
i2004
i3004
i4004
i5004
Time (s)
Center of Mass Position (cm)
0
1
2
3
4
5
6
7
0
10
20
30
40
50
60
70
80

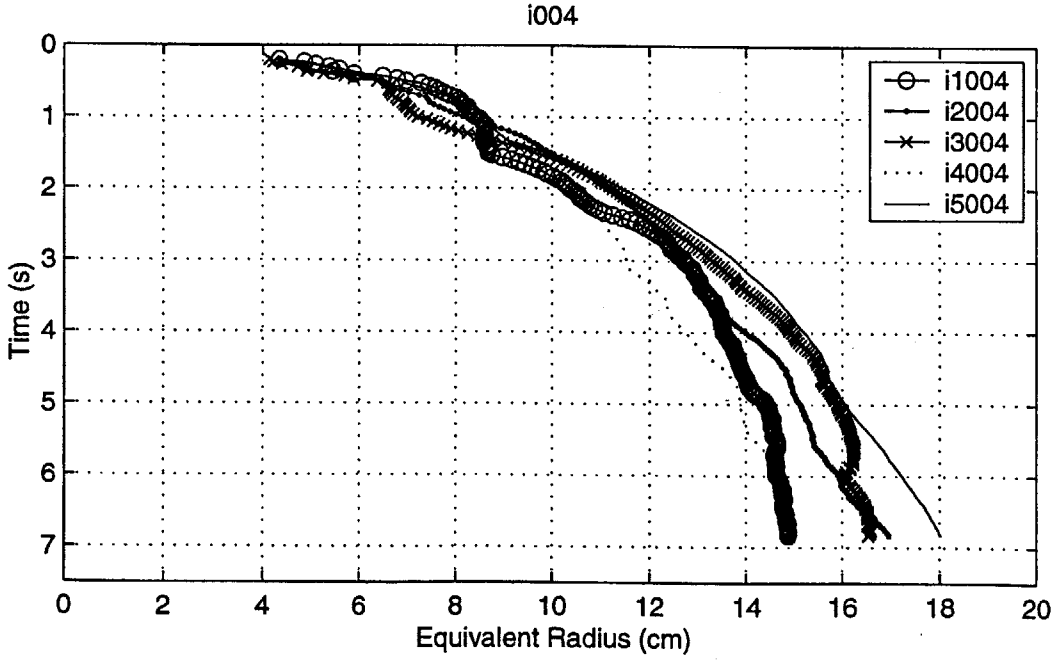
i004
i1004
i2004
i3004
i4004
i5004
Time (s)
Equivalent Radius (cm)
0
1
2
3
4
5
6
7
0
2
4
6
8
10
12
14
16
18
20

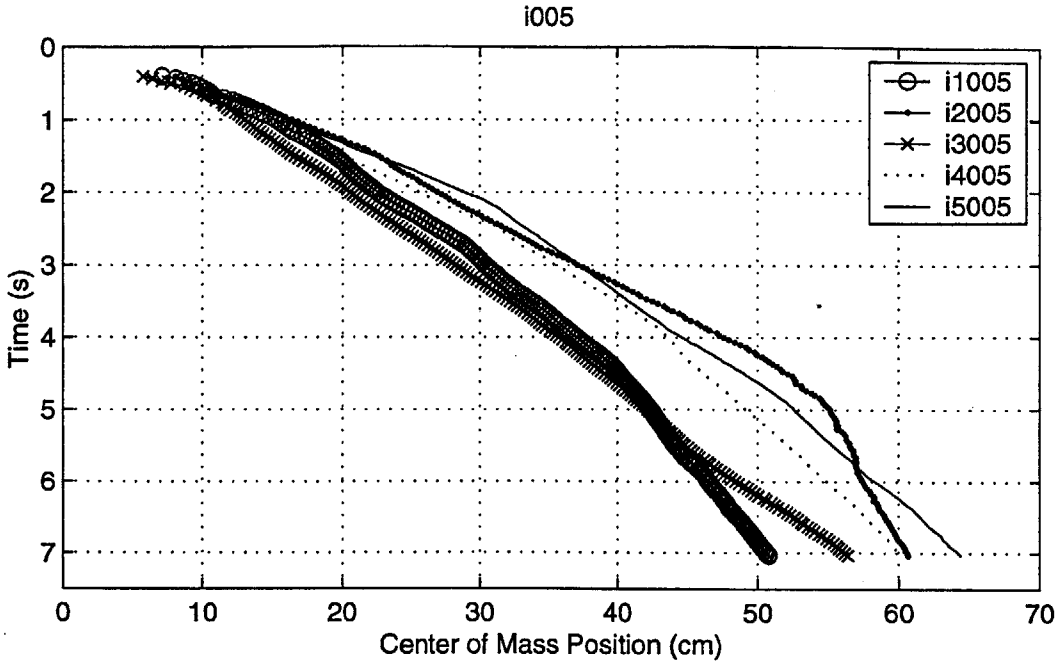
i005
i1005
i2005
i3005
i4005
i5005
Time (s)
Center of Mass Position (cm)
0
1
2
3
4
5
6
7
0
10
20
30
40
50
60
70

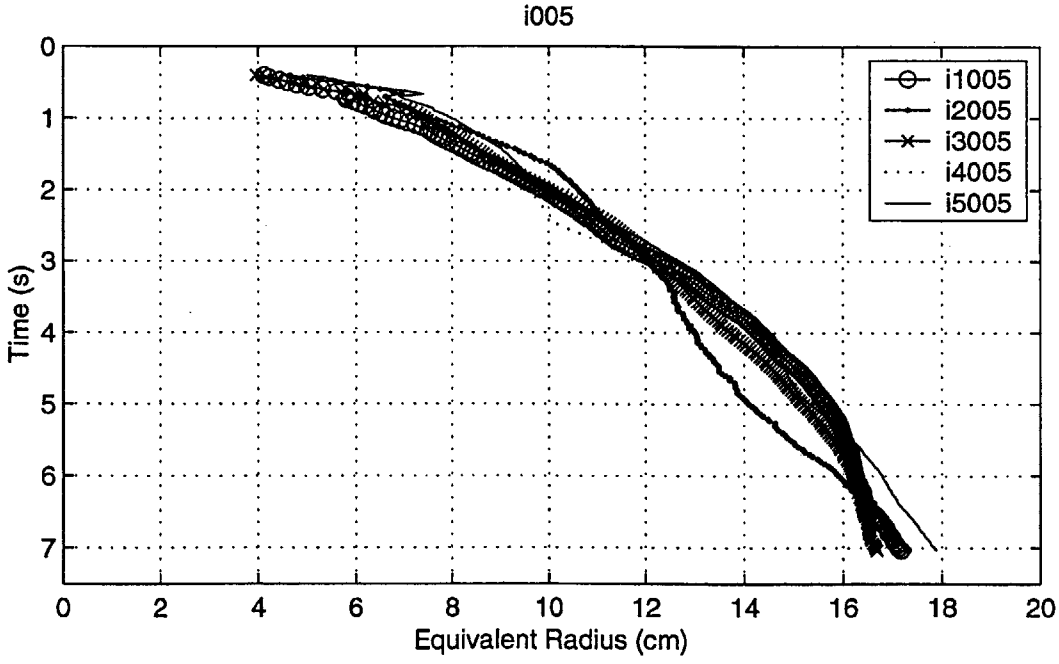
i005
i1005
i2005
i3005
i4005
i5005
Time (s)
Equivalent Radius (cm)
0
1
2
3
4
5
6
7
0
2
4
6
8
10
12
14
16
18
20

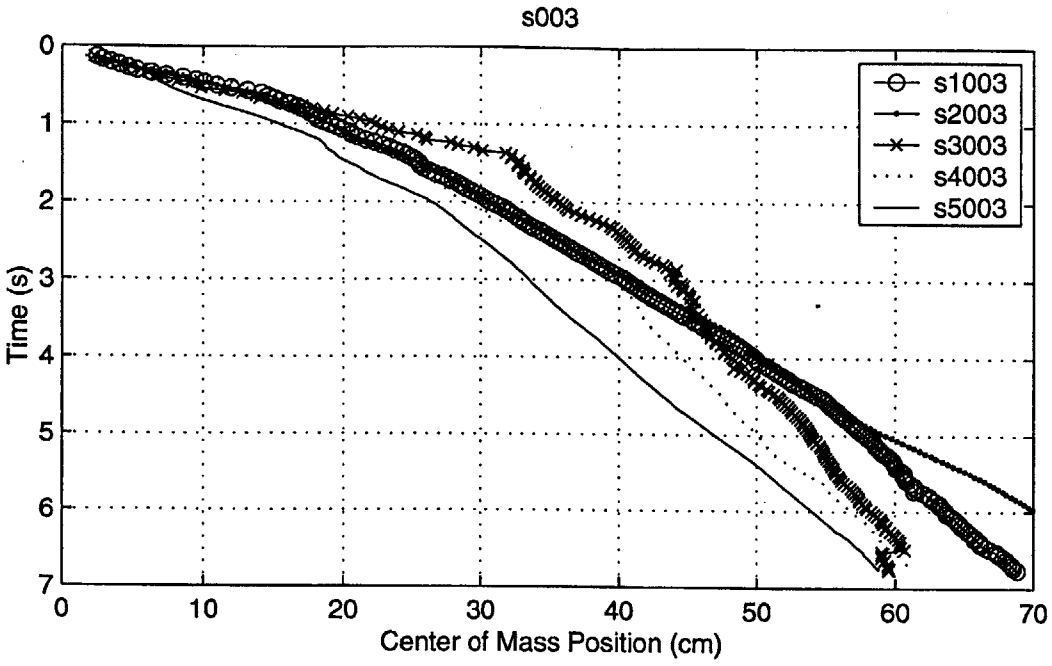
s003
s1003
s2003
s3003
s4003
s5003
Time (s)
Center of Mass Position (cm)
0
1
2
3
4
5
6
7
0
10
20
30
40
50
60
70

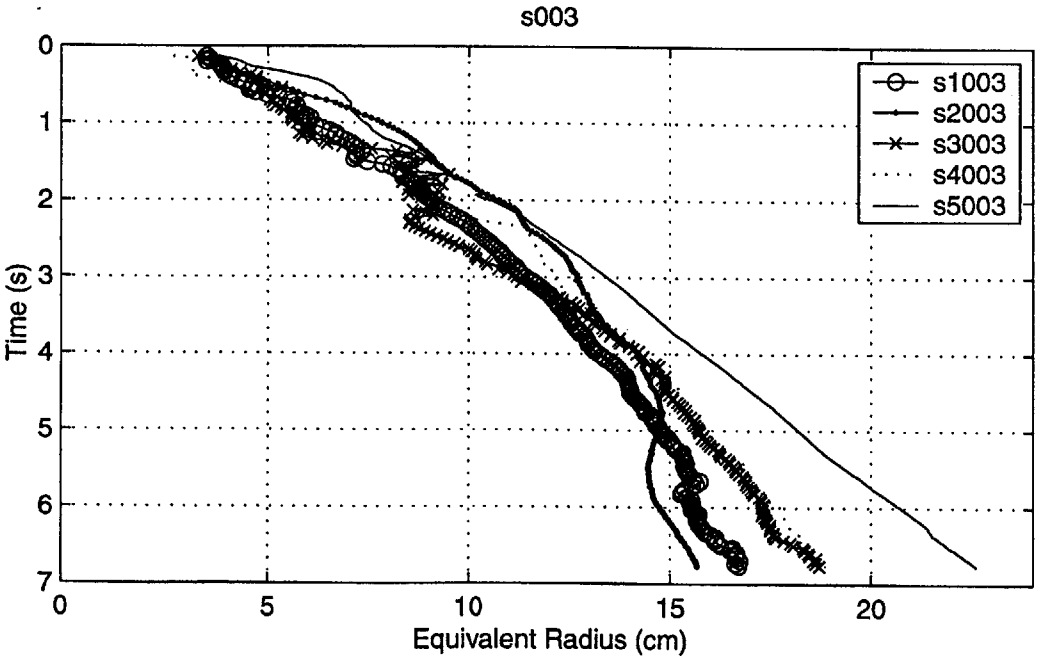
s003
s1003
s2003
s3003
s4003
s5003
Time (s)
Equivalent Radius (cm)
0
1
2
3
4
5
6
7
0
5
10
15
20

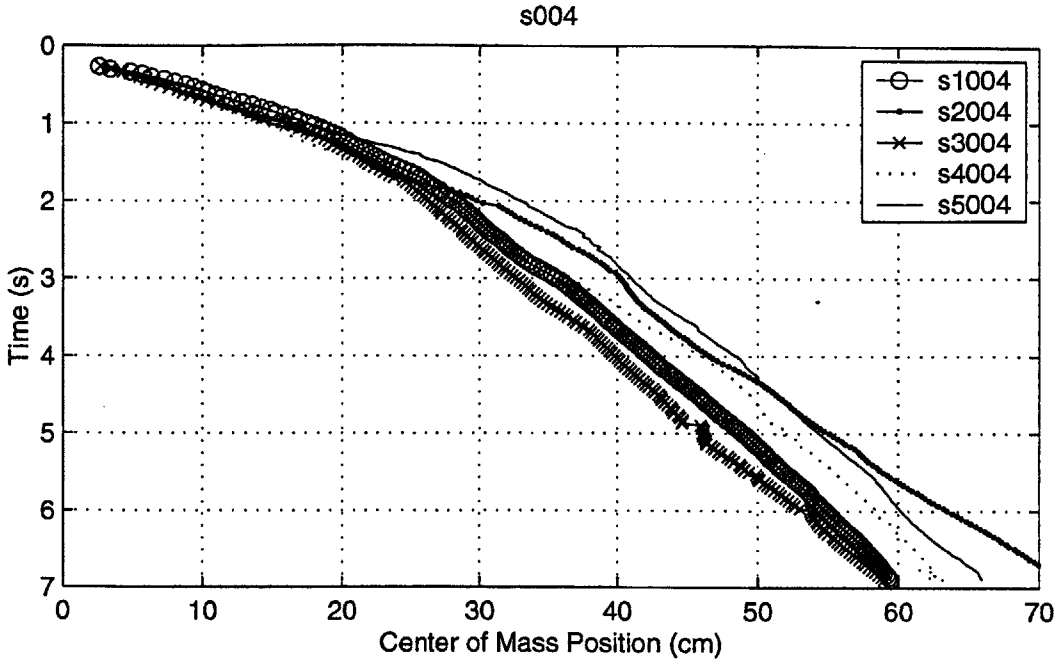
s004
s1004
s2004
s3004
s4004
s5004
Time (s)
Center of Mass Position (cm)
0
1
2
3
4
5
6
7
0
10
20
30
40
50
60
70

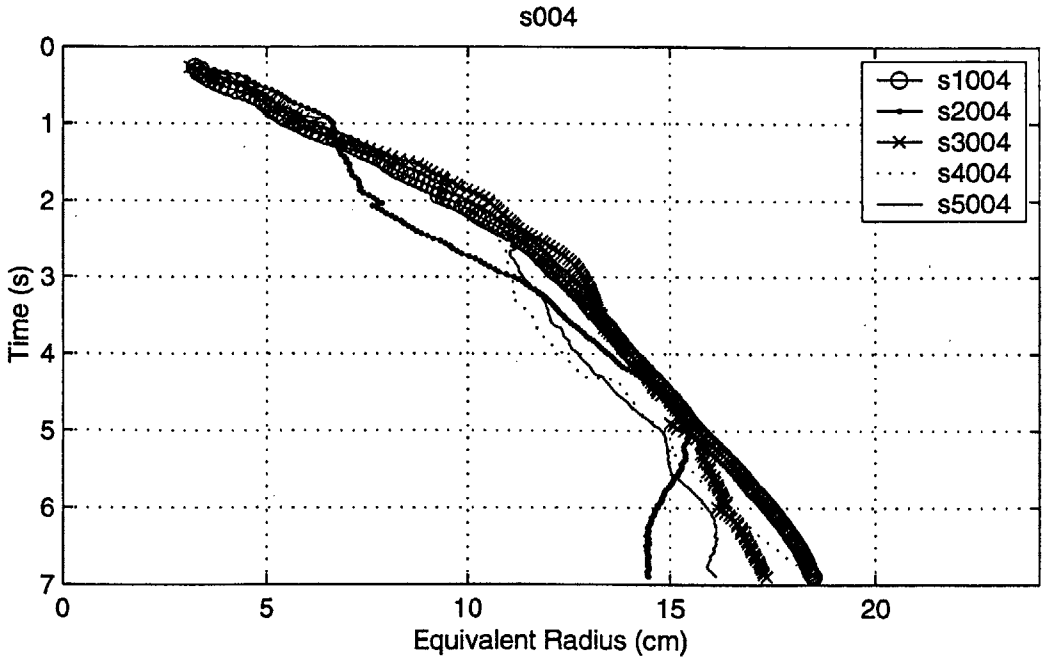
s004
s1004
s2004
s3004
s4004
s5004
Time (s)
Equivalent Radius (cm)
0
1
2
3
4
5
6
7
0
5
10
15
20

Appendix D

Entrainment Coefficient and Velocity Statistics

The standard deviations in the entrainment coefficient (α) associated with the standard deviations of the five radius versus depth curves are tabulated in Section D.1. The standard deviations in the first measured velocity (w_1) and maximum velocity (w_{max}) associated with the velocity profiles for the five realizations of each experiment are also provided in Section D.1. Representative profiles depicting the mean and standard deviations of the radius versus depth curves and velocity profiles are provided in Section D.2. A side-by-side comparison of entrainment coefficients calculated using the 100 % and 150 % cropping values (as discussed in Chapter 3) is included in Section D.3. The experimental Groups I, II, and III are described in the cross-reference table provided in Appendix A and discussed in detail in Chapter 4. The experiment numbers included in each group are also listed in the cross-reference table provided in Appendix A.

D.1 Entrainment Coefficient and Velocity Statistics – Experimental Groups I, II, and III.

Experiment	α_1	α_2	$w_1(\frac{cm}{s})$	$w_{max}(\frac{cm}{s})$
Group I Experiments				
3.18 cm Cyl., Dry	0.18 ± 0.01	0.14 ± 0.01	31.1 ± 1.6	34.2 ± 1.8
3.18 cm Cyl., Wet	0.17 ± 0.03	0.08 ± 0.03	37.4 ± 5.0	44.1 ± 0.9
4.45 cm Cyl., Dry	0.20 ± 0.02	0.16 ± 0.01	27.0 ± 1.6	29.9 ± 6.3
4.45 cm Cyl., Wet	0.22 ± 0.02	0.14 ± 0.01	24.9 ± 0.9	29.1 ± 0.4
Group II Experiments				
40 cm^3 H_2O, Sus., AW	0.27 ± 0.02	0.18 ± 0.01	32.6 ± 1.2	32.6 ± 1.2
40 cm^3 H_2O, Sus., BW	0.29 ± 0.05	0.18 ± 0.01	31.0 ± 0.7	31.0 ± 0.7
40 cm^3 H_2O, Set., AW	0.23 ± 0.01	0.16 ± 0.01	32.8 ± 2.6	32.8 ± 2.6
17 cm^3 H_2O, Sus., AW	0.28 ± 0.01	0.20 ± 0.01	29.6 ± 1.4	29.6 ± 1.4
Group III Experiments				
0.024 mm Beads, AW	0.23 ± 0.01	0.12 ± 0.02	12.2 ± 1.5	16.0 ± 6.4
0.024 mm Beads, BW	0.28 ± 0.06	0.20 ± 0.02	21.0 ± 1.3	21.0 ± 1.3
0.010 mm Silt, AW	0.27 ± 0.02	0.20 ± 0.08	18.1 ± 0.1	25.4 ± 6.9
0.010 mm Silt, BW	0.29 ± 0.03	0.24 ± 0.01	22.4 ± 1.1	28.5 ± 1.1

D.2 Example Radius and Velocity Profiles With Standard Deviations

In the following figures, mean values are denoted by the center dotted lines, and the associated standard deviations are denoted by the outer continuous lines.

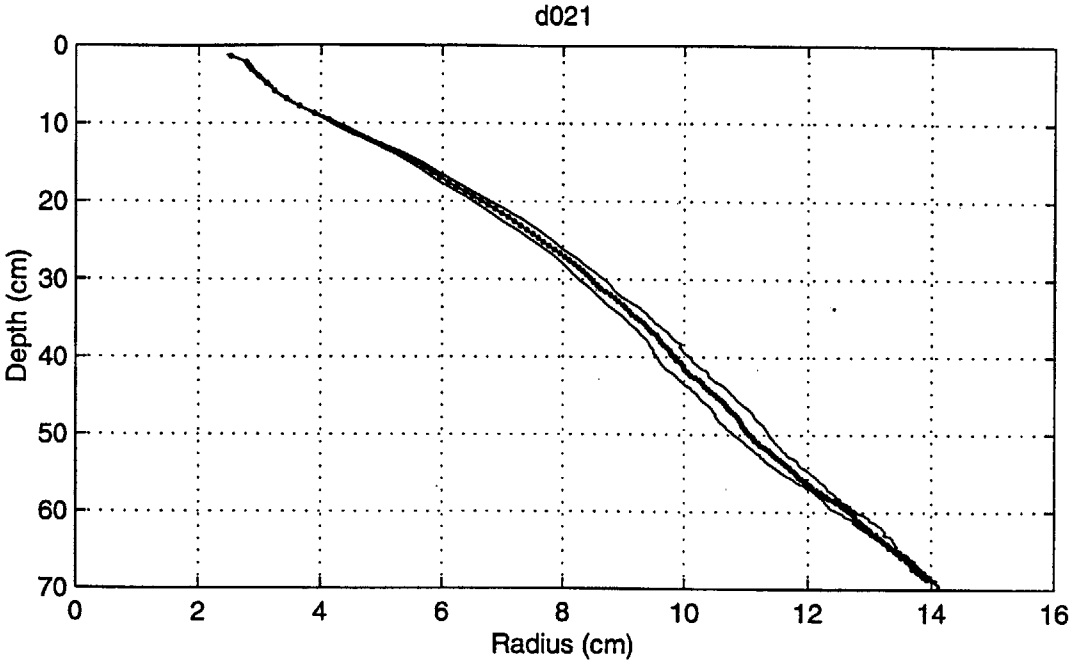
d021
Depth (cm)
Radius (cm)
0
10
20
30
40
50
60
70
0
2
4
6
8
10
12
14
16

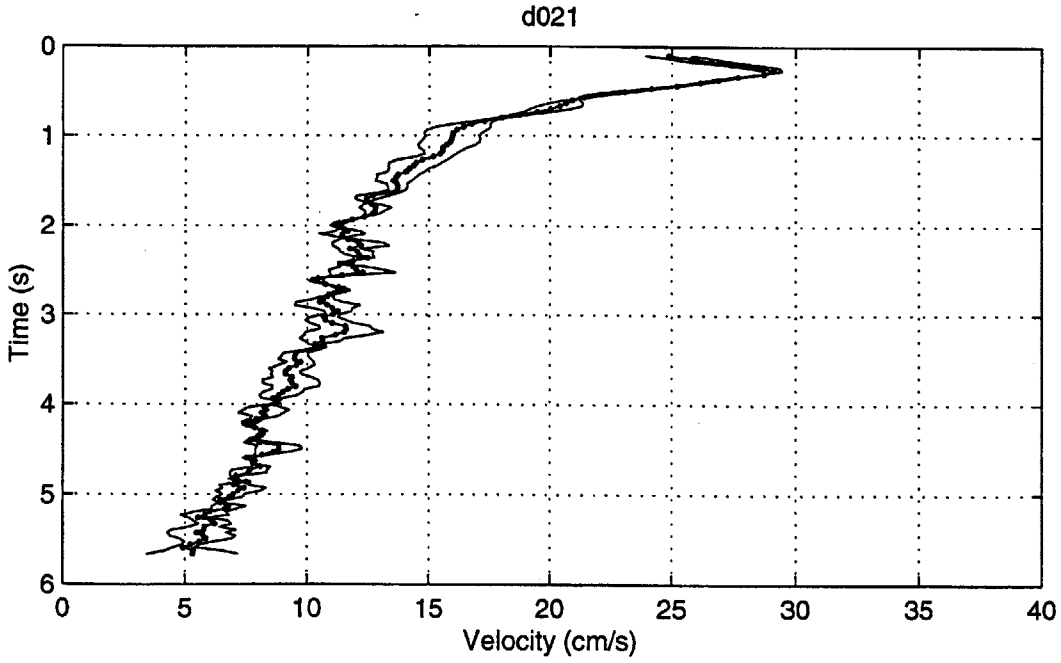
d021
Time (s)
Velocity (cm/s)
0
1
2
3
4
5
6
0
5
10
15
20
25
30
35
40

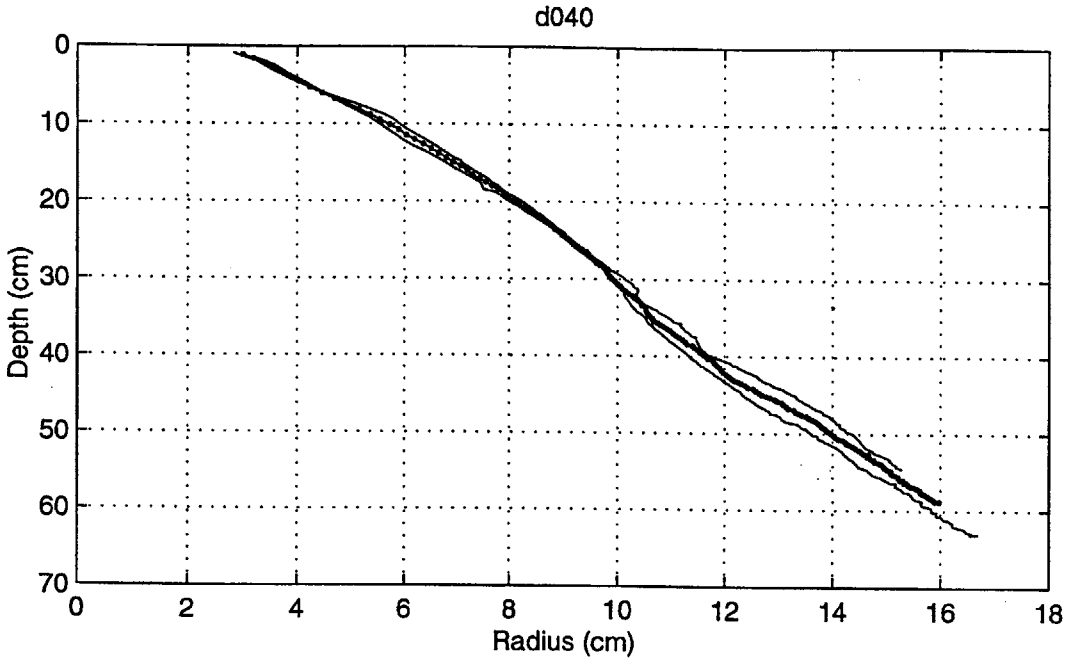
d040
Depth (cm)
Radius (cm)
0
10
20
30
40
50
60
70
0
2
4
6
8
10
12
14
16
18

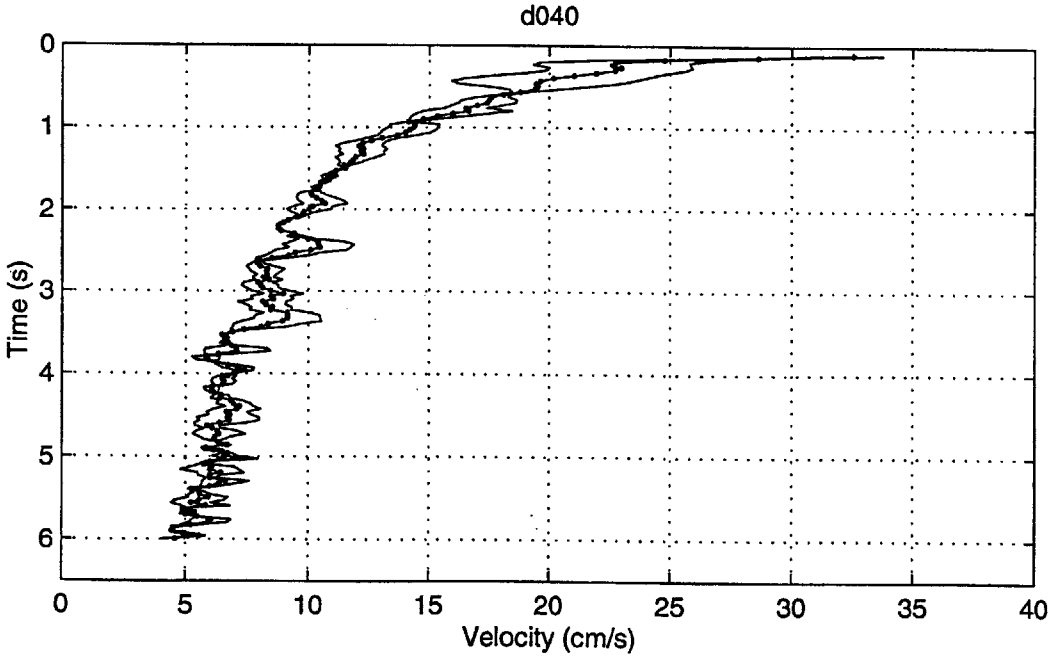
d040
Time (s)
Velocity (cm/s)
0
1
2
3
4
5
6
0
5
10
15
20
25
30
35
40

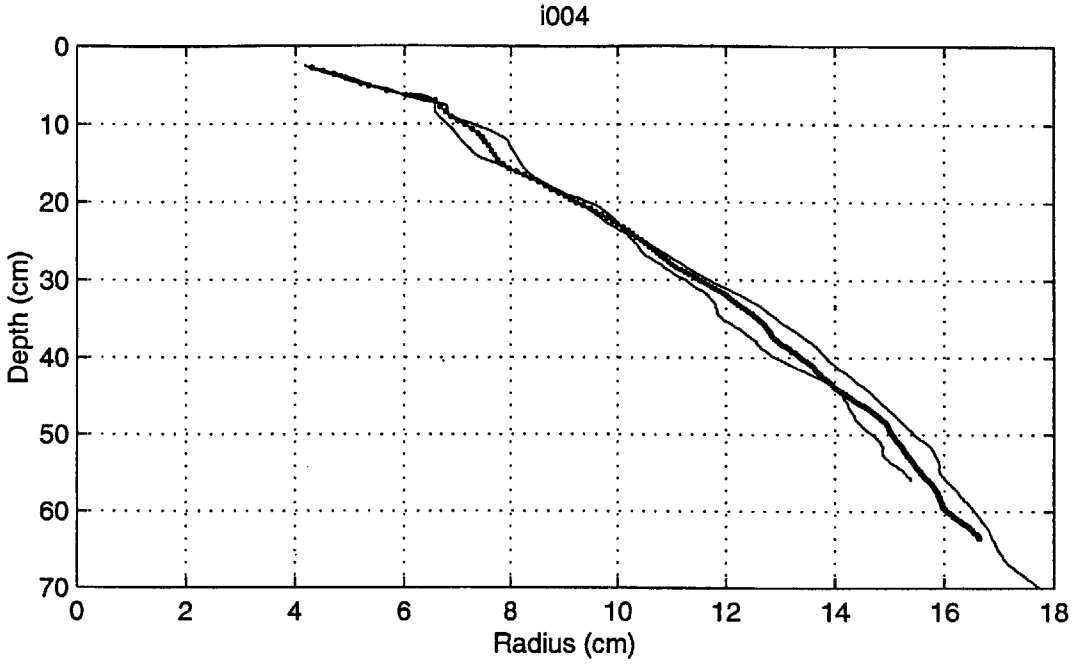
i004
Depth (cm)
Radius (cm)
0
10
20
30
40
50
60
70
0
2
4
6
8
10
12
14
16
18

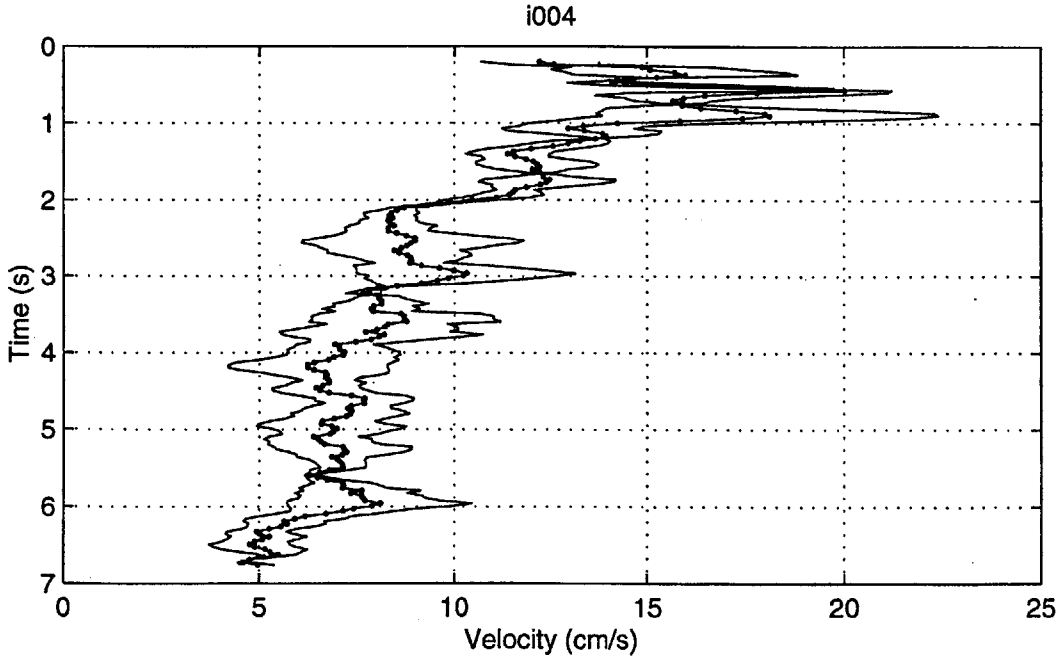
i004
Time (s)
Velocity (cm/s)
0
1
2
3
4
5
6
7
0
5
10
15
20
25

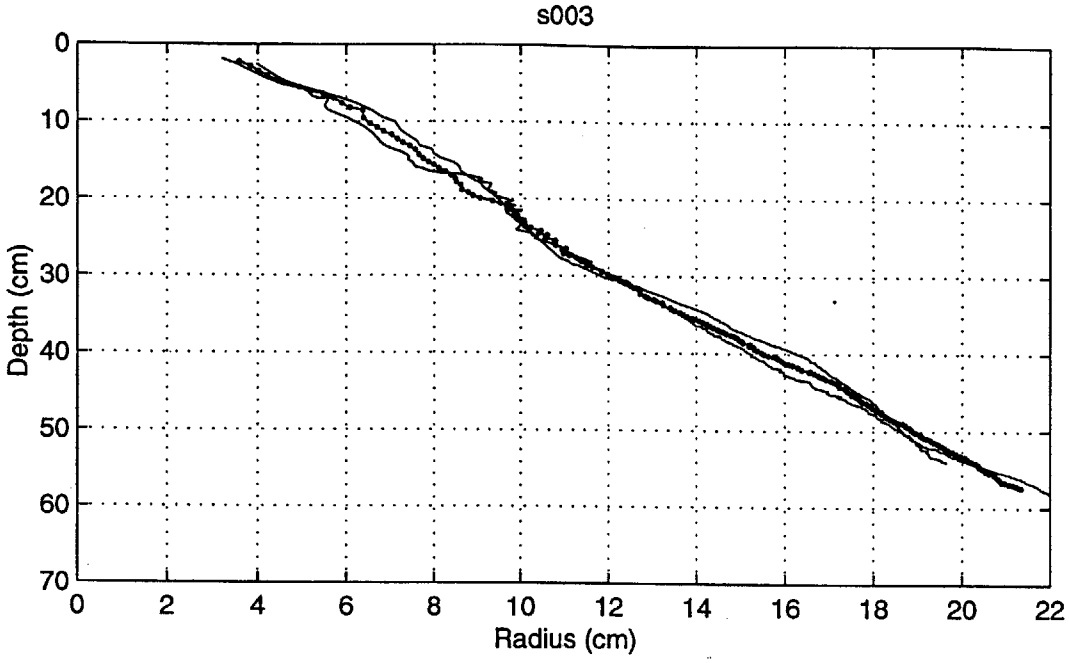
s003
Depth (cm)
Radius (cm)
0
10
20
30
40
50
60
70
0
2
4
6
8
10
12
14
16
18
20
22

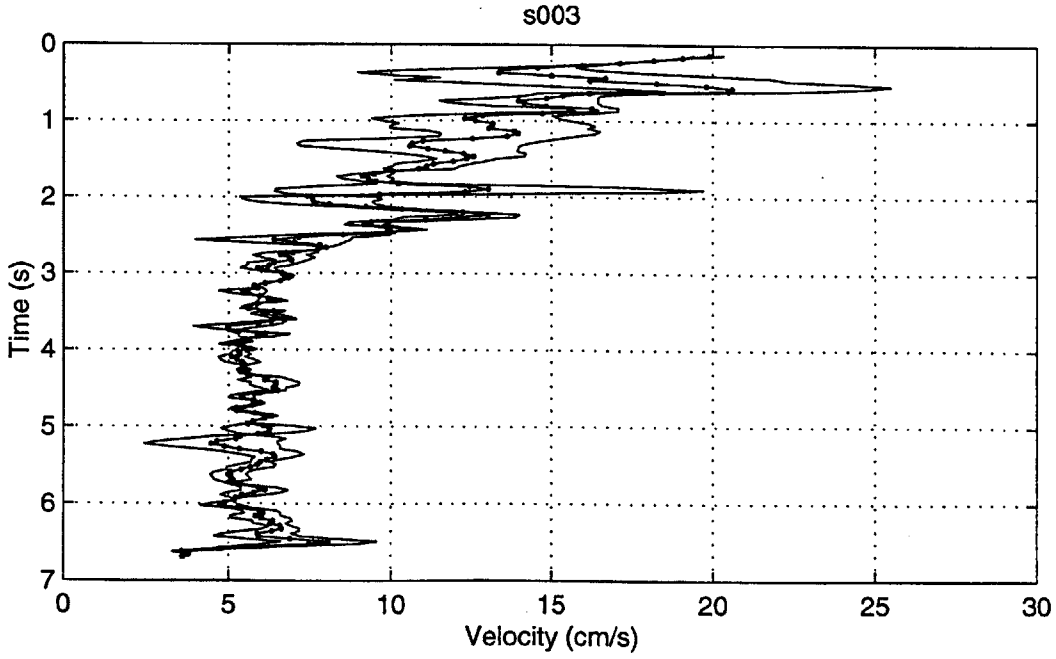
s003
Time (s)
Velocity (cm/s)
0
1
2
3
4
5
6
7
0
5
10
15
20
25
30

D.3 Effect of 100 % and 150 % Cropping Criteria on Entrainment Coefficients

Experiment	$\alpha_1{}^1$	$\alpha_2{}^1$	$\alpha_1{}^2$	$\alpha_2{}^2$
Group I Experiments				
3.18 cm Cyl., Dry	0.18	0.16	0.18	0.14
3.18 cm Cyl., Wet	0.15	0.10	0.17	0.08
4.45 cm Cyl., Dry	0.20	0.16	0.20	0.16
4.45 cm Cyl., Wet	0.22	0.14	0.22	0.14
Group II Experiments				
40 cm^3 H_2O, Sus., AW	0.27	0.18	0.27	0.18
40 cm^3 H_2O, Sus., BW	0.27	0.17	0.29	0.18
40 cm^3 H_2O, Set., AW	0.23	0.16	0.23	0.16
17 cm^3 H_2O, Sus., AW	0.28	0.20	0.28	0.20
Group III Experiments				
0.024 mm Beads, AW	0.23	0.14	0.23	0.12
0.024 mm Beads, BW	0.24	0.20	0.28	0.20
0.010 mm Silt, AW	0.27	0.20	0.32	0.32
0.010 mm Silt, BW	0.29	0.24	0.34	0.30

1 - Cropping criterion = 100 % of maximum diameter.

2 - Cropping criterion = 150 % of maximum diameter.

Appendix E

Results for 0.556 mm Glass Bead Experiments

Eight experiments were conducted using the 0.556 mm glass beads and all four release cylinder sizes. The buoyancy was held constant for all experiments with an initial solids mass of 40 g. Four of the experiments were performed using initially dry beads ("Dry" experiments), and four experiments were performed with $17cm^3$ of water added to the initial volume of beads ("Wet" experiments). All experiments were conducted with the bottom of the releasé cylinder positioned immediately above the water surface ("AW").

As with the other experiments, each experiment was repeated five times. Selected images depicting all five repetitions for the particle clouds produced by the "wet" experiments are provided in Section E.1. Equivalent radius versus depth curves and center of mass velocity versus time profiles based on mean values of the five realizations are provided in Section E.2. Entrainment coefficients estimated from the equivalent radius versus depth curves are provided in Section E.3 along with the initial and maximum velocity values for each experiment. Only one α value was estimated for each experiment, since the transition from α_1 to α_2 was not as apparent in these experiments as it was in the plots generated from the experiments using the smaller glass beads. The transition is more apparent in the "Wet" experiments, occurring at a depth of about 30 cm for the two narrowest cylinders and at about 18 cm

for the two largest cylinder sizes. The absence of a marked transition in α associated with the "turbulent thermal" and "circulating thermal" phases may be attributed to the following: (1) the fact that turbulence was quickly suppressed in the first phase, as the clouds took on a laminar appearance within the 1 s of descent; (2) particles began to settle out of the cloud early in the "circulating thermal" phase (after 2 s) decreasing the circulation and increasing α.

E.1 Selected Images for "Wet" Experiments

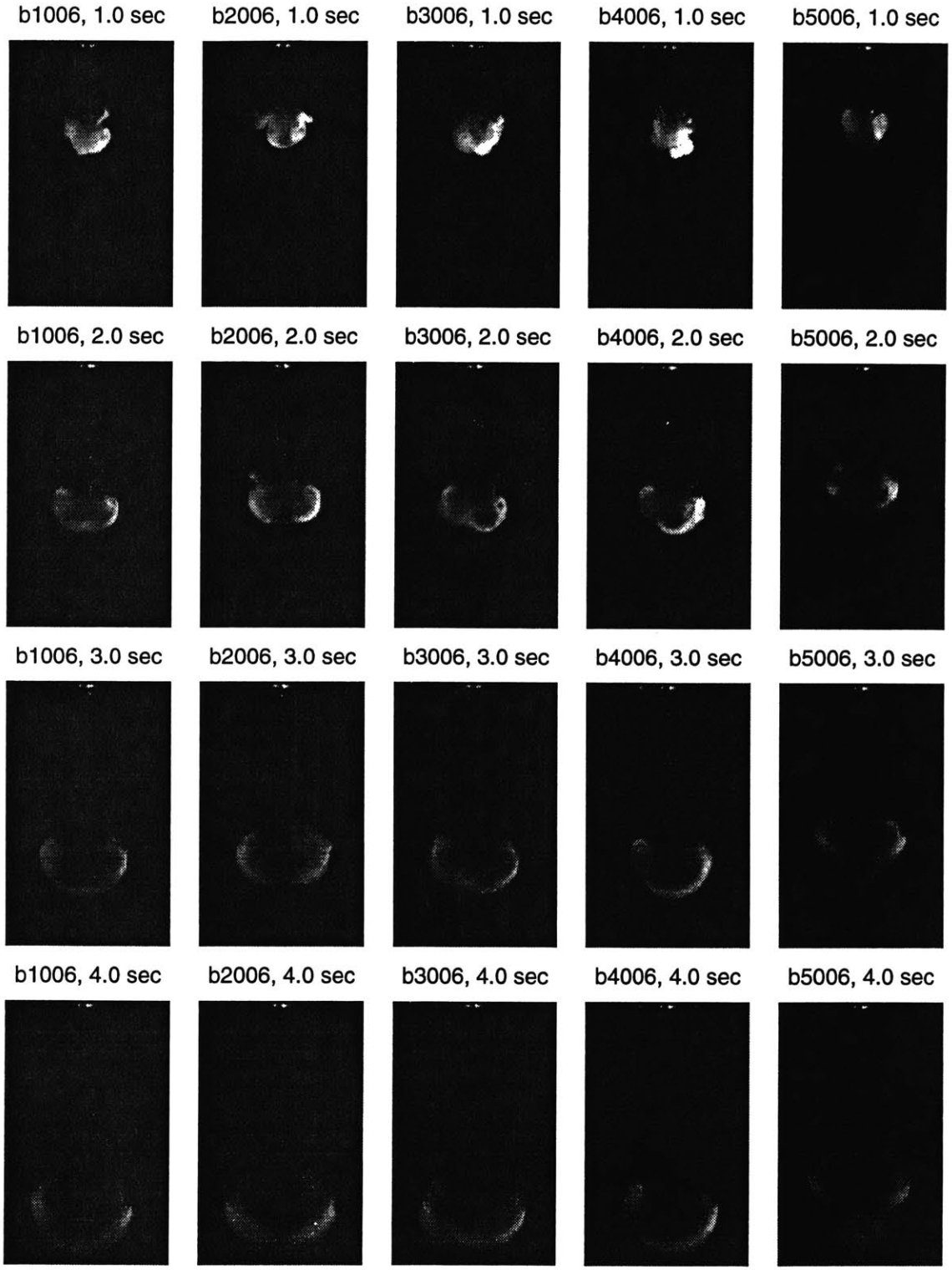
b1006, 1.0 sec
b2006, 1.0 sec
b3006, 1.0 sec
b4006, 1.0 sec
b5006, 1.0 sec
b1006, 2.0 sec
b2006, 2.0 sec
b3006, 2.0 sec
b4006, 2.0 sec
b5006, 2.0 sec
b1006, 3.0 sec
b2006, 3.0 sec
b3006, 3.0 sec
b4006, 3.0 sec
b5006, 3.0 sec
b1006, 4.0 sec
b2006, 4.0 sec
b3006, 4.0 sec
b4006, 4.0 sec
b5006, 4.0 sec

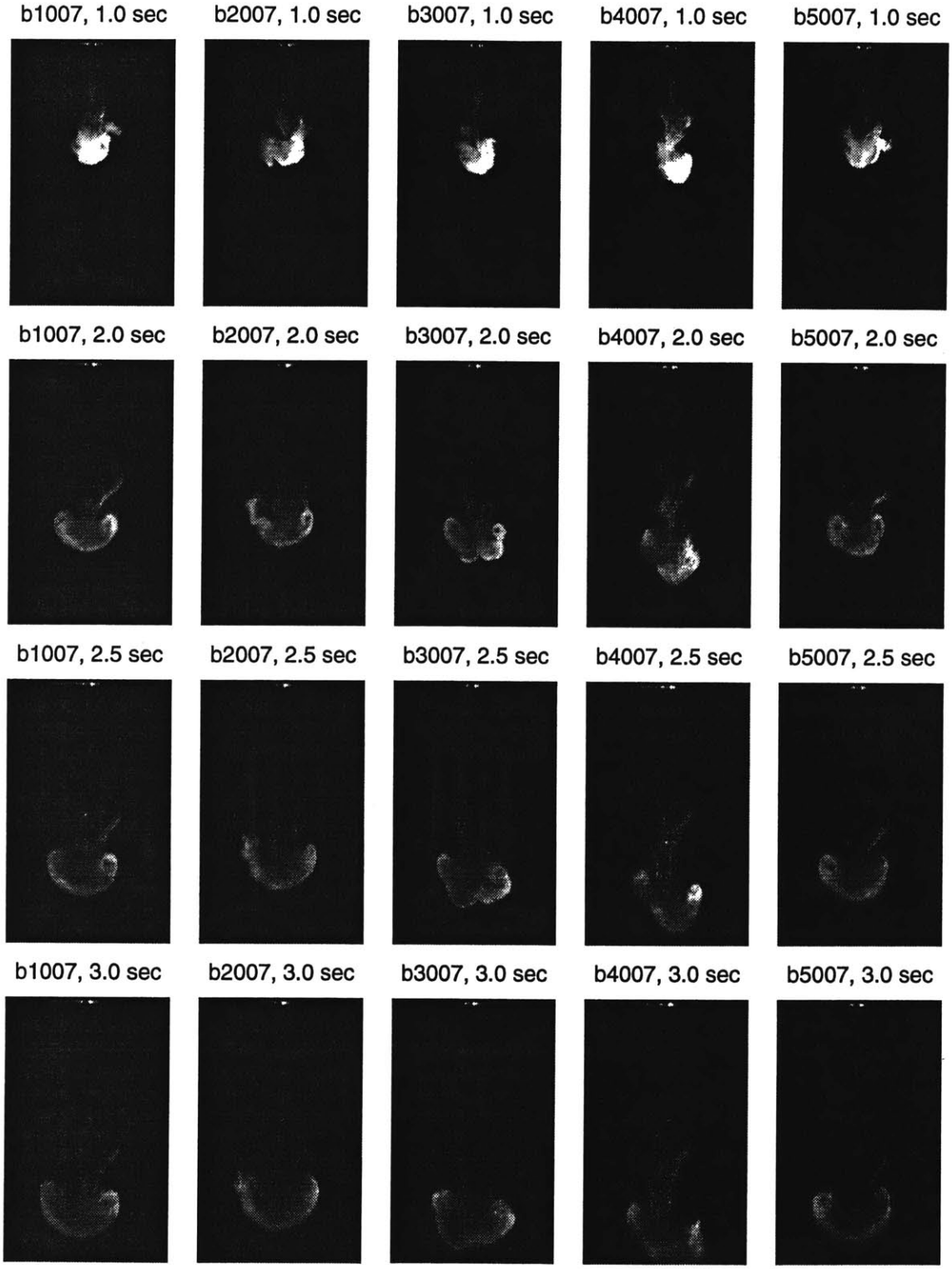
b1007, 1.0 sec
b2007, 1.0 sec
b3007, 1.0 sec
b4007, 1.0 sec
b5007, 1.0 sec
b1007, 2.0 sec
b2007, 2.0 sec
b3007, 2.0 sec
b4007, 2.0 sec
b5007, 2.0 sec
b1007, 2.5 sec
b2007, 2.5 sec
b3007, 2.5 sec
b4007, 2.5 sec
b5007, 2.5 sec
b1007, 3.0 sec
b2007, 3.0 sec
b3007, 3.0 sec
b4007, 3.0 sec
b5007, 3.0 sec

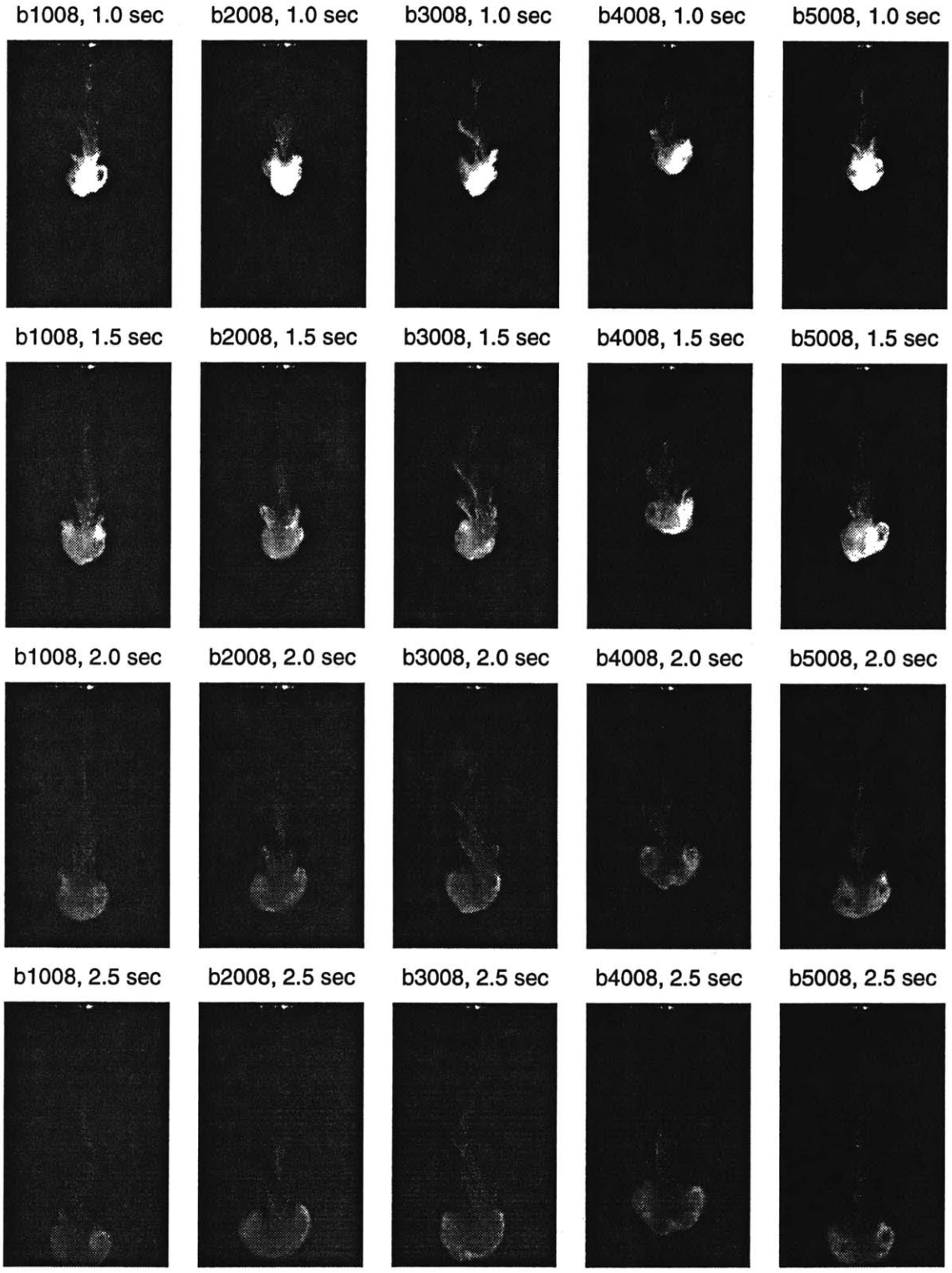
b1008, 1.0 sec
b2008, 1.0 sec
b3008, 1.0 sec
b4008, 1.0 sec
b5008, 1.0 sec
b1008, 1.5 sec
b2008, 1.5 sec
b3008, 1.5 sec
b4008, 1.5 sec
b5008, 1.5 sec
b1008, 2.0 sec
b2008, 2.0 sec
b3008, 2.0 sec
b4008, 2.0 sec
b5008, 2.0 sec
b1008, 2.5 sec
b2008, 2.5 sec
b3008, 2.5 sec
b4008, 2.5 sec
b5008, 2.5 sec

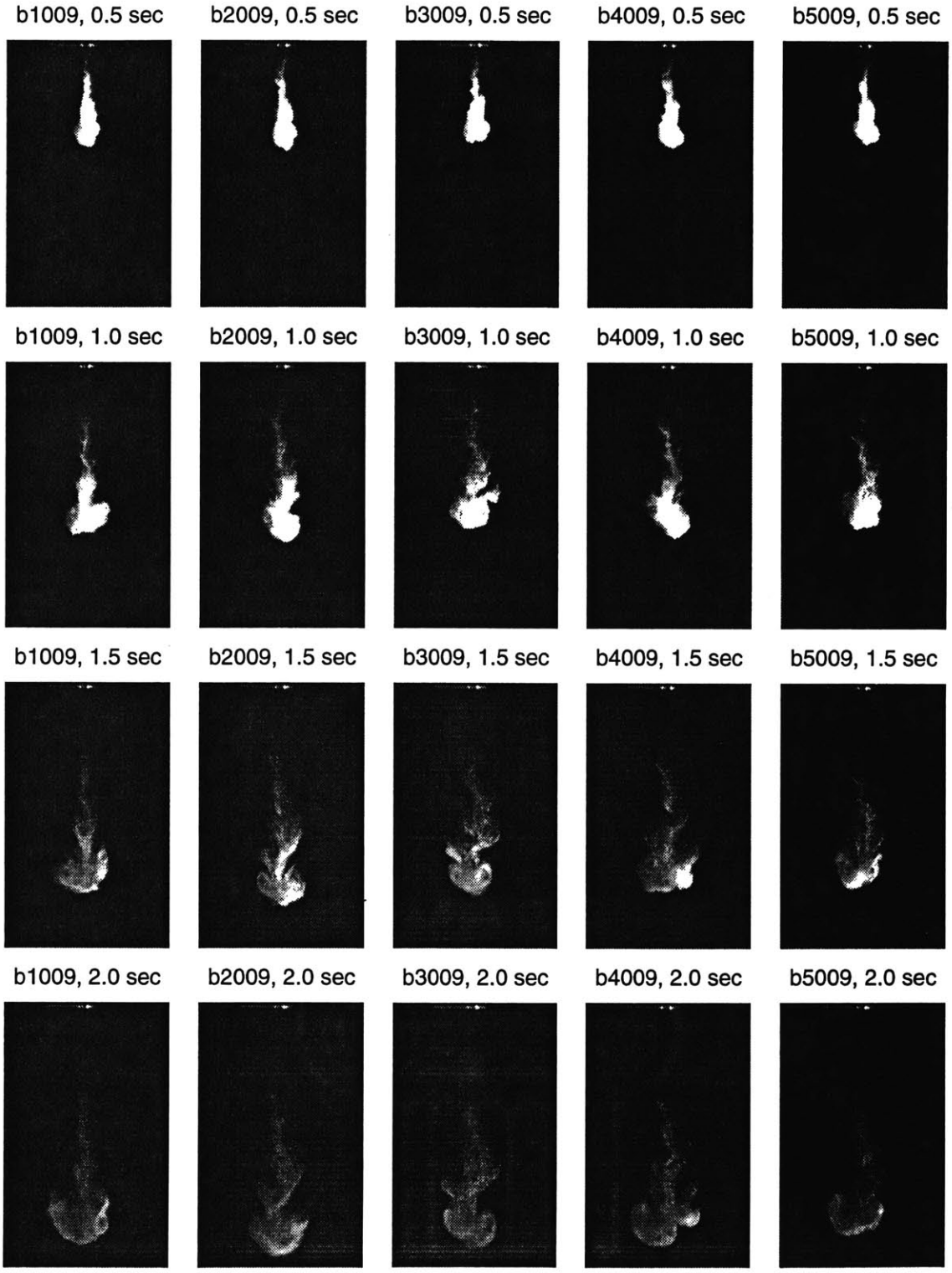
b1009, 0.5 sec
b2009, 0.5 sec
b3009, 0.5 sec
b4009, 0.5 sec
b5009, 0.5 sec
b1009, 1.0 sec
b2009, 1.0 sec
b3009, 1.0 sec
b4009, 1.0 sec
b5009, 1.0 sec
b1009, 1.5 sec
b2009, 1.5 sec
b3009, 1.5 sec
b4009, 1.5 sec
b5009, 1.5 sec
b1009, 2.0 sec
b2009, 2.0 sec
b3009, 2.0 sec
b4009, 2.0 sec
b5009, 2.0 sec

E.2 Equivalent Radius and Velocity Profiles

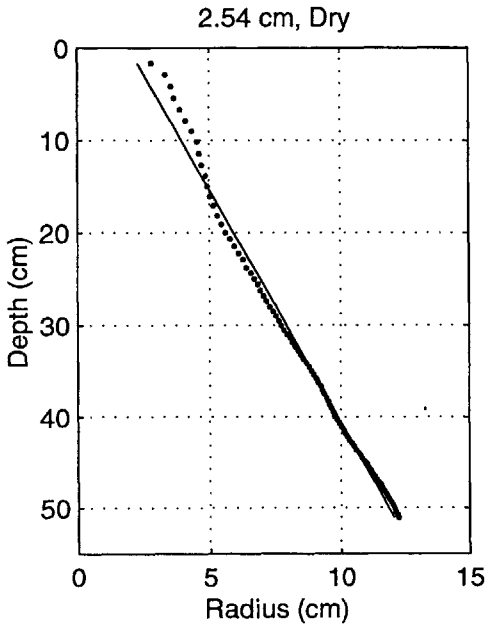
2.54 cm, Dry
Depth (cm)
Radius (cm)
0
10
20
30
40
50
0
5
10
15

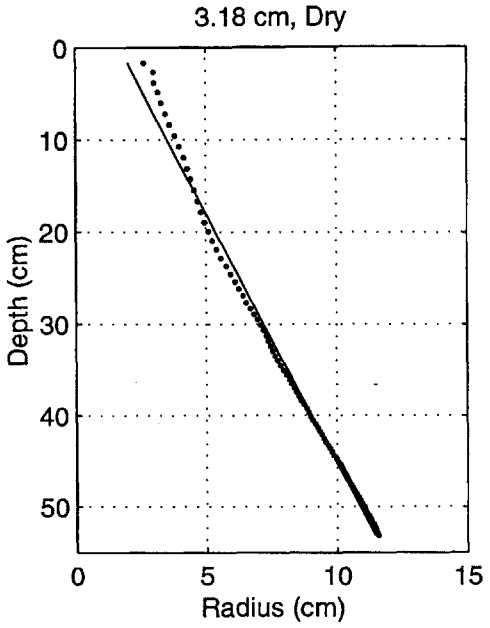
3.18 cm, Dry
Depth (cm)
Radius (cm)
0
10
20
30
40
50
0
5
10
15

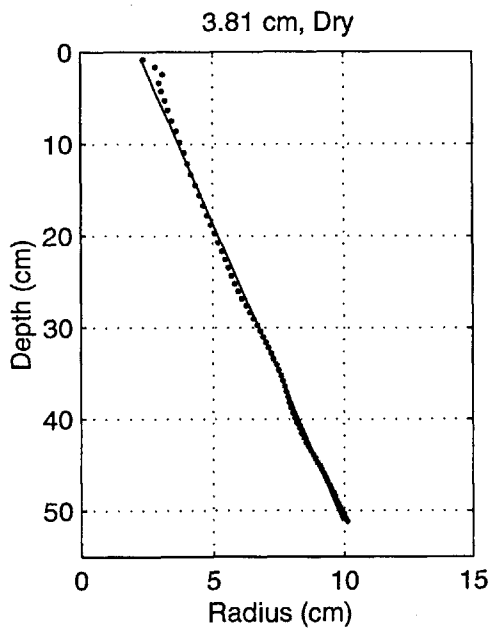
3.81 cm, Dry
Depth (cm)
Radius (cm)
0
10
20
30
40
50
0
5
10
15

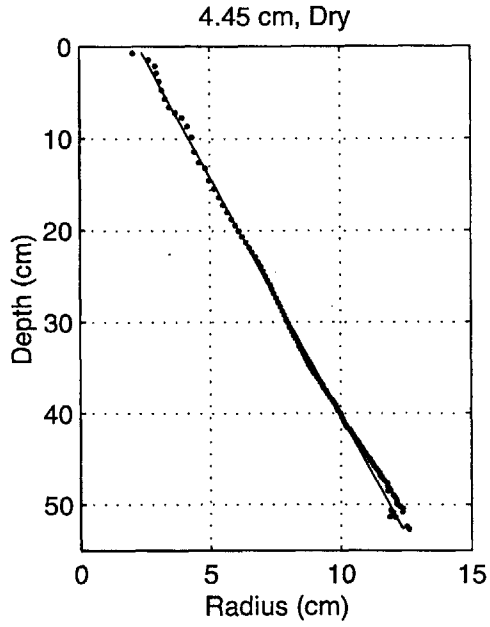
4.45 cm, Dry
Depth (cm)
Radius (cm)
0
10
20
30
40
50
0
5
10
15

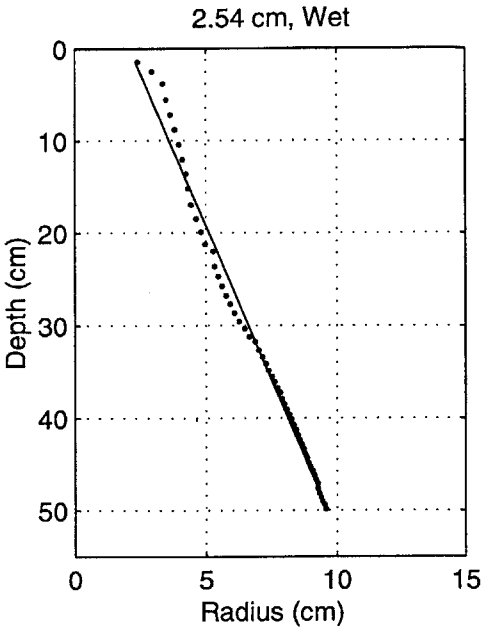
2.54 cm, Wet
Depth (cm)
Radius (cm)
0
10
20
30
40
50
0
5
10
15

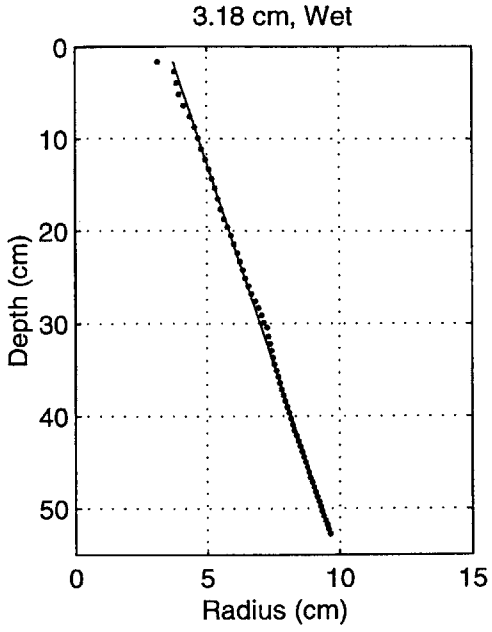
3.18 cm, Wet
Depth (cm)
Radius (cm)
0
10
20
30
40
50
0
5
10
15

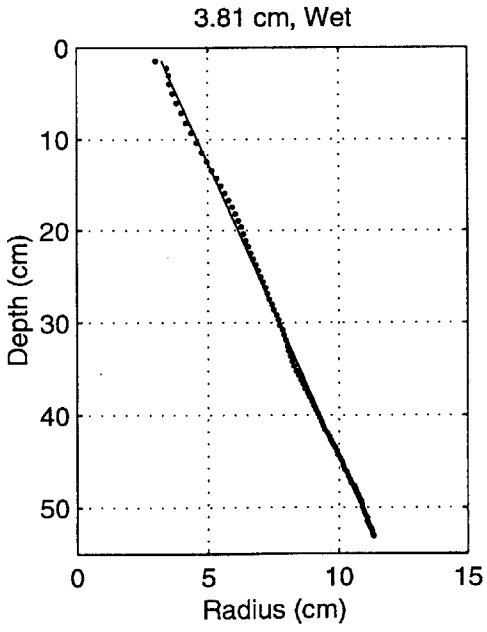
3.81 cm, Wet
Depth (cm)
Radius (cm)
0
10
20
30
40
50
0
5
10
15

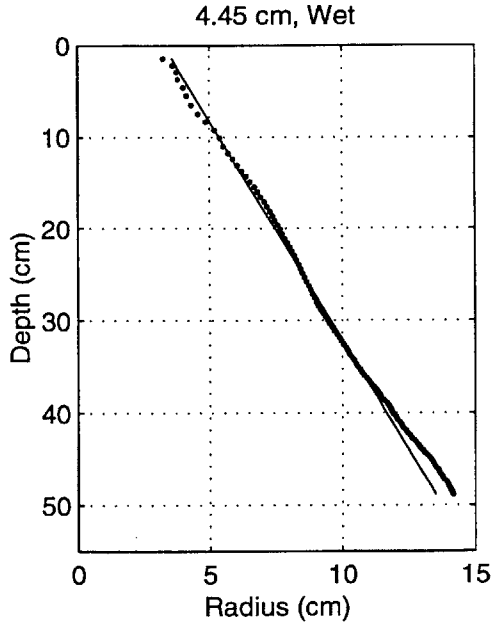
4.45 cm, Wet
Depth (cm)
Radius (cm)
0
10
20
30
40
50
0
5
10
15

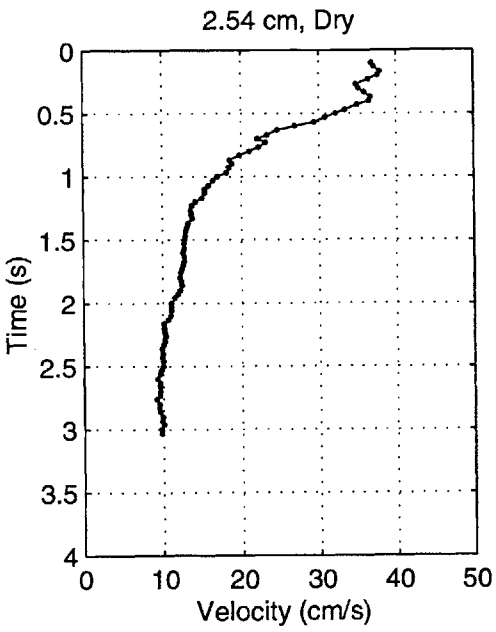
2.54 cm, Dry
Time (s)
Velocity (cm/s)
0
0.5
1
1.5
2
2.5
3
3.5
4
0
10
20
30
40
50

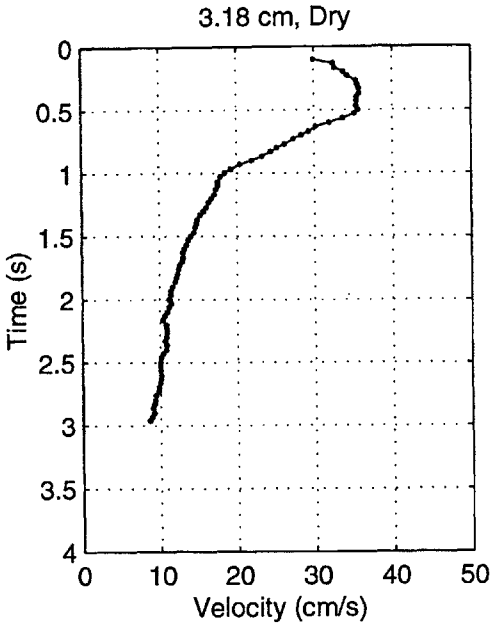
3.18 cm, Dry
Time (s)
Velocity (cm/s)
0
0.5
1
1.5
2
2.5
3
3.5
4
0
10
20
30
40
50

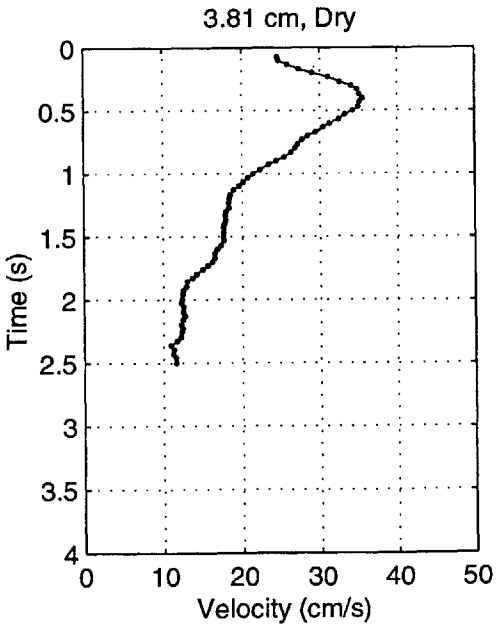
3.81 cm, Dry
Time (s)
Velocity (cm/s)
0
0.5
1
1.5
2
2.5
3
3.5
4
0
10
20
30
40
50

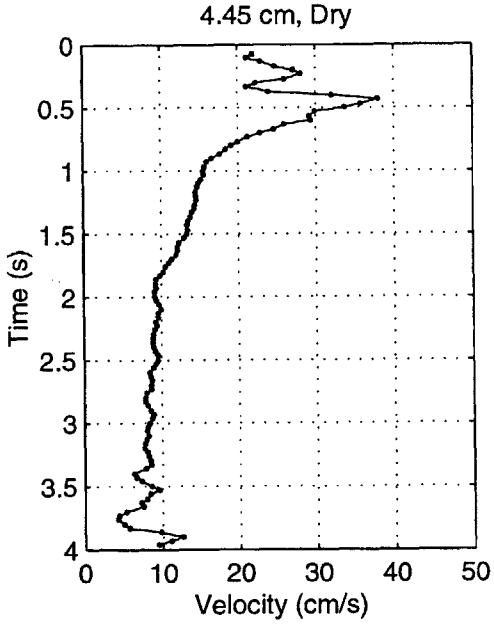
4.45 cm, Dry
Time (s)
Velocity (cm/s)
0
0.5
1
1.5
2
2.5
3
3.5
4
0
10
20
30
40
50

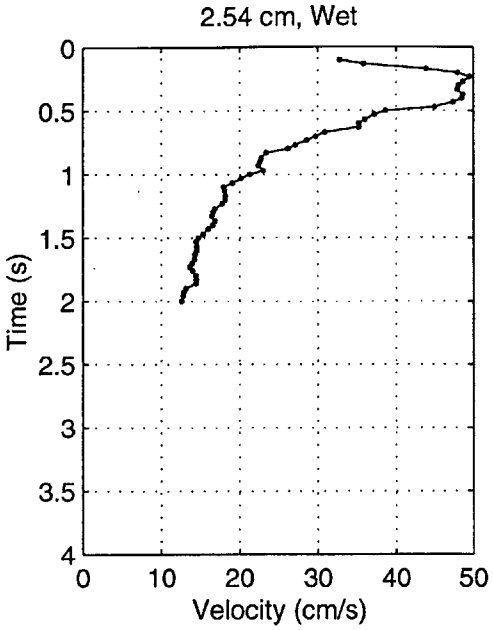
2.54 cm, Wet
Time (s)
Velocity (cm/s)
0
0.5
1
1.5
2
2.5
3
3.5
4
0
10
20
30
40
50

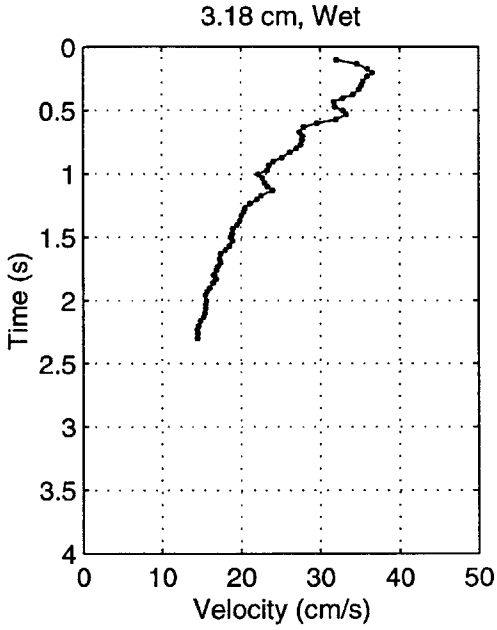
3.18 cm, Wet
Time (s)
Velocity (cm/s)
0
0.5
1
1.5
2
2.5
3
3.5
4
0
10
20
30
40
50

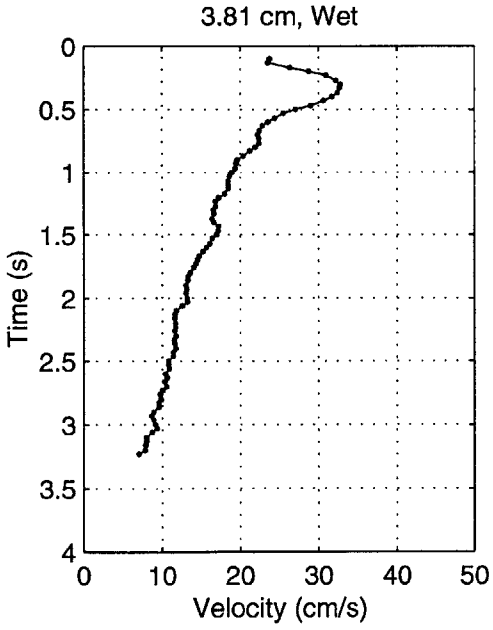
3.81 cm, Wet
Time (s)
Velocity (cm/s)
0
0.5
1
1.5
2
2.5
3
3.5
4
0
10
20
30
40
50

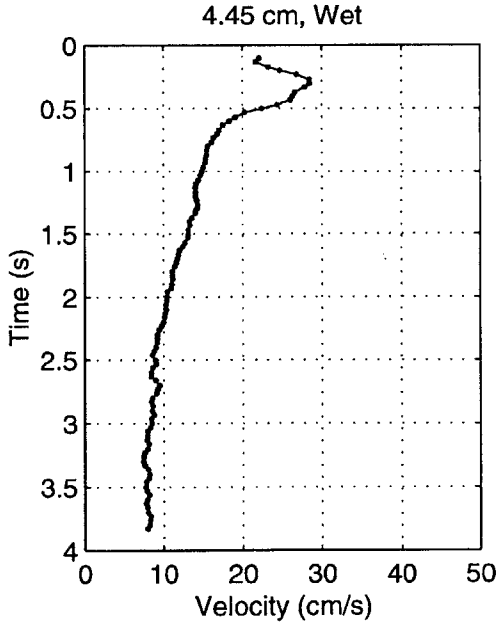
4.45 cm, Wet
Time (s)
Velocity (cm/s)
0
0.5
1
1.5
2
2.5
3
3.5
4
0
10
20
30
40
50

E.3 Entrainment Coefficients and Velocity Data

Experiment	α	$w_1(\frac{cm}{s})$	$w_{max}(\frac{cm}{s})$
2.54 cm Cyl., Dry	0.20	36.8	37.9
2.54 cm Cyl., Wet	0.15	32.8	49.5
3.18 cm Cyl., Dry	0.19	29.9	35.7
3.18 cm Cyl., Wet	0.12	32.0	36.6
3.81 cm Cyl., Dry	0.15	24.5	35.5
3.81 cm Cyl., Wet	0.16	23.8	32.8
4.45 cm Cyl., Dry	0.21	21.9	37.9
4.45 cm Cyl., Wet	0.23	22.1	28.4

Appendix F

Radius and Velocity Profiles for Boston Blue Clay Experiments

The following two pages depict the leading edge velocity and maximum radius profiles for the three repetitions performed for each of the four Boston Blue Clay experiments described in Chapter 7. The experiment numbers included in the figures are described in the cross-reference table provided in Appendix A.

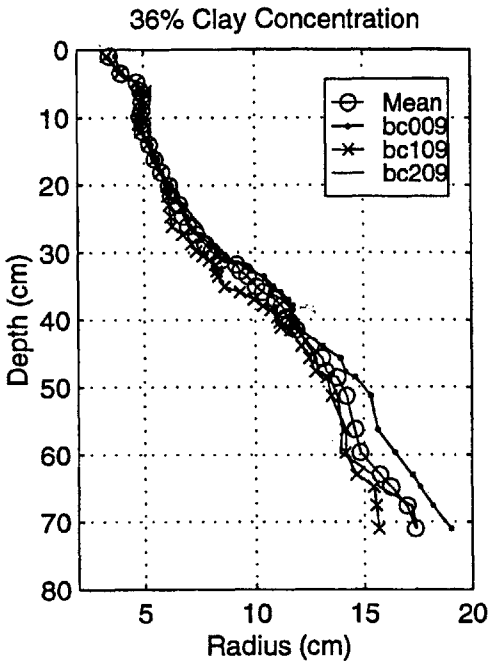
36% Clay Concentration
Mean
bc009
bc109
bc209
Depth (cm)
Radius (cm)
0
10
20
30
40
50
60
70
80
5
10
15
20

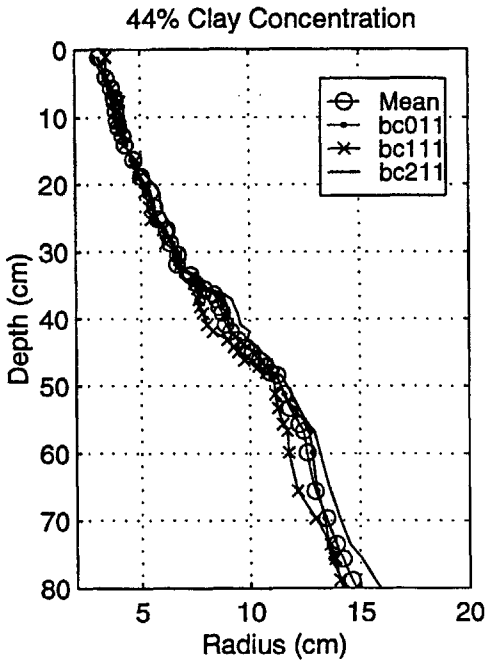
44% Clay Concentration
Mean
bc011
bc111
bc211
Depth (cm)
Radius (cm)
0
10
20
30
40
50
60
70
80
5
10
15
20

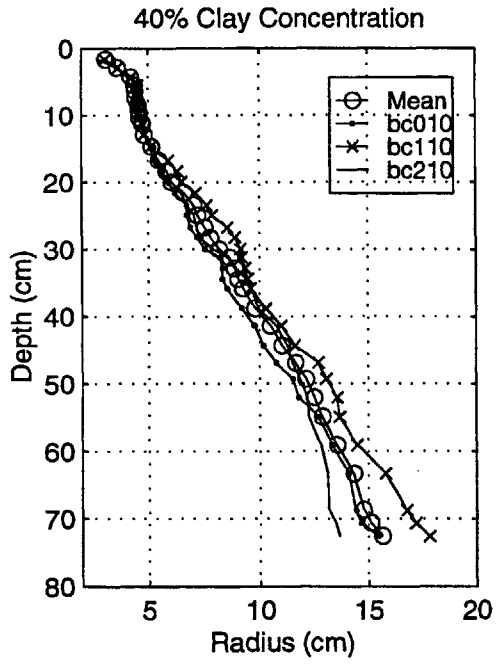
40% Clay Concentration
Mean
bc010
bc110
bc210
Depth (cm)
Radius (cm)
0
10
20
30
40
50
60
70
80
5
10
15
20

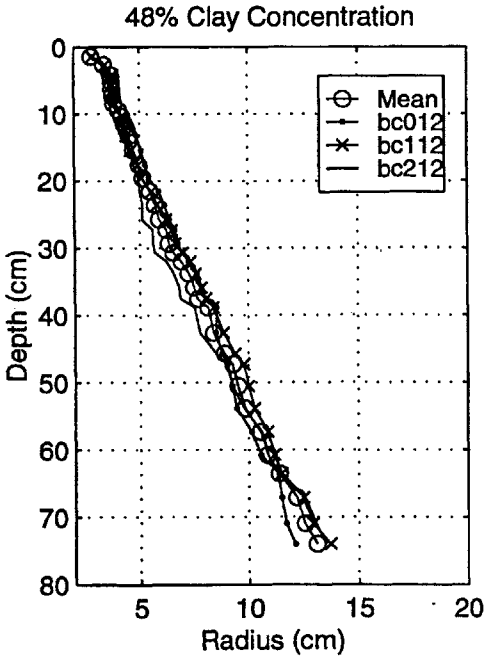
48% Clay Concentration
Mean
bc012
bc112
bc212
Depth (cm)
Radius (cm)
0
10
20
30
40
50
60
70
80
5
10
15
20

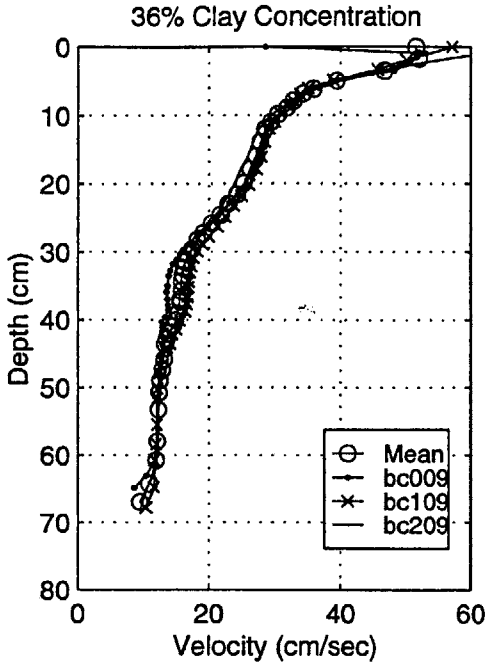
36% Clay Concentration
Depth (cm)
Velocity (cm/sec)
Mean
bc009
bc109
bc209

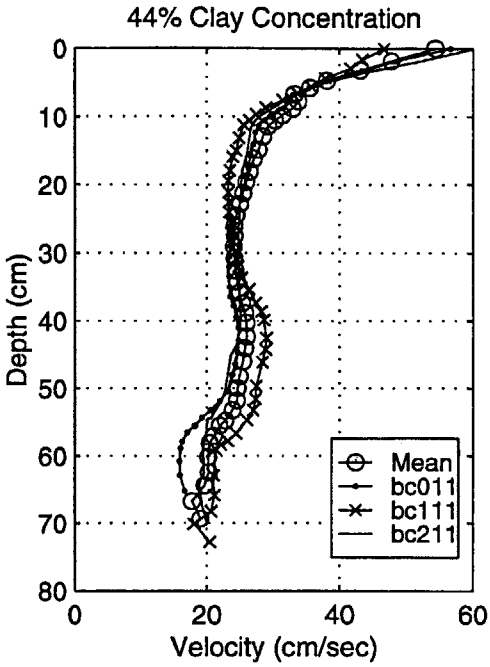
44% Clay Concentration
Depth (cm)
Velocity (cm/sec)
Mean
bc011
bc111
bc211

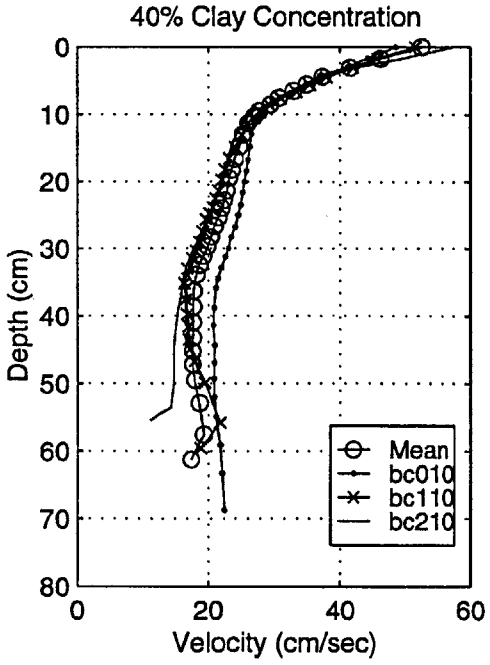
40% Clay Concentration
Depth (cm)
Velocity (cm/sec)
Mean
bc010
bc110
bc210

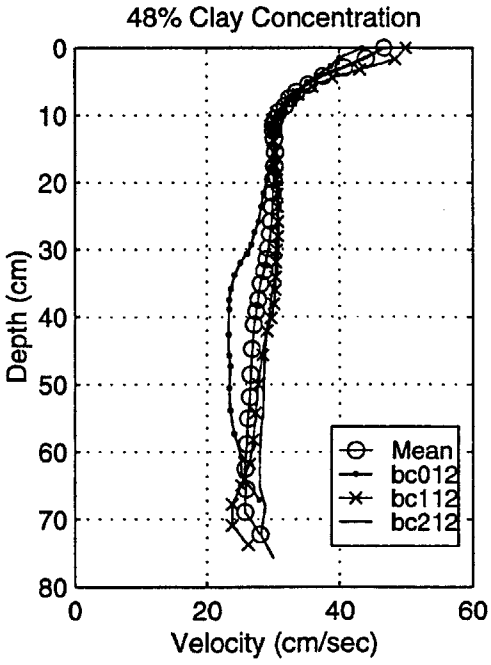
48% Clay Concentration
Depth (cm)
Velocity (cm/sec)
Mean
bc012
bc112
bc212

Bibliography

[1] Abdelrhman, M.A. and E.H. Dettmann. (1993). "Dredged material transport at deep-ocean disposal sites." *Proc. 8th Symp. on Coastal and Ocean Management*, American Shore and Beach Preservation Assoc./ASCE, New Orleans, LA.

[2] Baines, W.D. and E.J. Hopfinger. (1984). "Thermals with large density difference." *Atmos. Environ.* 18(6): 1051-1057.

[3] Batchelor, G.K. (1954). "Heat convection and buoyancy effects in fluids." *Quarterly J. Royal Met. Soc.*, 80:339-358.

[4] Bokuniewicz, H.J., et al. (1978). Field Study of the Mechanics of the Placement of Dredged Material at Open-Water Sites. Technical Report D-78-7, prepared by Yale University for the U.S. Army Engineer Waterways Experiment Station, Vicksburg, MS.

[5] Boothroyd, R.G.(1971). Flowing Gas-Solids and Suspensions. Chapman and Hall, London.

[6] Bowers, G.W. and M.K. Goldenblatt (1978). Calibration of a Predictive Model for Instantaneously Discharged Dredged Material. EPA/600/3-78-089, US Environmental Protection Agency, Corvallis, Oregon.

[7] Brandsma, M.G. and D.J. Divoky (1976). Development of Models for Prediction of Short-Term Fate of Dredged Material Discharged in the Estuarine Environment, Contract Report D-76-5, U.S. Army Engineer Waterways Experiment Station, Vicksburg, MS.

[8] Brodkey, R.S. (1967). The Phenomena of Fluid Motions. Addison-Wesley Publishing Company, Reading, MA.

[9] Bruce, E.J. (1988). The characterization of particle clouds using optical imaging techniques. Master Thesis, Dept. of Ocean Engineering, MIT, Cambridge, MA.

[10] Bühler J. and D.A. Papantoniou (1991). "Swarms of coarse particles falling through a fluid." *Environmental Hydraulics.* Lee and Cheung, eds. Balkema, Rotterdam.

[11] Clark, B.D., et al. (1971). The Barged Disposal of Wastes, a Review of Current Practice and Methods of Evaluation. Pacific Northwest Water Quality Laboratory, Northwest Region, U.S. Environmental Protection Agency, Corvallis, Oregon.

[12] Davies, J.T. and E.K. Rideal. (1961). Interfacial Phenomena. Academic Press, NY. p. 392.

[13] Davis, R.H. (1996). "Hydrodynamic diffusion of suspended particles: a symposium." *Journal of Fluid Mechanics.* 310:325-335.

[14] Dietrich, W. (1982). *Water Resources Research.* 18(6):1615-1626.

[15] Eckstein, E.C., Bailey, D.G., and A.H. Shapiro. (1977). "Self-diffusion of particles in shear flow of a suspension." *Journal of Fluid Mechanics.* 79(1):191-208.

[16] Escudier, M.P. and T. Maxworthy. (1973). "On the motion of turbulent thermals." *Journal of Fluid Mechanics.* 61(3):541-552.

[17] Gordon, R.B. (1974). "Dispersion of dredge spoil dumped in nearshore waters." *Estuarine and Coastal Marine Science.* 2:349-358.

[18] Hill, M.J.M. (1894). "On a spherical vortex." *Philos. Trans. Roy. Soc. London Ser. A* 185:213-245.

[19] Johnson, B.H. and B.W. Holliday (1977). Numerical Model Results of Dredged Material Disposal at Ten Proposed Ocean Disposal Sites in the Hawaiian Islands, Final Report, Misc. Paper H-77-6, Hydraulics Laboratory, U.S. Army Engineer Waterways Experiment Station, Vicksburg, MS.

[20] Johnson, B.H., (1992). Numerical Disposal Modeling, Dredging Research Technical Notes DRP-1-02, U.S. Army Engineer Waterways Experiment Station, Vicksburg, MS.

[21] Johnson, B.H., et al. (1993). Development and Verification of Numerical Models for Predicting the Initial Fate of Dredged Material Disposed in Open Water; Report 1, Physical Model Tests of Dredged Material Disposal from a Split-Hull Barge and a Multiple Bin Vessel, Technical Report DRP-93-1, U.S. Army Engineer Waterways Experiment Station, Vicksburg, MS.

[22] Johnson, B.H., and Fong, M.T. (1995). Development and Verification of Numerical Models for Predicting the Initial Fate of Dredged Material Disposed in Open Water; Report 2, Theoretical Developments and Verification Results, Technical Report DRP-93-1, Final Report, U.S. Army Engineer Waterways Experiment Station, Vicksburg, MS.

[23] Koh, R.C.Y. and Y.C. Chang (1973). Mathematical Model for Barged Ocean Disposal of Waste. Environmental Protection Technology Series EPA 660/2-73-029, U.S. Army Engineer Waterways Experiment Station, Vicksburg, MS.

[24] Kraus, N.C., ed (1991). Mobile, Alabama Field Data Collection Project, 18 August - 2 September 1989; Report 1, Dredged material plume survey data report, Technical Report DRP-1-09, U.S. Army Engineer Waterways Experiment Station, Vicksburg, MS.

[25] Lamb, Sir Horace. (1932). Hydrodynamics, 6th Edition. Cambridge University Press.

[26] Li C.W. (1997). "Convection of particle thermals." *J. of Hydraulic Res.* 35(3): 363-377.

[27] Luketina, D. and D. Wilkinson. (1994). "Particle clouds in density stratified environments." *Proc. 4th Int. Symp. of Stratified Flows,* Grenoble, France, June 29 - July 2.

[28] Massport and USACE. (1995). Boston Harbor, Massachusetts Navigation Improvement Project and Berth Dredging ProjectL Massachusetts Port Authority, US Army Corps of Engineers.

[29] Maxworthy, T. (1974). "Turbulent vortex rings." *Journal of Fluid Mechanics.* 64(2):227-239.

[30] Maxworthy, T. (1977). "Some experimental studies of vortex rings." *Journal of Fluid Mechanics.* 81(3):465-495.

[31] McLellan, H.J. (1965). Elements of Physical Oceanography. Pergamon Press, Oxford. pp. 28-36.

[32] Morton, B.R., Taylor, G.I., and J.S. Turner (1956). "Turbulent gravitational convection from maintained and instantaneous sources." *Proc. Roy. Soc. Lond. A.* 234:1-23.

[33] Nakatsuji, K., M. Tamian, and A.M. Murta (1990). "Dynamic behavior of sand cloud in water." *Proc. Conf. on Phys. Modeling of Transport and Dispersion,* MIT, Boston. 8C.1-8C.6.

[34] National Research Council. (1997). Contaminated Sediments in Ports and Waterways, Cleanup Strategies and Technologies. Committee on Contaminated Marine Sediments. National Academy Press, Washington, D.C.

[35] Neves, M.J.V. and P.D. Almeida. (1991). "The influence of density on thermal motion." *Environmental Hydraulics. Lee and Cheung, eds.* Balkema, Rotterdam, pp. 141-146.

[36] Nitsche, J.M. and G.K. Batchelor. (1997). "Break-up of a falling drop containing dispersed particles." *Journal of Fluid Mechanics.* 340:161-175.

[37] Noh, Y. and H.J.S. Fernando. (1993). "The transition in the sedimentation pattern of a particle cloud." *Phys. Fluids A.* 5(12):3049-3055.

[38] Papantoniou, D., Bühler J., and T. Dracos (1990). "On the internal structureof thermals and momentum puffs." *Proc. Int. Conf. on Phys. Modeling of Transport and Dispersion.* MIT, Boston, MA. A.31-A.36.

[39] Powell, R.L. and S.G. Mason. (1982). "Dispersion by laminar flow." *AIChE Journal.* 28(2):286-293.

[40] Rahimipour H. and D. Wilkinson. (1992). "Dynamic behavior of particle clouds." *Proc. 11th Australasian Fluid Mechanics Conf.* University of Tasmania, Hobart, Australia, 14-18 Dec. pp. 743-746.

[41] Resto, C. (1999). Senior Project Report, Dept. of Civil and Environmental Engineering, MIT, Cambridge, MA.

[42] Richards, J.M. (1961). "Experiments on the penetration of an interface by buoyant thermals." *Journal of Fluid Mechanics.* 11: 369-384.

[43] Science Applications International Corporation (SAIC). (1984). Dredged Material Disposal Operations at the Boston Foul Ground, June 1982 - February 1983, Contribution No. 41, prepared for the New England Division of the U.S. Army Corps of Engineers, Waltham, MA.

[44] Science Applications International Corporation (SAIC). (1988). Distribution of Dredged Material at the Rockland Disposal Site, May 1985, Contribution No. 50, prepared for the New England Division of the U.S. Army Corps of Engineers, Waltham, MA.

[45] Science Applications International Corporation (SAIC). (1997). Postcap Monitoring of Boston Harbor Navigation Improvement Project (BHNIP) Phase 1:

Assessment of Inner Confluence CAD Cell. SAIC Report No. 413, prepared for the New England Division of the U.S. Army Corps of Engineers, Waltham, MA.

[46] Scorer, R.S. (1957). "Experiments on Convection of Isolated Masses of Buoyant Fluid." *Journal of Fluid Mechanics.* 2: 583-595.

[47] Socolofsky, S. A. (2000), "Laboratory experiments of multi-phase plumes in stratification and crossflow", Ph.D. Thesis, Dept. of Civil and Environmental Engineering, MIT, Cambridge, MA. (in prep.).

[48] Sumeri, A. (1984). "Capped in-water disposal of contaminated dredged material." *Dredging '84*, Clearwater Beach, Fl., ASCE.

[49] Sumeri, A. (1991). "Capping of contaminated bottom sediment in Elliott Bay, Washington." *Conference Proceedings from Puget Sound Research '91.*

[50] Sustar, J. and T. Wakeman (1977). Dredged Material Study, San Francisco Bay and Estuary - Main Report. U.S. Army Engineer District, San Francisco, San Francisco, California.

[51] Swanson, J.C., Spaulding, M.L. and T. Isaji. (1994). "DREDGEMAP: A PC-based system to predict the fate of dredged material." *Dredging '94: Proc. of the 2nd Int. Conf. of Dredging and Dredged Material Placement.* E.C. McNair, Jr. Ed., NY, ASCE. 201-209.

[52] Tamai, M. and K. Muraoka. (1991). "Diffusion process of turbidity in direct dumping of soil." *Environmental Hydraulics.* Lee and Cheung, eds. Balkema, Rotterdam.

[53] Tavolaro, J.F. (1984). "A sediment budget study of clamshell dredging and ocean disposal activities in the New York Bight," Environmental Geology and Water Science 6(3): 133-140.

[54] Teeter, A.M. (1984). "Vertical transport in fine-grained suspension and newly deposited sediment." Lecture notes on coastal and estuarine studies. Estuarine Cohesive Sediment Dynamics, A.J. Mehta, Ed. Springer-Verlag, NY.

[55] The Math Works, Inc. (1997). MATLAB^{TM} numeric computing environment and image processing toolbox, version 2. Natick, MA.

[56] Thomas, D.G.(1963). *AIChE Journal.* 9:310-316.

[57] Turner, J.S. (1957). "Buoyant vortex rings." *Proc. Roy. Soc. Lond. A.* 239:61-75.

[58] Turner, J.S. (1960). "A comparison between buoyant vortex rings and vortex pairs." *Journal of Fluid Mechanics.* 7: 419-432.

[59] Turner, J.S. (1964). "The dynamics of spheroidal masses of buoyant fluid," Journal of Fluid Mechanics 19: 481-490.

[60] Turner, J.S. (1973). Buoyancy Effects in Fluids. Cambridge University Press, 367 pp.

[61] Wang, C.P. (1971). "Motion of an isolated buoyant thermal." *The physics of fluids.* 14(8):1643-1647.

[62] Wen F. and A. Nacamuli. (1996). "The effect of the Raleigh number on a particle cloud." *Hydrodynamics, Chwang, Lee and Leung, eds.* Balkema, Rotterdam. pp. 1275-1280.

[63] Woodward, B. (1959). "The motion in and around isolated thermals." *Quarterly J. Royal Met. Soc.* 85:144-151.

[64] Zreik, D. A. (1994), "Behavior of cohesive soils and their drained, undrained, and erosional strengths at ultra-low stresses", Ph.D. Thesis, Dept. of Civil and Environmental Engineering, MIT, Cambridge, MA.